Polar intermetallic crystals and quasicrystals

by

Joyce Pham
(Minh-Trang Pham)

A dissertation submitted to the graduate faculty

in partial fulfillment of the requirements for the degree of

DOCTOR OF PHILOSOPHY

Major: Chemistry

Program of Study Committee:
Gordon J. Miller, Major Professor
Joseph W. Burnett
Vitalij K. Pecharsky
Patricia A. Thiel
Julia V. Zaikina

The student author, whose presentation of the scholarship herein was approved by the program of study committee, is solely responsible for the content of this dissertation. The Graduate College will ensure this dissertation is globally accessible and will not permit alterations after a degree is conferred.

Iowa State University

Ames, Iowa

2018

DEDICATION

For my brother Hoang Joseph Pham and sister Thuy Carol Pham

Perhaps it is good to have a beautiful mind,
but an even greater gift is to discover a beautiful heart.
–A Beautiful Mind

TABLE OF CONTENTS

ACKNOWLEDGEMENTS

This work would not be possible without your gentle encouragement and unwavering confidence in me. Thank you for helping me create a work-life balance and for being a voice of reason especially amidst my bleakest self-doubts.

Many thanks to the faculty at ISU who helped shape my graduate school experience. To my cello professor and friend, George Work: your patient teaching has helped transform my own approach to teaching and learning. Creating music with you has kept me creative and motivated me to look for the silver-lining. To Irmi Schewe-Miller, whose door has always been open for me from the beginning of my graduate journey, and whose listening heart has helped me to feel welcome. To Kathy Burke who provided me with a perspective to appreciate the Midwest during my initial adjustments to graduate school. Thanks to my *PFF* advisers Emily Smith and Arthur Winter, who have shared their candid stories in academia and provided me with valuable career advice. Thanks to Theresa Windus, from whom I learned more about quantum mechanics applicable to my research, and with whom through teaching together, I learn to give others the benefit of the doubt. It may take a village to raise a child, but it takes a department to mold a scientist. Thanks for all the support from the ISU chemistry department.

My mentor and friend who introduced me to crystallography and taught me how to ask meaningful questions, Professor Håkon Hope of UC Davis: thank you for igniting and kindling a flame of curiosity in me and for your continued friendship.

Special thanks to my friends and "Phamily", without whom this research and dissertation would not be possible. Joshua LaJeunesse and Liana Hie: thank you for your many visits, letters, and care packages. Thank you for listening to my struggles and providing encouragement ceaselessly. To my friends in Ames who have, somewhere along my journey, helped make ISU my home and provided a reason for me to stay in graduate school: thank you

ABSTRACT

Two main questions guide these investigations of *polar intermetallic compounds*: (1) Where are the atoms, based on observed electron densities via diffraction? and (2) What gives rise to the observed structures, based on chemical bonding and electronic structure theory? At nearly equal Au: Al molar ratios, $NaZn_{13}$-derivatives of $Sr/Ca(Au_xAl_{1-x})_{12-13}$ show a progression from cubic to tetragonal, to orthorhombic, and then monoclinic symmetry with subtle decreasing Au concentrations, results which reveal preferential ordering of Au and Al to maximize the number of Au–Al (or Al-rich) shortest distances. In the Au-rich region of the Ca–Au–Al system, the 1/0 crystalline approximant (CA) $CaAu_{3+x}Al_{1-x}$ and icosahedral quasicrystal (i-QC) $CaAu_{4.5-x}Al_{1.5+x}$ were discovered, and the i-QC is shown to irreversibly transform into the 2/1 CA $Ca_{13}Au_{56.79(6)}Al_{21.20}$ via *in-situ*, high-energy, variable-temperature powder X-ray diffraction (XRD). The QC was characterized from high-energy single-crystal XRD to have icosahedral symmetry, $Pm\overline{3}\overline{5}$, and a quasilattice ($a_{QC}$ = 5.383(4) Å) in close agreement to those calculated from the 1/0 and 2/1 CAs ($a_{QC\text{-}Calc.1/0}$ = 5.336(2)–5.354(2) Å; $a_{QC\text{-}Calc.2/1}$ = 5.364(6) Å). Following the polar intermetallic depiction from the calculated electronic structures, the 1/0 and 2/1 CA crystal structures show formally electronegative Au+Al sharing polyhedra and electropositive Ca in the voids or in intervening shells so that overall, the 2/1 CA can be described as interpenetrating and edge-sharing icosahedra. The origin of hexagonal ScAuAl, in which the unit cell is distorted due to long-short alternating Au–Au chains, is rationalized from a Peierls-type distortion of its calculated electronic structures. Chemical pressure effects and valence electron count variations were examined in the series CaAuAl–ScAuAl–TiAuAl. In general, the calculated electronic structures of all these (Sr/Ca/Sc)–Au–Al crystalline compounds reveal significant Sr/Ca/Sc–(Au+Al) polar-covalent interactions that contribute to structural cohesion and preferential ordering to maximize the number of Au–Al shortest distances.

CHAPTER 1

INTRODUCTION

Generally, the nonmetal-metal dichotomy respectively simplifies electronic distributions as either "localized", usually through covalent bonds among atoms, and "delocalized" throughout the solid. As such, whereas chemistry of nonmetals often depicts molecular and electronic features such as those seen in Lewis dot structures or molecular orbital energy diagrams, metals are often only represented at the atomic-packing level with the caveat that they have "delocalized" electrons and serve as electron donors to nonmetals generally due to their respective lower electronegativities.

The question remains as to just *how* "delocalized" are the electrons in metals. How do electrons interact among one another at the atomic level of metals and intermetallics, i.e., compounds with two or more metallic elements combined at specific molar ratios? Although studies of nonmetals are abundant and diverse with even general chemistry textbooks providing a plethora of examples using nonmetals, metals and metalloids comprise almost three-quarters of the periodic table! Thus, intermetallics provide a fertile ground to study, predict, and modulate the relationships among chemical compositions, atomic and electronic structures, and physical properties.

This dissertation addresses the fundamental study of main-group intermetallics by specifically examining *polar intermetallic compounds* and the investigations are guided by two main questions: (1) Where are the atoms, based on observed electron densities via diffraction? and (2) What gives rise to the observed structures, based on chemical bonding and electronic structure theory?

What Are Polar Intermetallic Compounds?

Polar intermetallic compounds are comprised of formally electropositive metals in the first four groups of the periodic table, including rare-earth elements, and electronegative elements of the late transition metals and early *p*-block. According to a classification using valence electron counts, which are evaluated as the total number of valence electrons per electronegative metal atom (*e/a* value), they fall in the region $2.0 \leq e/a < 4.0$. As such, polar intermetallics are considered an intermediate class between the Hume-Rothery (H-R) and Zintl-Klemm (Z-K) phases, and are often described with respect to these phases, which have both been reported more extensively in main-group intermetallic chemistry.

Hume-Rothery phases. Hume-Rothery[1] phases fall in the region $1.0 \leq e/a < 2.0$, and are also called "electron compounds," because in 1926, William Hume-Rothery assembled the common valence electron counting basis for rationalizing structures of β-brass Cu–Zn, Cu–Al and Cu–Sn binaries.[2] His research led to the systematization showing that electron count variations directly correlated with changes in defect-BCC γ-brass structures in the region $1.54 \leq e/a \leq 1.70$, which was later expanded to include FCC α-($1.0 \leq e/a \leq 1.42$) and HCP η-($1.93 \leq e/a < 2.00$) brasses. Like the Cu–Zn, Cu–Al, and Cu–Sn brass systems, Hume-Rothery phases contain elements with similar electronegativities and sizes from the late- and post-transition metals, and crystallize in densely packed structures with large coordination spheres, such as seen in the γ-brass type with 26-atom clusters involving four fused icosahedra. The *e/a* ratio is evaluated by counting the total number of electrons divided by all the metals.[3]

Zintl-Klemm phases. In the region $e/a \geq 4.0$, Zintl-Klemm[4] phases are comprised of electropositive metals (i.e., alkali, alkaline-earth or rare-earth metals) and electronegative metals around the "Zintl border" between groups 13 and 14 of the periodic table,[5] crystallize

in structures built of networks of the electronegative metals that are often electron-specific following the octet or Wade's rules,[6] and count the total number of valence electrons divided by the sum of only the electronegative metal atoms. They are considered "salt-like compounds" due to the electronegativity differences between the different components. In Eduard Zintl's seminal investigation and analysis of the prototypic NaTl compound in 1929, Na is seen as actively donating its $3s$ electron to create salt-like "Na$^+$" and "Tl$^-$" ions, the anions of which obey the octet rule so that each "Tl$^-$" is covalently and tetrahedrally coordinated to four other "Tl$^-$" atoms while "Na$^+$" provides charge balance.[7] Because of electronegativity differences between the active metals (e.g., Na) and metals of the anionic framework (e.g., Tl), the atomic interactions and bonding in Z-K phases exhibit more ionic character than in H-R phases.[8]

Polar intermetallics as "hybrids" of Hume-Rothery and Zintl-Klemm phases. Like Z-K phases, polar intermetallic compounds contain combinations of electropositive and electronegative metals with the former actively donating valence electrons to the latter, which, due to more similar electronegativities among the elements than in Z-K phases, also engage in electronic back-donation for structural cohesion.[9] The salt-like Z-K compounds such as NaTl can be rationalized from "Tl$^-$" and "Na$^+$" ions, without clear electronic back donation from the anionic framework to virtual orbitals of Na because of the large electronegativity difference between Na and Tl. In comparison, for polar intermetallic compounds, the electronegativity difference between metals of the anionic framework and the active metal is closer than that of Z-K compounds, and therefore results in significant electronic back-donation to the virtual orbitals of the "cationic" species. This electronic back-donation by the electronegative metals results in electron deficiency for two-center two-electron bonding within the network of these species, which therefore form polyhedra or condensed clusters.

As a result, polar intermetallic compounds form a "hybrid" class between the H-R and Z-K phases because the atomic constituents possess large coordination spheres, as seen in H-R phases, but the atomic sizes between "cations" and "anions" can differ substantially. On the other hand, the electronegativity differences between electropositive and electronegative elements of polar intermetallics resemble those of Z-K phases, but the electron counting rules used to rationalize Z-K phases cannot easily rationalize the structures of polar intermetallic compounds because there are no clear two-center, two-electron bonds nor discrete clusters. To date, there are no "simple", overarching valence electron counting rules to rationalize the observed composition-structure-bonding relationships among polar intermetallic compounds.

Polar Intermetallic Quasicrystals

Many polar intermetallic compounds contain complex structures with large atomic coordination spheres, mixed site occupancies, and networks and clusters of polyhedra so that it is not surprising many quasiperiodic crystals ("quasicrystals" for short; QCs) and their corresponding crystalline approximants (CAs) are polar intermetallics.

QCs are a class of solids with crystallographic incompatible 5-, 7-, 8-, or higher-order rotational symmetry so that there is long-range quasiperiodic translational and orientational order.[10] Out of the known QC classes, icosahedral quasicrystals (i-QCs) form the largest and most complex one because icosahedral symmetry requires quasiperiodicity in 3-dimensional (3D) space unlike, for instance, decagonal QCs, which are quasiperiodic in 2D.[11] To answer question (1) of the dissertation for i-QCs, "where are the atoms, based on observed electron densities via diffraction?", 3D crystallography is insufficient,[12] and therefore, the structures of most multinary i-QCs are inferred from their CAs, which are compounds in close chemical
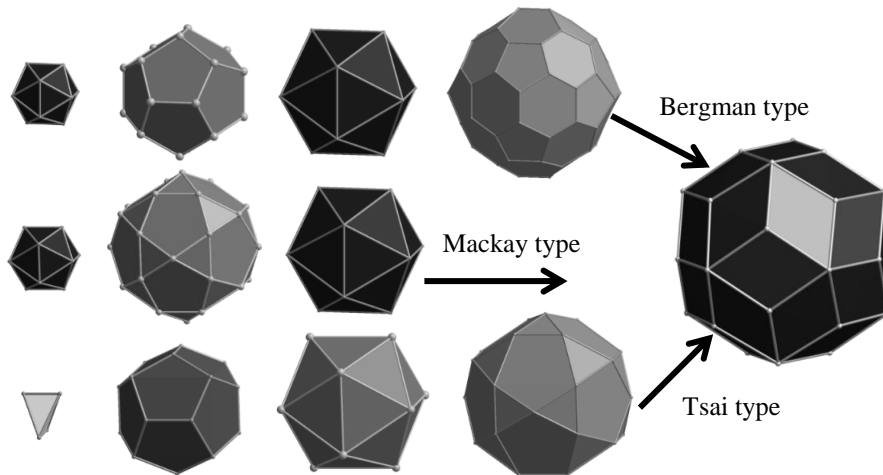
Figure 1. Three cubic crystalline approximant structure types, all with at least one distorted icosahedron and are all encapsulated by a triacontahedral shell.

composition to the i-QC with periodic structures and are proposed to approximate the local structures of the i-QC.[13]

Crystalline approximants of icosahedral quasicrystals. Since the discovery of the Al–Mn i-QC by Dan Shechtman in 1984,[14] there are three cubic structure types identified as CAs and are depicted via clusters of concentric shells: Mackay-,[15] Bergman-,[16] and Tsai-types (Figure 1).[17] The Mackay type is drawn as three shells with icosahedra as the inner and outermost shells and a 30-atom icosidodecahedron as the second, middle shell. The Bergman-type is similar to the Mackay-type but has a dodecahedron as the second shell and a 60-atom Buckminsterfullerene-type truncated icosahedron as an additional fourth shell. The Tsai-type most resembles the Bergman-type but contains orientationally disordered tetrahedral clusters as the innermost shell and an icosidodecahedral fourth shell of atoms. Recent literature represents the fifth shell of Tsai-type CAs as a 92-atom rhombic triacontahedron with rhombohedra between these triacontahedral clusters,[11b, 18] which is a structural similarity in all three CA types in longer-range order. Similar to 3D crystalline solids, which are described by their unit cell parameters and Bravais lattices, i-QCs are analogously identified by their

quasilattice (a_{QC}) and symmetry comparable to 3D space groups, which includes either the primitive (*P*), body-centered (*I*), or face-centered (*F*) designation.

In addition to the structure-type categorization, CAs are also classified by a rational order, "*L/S*", such as "1/1" or "2/1", based on two consecutive numbers in the Fibonacci sequence, and how closely the CA relates to its i-QC. As the *L/S* designation moves further along the Fibonacci sequence, the lattice constant of the cubic CA, $a_{L/S}$, steadily increases. The higher the *L/S* order, the more closely the CA relates to the i-QC, so that $a_{L/S}$, a_{QC} (the quasilattice constant), and the golden mean ($\tau = \left(\frac{1+\sqrt{5}}{2}\right) = 1.618...$) can be related as follows:[13a]

$$a_{QC} = \frac{a_{L/S}(2+\tau)^{1/2}}{2(S+L\tau)} \qquad (eq.\,1)$$

Indexing quasicrystals. Because i-QCs are aperiodic in 3D, indexing of their diffraction peaks may use a cut-and-project method to a 3D cube from the 6D hyperspace, in which i-QCs are expected to be periodic.[12b] Each XRD peak is then related to six integers n_1–n_6 that are the integer coefficients of a linear combination of six basis vectors from the origin to the six vertices of a regular icosahedron that are not related by inversion. The equivalent Miller indices in hyperspace would correspond to:

$$\begin{array}{ll} h = n_1 - n_4 & h' = n_2 + n_5 \\ k = n_3 - n_6 & k' = n_1 + n_4 \qquad (eq.\,2) \\ l = n_2 - n_5 & l' = n_3 + n_6 \end{array}$$

whereby:

$$\begin{array}{ll} N = h^2 + k^2 + l^2 + h'^2 + k'^2 + l'^2 & \text{and} \\ M = h'^2 + k'^2 + l'^2 + 2(hh' + kk' + ll'), & (eq.\,3) \end{array}$$

so that the quasilattice, a_{QC}, is calculated from the diffraction spacing $Q_{||}$ (Å^{-1}) as follows[19]:

$$(\sqrt{2})a_{QC} = \frac{2\pi}{Q_{||}}\sqrt{\frac{N+M\tau}{2(2+\tau)}} \qquad (eq.\,4)$$

Structural characterization using both 3D crystallography and hyperspace methods provides a means to answer question (1) of this research, but to answer question (2) and assess the interactions among atoms that form the foundation for the observed crystalline and quasicrystalline structures of polar intermetallics, electronic structure theory was utilized.

AE/RE–Au–Al: Site- and Bond-Energies from Electronic Structure Theory

The total electronic energy for a given structure is evaluated by using the Born-Oppenheimer approximation and involves one- and two-electron energy terms. A comparison of total electronic energies for two or more different structural models can be estimated using the total band energy derived from the one-electron terms as long as certain constraints are placed on the two-electron terms.[20] Such strategies include the Structural Energy Theorem[21] and Second Moment Scaling,[22] which can be accomplished by comparing isocompositional structures with the same volume per formula unit. Within the tight-binding approach used in this research, the total band energy for an extended solid can be separated into two terms: (1) the "site energy" term, which can be indirectly evaluated by assessing charge and population distributions respectively from Bader charge or Mulliken population analysis, or by comparing energetic stability of isocompositional models of different colorings[23], and (2) the "bond energy term".[20]

Within density functional theory, the bond energy term is the integration of the crystal orbital Hamilton population (COHP), which is a "bond-weighted" density of states (DOS) between adjacent atoms,[24] and the DOS is the analog of the molecular orbital energy diagram for extended solids. In this research, the total DOS is often decomposed into their atomic orbital contributions to elucidate the underlying electronic interactions. Both the COHP and DOS are significantly affected by the electronegativity (χ) of the constituent metals. Electronegativity,

as defined by Pearson, is the average electron affinity and first ionization energy of a gas phase atom.[25] Of all the metals, Au has the largest electronegativity (χ_{Au} = 5.77 eV) and was thus selected for further study. The electronic configuration of Au is $[Xe]4f^{14}5d^{10}6s^1$, so that it can be counted as contributing one valence electron because the $5d$ band is filled and lies well below the Fermi level. However, theoretically, the $6s^1$ electron wavefunction has a finite non-zero probability distribution to penetrate the nucleus, so that the velocity of the electron approaches that of the speed of light,[26] which affects the $6s$ electron mass and energy, and contracts the $6s$ orbital. The $6s$ orbital contraction toward the nucleus thus shields the $5d$ orbitals and destabilizes the $5d^{10}$ electrons to lie closer to the $6s^1$ electron so that Au can sometimes be counted as contributing 11 total valence electrons.[27] Coupled with Au, which is rich in $5d$ electrons and highly electronegative, Al ($[Ne]3s^23p^1$; χ_{Al} = 3.23 eV) is introduced, which is $3p$ electron-poor, has virtual d orbitals, and is the least electronegative of its group 13 family touching the Zintl-border. Au and Al are both electron poor, in terms of $6p$ and $3p$ occupations, respectively, although they are both more electronegative in comparison to the far-left of the periodic table.

In many ways, Au–Al binaries are Hume-Rothery compounds. For instance, Au_4Al[28] (e/a = 1.40) contains 3 atoms in the asymmetric unit cell (Al(4a), Au1(4a), and Au2(12b)) and each is icosahedrally coordinated so that it is a binary derivative of elemental β-Mn. Its valence electron count and large atomic coordination spheres fall within the Hume-Rothery classification and the similar metallic radii between its constituents (R_{Au} = 1.44 Å, R_{Al} = 1.43 Å) further abide by Hume-Rothery rules to attain substitutional solid-solution.

To probe the interatomic interactions within polar intermetallics, alkaline-earth (AE) and rare earth (RE) elements are introduced to the Au–Al system, where the underlying

(AE/RE)–(Au+Al) polar covalent interactions give rise to structural cohesion. Binary AE/RE–Au compounds, then, may follow the Zintl-Klemm structural rationale. For instance in $(Sr/Ca)Au_2$,[29] Sr/Ca formally donates electrons to attain "Sr/Ca^{2+}" and "$2Au^-$", in which the active Sr/Ca are in channel-like cavities of the tetrahedrally-distorted Au-coordinations. Therefore, polar intermetallic AE/RE–Au–Al have features of both Hume-Rothery and Zintl-Klemm phases based on their binary break-down.

In this dissertation, the choice of AE and RE elements spans both investigations of electron count effects as well as "chemical pressure". The latter is addressed by considering metallic radius effects among the different AE and RE elements. For instance, since Ca has a smaller metallic radius than Sr ($R_{Sr,Ca}$ = 2.15, 1.97 Å), at similar molar ratio compositions Sr/Ca:(Au+Al), what are the crystal structure ramifications? Substituting Ca for Sr in the similar compositions "chemically imposes pressure" on the structure, which needs to accommodate the smaller Ca because Sr/Ca–(Au+Al) polar covalent interactions contribute to structural cohesion. Then, going from divalent Sr/Ca to trivalent Y/Sc ($R_{Y,Sc}$ = 1.80, 1.64 Å), also at similar molar ratio compositions, what are the electronic and crystallographic effects?

To address the site-energy term, which is especially relevant to this study because formally electronegative Au and Al share a framework with intervening AE/RE in the voids so that Au and Al even sometimes share the same Wyckoff sites, isocompositional models and their calculated total energies were examined. This atomic site preference arrangement is known as the "coloring problem"[23] and can be simplified to resemble the investigation of isomeric stability in molecular inorganic chemistry:

$IO_2F_2^-$ reacts with excess fluoride to form $IO_2F_3^{2-}$, which can be drawn with minimal formal charges as any of the three square-pyramidal isomers below:

10
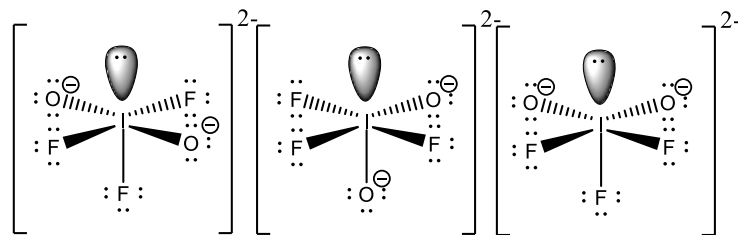
Figure 2. Isomers of molecular $IO_2F_2^-$ illustrating the use of electronegativity and atomic radius to rationalize structural stability as applied to extended solids of polar intermetallic compounds.

The middle isomer, with lone-pair electrons trans to O, is the most likely atomic arrangement, because the lone-pair is in the axial position with the least repulsion from the four bond-pairs in the square planar geometry (3 from F and 1 from O ligands). Since F is more electronegative than O and has a smaller atomic radius, this is favorable over the third isomer, which has 2 lone-pair–bond-pair repulsions of each O and F ligands.

This example considers atomic sizes and electron pair interactions to rationalize the most preferred atomic arrangement. In a similar manner, this dissertation examines metallic radii and electronic interactions to elucidate the crystallographic structures of polar intermetallic compounds.

Overview of Dissertation Chapters

A final point of consideration in the study of polar intermetallic compounds are the effects of synthetic schemes and compositional choices. Therefore, the study of intermetallics can generally be broken up into four main parts: (1) syntheses and compositions; (2) atomic structures; (3) electronic structures and chemical bonding; and (4) properties. This dissertation examines the first three of these foci in the following chapters:

Chapter 2. General experimental and computational methods. This chapter explains the main experimental techniques and computational tools used throughout the later chapters with emphasis on their fundamental usefulness and limitations. Readers are encouraged to review the accompanying references for more scientific discussion.

Chapter 3. Structure-composition subtleties in NaZn$_{13}$-type derivatives of Sr/Ca(Au$_x$Al$_{1-x}$)$_{12-13}$. As the first project of my graduate studies, this chapter builds off previous research that examined Ba/Sr–Cu/Ag/Au–Al polar intermetallics. In the nearly equimolar mixtures of Au and Al, five new ternary NaZn$_{13}$-derivatives of Sr/Ca(Au$_x$Al$_{1-x}$)$_{12-13}$ were discovered that show a progression from cubic to tetragonal and monoclinic structures with subtly decreasing Au concentrations. In these structures, Au and Al atoms form icosahedral frameworks with voids that are filled by Sr or Ca with snub-cube coordination spheres. The decreased symmetry from cubic to tetragonal and monoclinic reveals preferential ordering of Au and Al to maximize the number of Au–Al (or Al-rich) shortest distances. To observe chemical pressure effects, Ca was substituted for Sr and showed an orthorhombic variation. This chapter initiates the investigation of polar intermetallics in this dissertation by closely examining subtle effects of compositions on structures.

Chapter 4. An icosahedral quasicrystal and its 1/0 crystalline approximant in the Ca–Au–Al system. This chapter expands on the general investigation of the Ca–Au–Al system by moving into the Au-rich region of the ternary phase space, in which analogous systems have exhibited diverse and complex structures. Valence electron counts were used to target compositions that have reported i-QCs and CAs and resulted in the discovery of a CaAu$_{4.5-x}$Al$_{1.5+x}$ ($0.11 \leq x \leq 0.40(6)$) i-QC and its lowest order 1/0 CA CaAu$_{3+x}$Al$_{1-x}$ ($0 \leq x \leq 0.31(1)$). The i-QC was characterized using high-energy, single-crystal X-ray diffraction with the precession technique to determine its symmetry as $Pm\overline{3}\overline{5}$. The polar-covalent interactions of Ca–(Au+Al) were addressed from the calculated electronic structures and from the atomic depiction of {Ca$_{4/4}$[Au$_{3-x}$Al$_{1+x}$]} tetrahedral stars, and the phase width was rationalized from the electronic interactions of nearest atomic neighbors.

Chapter 5. From quasicrystals to crystals with interpenetrating icosahedra in Ca–Au–Al: *in-situ* variable-temperature transformation. The metastable i-QC discovered in Chapter 4 is showed to irreversibly transform into its 2/1 CA $Ca_{13}Au_{56.79(6)}Al_{21.20}$ ($CAu_{4.37(1)}Al_{1.63}$) via *in-situ*, high-energy powder X-ray diffraction. The structure of the 2/1 CA is depicted in the Tsai-type in concentric shells with (Au+Al) atoms sharing shells and Ca atoms in intervening shells, per the polar-covalent interactions of the compound, which are a signature of polar intermetallics. The most intense PXRD peaks that changed during the transformation were analyzed to show direct correlations between the i-QC and 2/1 CA and atomic site preferences of Au and Al atoms were analyzed from the coordination spheres of the split sites. From electronic structure calculations, a 1/1 CA "$Ca_{24}Au_{88}Al_{64}$" is proposed.

Chapter 6. AAuAl (A = Ca, Sc, and Ti): Peierls distortion, atomic coloring, and structural competition. This chapter studies the active metal electronic and metallic size effects on polar-intermetallics. Although no i-QCs were identified in Sc–Au–Al, a combination of computational and crystallographic studies showed the ScAuAl compound experiencing an electronic pseudo-Peierls distortion that led to alternating long-short Au–Au chains. Additionally, based on calculations of unit cell volumes as a function of energy, the competing Co_2Si-(TiNiSi-type), Fe_2P-, and Ni_2In-types structures, which are all commonly observed in many polar intermetallic compounds and in AAuAl, were rationalized in terms of decreasing metallic radius and increasing valence electron concentrations on going from Ca to Sc and Ti.

Chapter 7. Y/Gd–Au–Al 1/1 crystalline approximants, structures with hexagonal stars and noncentrosymmetry. With trivalent Gd and Y as active metals, 1/1 CA's are once again present as similarly seen in the case of Ca–Au–Al. This chapter tabulates the structures observed in Y/Gd–Au–Al. Synthetic compositions that had yielded the 2/1 and 1/0 CAs in Ca–

Au–Al instead led respectively to the 1/1 CA's and new (Y/Gd)Au$_{2.929(4)}$Al$_{0.659}$ compounds with hexagonal stars. Moving into Al-rich compositions led to new noncentrosymmetric hexagonal (Gd/Y)$_4$Au$_{9.00(3)}$Al$_{13}$.

References

1. Mizutani, U., *Hume-Rothery rules for structurally complex alloy phases*. CRC Press Taylor & Francis Group: Boca Raton 2010.

2. Hume-Rothery, W., Researches on the nature, properties, and condition of formation of intermetallic compounds. *J. Inst. Met* **1926,** *35*, 319-335.

3. Mizutani, U.; Sato, H., The physics of the Hume-Rothery electron concentration rule. *Crystals* **2017,** *7* (1), 9.

4. Miller, G.; Schmidt, M.; Wang, F.; You, T.-S., Quantitative advances in the Zintl–Klemm formalism. *Structure and Bonding* **2011,** *139* (Zintl Phases), 1-55.

5. Miller, G. J. L., C.-S.; Choe, W. , Structure and bonding around the Zintl border. In *Inorganic Chemistry Highlights*, Meyer, G., Naumann, D., Wesemann, L., , Ed. Wiley-VCH: Wein-heim: Germany, 2002; pp 21-53.

6. Wade, K., The structural significance of the number of skeletal bonding electron-pairs in carboranes, the higher boranes and borane anions, and various transition-metal carbonyl cluster compounds. *Journal of the Chemical Society D: Chemical Communications* **1971,** (15), 792-793.

7. Zintl, E., Intermetallische Verbindungen. *Angewandte Chemie* **1939,** *52* (1), 1-6.

8. Schäfer, H.; Eisenmann, B.; Müller, W., Zintl Phases: Transitions between metallic and ionic bonding. *Angewandte Chemie International Edition in English* **1973,** *12* (9), 694-712.

9. Miller, G. J.; Reedijk, J.; Poeppelmeier, K. R., Metal-rich compounds of the *d*-metals Comprehensive Inorganic Chemistry II. *Comprehensive Inorganic Chemistry II* **2013,** *2*, 311-357.

10. (a) Levine, D.; Steinhardt, P. J.; Quasicrystals. I. Definition and structure. *Phys. Rev. B* **1986,** *34*, 596; (b) Levine, D.; Steinhardt, P. J., Quasicrystals: a new class of ordered structures. *Physical Review Letters* **1984,** *53* (26), 2477-2480.

11. (a) Steurer, W.; Deloudi, S., Decagonal quasicrystals–What has been achieved? *Comptes Rendus Physique* **2014,** *15* (1), 40-47; (b) Steurer, W., Why are quasicrystals quasiperiodic? *Chemical Society Reviews* **2012,** *41* (20), 6719-6729.

12. (a) Janot, C., The crystallography of quasicrystals. *Proceedings: Mathematical and Physical Sciences* **1993,** *442* (1914), 113-127; (b) Janot, C., *Quasicrystals: a Primer*. 1994.

13. (a) Goldman, A. I.; Kelton, R. F., Quasicrystals and crystalline approximants. *Reviews of Modern Physics* **1993,** *65* (1), 213-230; (b) Dong, C., The concept of the approximants of quasicrystals. *Scripta Metallurgica et Materialia* **1995,** *33* (2), 239-243.

14. Shechtman, D.; Blech, I.; Gratias, D.; Cahn, J. W., Metallic phase with long-range orientational order and no translational symmetry. *Physical Review Letters* **1984,** *53* (20), 1951-1953.

15. Mackay, A., A dense non-crystallographic packing of equal spheres. *Acta Crystallographica* **1962,** *15* (9), 916-918.

16. Bergman, G.; Waugh, J. L. T.; Pauling, L., The crystal structure of the metallic phase $Mg_{32}(Al, Zn)_{49}$. *Acta Crystallographica* **1957,** *10* (4), 254-259.

17. (a) Guo, J. Q. A., E.; Tsai, A.P., Stable icosahedral quasicrystals in binary Cd-Ca and Cd-Yb systems. *Physical review. B, Condensed matter* **2000,** *62* (22), R14605; (b) Gómez, C. P.; Lidin, S., Structure of $Ca_{13}Cd_{76}$: a novel approximant to the $MCd_{5.7}$ quasicrystals (M=Ca, Yb). *Angewandte Chemie International Edition* **2001,** *40* (21), 4037-4039.

18. (a) Guyot, P.; Audier, M., Quasicrystals and atomic clusters. *Comptes Rendus Physique* **2014,** *15* (1), 12-17; (b) Gómez, C. P.; Tsai, A. P., Crystal chemistry and chemical order in ternary quasicrystals and approximants. *Comptes Rendus Physique* **2014,** *15* (1), 30-39.

19. Cahn, J. W.; Shechtman, D.; Gratias, D., Indexing of icosahedral quasiperiodic crystals. *Journal of Materials Research* **1986,** *1* (01), 13-26.

20. Burdett, J. K. *Chemical Bonding in Solids*. New York: Oxford University Press, **1995**.

21. Pettifor, D. G., A physicist's view of the energetics of transition metals. *Calphad* **1977,** *1*, 305-324.

22. Burdett, J. K.; Lee, S., Moments method and elemental structures. *Journal of the American Chemical Society* **1985,** *107* (11), 3063-3082.

23. Miller, G. J., The "Coloring Problem" in solids: how it affects structure, composition and properties. *European Journal of Inorganic Chemistry* **1998,** *1998* (5), 523-536.

24. Dronskowski, R.; Blöchl, P. E., Crystal orbital Hamilton populations (COHP): energy-resolved visualization of chemical bonding in solids based on density-functional calculations. *The Journal of Physical Chemistry* **1993,** *97* (33), 8617-8624.

25. Pearson, R. G., Absolute electronegativity and hardness: application to inorganic chemistry. *Inorganic Chemistry* **1988,** *27* (4), 734-740.

26. Pyykkö, P., Theoretical chemistry of gold. *Angewandte Chemie International Edition* **2004,** *43* (34), 4412-4456.

27. Jansen, M., Effects of relativistic motion of electrons on the chemistry of gold and platinum. *Solid State Sciences* **2005,** *7* (12), 1464-1474.

28. Villars, P.; Cenzual, K.; Daams, J.; Gladyshevskii, R.; Shcherban, O.; Dubenskyy, V.; Melnichenko-Koblyuk, N.; Pavlyuk, O.; Stoiko, S.; Sysa, L., Au_4Al. In *Structure Types. Part 2: Space Groups (218) P$\bar{4}$3n (195) P*23, Villars, P.; Cenzual, K., Eds. Springer Berlin Heidelberg: Berlin, Heidelberg, **2005**.

29. Zachwieja, U., Synthesis and structure of $CaAu_2$ and $SrAu_2$. *Journal of Alloys and Compounds* **1996,** *235* (1), 12-14.

CHAPTER 2

GENERAL EXPERIMENTAL AND COMPUTATIONAL METHODS

This chapter outlines the general procedures used in this research from the experimental syntheses and characterizations via X-ray diffraction and elemental analyses to the computational techniques utilizing electronic structure theory. The goal is to summarize the fundamentals of each method and provide a rationale for their use.

Syntheses

Many of the syntheses started with a question on the effects of composition on the structure, in which case, the melting points and relative amounts of the respective starting elements were considered. For instance, in chapter 3, the subtle effects of compositions in the 1:12–1:13 ratio range were examined for (Sr/Ca):(Au+Al) to show geometric and atomic decoration variations within the same structural family. Later chapters report the compositional ~1:5.3–1:6 ratio of (Ca/Y/Gd):(Au+Al) that led to quasicrystals and their crystalline approximants. In these syntheses, binary phase diagrams may be useful to determine a suitable heating profile for the ternary compositions, although some of the syntheses were coupled with thermogravimetric data.

Starting reactants. The high-purity ($\geq 99.9\%$) starting elements for all syntheses are listed in Table 1 and were used as received. All elements were stored in an argon- or nitrogen-filled glovebox with moisture levels maintained at less than or equal to 0.1 ppm by volume and were cut into pieces from their original form so that the total sample masses were either 300.0(1) or 800.0 mg. Specifically with Sr, the surfaces were scraped with a scalpel directly prior to loading into their tantalum reaction vessels to avoid oxidized areas.

Table 1. Reactants for all syntheses

Metal	Origin	Purity%	Melting Point (°C)	Form
Au	Ames Laboratory	99.99	1064	Spheres
Al	Alfa-Aesar	99.999	660.3	Ingots
Ca	Sigma Aldrich	99.99	842	Chunks
Sr	Alfa-Aesar	99.9	777	Dendrites
Sc	APL-Aldrich	99.9	1541	Chunks
Y	Ames Laboratory	99.995	1526	Chunks
Gd	Ames Laboratory	99.995	1312	Pieces

Tube furnace synthesis. A programmable tube-furnace is useful because of its time and temperature programmable capabilities, and its maximum limit of ~1200 °C is higher than the temperatures used in this research to achieve solid solutions. Tantalum ampoules, with starting reactants inside for the targeted compositions, were arc-welded shut under argon and sealed under vacuum in a secondary silica jacket to avoid oxidation of the tantalum at reaction temperatures, and were then placed into programmable tube furnaces. Depending on the sample, either an annealing heating profile or a rapid quenching of the reactions was used, and the latter was particularly important for the syntheses of quasicrystalline products.

Characterization

All X-ray diffraction characterization techniques are summarized in Table 2.

Powder X-ray diffraction. Phase analyses of all products were initially carried out by use of powder X-ray diffraction with the Stoe Stadi P diffractometer equipped with a position-sensitive image-plate detector (Cu $K_{\alpha 1}$, λ = 1.54060 Å) at ~25 °C. Crystalline samples were ground, dispersed onto, and sandwiched between two transparent acetate or mylar films with the use of vacuum grease. To ensure instrument alignment, external NBS Si 640b powder was also mixed homogenously with some of the ground products for measurement comparison against the PXRD pattern of a 1923 Si-standard (ICSD identification no. 53783).[1] If the instrument is misaligned, the PXRD patterns are then manually shifted to orient the peaks of the Si-standard in its known 2θ positions. Subsequent measurements of the same sample batch

Table 2. X-ray diffraction instrument specification and usage summary

	Stoe Stadi P PXRD	APS PXRD	Bruker CCD APEX II	D8 VENTURE APEX III	STOE IPDS II	APS four-circle single crystal XRD
purpose	phase width and purity analysis	*in-situ* heating to see phase changes	single specimens for refined structural solution	data of small specimens with large absorption	full reciprocal lattice diffraction for testing	quasi-lattice calculation from precession diffraction
λ (Å)	Cu$K_{\alpha1}$ (1.54060)	0.17712	Mo $K_{\alpha1}$ (0.71073)	Mo $K_{\alpha1}$ (0.71073)	Mo $K_{\alpha1}$ (0.71073)	0.18352
sample-detector (mm)	130	1821.595	50–70	60	100	834.2732

after instrument alignment may not include the Si-standard. Phase analysis was performed by juxtaposing the observed PXRD patterns against PXRD patterns calculated from single-crystal XRD refined crystallographic solutions and PXRD patterns of known compounds. Hence, the PXRD patterns serve as a fingerprint identification of the products. In many cases, a Rietveld refinement with a Le Bail decomposition of the observed PXRD patterns was used to extract the sample lattice parameters and atomic coordinates,[2] which are then a course-grained average of the sample, instead of those provided by single-crystal XRD and are more specific to the individual specimen.

In chapter 5, high-energy PXRD ($\lambda = 0.17712$ Å) as a function of temperature was employed to observe an *in-situ* transformation via PXRD pattern changes using the Advanced Photon Source (APS) at Argonne National Lab (ANL). Although PXRD is a useful and quick characterization technique for phase analysis, it is inherently 1-dimensional (1D).

Single crystal X-ray diffraction. Therefore, crystallographic modeling from single-crystal XRD, which maps out the reciprocal space in 3D and implicitly provides more data on 3D thermal oscillations, was carried out. Selected specimens from the bulk products were mounted onto the tips of glass fibers and held fixed with vacuum grease. Most single-crystal

XRD data were collected at ~25 °C with a Mo $K_{\alpha 1}$ radiation source ($\lambda = 0.71073$ Å) on a Bruker CCD APEX II diffractometer, although a STOE-IPDS II, a D8 VENTURE APEX III, as well as a four-circle diffractometer with an X-ray precession technique using the APS ($\lambda = 0.183520$ Å) at ANL were employed for some of the specimens as well.

For the Bruker CCD APEX II and D8 VENTURE APEX III diffractometers, the Bruker-SMART program[3] was used to acquire data between one-half and a full sphere in reciprocal space and the program XPREP was used to determine the space groups.[4] For the STOE-IPDS, the X-Area suite was used for data acquisition and analysis.[5] Due to the large absorption of Au, data were corrected semi-empirically or numerically[6] using the programs SADABS or X-Shape and X-Red, respectively.[5, 7] The STOE-IPDS was useful for indexing and performing test runs of selected specimens for diffraction in the full reciprocal space, but full data sets were collected on the Bruker CCD instead, because of the relative faster data collection speed. For instance, the STOE-IPDS would show the full 5-fold and 3-fold diffraction patterns of a quasicrystal and its respective cubic crystalline approximant in reciprocal space as illustrated in chapter 4, but each measurement took more than ~30 hours for the full data set otherwise collected on the Bruker CCD for ~12 hours each. The D8 VENTURE was useful because of its high-focused beam for diffraction data on small (≤ 50 μm longest cross section) specimens with a large crystallographic R-internal refinement caused by large absorption such as those with Au-rich compositions. The APS four-circle single-crystal diffractometer with the precessed diffraction technique[8] provided data for indexing the quasicrystalline sample to determine the quasilattice constant and its centering (i.e., primitive, face-centered, or body-centered).

All crystallographic structures were solved using direct methods and refined using SHELXTL[4] with some structures also solved using JANA2006[9] for comparison. In X-ray diffraction and according to Friedel's law, the structural phase is lost during data collection and Fourier transformation. Only the magnitude-squared of the structure factor or the diffraction amplitude is experimentally available, so that the intensities of the (h,k,l) and $(\bar{h}, \bar{k},\bar{l})$ reflections (i.e., Friedel pair) are equal. As a result, noncentrosymmetric and centrosymmetric structures are indistinguishable.[10] In chapter 6, where the ScAuAl structure is refined in the noncentrosymmetric space group, an additional absolute structure factor is introduced in the direct methods solution and subsequent structural refinements by considering it a "twinned" crystal.[11] In many cases during crystallographic refinement, increasing the total parameters to model a structure may yield lower R-refinement values. In these cases, a Hamilton test is useful for assessing whether the increased parameters resulted in a statistically relevant improvement to the overall model.[12] Although single-crystal X-ray diffraction is a useful technique for elucidating structural arrangements with reliable information on atomic occupancies, it inherently relies on atomic scattering factors that do not clearly identify the elements involved, especially those with close atomic scattering factors. To confirm the resulting refined composition, elemental analysis is a good accompanying tool.

Elemental analysis. Most elemental analyses were performed on ground powdered products or single-crystals after XRD analyses using Energy Dispersive X-ray Spectroscopy (EDS), under vacuum, on a Scanning Electron Microscope (SEM), to obtain an elemental percent composition. Atomic-level resolution and electron-diffraction imaging using a Transmission Electron Microscope (TEM) were also performed in conjunction with the SEM elemental mapping, specifically for the quasicrystals and their crystalline approximants in

chapter 5. Specimens were prepared from the products with a focused ion beam (FIB) source using standard lift-out techniques, in which thin and flat cross-sections of the crystal/quasicrystal were removed for analysis.[13]

Although elemental analysis provides a good estimate of the chemical distribution and sample homogeneity and TEM diffraction provides a good structural overview of the atomic clustering beyond the surface, the detailed crystallographic arrangements, disorders, and atomic distributions are still best studied using single-crystal X-ray diffraction. However, when used in conjunction, EDS and crystallography together provide a good characterization of both composition and structure.

Computational Methods for Electronic Structural Studies

To study the underlying factors contributing to the stability, compositions, and atomic distributions of the resulting polar intermetallic compounds in this research, electronic structure theory was utilized. Determination of the electronic structures involves solving the Schrödinger equation, with the Hamiltonian operator containing information about both the kinetic and potential energies affecting electrons. In this method, electron-electron potential energy terms are most challenging to solve and thus require approximations.

Tight-binding linear muffin-tin orbital atomic-sphere approximation. The Stuttgart TB-LMTO-ASA code[14] applying the local density approximation (LDA) uses density-functional theory (DFT), which involves three significant terms to the total electronic energy: (1) kinetic energy; (2) coulombic energy from all charged particle interactions, and (3) electron-electron exchange-correlation energy. In LDA with the free-electron gas model, the exchange-correlation potential is self-consistently evaluated by treating electron densities in the free-electron gas expression to obtain an energy term. In TB-LMTO, the valence electrons

are held "tightly" by the atoms modeled as spherical muffin-tin potentials and, like Molecular Orbital Theory but for solids, uses a linear combination of atomic-like orbitals (LCAO) as the basis set.[15] LMTO requires the use of space-filling of spherical atomic potentials or "empty sphere" potentials so that the unit cell volume equals to the total volume sum of the basis set and there are no "real" interstitial regions. Thus, there are spherical overlaps so that isocompositions of different structures with now different Wigner Seitz (WS) radii cannot be easily compared. Within LMTO, the band structures, densities of states (DOS), and crystal orbital Hamilton population (COHP)[17] curves can be constructed, which respectively provide the electron dispersion in reciprocal space in relation to energy, patterns and numbers of electronic states, and pair-wise atomic orbital interactions for analysis of the electronic structural effects on compositions and crystal structural stability.

Vienna ab-initio simulation package. VASP[18] uses pseudopotentials that treat the core and valence electrons and it utilizes plane waves with energy cutoffs at 500 eV for this research. The exchange-correlation potential is approximated nonlocally by treating the electron densities as well as their gradients as the basis set in the generalized-gradient approximant (GGA) as constructed by Perdew, Burke, and Ernzerhof (PBE).[19] VASP is useful for structural relaxation and total energy calculations of competing isocompositional models because it does not rely on filling space with WS spheres that might lead to spherical overlaps as in LMTO. However, VASP calculations take a relatively longer time than LMTO, and COHP curves are constructed through an external program. Both LMTO and VASP, however, are first-principles self-consistent calculations that generally lead to more accurate data, but also require more time than semi-empirical methods.

Semi-empirical extended Hückel. Semi-empirical EH calculations explicitly ignore electron-electron interactions in the calculation and thus yield more qualitative results, but are also generally faster than the self-consistent first-principles methods found in LMTO and VASP. Mulliken population analysis using EH consisted of single (for *s* and *p* orbitals) and double (*d* orbitals) zeta slater-type orbital basis sets and was useful for calculating the site energy of a structural arrangement such as those seen in the "Au_6Al_6" icosahedral molecular building blocks of chapter 3.

References

1. Kuestner, H. R., H., Struktur des siliziums. *Physikalische Zeitschrift* **1923,** *24*, 25-29.

2. (a) Rietveld, H., A profile refinement method for nuclear and magnetic structures. *Journal of Applied Crystallography* **1969,** *2* (2), 65-71; (b) Le Bail, A.; Duroy, H.; Fourquet, J. L., Ab-initio structure determination of $LiSbWO_6$ by X-ray powder diffraction. *Materials Research Bulletin* **1988,** *23* (3), 447-452.

3. *SMART*. ed. 5; Bruker AXS: Madison, WI, **2003**.

4. Sheldrick, G., *SHELX*. ver. 6.14; Bruker AXS: Madison, WI, **2000-2003**.

5. STOE & Cie GmbH *Stoe . X-SHAPE, X-RED, and X-AREA*, Darmstadt, Germany, 2006.

6. Blessing, R., An empirical correction for absorption anisotropy. *Acta Crystallographica Section A* **1995,** *51* (1), 33-38.

7. Sheldrick, G. M. *SADABS*, University of Gottingen: Gottingen, Germany, 2001.

8. Goldman, A. I.; Kreyssig, A.; Nandi, S.; Kim, M. G.; Caudle, M. L.; Canfield, P. C., High-energy X-ray diffraction studies of i-$Sc_{12}Zn_{88}$. *Philosophical Magazine* **2011,** *91* (19-21), 2427-2433.

9. *JANA2006*, Petricek, V., Dusek, M. & Palatinus, L. 2014.

10. Pecharsky, V. K.; Zavalij, P., *Fundamentals of Powder Diffraction and Structural Characterization of Materials*. **2003.**

11. Parsons, S.; Flack, H. D.; Wagner, T., Use of intensity quotients and differences in absolute structure refinement. *Acta Crystallographica Section B* **2013,** *69* (3), 249-259.

12. Hamilton, W., Significance tests on the crystallographic R factor. *Acta Crystallographica* **1965,** *18* (3), 502-510.

13. (a) Yaguchi, T.; Kamino, T.; Ishitani, T.; Urao, R., Method for Cross-sectional Transmission Electron Microscopy Specimen Preparation of Composite Materials Using a Dedicated Focused Ion Beam System. *Microscopy and Microanalysis* **2002,** *5* (5), 365-370; (b) Giannuzzi, L. A.; Kempshall, B. W.; Schwarz, S. M.; Lomness, J. K.; Prenitzer, B. I.; Stevie, F. A., FIB Lift-Out Specimen Preparation Techniques. In *Introduction to Focused Ion Beams: Instrumentation, Theory, Techniques and Practice*, Giannuzzi, L. A.; Stevie, F. A., Eds. Springer US: Boston, MA, **2005**; pp 201-228.

14. Jepson, O.; Burkhrdt, A.; Andersen, O. K., *The Program TB-LMTO-ASA,4.7;* **1999,** *Max-Planck-Institut für Festkörperforschung, Stuttgart, Germany*.

15. Lambrecht, W. R. L.; Andersen, O. K., Minimal basis sets in the linear muffin-tin orbital method: Application to the diamond-structure crystals C, Si, and Ge. *Physical Review B* **1986,** *34* (4), 2439-2449.

16. Dronskowski, R.; Blöchl, P. E., Crystal orbital Hamilton populations (COHP): Energy-resolved visualization of chemical bonding in solids based on density-functional calculations. *The Journal of Physical Chemistry* **1993,** *97* (33), 8617-8624.

17. (a) Blöchl, P. E., *Phys. Rev. B* **1994,** *50*, 17953; (b) Kresse, G.; Furthmüller, F., *Comput. Mater. Sci.* **1996,** *6*, 15.

18. Perdew, J. P.; Burke, K.; Ernzerhof, M., Generalized gradient approximation made Simple. *Phys. Rev. Lett.* **1996,** *77*, 3865.

CHAPTER 3

STRUCTURE-COMPOSITION SUBTLETIES IN NaZn$_{13}$-TYPE DERIVATIVES OF Sr/Ca(Au$_x$Al$_{1-x}$)$_{12-13}$

To be submitted for publication in spring 2018

Joyce Pham, Andriy Palasyuk, and Gordon J. Miller
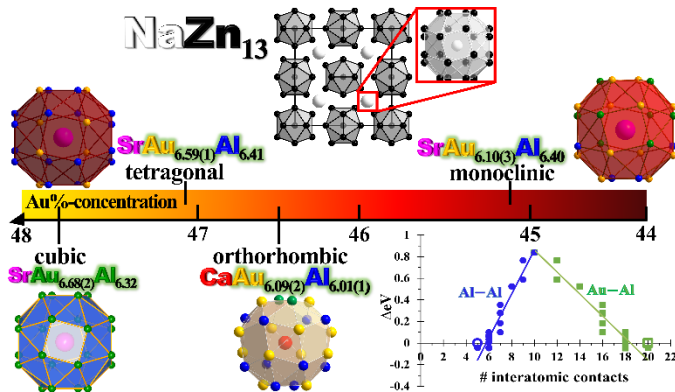
Abstract

In the ~5–8 at% Sr/Ca phase space with nearly equimolar mixture of Au and Al, five new NaZn$_{13}$-derivatives Sr/Ca(Au$_x$Al$_{1-x}$)$_{12-13}$ were discovered and their atomic site preferences and electronic structures were elucidated: (1) cubic SrAu$_x$Al$_{13-x}$ (7.24(2) ≥ x ≥ 6.68(2)) shows no obvious atomic site preference due to mixed Au:Al occupancies of nearly 1:1; (2) at lower Au-content (higher valence electron concentrations), a tetragonal SrAu$_x$Al$_{13-x}$ phase (6.59(1) ≥ x ≥ 6.35(3)) shows all icosahedra centered by Al and preferential atomic arrangements to maximize the number of Au–Al (or Al-rich) shortest distances; (3) a monoclinic SrAu$_{6.10(3)}$Al$_{6.40}$ compound was uncovered that shows even more pronounced geometric distortion from the NaZn$_{13}$-type structure as well as preferential arrangements for Au–Al nearest contacts; (4) tetragonal SrAu$_{5.75(2)}$Al$_{6.25}$ with all empty icosahedra; and (5) to observe effects of chemical pressure, CaAu$_{6.09(2)}$Al$_{6.01(1)}$ crystallizes in an orthorhombic class with

icosahedra that are half empty and half partially occupied by Al. Electronic DOS and COHP curves were used to rationalize the structural depiction of Sr/Ca(Au$_x$Al$_{1-x}$)$_{12-13}$ as icosahedra packing of (Au$_x$Al$_{1-x}$)$_{12-13}$ with voids filled by the electropositive Sr/Ca.

Introduction

Metals and metalloids comprise almost three-quarters of the periodic table and intermetallics, which consist of two or more metallic elements combined in specific molar ratios, provide a fertile ground to study, predict, and modulate the relationships among chemical compositions, atomic and electronic structures, and physical properties. Many intermetallic compounds are formed via exothermic reactions with heats of formation (~50 kJ/mol) lower than salt-type solids, and often exhibit finite compositional ranges, i.e., "homogeneity range" for single-phase formation.

For main group intermetallic compounds, there are three common classifications: Hume-Rothery (H-R), polar intermetallics, and Zintl-Klemm (Z-K), which are typically categorized by their valence electron concentrations, which are evaluated as the total number of valence electrons per atom (*e/a* value). In the region $1.0 \leq e/a < 2.0$, Hume-Rothery phases[1] contain elements with similar electronegativities and sizes from among the late- and post-transition metals, crystallize in densely packed structures with large coordination spheres, and count the total number of valence electrons divided by all the atoms. In the region $e/a \geq 4.0$, Zintl-Klemm phases[2] are comprised of electropositive metals (i.e., alkali, alkaline-earth or rare-earth metals) and electronegative metals around the "Zintl border" between groups 13 and 14 of the periodic table, crystallize in structures built of networks of the electronegative metals that are often electron-specific following the octet or Wade's rules[3], and count the total number of valence electrons divided by the sum of only the electronegative metals. The interactions

between the active metals and electronegative components exhibit more ionic character than observed in H-R phases.[4] The intermediate region $2.0 \leq e/a < 4.0$ is assigned to polar intermetallic compounds,[5] which, like Z-K phases, contain combinations of electropositive and electronegative metals. The active metals formally donate valence electrons to the electronegative metals, which also engage in electronic back-donation to the active metals for their structural cohesion. This electronic back-donation by the electronegative metals results in electron deficiency for two-center two-electron bonding within the network of the electronegative species, which therefore form polyhedra or condensed clusters. As a result, polar intermetallic compounds form a "hybrid" class between the H-R and Z-K phases because the atomic constituents possess large coordination spheres, as seen in H-R phases, but the atomic sizes can differ substantially. On the other hand, the electronegativity differences between electropositive and electronegative elements of polar intermetallics resemble those of Z-K phases, but the electron counting rules used to rationalize Z-K phases cannot rationalize the structures of polar intermetallic compounds because there are no clear two-center, two-electron bonds nor discrete clusters.[6] To date, there are no "simple", overarching valence electron counting rules to rationalize the observed composition-structure-properties relationships among polar intermetallic compounds.

To contribute to the search for tools that address this shortcoming, we have been studying the NaZn$_{13}$-type structure, which consists of components of both the H-R and Z-K phases in that it possesses networks of stuffed icosahedra, which is a feature of the H-R class, but also large differences in electronegativity between the components, a feature of the Z-K class. NaZn$_{13}$-type compounds are widely represented among intermetallics formed by an alkali, alkaline-earth, or rare-earth element with late transition metals and trielide elements (Al,

Ga, In).[7] Recent investigations even examined various atomic features leading to $NaZn_{13}$-type

compounds[8] for stable structural arrangement as well as potential magnetocaloric effects of

$NaZn_{13}$ derivatives.[9] From the investigation of $NaZn_{13}$-type $BaCu_xAl_{13-x}$[7] and magnetocaloric

$LaFe_{13-x}Si_x$,[11] the atomic arrangement ("coloring"[10]) maximizes the number of heteroatomic

Cu−Al or Fe−Si interactions within the polyanionic icosahedral network, both within the

icosahedra and between adjacent icosahedra. Progressions of the Ba–Cu–Al investigation

involving substitution for Ba or Cu revealed indications of tetragonal distortions of the $NaZn_{13}$-

structure in Sr–Au–Al and Ba–Pd–Al systems. These preliminary investigations showed just

two compositions, $SrAu_{5.96}Al_{6.34}$ and $BaPd_{3.49}Al_{9.51}$, with the tetragonal distortion and

warranted further examination beyond just their structural descriptions.[12] Therefore, herein,

we examine $NaZn_{13}$-type phases existing in the Sr–Au–Al system, their possible structural

distortions, any homogeneity range, and atomic site preferences. To examine metallic size

effects as part of a broader investigation of chemical pressure on $NaZn_{13}$-type phases, we also

report on the outcomes of substituting Ca for Sr.

Experimental Section

  Synthesis. The starting elements were dendritic Sr (99.9%, Alfa-Aesar), Ca chunks

(99.99%, Sigma Aldrich), Au spheres (99.99%, Ames Laboratory), and Al ingots (99.999%,

Alfa-Aesar) and were all handled in a nitrogen- or argon-filled glove-box, in which the

moisture levels were maintained at no greater than 0.1 ppm by volume. Samples containing Ca

were weighed to 300.0 mg total and samples containing Sr were weighed to 800.0 mg total

corresponding to their target compositions into tantalum ampoules, which were arc-welded

shut under argon and subsequently enclosed in a secondary silica jacket under vacuum to

prevent oxidation of the tantalum reaction vessels at reaction temperatures. Sr–Au–Al samples

were heated to 1000 °C for 1 day and cooled (5 °C/h) to 750 °C for an annealing period of 3 days from which they were left to cool to room temperature in the furnace after it is shut off. Ca–Au–Al samples were also heated to 1000 °C for 1 day and cooled (10 °C/h) to 700 °C for an annealing period of 5 days from which they were quenched into room temperature water. Ca–Au–Al samples were quenched because thermal analysis reveals a small liquidus event at ~630°C that is present on cooling but not on heating and, therefore, may indicate the presence of another phase.

Thermal analysis. A Netzsch 404C differential scanning calorimeter was used for thermal analysis of the Ca–Au–Al samples, which (~30.0 mg) were sealed into tantalum tubes, then placed into secondary alumina crucibles, purged with helium, and heated to 850 °C and back to room temperature (~25 °C).

Phase analysis. Phase analysis by powder X-ray diffraction (PXRD) was carried out on polycrystalline samples of ground products spread over and sandwiched between two transparent films (mylar for samples with Sr and acetate for samples with Ca) held together with a thin layer of vacuum grease and inserted into an airtight sample holder. All data were collected at 30 °C on a diffractometer with Cu $K_{\alpha 1}$ radiation ($\lambda = 1.54060$ Å).

Data for Sr–Au–Al samples were recorded on a Huber 670 Guinier camera equipped with an image plate detector. The diffractometer was calibrated with the NBS Si 640b standard, and the detection limit for the second phase in the sample was conservatively estimated to be ~5% by volume in equivalent scattering power. Data were recorded in the 4–100° 2θ range, step size 0.005°, and an exposure time of 30 min.

Data for Ca–Au–Al samples were collected on a Stoe Stadi P line-scan transmission diffractometer with a position-sensitive image-plate detector, in the 10–125° 2θ range, step size

0.03° 2θ, and an exposure time of 1 hour. For a smaller step size, data were also collected on the Panalytical X'pert Pro step-scan reflection diffractometer equipped with a scintillation counter detector. Ground polycrystalline products were scattered over a silicon wafer and mounted onto a zero-background holder. Data were recorded in the $5-110^{\circ}$ 2θ range with a step size of 0.017° in 2θ for an exposure time of 2 hours. Phase identification was performed using the program *PowderCell* by juxtaposing the simulated patterns from refined single-crystal XRD data and reported XRD data against the observed PXRD patterns.[13]

Unit cell parameters of the samples containing Sr were obtained by least-squares refinement on 15–20 of the most intense peaks in the 2θ region $10-100^{\circ}$ using the program WinXPow and were employed in all distance calculations from single-crystal positional refinements.[14] A Rietveld refinement with a Lebail decomposition was used to attain the lattice parameters and atomic coordinates from PXRD data of samples containing Ca using the program JANA2006.[15]

Single crystal X-ray diffraction. Single-crystal diffraction data were collected at ambient conditions (~25 °C) on either a Bruker SMART APEX II or APEX I (for the samples with Sr) CCD diffractometer with a Mo $K_{\alpha 1}$ radiation ($\lambda = 0.71073$ Å).[16] Specimens were selected and mounted onto the tips of glass fibers and their data were collected using the SMART software over one-half or full spheres in reciprocal space at scan increments of 0.3–0.5° in ω and exposure times of 10–30 seconds per frame. Reflection intensities were integrated with the program SAINT in the SMART software package and absorption was empirically corrected[17] using the program SADABS.[18] The space groups were determined using the program XPREP and all structures were solved using direct methods and refined by the full-

matrix least-squared on F_o^2 with anisotropic thermal displacement and secondary extinction parameters using the program suite SHELXTL.[19]

Electronic structures and site preferences. The tight binding linear muffin-tin orbital method employing the atomic sphere approximation (TB-LMTO-ASA)[20] as implemented in the Stuttgart code was used for self-consistent electronic structure calculations. Exchange and correlation were treated by the local density approximation (LDA), which was parametrized per von Barth and Hedin.[21] Relativistic effects were considered using a scalar relativistic approximation.[22] The Wigner-Seitz (WS) radii of all atoms were assigned automatically and subjected up to 18% overlap between WS spheres, leading to no greater than 9% volume overlaps with no need for empty spheres. To visualize the electronic density of states (DOS) and nearest (≤ 3.5 Å apart) pairwise crystal orbital Hamilton population (COHP)[23] of the irreducible wedge from the first Brillouin zone, 801 (Sr-models) and 8001 (Ca-models) k-points were used for plotting.

To handle mixed site occupancies, ordered models were created by either lowering the experimentally determined space group or assigning all mixed Au/Al sites as their majority component. The following atomic basis set was used:[24] Ca ($4s$, $3d$), Sr ($5s$, $4d$), Au ($6s$, $6p$, $5d$), and Al ($3s$, $3p$), with Ca ($4p$, $4f$), Sr ($5p$, $4f$), Au ($4f$), and Al ($3d$) downfolded.

For the Ca–Au–Al structures, the DOS was also calculated for comparison against the TB-LMTO-ASA method using the projected augmented wave method (PAW) of the Vienna ab-Initio Simulation Package (VASP 4.6.34),[25] in which the generalized gradient approximation (GGA) was employed with the Perdew, Burke, and Ernzerhof (PBE) exchange and correlation potentials,[26] a 500 eV energy cutoff, a 0.01 meV self-consistent convergence

criterion, and the following atomic orbital basis set: Ca $(3s^23p^64s^2)$, Au $(5d^{10}6s^1)$, and Al $(3s^23p^1)$.

To understand factors leading to the Au and Al atomic site preferences[10] in the "CaAu$_6$Al$_6$" model, 18 molecular models of the empty ordered icosahedron [Au$_6$Al$_6$] were constructed using the averaged interatomic distances of the experimentally determined structure, so that the icosahedral edges parallel to the unit cell edges (6×) are slightly longer than the edges orthogonal to the body diagonal (24×). For each model, the total energies and interatomic overlap populations were assessed using semi-empirical Extended Hückel (EH) calculations. The EH calculations used single (for s and p orbitals) and double (for d orbitals) zeta (ζ) Slater-type orbitals as follows: Al $3s$ ($H_{3s-3s} = -12.30$ eV, $\zeta_{3s} = 1.37$), and $3p$ ($H_{3p-3p} = -6.50$ eV, $\zeta_{3p} = 1.36$); Au $6s$ ($H_{6s-6s} = -10.92$ eV, $\zeta_{6s} = 2.60$), $6p$ ($H_{6p-6p} = -5.55$ eV, $\zeta_{6p} = 2.58$), and $5d$ ($H_{5d-5d} = -15.07$ eV, $\zeta_{5d1} = 6.16$ ($c_1 = 0.6444$), $\zeta_{5d2} = 2.790$ ($c_2 = 0.5357$)).[27]

Results and Discussion

Synthesis and phase analysis. At ~5–8 at% Sr/Ca and at nearly equal Au and Al concentrations, several samples were prepared to identify the corresponding phases and structures of the (Sr, Ca)–Au–Al systems showing the NaZn$_{13}$-type structure and its derivatives, consisting of a cubic packing of atom-centered icosahedra with the larger formal cation in snub cube voids. Table 1 includes samples with (Sr, Ca):(Au+Al) loaded molar ratios of 1:13 and 1:12, as well as 1:15.7 specifically for Sr:(Au+Al), that led to NaZn$_{13}$-type derivatives and other phases nearby in composition with the Au:Al molar ratio varying from ~1.4 (Au-rich) to ~0.5 (Al-rich). These reactions were chosen: (1) to reproduce the incompletely characterized 1:12 phase ~SrAu$_{5.96}$Al$_{6.34}$,[12] which was assigned as a tetragonal

Table 1. Phase analysis of (Sr/Ca)–Au–Al from loadings and refinements using XRD

	loading	phase analysis	composition (single-crystal XRD)	refined lattice parameters from XRD (Å)					
				single-crystal			powder		
				a	b	c	a	b	c
1:13	$SrAu_{7.4}Al_{5.6}$	[C]cub + [U]u.ph						12.523(2)	
	$SrAu_{7.0}Al_{6.0}$	cub						12.498(2)	
	$SrAu_{6.7}Al_{6.3}$	cub	$SrAu_{6.68(2)}Al_{6.32}$		12.482(2)			12.476(2)	
	$SrAu_{6.0}Al_{7.0}$	[M]mono	$SrAu_{6.10(3)}Al_{6.40}$	12.260(2)	12.470(2)	12.320(2)			
1:12	$SrAu_{6.8}Al_{5.2}$	cub + [H]hex	$SrAu_{7.24(2)}Al_{5.76}$		12.528(2)			12.522(2)	
							12.628(2)		7.091(2)
	$SrAu_{6.5}Al_{5.5}$	cub + hex						12.502(3)	
							8.634(2)		7.096(2)
	$SrAu_{6.0}Al_{6.0}$	[T]tetra + hexa					8.883(2)		12.487(6)
							8.657(2)		7.101(2)
	$SrAu_{5.5}Al_{6.5}$	tetra + hexa + [O]orth	$SrAu_{5.75(2)}Al_{6.25}$	8.698(2)		12.397(6)	8.687(2)		12.403(7)
1:15.7	$SrAu_{9.0}Al_{6.7}$	cub + u.ph						12.525(2)	
	$SrAu_{8.3}Al_{7.4}$	cub + u.ph						12.502(2)	
	$SrAu_{7.9}Al_{7.8}$	tetra	$SrAu_{6.59(2)}Al_{6.41}$	8.789(3)		12.505(6)	8.790(2)		12.535(5)
	$SrAu_{7.4}Al_{8.3}$	tetra + u.ph	$SrAu_{6.55(2)}Al_{6.45}$				8.755(2)		12.503(5)
	$SrAu_{5.8}Al_{5.8}$	tetra + u.ph	$SrAu_{6.35(3)}Al_{6.65}$	8.842(3)		12.505(6)			
1:13	$CaAu_{6.7}Al_{6.3}$	ortho + u.ph	$CaAu_{6.14(4)}Al_{6.05(3)}$	12.2321(8)	12.4512(8)	12.2898(7)	12.052(4)	12.273(5)	12.142(5)
	$CaAu_{6}Al_{7}$	ortho + u.ph	$CaAu_{6.16(2)}Al_{6.05(2)}$	12.481(2)	12.299(2)	12.256(2)	12.451(4)	12.286(4)	12.223(4)
1:12	$CaAu_{7}Al_{5}$	[Te]tetrag + u.ph	$CaAu_{6.81}Al_{4.00}$	8.5536(4)		34.005(2)			
	$CaAu_{6}Al_{6}$	[Or]ortho + u.ph	$CaAu_{6.09(2)}Al_{6.01(1)}$	12.4481(4)	12.2776(4)	12.2096(5)	12.4484(4)	12.2792(6)	12.2145(7)
	$CaAu_{4}Al_{8}$	[Ort]orthorm + u.ph	$CaAu_{3.488(3)}Al_{4.512}$	13.1023(3)	4.15930(10)	12.0136(3)	12.408(6)	3.912(2)	11.557(6)

[C]cub–cubic $NaZn_{13}$-type, [U]u.ph–unidentified phases, [M]mono–monoclinic $NaZn_{13}$-type derivative, [H]hex–hexagonal $Ba_3Ag_{14.6}Al_{6.4}$-type $Sr_3Au_xAl_{21-x}$,[28] [T]tetra–tetragonal $NaZn_{13}$-type, [O]orth–orthorhombic $BaZn_5$-type $SrAu_xAl_{5-x}$[29] [Te]tetragonal phase unrelated to $NaZn_{13}$. [Or]ortho–orthorhombic $NaZn_{13}$-type, [Ort]orthorhombic phase unrelated to $NaZn_{13}$.

derivative of the $NaZn_{13}$-type structure; and (2) to extend the investigation of chemical pressure of cubic $NaZn_{13}$-type $BaCu_{5.10(7)}Al_{7.90}$ on going from Ba to Sr to Ca and from Cu to Au.

For the 1Sr: 13(Au+Al) ratio, or ~7.1 at% Sr, there are three distinct $SrAu_xAl_{13-x}$ structures observed on decreasing Au-content: cubic; tetragonal; and monoclinic $NaZn_{13}$-type derivatives. At higher Au content, which refined as $7.24(2) \geq x \geq 6.68(2)$ from single crystals and obtained from loadings $7.4 \geq x \geq 6.5$, PXRD patterns can be indexed and single crystals were refined as cubic $NaZn_{13}$-type. The corresponding lattice parameters ($a = 12.476(2)$–$12.525(2)$ Å) decrease with decreasing Au content, a result consistent with the relative atomic sizes of Au ($R_{Au} = 1.44$ Å) and Al ($R_{Al} = 1.43$ Å). At lower Au content, i.e., $6.59(1) \geq x \geq 6.35(3)$ refined from single crystals, there is evidence of transformation to a tetragonal derivative of the $NaZn_{13}$-type structure. The similarities of PXRD patterns (see Figure 1) between the cubic and tetragonal phases called for single-crystal XRD analysis, which confirmed that $SrAu_{6.59(1)}Al_{6.41}$, $SrAu_{6.55(2)}Al_{6.45}$, and $SrAu_{6.35(3)}Al_{6.40}$ are tetragonal.

A tetragonal $NaZn_{13}$-type derivative also occurs for the 1Sr: 12(Au+Al) ratio (~7.7 at% Sr) as $SrAu_{5.75(2)}Al_{6.25}$, but with the centers of each icosahedron empty, in contrast to the tetragonal 1:13 phase at $6.59(1) \geq x \geq 6.35(3)$, in which all icosahedra are centered by Al atoms. The tetragonal phases, $SrAu_{6.59(1)}Al_{6.41}$, $SrAu_{6.55(2)}Al_{6.45}$, and $SrAu_{6.35(3)}Al_{6.40}$ as refined from single-crystal XRD, were selected from the respective "$SrAu_{7.9}Al_{7.8}$", "$SrAu_{7.4}Al_{8.3}$" and "$SrAu_{5.8}Al_{5.8}$" sample loadings, which do not correspond to the typical 1:12 and 1:13 Sr:(Au+Al) ratios of $NaZn_{13}$ derivatives. At first, isolation of a 1:13 tetragonal phase was interfered by impurities; some byproducts were identified as hexagonal $Sr_3Au_xAl_{21-x}$[28] and orthorhombic $SrAu_xAl_{5-x}$[29] compounds (see Table 1). To address the purity issue, the 1Sr: 15.7(Au+Al) region (~6 at% Sr) was explored under the assumption that no complex ternary
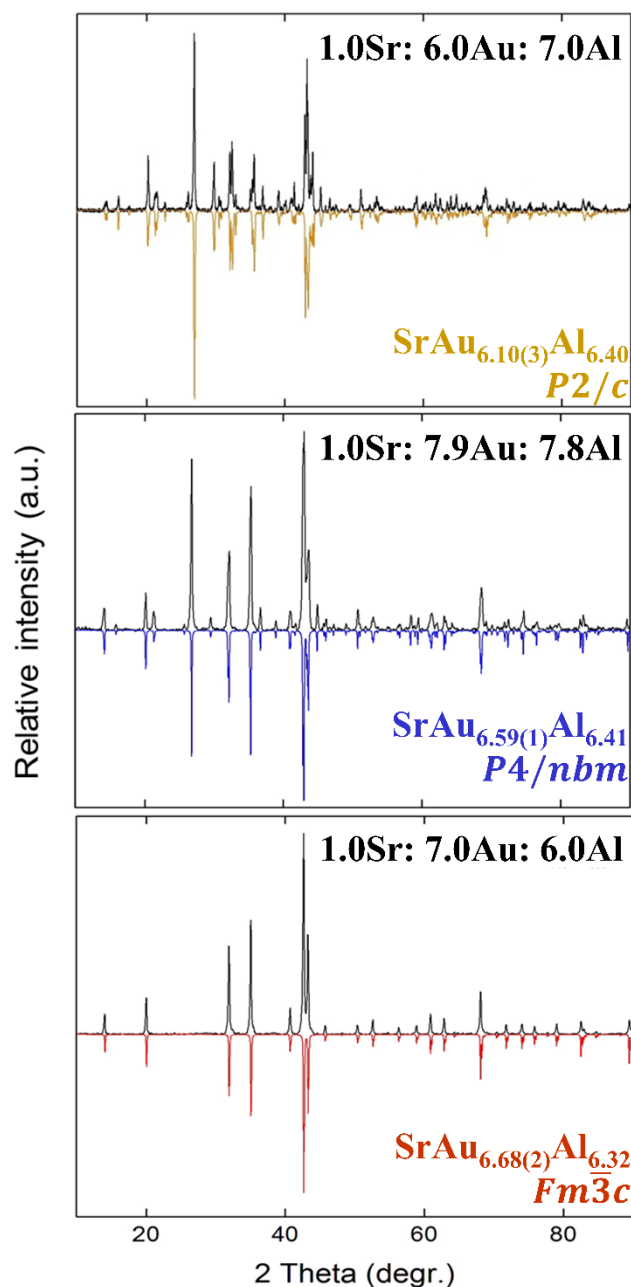
Figure 1. Observed and calculated PXRD patterns of monoclinic $SrAu_{6.10(3)}Al_{6.40}$ (top), tetragonal $SrAu_{6.59(1)}Al_{6.41}$ with all stuffed-icosahedra (middle), and cubic $SrAu_{6.68(2)}Al_{6.32}$ (bottom) $NaZn_{13}$ derivatives.

phases might form with Sr content < 7 at%. Instead, the monoclinic AuAl compound[30] was

assumed to be the only other phase that could exist in equilibrium with the targeted tetragonal

phase. PXRD patterns of the resulting products were juxtaposed against the simulated AuAl

PXRD pattern to show that AuAl was not a side product in the synthesis and that the 1Sr:
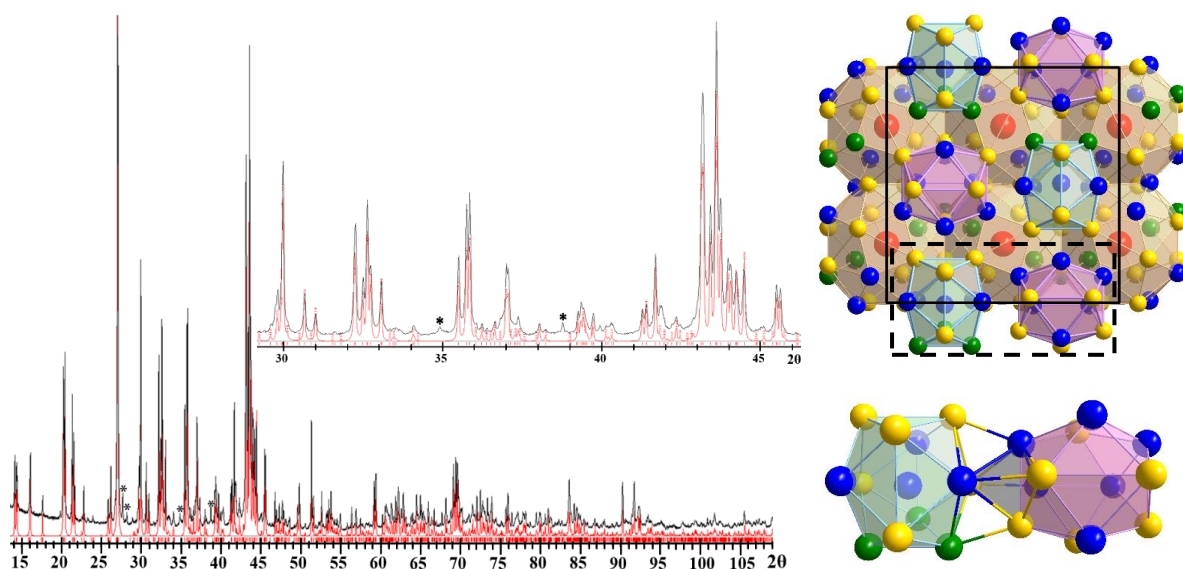
Figure 2. PXRD of observed "CaAu$_6$Al$_6$" (black) and refined CaAu$_{6.09(2)}$ Al$_{6.01(1)}$ simulated from single-crystal XRD with enlarged inset (left). Structure with snub cube, icosahedra, and tetrahedral star building blocks (right). Ca are colored red, Au are gold, Al are colored blue, and mixed Au/Al sites are colored green.

15.7(Au+Al) loading ratios led to the tetragonal phase with no obvious impurities exceeding the X-ray detection limit of ~5 wt.% at the optimal loading ratio 1Sr: 7.9Au: 7.8Al, so that the phase width for the tetragonal NaZn$_{13}$-type SrAu$_x$Al$_{13-x}$ derivative is assigned as $6.59(1) \geq x \geq 6.35(3)$. For the loading of 1Sr: 6Au: 7Al ($x = 6$), the PXRD pattern includes broad diffraction peaks that could be assigned if both the tetragonal and cubic models were overlaid together onto the observed pattern so that, at first, the product seemed to be a mixture of phases. However, several peaks in the 2θ range 29.3–30.9° remained unindexed and suggested an unknown phase. A single specimen selected from this loading for single-crystal X-ray diffraction analysis refined as a monoclinic derivative of the NaZn$_{13}$-type structure with the composition SrAu$_{6.10(3)}$Al$_{6.40}$. The structure has alternating stuffed and empty icosahedra and for which the simulated PXRD pattern matches the observed PXRD pattern (see Figure 1).

Table 2. Selected crystallographic refinements of Sr/Ca(Au$_x$Al$_{1-x}$)$_{12-13}$

	SrAu$_{6.7}$Al$_{6.3}$	SrAu$_{7.3}$Al$_{8.3}$	SrAu$_6$Al$_7$	SrAu$_{5.5}$Al$_{6.5}$	Ca$_{1.00(6)}$Au$_{5.99(1)}$Al$_{5.86(8)}$
loading composition	SrAu$_{6.7}$Al$_{6.3}$	SrAu$_{7.3}$Al$_{8.3}$	SrAu$_6$Al$_7$	SrAu$_{5.5}$Al$_{6.5}$	Ca$_{1.00(6)}$Au$_{5.99(1)}$Al$_{5.86(8)}$
refined composition	SrAu$_{6.68(2)}$Al$_{6.32}$	SrAu$_{6.59(1)}$Al$_{6.41}$	SrAu$_{6.10(3)}$Al$_{6.40}$	SrAu$_{5.75(2)}$Al$_{6.25}$	CaAu$_{6.09(2)}$Al$_{6.01(1)}$
θ range data collection	3.3–23.2°	1.6–23.1°	1.7–23.3°	1.6–23.3°	1.6–27.8°
absorp. coeff. μ (mm^{-1})	106.29/ empirical	105.72/ empirical	100.78/ empirical	95.71/ empirical	96.46/ empirical
meas./ indpnt./ obs. [I > 2σ(I)]/ para.	2230/ 71/ 67/ 11	5733/ 388/ 323/ 49	9987/ 2494/ 1695/ 251	5329/ 385/ 355/ 44	22258/ 2192/ 1513/ 138
R[F^2 > 2σ(F^2)]/ wR(F^2)/ R$_{int}$/ GOF	0.021/ 0.049/ 0.062/1.38	0.039/ 0.078/ 0.094/ 1.21	0.055/ 0.116/ 0.088/ 1.05	0.023/ 0.048/ 0.061/ 1.07	0.038/ 0.077/ 0.111/1.00
space group/ Pearson	$Fm\bar{3}c$ (no. 226)/ cF112	$P4/nbm$ (no. 125)/ tP56	$P2/c$ (no. 13)/ mP108	$P4/nbm$ (no. 125)/ tP52	$Pbcm$ (no. 57)/ oP108
Δρ$_{max}$, Δρ$_{min}$ (e Å^{-3})	1.06, –1.20	1.92, –1.50	–3.16, 3.01	–1.09, 1.05	2.82, –2.77
dimensions (Å)	$a=b=c=$ 12.482(2)	$a=b=$8.789(3) $c=$12.505(6)	$a=$12.260(8) $b=$12.470(9); β=90.26(2) $c=$12.320(9)	$a=b=$8.698(2) $c=$12.397(6)	a = 12.4481(4) b = 12.2776(4) c = 12.2096(5)
volume (Å^3)/ Z	1944.7(6)/ 8	965.9(7)/ 4	1883(2)/ 8	937.9(6)/ 4	1866.03(1)/ 8
index ranges	-13 ≤ h, k, l ≤ 13	−9 ≤ h, k ≤ 9 −13 ≤ l ≤ 13	13 ≤ h, k, l ≤ 13	−9 ≤ h, k ≤ 9 −13 ≤ l ≤ 13	−15 ≤ h, k ≤ 15 −15 ≤ l ≤ 12

Table 3. Sr/Ca(Au$_x$Al$_{1-x}$)$_{12-13}$ crystallographic parameters

	atom	*Wyck.*	sym.	x	y	z	U_{iso}	occ. (<1)
SrAu$_{6.68(2)}$Al$_{6.32}$	Sr	8*a*	432	1/4	1/4	1/4	0.012(1)	
	Au/Al1	96*i*	*m*..	0.32087(5)	0.37292(6)	0.0008(2)	0.0250(4)	0.65(1)/0.44
	Au/Al2	8*b*	$m\bar{3}$.	1/2	1/2	0	0.012(2)	0.117(8)/0.883
SrAu$_{6.59(1)}$Al$_{6.41}$	Sr1	2*a*	422	1/4	1/4	0	0.014(2)	
	Sr2	2*b*	422	1/4	1/4	1/2	0.014(2)	
	Au/Al1	8*m*	..*m*	0.9262(1)	0.0738(1)	0.3776(1)	0.0248(7)	0.91(2)/0.09
	Au/Al2	8*m*	..*m*	0.1180(1)	0.8820(1)	0.0693(1)	0.0275(7)	0.905(18)/0.095
	Au/Al3	16*n*	1	0.1921(2)	0.0571(2)	0.2464(1)	0.0209(7)	0.54(1)/0.46
	Al/Al4	8*m*	..*m*	0.6307(3)	0.1307(3)	0.4264(3)	0.023(2)	0.215(9)/0.785
	Au/Al5	8*m*	..*m*	0.9261(5)	0.0739(5)	0.1289(5)	0.030(3)	0.121(8)/0.879
	Au/Al6	4*h*	2.*mm*	3/4	1/4	0.2481(5)	0.011(3)	0.129(9)/0.871
SrAu$_{6.10(3)}$Al$_{6.40}$	Sr1	2*e*	2	0	0.9951 (5)	1/4	0.007 (2)	
	Sr2	2*f*	2	1/2	0.9953 (5)	1/4	0.009 (2)	
	Sr3	2*f*	2	1/2	0.4959 (5)	1/4	0.008 (2)	
	Sr4	2*e*	2	0	0.4965 (5)	1/4	0.009 (2)	
	Au1	4*g*	1	0.7503 (2)	0.6151 (2)	0.1809 (2)	0.0076 (5)	
	Au2	4*g*	1	0.8818 (2)	0.9298 (2)	0.9824 (2)	0.0106 (5)	
	Au3	4*g*	1	0.6185 (2)	0.9296 (2)	0.9823 (2)	0.0105 (5)	
	Au4	4*g*	1	0.0796 (2)	0.6221 (2)	0.0029 (2)	0.0101 (5)	
	Au5	4*g*	1	0.7502 (2)	0.0579 (2)	0.1286 (2)	0.0109 (5)	
	Au6	4*g*	1	0.7501 (2)	0.3661 (2)	0.3418 (2)	0.0092 (5)	
	Au7	4*g*	1	0.5796 (2)	0.3776 (2)	0.9970 (2)	0.0106 (5)	
	Au8	4*g*	1	0.7410 (2)	0.0873 (2)	0.8635 (2)	0.0132 (5)	
	Au9	4*g*	1	0.6238 (2)	0.2456 (2)	0.1838 (2)	0.0104 (5)	
	Au10	4*g*	1	0.1236 (2)	0.7543 (2)	0.8163 (2)	0.0108 (5)	
	Au11	4*g*	1	0.9313 (2)	0.7534 (2)	0.1201 (2)	0.0086 (5)	
	Au12	4*g*	1	0.5686 (2)	0.7531 (2)	0.1200 (2)	0.0095 (5)	
	Au/Al13	4*g*	1	0.3681 (9)	0.745 (1)	0.1817 (8)	0.006 (4)	0.040(9)/0.960
	Au/Al14	4*g*	1	0.1311 (9)	0.745 (1)	0.1822 (8)	0.008 (4)	0.043(9)/0.957
	Au/Al15	4*g*	1	0.131 (1)	0.426 (1)	0.910 (1)	0.009 (6)	0.018(10)/0.982
	Au/Al16	4*g*	1	0.750 (1)	0.5689 (9)	0.383 (1)	0.014 (5)	0.045(10)/0.955

	Table 3 (continued).							
	Au/Al17	4g	1	0.070 (1)	0.752 (1)	0.617 (1)	0.026 (5)	0.056(1)/0.944
	Al1	4g	1	0.586 (1)	0.134 (1)	0.004 (1)	0.007(3)	
	Al2	4g	1	0.632 (1)	0.577 (1)	0.011 (1)	0.008(4)	
	Al3	4g	1	0.917 (1)	0.133 (1)	0.004 (1)	0.008(4)	
	Al4	4g	1	0.431 (1)	0.250 (1)	0.117 (1)	0.000(3)	
	Al5	4g	1	0.749 (1)	0.124 (1)	0.320 (1)	0.005(3)	
	Al6	4g	1	0.750 (1)	0.247 (1)	−0.005 (1)	0.003(3)	
	Al7	4g	1	0.749 (1)	0.859 (1)	0.153 (1)	0.014(4)	
	Al8	4g	1	0.752 (1)	0.413 (1)	0.126 (1)	0.001(3)	
$CaAu_{6.09(2)}Al_{6.01(1)}$	Ca1	4c	2..	0.0042(3)	1/4	0	0.0230(9)	
	Ca2	4c	2..	0.5068(4)	1/4	0	0.0266(9)	
	Au1	4d	..m	0.38680(6)	0.31861(6)	1/4	0.0188(2)	
	Au2	4d	..m	0.63413(6)	0.15682(6)	1/4	0.0191(2)	
	Au3	8e	1	0.06756(4)	0.52039(5)	0.11328(5)	0.0210(2)	
	Au4	4d	..m	0.08700(7)	0.13722(7)	1/4	0.0221(2)	
	Au5	4d	..m	0.05672(6)	0.87008(7)	1/4	0.0219(2)	
	Au6	8e	1	0.37633(5)	0.00262(4)	0.08001(5)	0.0207(2)	
	Au7	8e	1	0.75428(4)	0.31429(5)	0.12327(5)	0.0200(2)	
	Au8	8e	1	0.24517(4)	0.38076(5)	0.06873(5)	0.0196(2)	
	Au/Al9	4d	..m	0.4305(4)	0.1149(4)	1/4	0.016(2)	0.045(5)/0.955
	Au/Al10	8e	1	0.2556(3)	0.1828(3)	0.1335(3)	0.018(1)	0.043(4)/0.957(4)
	Al1	8e	1	0.2516(3)	0.6117(4)	0.0704(4)	0.0161(9)	
	Al2	4d	..m	0.5893(5)	0.3744(5)	1/4	0.018(1)	
	Al3	4d	..m	0.1446(5)	0.3508(5)	1/4	0.019(1)	
	Al4	8e	1	0.4243(3)	0.4894(3)	0.1295(4)	0.0169(9)	
	Al5	4d	..m	0.1260(5)	0.6765(5)	1/4	0.022(1)	
	Al6	8e	1	0.1378(4)	0.5042(3)	0.5891(4)	0.0204(9)	
	Al7	4d	..m	0.250(2)	0.006(2)	1/4	0.008(8)	0.23(3)

Thus, from crystallographic refinements, the distinct $SrAu_xAl_{13-x}$ phase regions are: cubic $NaZn_{13}$-type for $7.24(2) \geq x \geq 6.68(2)$; and tetragonal $NaZn_{13}$-derivative for $6.59(1) \geq x \geq 6.35(3)$. A monoclinic $NaZn_{13}$-derivative is observed from a single specimen with the refined composition $SrAu_{6.10(3)}Al_{6.40}$, which lies between the 1:12 and 1:13 Sr:(Au+Al) ratios. From the 1:12 loading ratio, existence of the tetragonal compound $SrAu_{5.75(2)}Al_{6.25}$ with empty icosahedra suggested variable occupation of the central Al-atom, as shown for $SrAu_{5.96}Al_{6.34}$.[12]

The variable occupation of the Al site stuffing the icosahedra for structures with the 1Sr: 12(Au+Al) ratio (~7.7 at% Sr) suggested examination of the effects of chemical pressure on moving from Sr ($R_{Sr} = 2.15$ Å) to Ca ($R_{Ca} = 1.97$ Å). For a loading in the ~7.7 at% Ca region
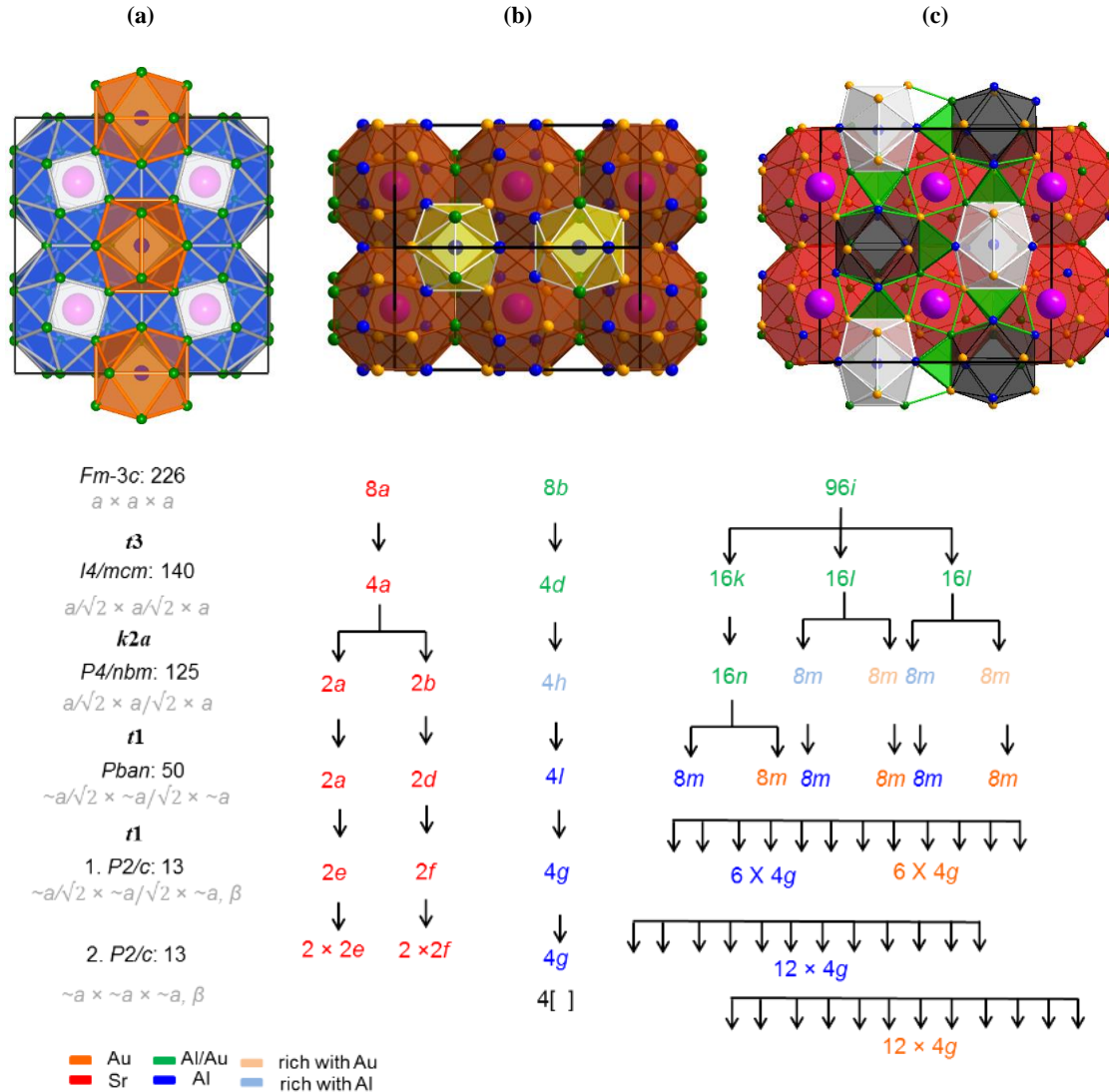
Figure 3. Polyhedra packing in cubic $SrAu_{6.68(2)}Al_{6.32}$ (a), tetragonal $SrAu_{6.59(1)}Al_{6.41}$ (b), and monoclinic $SrAu_{6.10(3)}Al_{6.40}$ (c). Sr are drawn in dark pink, Au/Al sites with 1:1 ratio are in green, Au and Au-rich (Au/Al) sites are in gold, and Al and Al-rich (Au/Al) sites are in blue (top). Group-subgroup relationships between the three structures (bottom).

$(CaAu_xAl_{12-x})$, an orthorhombic defect $NaZn_{13}$-derivative $CaAu_{6.09(2)}Al_{6.01(1)}$ is observed in which the icosahedra are partially occupied by Al atoms. Unlike the Sr–Au–Al system, which shows structural variation from the 1:12 (7.7 at% Sr)–1:13 (7.1 at% Sr) ratios, loadings of 1Ca: 13(Au+Al) (~7.1 at% Ca) still yield the orthorhombic phase. As the Al content increases, the unit cell volume increases, and the Al occupancy of the icosahedra-centering site also increases, but never achieves full occupancy.

Atomic structures. *Cubic SrAu$_x$Al$_{13-x}$ (7.24(2) ≥ x ≥ 6.68(2))*. The cubic NaZn$_{13}$-type structure occurs in the Au-rich region of the SrAu$_{13-x}$Al$_x$ (7.24(2) ≥ x ≥ 6.68(2)) system, and is refined for two single crystals, SrAu$_{6.68(2)}$Al$_{6.32}$ and SrAu$_{7.24(2)}$Al$_{5.76}$, which were selected, respectively, from the loadings "SrAu$_{6.7}$Al$_{6.3}$" and "SrAu$_{6.8}$Al$_{5.2}$". The face-centered (space group $Fm\overline{3}c$) unit cell consists of 112 atoms (cF112), which derive from three crystallographic sites: 8a (O or 432 symmetry), 8b (T_h or $m\overline{3}$ symmetry), and 96i (C_s or m.. symmetry). The 8a site is occupied by Sr, which centers a 24-vertex snub cube that is constructed of Au/Al atomic mixtures of almost equal ratios from the 96i site (0.556(10)/0.444 and 0.59(1)/0.41, respectively for each sample). Three different distances form the 60-edge lengths of the snub cube (2.504(1) Å (×24); 2.8180(8) Å (×24); and 2.856(1) Å (×12) from sample SrAu$_{6.68(2)}$Al$_{6.32}$) so that there are 6 squares formed by the shortest (2.504(1) Å) edges. The distances from the central Sr to the 24 vertex Au/Al atoms (8a–96i) are 3.5879(6–9) Å. The second Wyckoff site, 8b, refines as Al-rich for a Au/Al mixture (0.117(8)/0.883 and 0.11(1)/0.89), and centers the nearly-regular icosahedra formed by the 96i sites. These icosahedra are comprised of two inequivalent lengths: the 24 edges orthogonal to body-diagonals of the cubic unit cell are shorter (2.818(1) Å) than the 6 edges parallel to the cell edges (3.1724(5) Å). The 8a and 8b sites together relate to the CsCl (B2) type arrangement. However, the structure is more complex than CsCl because neighboring icosahedra surrounding the 8b sites are oriented perpendicular to one another and are linked by tetracapped tetrahedra or tetrahedral stars. The 8 distances of the tetrahedral stars connecting two perpendicular icosahedra are 2.504(1) Å (×4) and 2.8562(10) Å (×4), indicating that the inter-icosahedra distances are shorter than the intra-icosahedra distances. Thus, according to this
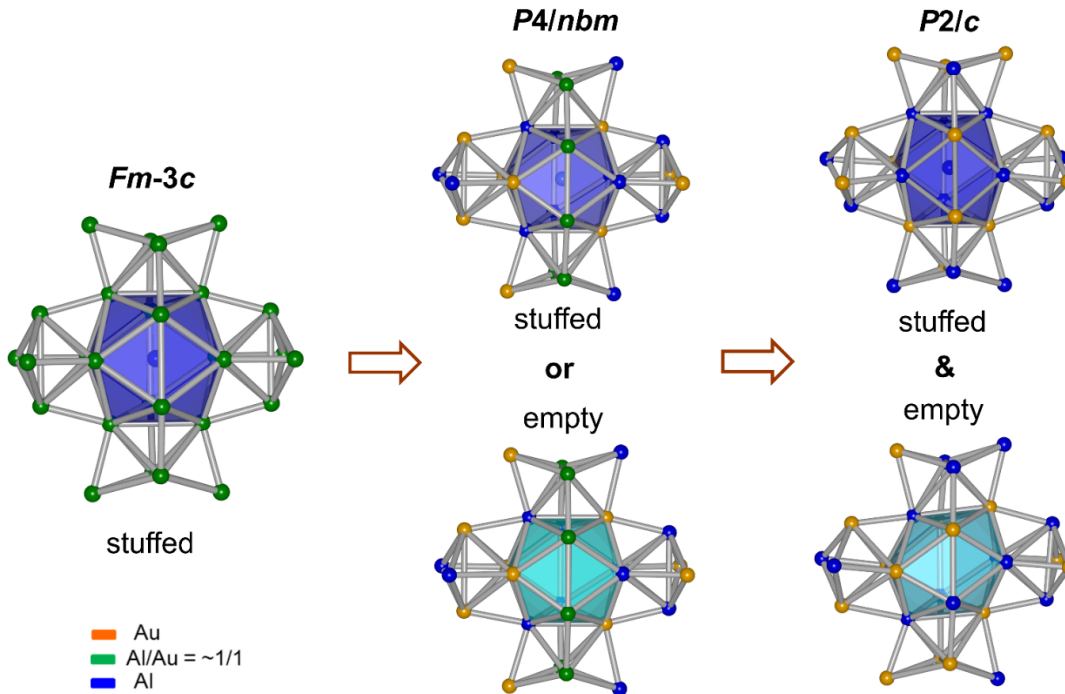
Figure 4. Icosahedra and tetrahedral star building blocks progression from cubic (left) to tetragonal (middle) to monoclinic (right) derivatives of the NaZn$_{13}$-type structures in Sr(Au$_x$Al$_{1-x}$)$_{12-13}$.

polyhedral description, the structure can be broken down into three basic building blocks: a 24-vertex snub cube, a 12-vertex irregular icosahedron, and an 8-vertex tetrahedral star connecting perpendicularly oriented icosahedra. (See Tables 2–3 for selected crystallographic refinements and structural parameters.)

Tetragonal SrAu$_{13-x}$Al$_x$ (6.59(1) ≥ x ≥ 6.35(3)) and SrAu$_{5.75(2)}$Al$_{6.25}$. Four single crystals were refined in the space group *P4/nbm* and their structures represent a tetragonal derivative of the cubic NaZn$_{13}$-type but with lattice relationships $\boldsymbol{a}_{tet} \approx (\boldsymbol{a}_{cub} - \boldsymbol{b}_{cub})/2$, $\boldsymbol{b}_{tet} \approx (\boldsymbol{a}_{cub} + \boldsymbol{b}_{cub})/2$, and $\boldsymbol{c}_{tet} \approx \boldsymbol{c}_{cub}$. The three polyhedral building blocks (i.e., snub cubes, icosahedra, and tetrahedral stars) from the cubic SrAu$_x$Al$_{13-x}$ are still present but more irregular in shape and their atomic decorations are different, both inherent traits of the lower symmetry with greater degrees of freedom on going from cubic to tetragonal. There are 8 inequivalent positions in the tetragonal unit cell: Sr atoms occupy 2*a* and 2*b* sites; Au+Al atoms occupy the 8*m* (4×), 16*n*,

and 4*h* sites, which arise from splitting the Au/Al mixed 96*i* sites of the cubic structure into one mixed almost-equivalent Au/Al 16*n* and four partially occupied 8*m* sites, two of which are predominantly (> 90%) Au and 2 are preferentially occupied by Al (> 87%). (See Figure 3 for the derivation of these different scenarios via group-subgroup relations.) In the fourth crystal, refined as $SrAu_{5.75(2)}Al_{6.25}$, the site splitting and occupancies are similar to tetragonal $SrAu_xAl_{13-x}$ phases, but the icosahedra are empty. Specifically for $SrAu_{6.59(1)}Al_{6.41}$, which is representative of other crystalline refinements, the 2 Sr sites are coordinated by distorted 24-vertex snub cubes with Sr–(Au/Al) distances ranging from 3.583(2) to 3.632(2) Å (for 2*a*) and 3.544(3)–3.619(5) Å (for 2*b*). The icosahedral edge lengths range from 2.714(3)–3.282(2) Å, and the icosahedron is overall more geometrically distorted than in the cubic structure: the 24 edges orthogonal to the unit cell body diagonals average 2.59(1) Å, and the 6 edges parallel to the unit cell edges average 3.11(1) Å. These averages are still longer than the 8 distances (2.551(4) and 2.791(5) Å, each 4×) forming the tetrahedral stars linking perpendicularly oriented icosahedra. Of these 8 tetrahedral star edges, the shorter distances (2.551(4) Å) correspond to Au-rich–Al-rich pairs of 8*m* sites, whereas the longer distances (2.791(5) Å) are Al-rich–Al-rich contacts. The preferential shorter Au–Al distances are not apparent in the cubic structures because the 96*i* sites comprising the icosahedra are occupied by a nearly equimolar mixture of Au and Al atoms. Thus, in contrast to the cubic structure, the tetragonal structure has more overall geometric polyhedral irregularity as well as more variable atomic decorations inherent in the lower crystallographic symmetry. However, overall inter-icosahedral distances remain shorter than intra-icosahedral distances and, on moving from the cubic to the tetragonal structure, there is preferential ordering of Au and Al atoms so that with partial site occupancies, the shorter distances feature contacts between Au-predominant and
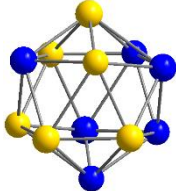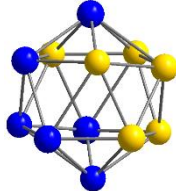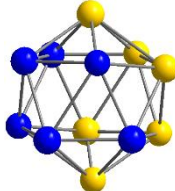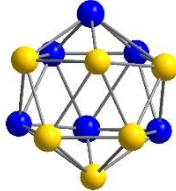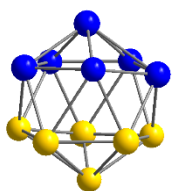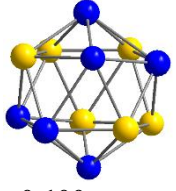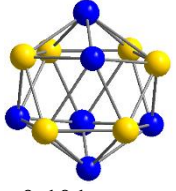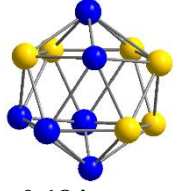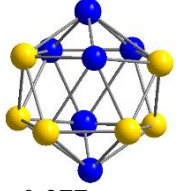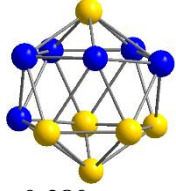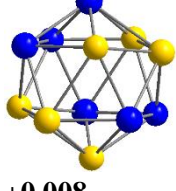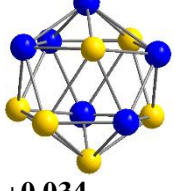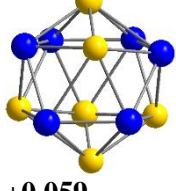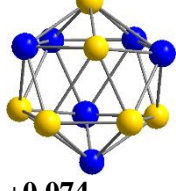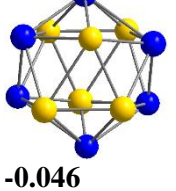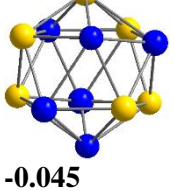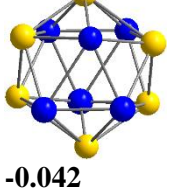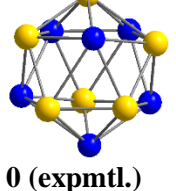
Al-predominant sites and longer interatomic distances are generally between two Al-predominant sites.

Monoclinic SrAu$_{6.10(3)}$Al$_{6.40}$. Also a defect NaZn$_{13}$-type derivative with one-half of the icosahedral building blocks empty, SrAu$_{6.10(3)}$Al$_{6.40}$ (space group $P2/c$; Pearson: $mP108$) was refined from a single specimen obtained by the loading 1Sr: 6Au: 7Al. It contains 29 independent sites so that 8 Sr occupy the two 2e and two 2f sites, and the 8b site of the cubic structure, which centers the icosahedra, is split into two independent 4g sites, one of which is empty, and the other is occupied by Al. The 96i site forming the icosahedra of the cubic NaZn$_{13}$-type structure is split into 24 separate 4g sites, of which 12 are occupied by Au only, 7 by Al only, and 5 by Au/Al mixtures but all preferentially (> 95%) Al. The edge lengths of the empty icosahedra range from 2.59(1)–3.23(5) Å and those of the stuffed icosahedra range from 2.61(1)–3.29(5) Å. Although the stuffed icosahedra follow the cubic and tetragonal structural trends with the 6 edges paralleling the unit cell longer (average 3.07(1) Å) than the 24 edges orthogonal to the body diagonals (average 2.73(1) Å), the empty icosahedra show variations, in which intermediate distances (2.91(2) Å) are on both types of icosahedral edges. Even so, of all the icosahedral edge lengths, the three longest intra-icosahedral distances (3.03(1)–3.33(5) Å) remain parallel to the unit cell edges. Also, unlike the cubic and tetragonal structures, the 8 inter-icosahedral distances (2.49(1)–2.84(1) Å) that form the tetrahedral star are no longer the shortest distances; some intra-icosahedral edges are shorter. When considering the 30 intra-icosahedral contacts from each of the two inequivalent icosahedra plus the 8 distances linking them and forming the tetrahedral star, Au and Al occupancies play a significant role in the geometric distortions: (i) each stuffed icosahedron contains 20 edges ≤ 2.86 Å, which is the shortest distance expected between two Al atoms based on metallic radii;

(ii) 16 of these edges are between Au and Al or Al-rich mixed Au/Al $4g$ sites; and (iii) 4 contacts connect two Al-rich $4g$ or Al sites, so that Au–Au contacts are further away. In the empty icosahedra, there are 22 edges ≤ 2.86 Å, 16 of these are between Au and Al or Al-rich mixed Au/Al $4g$ sites, 4 are between two Al or Al-rich sites, and 2 are between two Au sites. The 8 edges linking the two icosahedra and forming the tetrahedral stars are all ≤ 2.86 Å, 6 of which are between Au and Al or Al-rich sites, 1 is between an Al and Al-rich mixed Au/Al site, and 1 is between two Au atoms. Thus, out of the 50 shortest distances of the two perpendicularly oriented icosahedra and its linking tetrahedral star, the majority (38) are heteroatomic Au–Al contacts.

On moving from cubic to tetragonal to monoclinic derivatives of the $NaZn_{13}$-type structure, a trend which is accompanied by increasing structural degrees of freedom, the atomic decoration reveals a preference to maximize the number of closest Au–Al contacts. This site preference is not apparent in the cubic structure in which the $96i$ site is a Au/Al mixture in an almost 1:1 ratio. Site preferences become more apparent in the tetragonal structure that features 8 tetrahedral star distances linking perpendicularly oriented icosahedra with shorter Au–Al than Al–Al distances. (See Figure 4 for icosahedral and tetrahedral star building blocks and their distortions.) The geometric distortion is most pronounced in the monoclinic case, so that to retain the $NaZn_{13}$-type structure with the shortest distances between Au and Al or Al-rich sites, the polyhedral building blocks of the unit cell distort significantly. The cubic to tetragonal to monoclinic structural trend, then, are a ramification of Au and Al atomic site preferences. In addition, within each derivative, the increase in unit cell volume directly reflects the increasing Au-content, a result consistent with the relative atomic sizes of Au ($R_{Au} = 1.44$ Å) and Al ($R_{Al} = 1.43$ Å) (Table 1).

Table 4. Au₆Al₆ icosahedral coloring models and relative energies from extended Hückel calculations.

+0.354	+0.525	+0.589	+0.767	+0.839
+0.100	+0.101	+0.184	+0.277	+0.280
	+0.008	+0.034	+0.059	+0.074
	−0.046	−0.045	−0.042	0 (expmtl.)

Orthorhombic Ca(Au$_{1-x}$Al$_x$)$_{12.10–12.21(4)}$. To address potential chemical pressure effects, NaZn$_{13}$-derivatives with Ca (R_{Ca} = 1.97 Å) were examined. Six crystals were analyzed showing an orthorhombic NaZn$_{13}$-derivative of which the results for CaAu$_{6.09(2)}$Al$_{6.01(1)}$ are included in Tables 2–3 (See Table S1–3 for data of the 5 other specimens). CaAu$_{6.09(2)}$Al$_{6.01(1)}$ contains 108 atoms in the unit cell from 19 independent sites (space group *Pbcm* (no. 57); Pearson symbol *oP*108), and its distortions from cubic NaZn$_{13}$-type are reminiscent of those seen in monoclinic SrAu$_{6.10(3)}$Al$_{6.40}$. The 8*a* "cation" site from the cubic structure is split into two 4*c* sites occupied by Ca; the 8*b* sites stuffing the icosahedra are split into two 4*d* sites, one of which is vacant and the other is partially occupied (0.20–0.23(3)) by Al; and the 96*i* sites are split into sites

occupied solely by Au (4× 8e; 4× 4d), Al (3× 8e; 3× 4d), or Al-rich (> 92%) mixed Au/Al (1× 4d; 1× 8e). The partial occupancy of the 4d icosahedra-centering site is reminiscent of tetragonal $SrAu_{5.75(2)}Al_{6.25}$ with empty icosahedra and the structural solution of $SrAu_{5.96}Al_{6.34}$[12] that gave rise to this investigation. Thus, the chemical versatility of the $NaZn_{13}$-type structure lies in the subtle ratio range of 1:12–1:13 for $Sr/Ca(Au_xAl_{1-x})_{12-13}$ with the site centering the icosahedra being most variable. The question remains as to what gives rise to the flexibility associated with occupation of this central site.

Similar to monoclinic $SrAu_{6.10(3)}Al_{6.40}$, the geometric distortions leading to orthorhombic $CaAu_{6.09(2)}Al_{6.01(1)}$ reflect the site preferences of Au and Al. The stuffed icosahedron of $CaAu_{6.09(2)}Al_{6.01(1)}$ has 42 atomic connections total, which come from 30 icosahedral edges and 12 contacts between the centering Al-rich atom and each vertex; 32 of these contacts are less than or equal to 2.86 Å and 24/32 are between Au and Al or Al-rich sites. The empty icosahedron has 24 edges less than or equal to 2.86 Å, of which 18 are between Au and Al or Al-rich sites, 4 are between two Al atoms or Al-preferred sites, and the last two longer distances are between two Au atoms. The 8 distances forming the tetrahedral star edges are all less than or equal to 2.86 Å, 6 of which are between Au and Al or Al-rich sites, 1 is between an Al and Al-rich site, and 1 is between two Au atoms. Thus, out of the 64 total shortest distances (≤ 2.86 Å) in the unit cell building block comprised of two perpendicularly oriented icosahedra and their linking tetrahedral star, the majority (48) are heteroatomic Au–Al or Au–Al(rich) contacts. $CaAu_{6.09(2)}Al_{6.01(1)}$ (233.3 Å³/Ca) has the smallest volume of all the structures described herein based on crystallographic refinements of atomic composition and unit cell volume (Tables 1–2). Comparing tetragonal $SrAu_{5.75(2)}Al_{6.25}$ with empty icosahedra and $CaAu_{6.09(2)}Al_{6.01(1)}$ with half of the icosahedra partially occupied, both have Au and Al
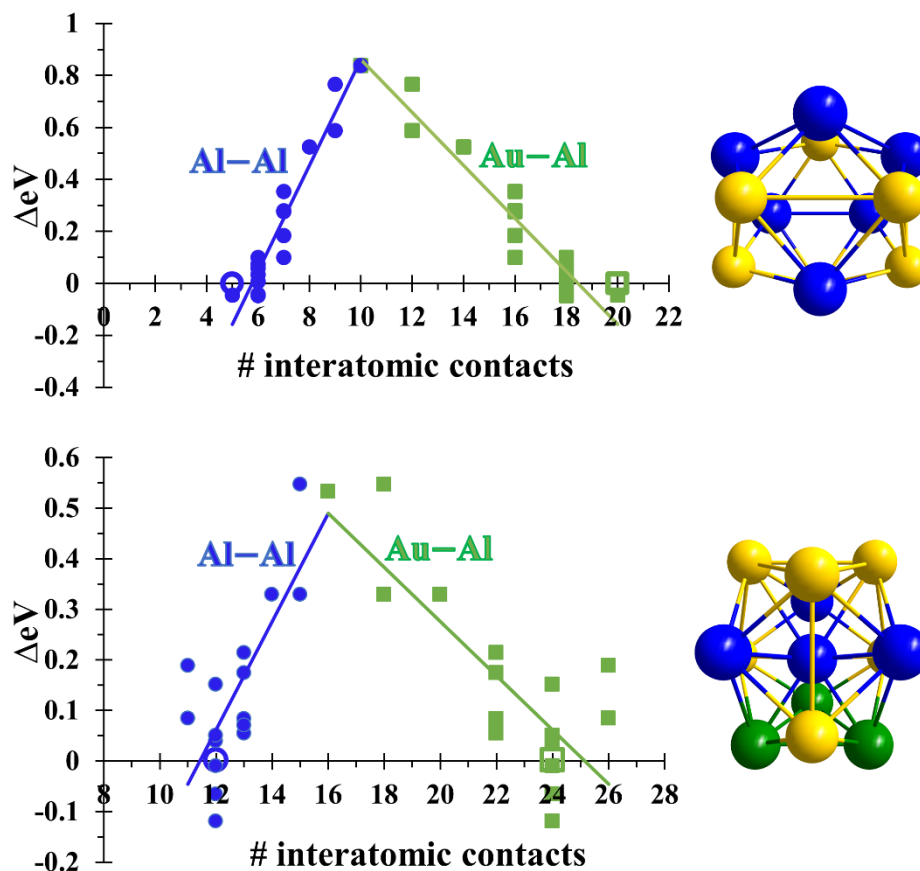
Figure 5. Relative total energies as a function of interatomic contacts for the empty (top) and stuffed (bottom) icosahedra as derived from Au_6Al_6 units of $CaAu_{6.09(2)}Al_{6.01(1)}$.

compositions adding to 12 and ~8.3 at% Sr/Ca. Thus, the more direct effect of chemical pressure while retaining the $NaZn_{13}$-structural family is evident in that on going from Sr to Ca, the volume decreased from 234.5 $Å^3$/Sr to 233.3 $Å^3$/Ca and from tetragonal to orthorhombic, a result reflecting the relative metallic radius decrease from Sr to Ca.

To further examine the Au and Al site preferences noted above, the icosahedral $[Au_6Al_6]$ molecular fragments observed specifically in $CaAu_{6.09(2)}Al_{6.01}$ were studied using EH total energy calculations. For all $NaZn_{13}$-derivatives described herein, the icosahedral edges parallel to the unit cell edges are generally longer than the edges orthogonal to the unit cell body diagonals. In particular, for $CaAu_{6.09(2)}Al_{6.01(1)}$, the average distances for the two types of

edges of the empty [Au$_6$Al$_6$] icosahedron are 2.7156 Å (24×) and 3.001 Å (6×), and the averaged related contacts of the stuffed "Al@[Au$_6$Al$_6$]" icosahedron distances are 2.709 Å (24×) and 3.020 Å (6×). Therefore, irregular [Au$_6$Al$_6$] icosahedra were generated to have the shape and sizes of the two types of observed icosahedra, reflecting the experimental atomic arrangement or coloring. In a regular icosahedron with two different atoms in a 1:1 ratio, i.e., each occupying 6 vertices, there are 18 different arrangements[31] and the energies of these are listed in Table 4 and plotted in Figure 5 as a function of the number of Au–Al and Al–Al intra-icosahedral interactions, so that for the empty icosahedron, there are 30 total interatomic contacts to consider and for the stuffed icosahedron, there are 42 total contacts. Without considering the 8 contacts from the tetrahedral star that link the two icosahedra, these calculations show that increasing the Au–Al interatomic contacts at the expense of Al–Al or Au–Au contacts is energetically favorable.

Electronic structures. Because all structures herein contain mixed Au/Al occupancy, models were generated by either lowering the observed space group symmetry to account for mixed-occupancy or selecting the predominant atom of each site and the rigid band model was used to approximate the electronic structures of the observed refined compositions. To calculate the electronic structures of cubic Sr(Au$_x$Al$_{1-x}$)$_{13}$ (7.24(2) ≤ x ≤ 6.68(2)), the experimentally determined space group ($Fm\overline{3}c$) was taken to its subgroup ($Fm\overline{3}$), so that the 8b and 96i sites that are Au/Al mixed with an almost 1:1 ratio were split into (4a + 4b) and two 48h sites, respectively. The 4a and 4b sites were respectively assigned Al and Au, and each 48h site was assigned as solely Al or Au, resulting in the hypothetical "SrAu$_{6.5}$Al$_{6.5}$" (28.0 e^-) with one set of icosahedra comprised of all Au and the second set comprised of all Al (see Figure 3 for group-subgroup breakdown). In a similar manner, the hypothetical tetragonal
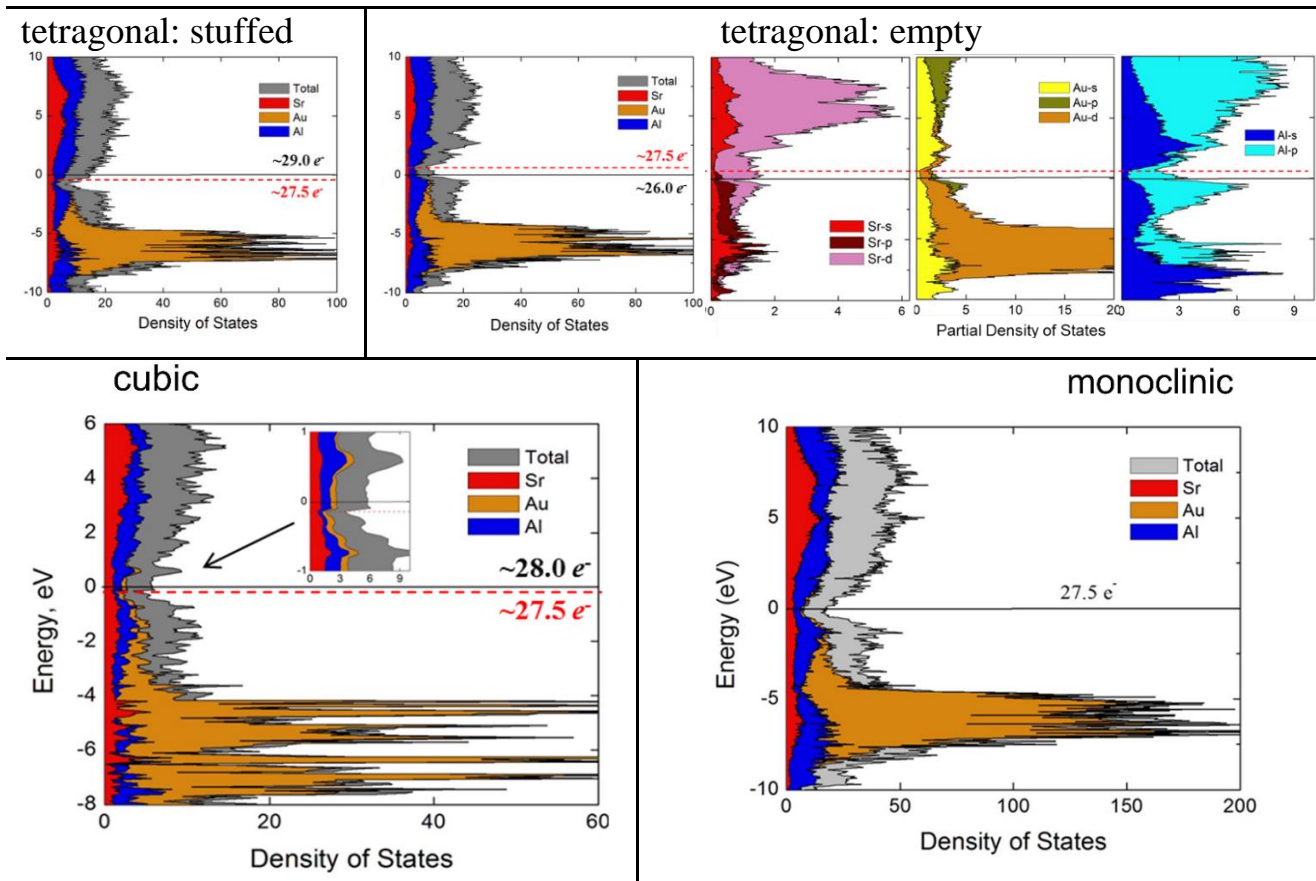
Figure 6. Electronic density of states (DOS) for Sr(Au$_x$Al$_{1-x}$)$_{13}$ cubic, tetragonal, and monoclinic derivatives. For all, the dashed lines close to E_F show electron counts close to the experimental compositions.

"SrAu$_{6.0}$Al$_{6.0}$" (26.0 e^-) with empty icosahedra and "SrAu$_{6.0}$Al$_{7.0}$" (29.0 e^-) with stuffed icosahedra, both observed in the space group $P4/nbm$, were calculated in its subgroup $Pban$, which excludes the 4-fold axis and breaks the 16n equivalency occupied by Au and Al atoms in a ~1:1 ratio. The two positions obtained from the symmetry reduction were assigned as Au and Al, whereas the other sites were treated as either pure Au or Al based on the majority component of the site in the tetragonal structure. In monoclinic "SrAu$_{6.0}$Al$_{6.5}$" (27.5 e^-) and orthorhombic "CaAu$_6$Al$_6$" (26 e^-), all mixed sites were assigned their majority components.

The electronic density of states (DOS) for all Sr- and Ca- models are respectively shown in Figures 6 and 7 with partial orbital breakdowns of the tetragonal "SrAu$_{6.0}$Al$_{6.0}$" that are analogously observed in all other models. Deep below E_F where the Au contribution is the largest or ~ –4 eV for all models, Sr (5s, "4d") orbitals interact most strongly with Au (6s, 5d) and Al (3s, 3p) with the latter two contributing significantly more than those of Sr to the total DOS, and contributions from Au (6p) and Sr ("5p") are relatively nonexistent. Moving toward E_F, as the Au (5d) contribution tapers off, Sr ("4d") contribution increases, so that at and above E_F, Sr ("4d") and Al (3p) are the largest contributors to the DOS. Furthermore, pairwise nearest neighbor orbital interactions (distances ≤ 3.5 Å) via COHP curves for "CaAu$_{6.0}$Al$_{6.0}$" (Figure 7) show trends also observed in the Sr-analogues (see Figures S2–3 for cubic "SrAu$_{6.5}$Al$_{6.5}$" and tetragonal "SrAu$_{6.0}$Al$_{6.0}$" COHP curves) such that at E_F, Au–Al bonding interactions predominate, followed by Sr/Ca–Au and Sr/Ca–Al, whereas Al–Al and Au–Au are essentially non- or antibonding. The DOS orbital breakdown and COHP interactions along with electronegativity differences among the constituent elements provide the foundation for the Sr/Ca–(Au+Al) polar-covalent interactions observed in polar intermetallics. Below E_F, Au and Al engage in covalent interactions arising from their smaller relative electronegativity
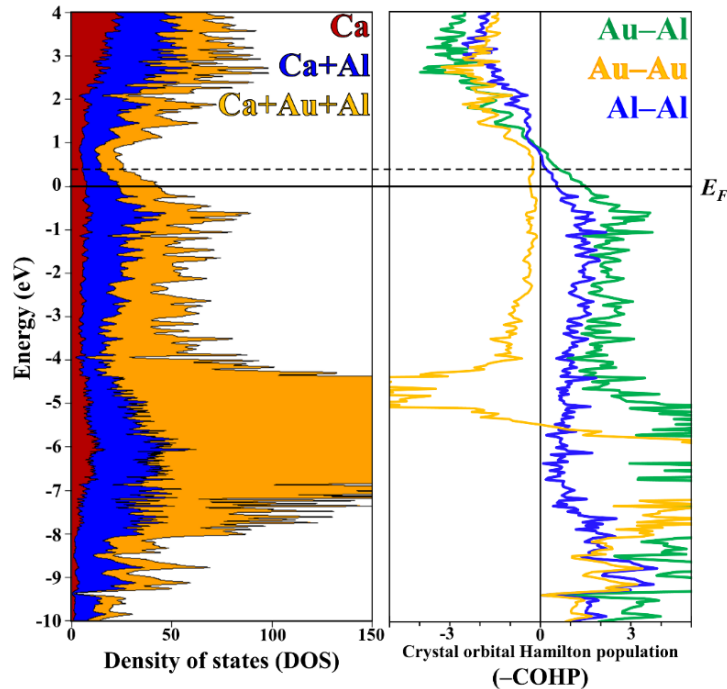
Figure 7. Density of states (DOS) and COHP curves for pairwise interactions ≤ 3.5 Å. The Fermi level (E_F) solid line was calculated for the hypothetical "CaAu$_6$Al$_6$" and the dashed line E_F was determined for the experimental composition CaAu$_{6.09(2)}$Al$_{6.01(1)}$, following the rigid band model. (–) COHP indicates antibonding and (+) indicates bonding interactions.

differences (Mulliken χ_{Sr} = 2.0, χ_{Ca} = 2.2, χ_{Au} = 5.77, and χ_{Al} = 3.23)[32], bonding states and large orbital contributions relative to those of Sr/Ca. Without Sr/Ca, Au+Al alone would more likely abide by the Hume-Rothery solubility rules since their metallic radii are also comparable. However, with the addition of the electropositive Sr/Ca, the DOS curves show Sr/Ca contributions well below E_F as electron donors to the more electronegative (Au+Al) framework, as evident also by the fact that there are no covalent Sr–Sr or Ca–Ca interactions even though the length scales of consideration (≤ 3.5 Å) are reasonable based on their elemental FCC arrangements. Toward and above E_F, the increase in Sr/Ca (3d/4d) contributions show their role as electron acceptors from the back-donation of (Au+Al) metals, with Au–Al interactions that generally cross into the nonbonding or antibonding regime.

Following the rigid band model, the experimental structures can be correlated to the calculated models based on valence electron counts. Accordingly, the calculated E_F for cubic

"SrAu$_{6.75}$Al$_{6.25}$" with 27.5 e^- falls in a pseudogap of the DOS that indicates its electronic stability; the Fermi levels for SrAu$_{7.24(2)}$Al$_{5.76}$ (26.5 e^-) and SrAu$_{6.68(2)}$Al$_{6.32}$ (~27.6 e^-) also fall within this pseudogap. Analogously, the hypothetical tetragonal "SrAu$_{6.0}$Al$_{6.0}$" (26.0 e^-), which features empty icosahedra, along with "SrAu$_{6.0}$Al$_{7.0}$" (29.0 e^-) with stuffed icosahedra, also give Fermi levels within pseudogaps of their DOS, so that "SrAu$_{5.25}$Al$_{6.75}$" (27.5 e^-) and the refined compositions SrAu$_{5.75(2)}$Al$_{6.25}$ (26.5 e^-) and SrAu$_{6.59(1)}$Al$_{6.41}$ (27.8 e^-) are nearby in their respective pseudogaps. Similar scenarios are afforded for monoclinic "SrAu$_{6.0}$Al$_{6.5}$" and orthorhombic "CaAu$_{6.0}$Al$_{6.0}$", for which electronic stability are observed for the refined compositions.

Conclusions

Five new NaZn$_{13}$-derivatives of Sr/Ca(Au$_x$Al$_{1-x}$)$_{12-13}$ were uncovered: (1) cubic SrAu$_x$Al$_{13-x}$ (7.24(2) $\geq x \geq$ 6.68(2)); (2) tetragonal SrAu$_x$Al$_{13-x}$ (6.59(1) $\geq x \geq$ 6.35(3)) with all-stuffed icosahedra; (3) monoclinic SrAu$_{6.10(3)}$Al$_{6.40}$; (4) tetragonal SrAu$_{5.75(2)}$Al$_{6.25}$ with all empty icosahedra; and (5) orthorhombic CaAu$_{6.09(2)}$Al$_{6.01(1)}$ with one-half empty icosahedra and the other half partially occupied by Al. Although Au and Al have similar metallic sizes so that the Hume-Rothery solubility rules might be applicable in a compound of only Au and Al, addition of Sr/Ca introduces Zintl-Klemm features as the electropositive Sr/Ca may donate electrons to the relatively more electronegative Au or Al, but that there is electronic back-donation by the (Au+Al) frameworks for structural cohesion. Atomic site preferences and electronic structures reveal closest Au–Al contacts that also contribute to structural cohesion.

References

1. Mizutani, U.; Sato, H., The physics of the Hume-Rothery electron concentration rule. *Crystals* **2017,** *7*, 9.

2. Miller, G.; Schmidt, M.; Wang, F.; You, T.-S., Quantitative advances in the Zintl–Klemm formalism. *Structure and Bonding* **2011,** *139* (Zintl Phases), 1-55.

3. Wade, K., The structural significance of the number of skeletal bonding electron-pairs in carboranes, the higher boranes and borane anions, and various transition-metal carbonyl cluster compounds. *Journal of the Chemical Society D: Chemical Communications* **1971,** (15), 792-793.

4. (a) Schäfer, H.; Eisenmann, B.; Müller, W., Zintl phases: Transitions between metallic and ionic bonding. *Angewandte Chemie International Edition in English* **1973,** *12* (9), 694-712; (b) Miller, G. J. L., C.-S.; Choe, W. , Structure and bonding around the Zintl border. In *Inorganic Chemistry Highlights*, Meyer, G., Naumann, D., Wesemann, L., , Ed. Wiley-VCH: Wein-heim: Germany, **2002**; pp 21-53

5. Corbett, J. D., Exploratory synthesis: The fascinating and diverse chemistry of polar intermetallic phases[††]This article is based on J. D. Corbett's address upon receipt of the 2008 American Chemical Society's F. Albert Cotton Award in Synthetic Inorganic Chemistry sponsored by the F. Albert Cotton Endowment Fund. *Inorganic Chemistry* **2009,** *49* (1), 13-28.

6. Miller, G. J.; Reedijk, J.; Poeppelmeier, K. R., Metal-Rich Compounds of the d-Metals *Comprehensive Inorganic Chemistry II* **2013,** *2*, 311-357.

7. Nordell, K. J.; Miller, G. J., Linking intermetallics and Zintl compounds: An investigation of ternary trielides (Al, Ga, In) forming the $NaZn_{13}$ Structure Type. *Inorganic Chemistry* **1999,** *38* (3), 579-590.

8. Smetana, V.; Steinberg, S.; Mudryk, Y.; Pecharsky, V.; Miller, G. J.; Mudring, A.-V., Cation-poor complex metallic alloys in Ba(Eu)–Au–Al(Ga) systems: Identifying the keys that control structural arrangements and atom distributions at the atomic level. *Inorganic Chemistry* **2015,** *54*, 10296-10308.

9. Phelan, W. A.; Kangas, M. J.; McCandless, G. T.; Drake, B. L.; Haldolaarachchige, N.; Zhao, L. L.; Wang, J. K.; Wang, X. P.; Young, D. P.; Morosan, E.; Hoffmann, C.; Chan, J. Y., Synthesis, structure, and physical properties of $Ln(Cu,Al,Ga)_{13-x}$ (Ln = La–Pr, and Eu) and $Eu(Cu,Al)_{13-x}$. *Inorganic Chemistry* **2012,** *51* (19), 10193-10202.

10. Miller, G. J., The "Coloring Problem" in solids: How it affects structure, composition and properties. *European Journal of Inorganic Chemistry* **1998,** *1998* (5), 523-536.

11. Han, M.-K.; Miller, G. J., An application of the "Coloring Problem": Structure−composition−bonding relationships in the magnetocaloric materials $LaFe_{13-x}Si_x$. *Inorganic Chemistry* **2008,** *47*, 515-528.

12. Nordell, K. Exploring aluminum-rich intermetallics with experiment and theory (aluminides, gold, trielides). Dissertation. Iowa State University **1997**.

13. Kraus, W.; Nolze, G., POWDERCELL-A program for the representation and manipulation of crystal structures and calculation of the resulting X-ray powder patterns. *Journal of Applied Crystallography* **1996,** *29* (3), 301-303.

14. StOE & Cie GmbH *Stoe . WinXPOW*, Darmstadt, Germany, **2006**.

15. (a) Rietveld, H., A profile refinement method for nuclear and magnetic structures. *Journal of Applied Crystallography* **1969,** *2* (2), 65-71; (b) *JANA2006*, Petricek, V., Dusek, M. & Palatinus, L.: 2014.

16. *SMART*. version 5; Bruker AXS: Madison, WI, **2003**.

17. Blessing, R., An empirical correction for absorption anisotropy. *Acta Crystallographica Section A* **1995,** *51* (1), 33-38.

18. Sheldrick, G. M. *SADABS*, University of Gottingen: Gottingen, Germany, **2001**.

19. Sheldrick, G., *SHELX*. version 6.14; Bruker AXS: Madison, WI, **2000-2003**.

20. Jepson, O. B., A.; Andersen, O.K., *The Program TB-LMTO-ASA,4.7;* **1999,** *Max-Planck-Institut für Festkörperforschung, Stuttgart, Germany*.

21. Barth, U. v.; Hedin, L., A local exchange-correlation potential for the spin polarized case. *Journal of Physics C: Solid State Physics* **1972,** *5* (13), 1629.

22. Koelling, D. D.; Harmon, B. N., A technique for relativistic spin-polarised calculations. *Journal of Physics C: Solid State Physics* **1977,** *10* (16), 3107.

23. Dronskowski, R.; Bloechl, P. E., Crystal orbital Hamilton populations (COHP): Energy-resolved visualization of chemical bonding in solids based on density-functional calculations. *The Journal of Physical Chemistry* **1993,** *97* (33), 8617-8624.

24. Lambrecht, W. R. L.; Andersen, O. K., Minimal basis sets in the linear muffin-tin orbital method: Application to the diamond-structure crystals C, Si, and Ge. *Physical Review B* **1986,** *34* (4), 2439-2449.

25. (a) Blöchl, P. E., *Phys. Rev. B* **1994,** *50*, 17953; (b) Kresse, G.; Hafner, J., *Phys. Rev. B* **1993,** *47*, 558; (c) Kresse, G.; Furthmüller, F., *Comput. Mater. Sci.* **1996,** *6*, 15.

26. Perdew, J. P.; Burke, K.; Ernzerhof, M., Generalized Gradient Approximation Made Simple. *Phys. Rev. Lett.* **1996,** *77*, 3865.

27. Gimarc, B. M., Topological charge stabilization. *J. Am. Chem. Soc.* **1983,** *105* (7), 1979-84.

28. (a) Palasyuk, A.; Grin, Y.; Miller, G. J., Turning gold into "diamond": A family of hexagonal diamond-type Au-frameworks interconnected by triangular clusters in the Sr–Al–Au system. *Journal of the American Chemical Society* **2014,** *136* (8), 3108-3117; (b) Cordier, G., Characteristics of the ternary aluminides barium copper aluminide ($Ba_5Cu_{1.9}Al_{3.1}$) and barium silver aluminide ($BaAg_{2.4}Al_{2.6}$, $Ba_{16}Ag_7Al_{27}$, and $Ba_3Ag_7Al_{27}$). *Journal of the less-common metals* **1991,** *170* (2), 333-357.

29. Baenziger, N. C.; Conant, J. W., The crystal structures of SrZn5 and $BaZn_5$. *Acta crystallographica* **1956,** *9* (4), 361-364.

30. Frank, K.; Schubert, K., Kristallstruktur von AuAl. *Journal of the Less Common Metals* **1970,** *22* (3), 349-354.

31. Teo, B. K.; Zhang, H.; Kean, Y.; Dang, H.; Shi, X., Binary icosahedral clusters: Atom and electron counting rules. *Journal of Chemical Physics* **1993,** *99* (4), 2929.

32. Pearson, R. G., Absolute electronegativity and hardness: application to inorganic chemistry. *Inorganic Chemistry* **1988,** *27* (4), 734-740.

CHAPTER 4

AN ICOSAHEDRAL QUASICRYSTAL AND ITS 1/0 CRYSTALLINE APPROXIMANT IN THE Ca–Au–Al SYSTEM

Modified from a publication in the journal *Inorganic Chemistry*

Joyce Pham,[†, §] *Andreas Kreyssig,*[§, ‡] *Alan I. Goldman,*[§, ‡] *and Gordon J. Miller,*[*, †, §]

[†]Departments of Chemistry, and [‡] Physics and Astronomy, Iowa State University,
[§]U.S. Department of Energy, Ames Laboratory, Ames, Iowa, 50011–3111

CaAu₃Al 1/0 crystalline approximant   "CaAu₄.₄Al₁.₆" icosahedral quasicrystal
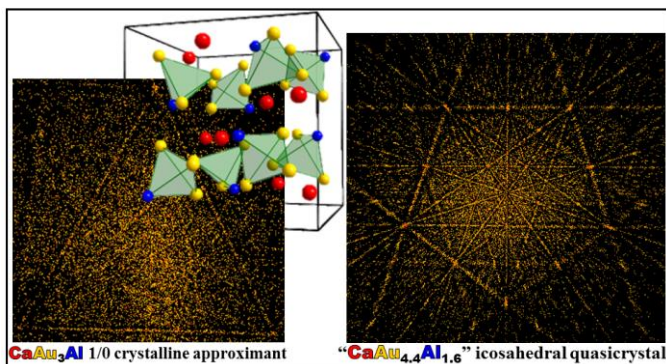
Abstract

A new icosahedral quasicrystalline phase, $CaAu_{4.5-x}Al_{1.5+x}$ ($0.11 \leq x \leq 0.40(6)$); for $CaAu_{4.4}Al_{1.6}$, $a_{QC} = 5.383(4)$, $Pm\overline{3}\overline{5}$) and its lowest order 1/0 cubic crystalline approximant phase, $CaAu_{3+x}Al_{1-x}$ ($0 \leq x \leq 0.31(1)$, $a = 9.0766(5)–9.1261(8)$ Å, $Pa\overline{3}$ (#205), Pearson symbol cP40) have been discovered in the Ca-poor region of the Ca–Au–Al system. In the crystalline approximant, eight $[Au_{3-x}Al_{1+x}]$ tetrahedra fill the unit cell and each tetrahedron is surrounded by four Ca atoms, thus forming a 3D network of $\{Ca_{4/4}[Au_{3-x}Al_{1+x}]\}$ tetrahedral stars. A computational study of Au and Al site preferences concurs with experimental results, which indicate preference of near-neighbor Au–Al interactions over Au–Au and Al–Al interactions. Analysis of the electronic density of states and the associated crystal orbital Hamilton population curves was used to rationalize the descriptions of $CaAu_{4.5-x}Al_{1.5+x}$ ($0.11 \leq x \leq 0.46(6)$) and $CaAu_{3+x}Al_{1-x}$ ($0 \leq x \leq 0.31(1)$) as polar intermetallic species, whereby Ca atoms

engage in polar covalent bonding with the electronegative, electron-deficient $[Au_{3-x}Al_{1+x}]$ tetrahedral clusters, and the observed phase width of the crystalline approximant.

Introduction

Polar intermetallic compounds are being scrutinized by various materials chemists because of their complex crystal and electronic structures as well as the lack of any holistic fundamental algorithm to explain and predict their compositions and structures.[1] From the simple standpoint of valence electron count per formula unit (VEC), polar intermetallics can be classified as an intermediate class between the valence electron-poor, densely packed Hume-Rothery phases $(VEC < 2)$[2] and the valence electron-specific, network-like Zintl-Klemm phases $(VEC \geq 4)$[3]. The myriad of research to elucidate the structures and compositions of Hume-Rothery and Zintl-Klemm phases has led to some fundamental concepts, such as valence electron-to-atom (e/a) and metallic radius ratio rules, that rationalize various structures and phase widths for both of these classes of solids.[4] A similar set of rules governing polar intermetallics remains undetermined to date, and warrants more investigation and systematization.

In a polar intermetallic compound, the electropositive metals formally donate valence electrons to the more electronegative metals. However, being metallic, there is an intrinsic back-donation of electrons from the electronegative metal into virtual orbitals of the electropositive metal, leading to polar covalent interactions between the two types of metallic elements. One result of this electron transfer mechanism is that, because of the back-donation of electrons by the electronegative metals, they remain electron deficient for two-center, two-electron bonding and often form polyhedral clusters or condensed clusters with specific valence electron counts, as seen in Zintl-Klemm phases. Yet, the valence electron counting

rules proposed for Hume-Rothery phases, derived from Fermi surface-Brillouin zone interactions for nearly free electron states, can also be used to rationalize the phase widths of many polar intermetallic compounds. As a result, polar intermetallics form a "hybrid" class of solids between the Zintl-Klemm and Hume-Rothery phases. For the Hume-Rothery valence electron-to-atom counting rules, the total number of valence electrons is divided over all atoms in the chemical formula instead of only the electronegative atoms, as is the case for Zintl-Klemm phases.[5] In the experimental design of this project, we used the Hume-Rothery valence electron-to-atom counting prescription to guide our targeted compositions but, for clarity, the Zintl-Klemm valence electron-to-atom counting ratios will also be provided in this paper. Another byproduct of this fundamental electron transfer mechanism in polar intermetallics is that the resulting diverse structural complexities hold potential physical properties relevant for applications such as in thermoelectrics or superconductors.

Two significant characteristics of polar intermetallic compounds are (1) a difference in coordination number between electropositive and electronegative metals, and (2) mixed site occupancies among electronegative metals. The electropositive metals are the larger alkali, alkaline-earth, or rare earth (including Sc and Y) elements, and the more electronegative metals are the smaller late transition through early post-transition elements. For instance, in the $NaZn_{13}$-type structure of $BaCu_5Al_8$, Cu/Al atoms form Cu-centered $[Cu_4Al_8]$ icosahedra on average so that each Ba atom is surrounded by a snub cube of 24 Cu/Al atoms.[6] As another example, in the Au-rich region of the Sr–Au–Al ternary system, Au atoms adopt a hexagonal diamond framework with voids filled by Sr atoms or planar triangles of $[Al_3]$ or $[Au_xAl_{3-x}]$ rings so that the average coordination number of Sr is 20.[7] Thus, networks and clusters of polyhedra with mixed site occupancies as well as large structural voids and high coordination

numbers are some of the structural features often exhibited by polar intermetallics. Due to these structural complexities, it is reasonable that some investigations of polar intermetallic systems can lead to the discovery of new quasicrystals (QCs) and their corresponding crystalline approximants (CAs). Ca–Au–Sn,[8] Na–Au–Ga,[9] and Sc–Cu–Al/Ga[10] are examples of ternary systems in which icosahedral quasicrystals (i-QCs) have been discovered and they can also be classified under the broader category of polar intermetallics.

Research on QCs is often concerned with addressing the question, "Where are the atoms?".[11] Of the various reported QC classes, i-QCs form the largest group, yet it is one of the most enigmatic because icosahedral symmetry requires quasiperiodicity throughout 3-dimensional (3D) space unlike decagonal or octagonal QCs, which are periodic along one-dimension.[12] Therefore, characterization techniques used to elucidate structural features of decagonal or octagonal QCs do not apply to i-QCs.[13] For example, Takakura et al.[14] have reported a model for the structure of the $YbCd_{5.7}$ i-QC from high-energy synchrotron diffraction data using hyperspace crystallography[15] from 6-dimensional (6D) space, in which i-QCs are periodic. The 6D space is decomposed into two orthogonal 3D subspaces that are decorated by 3D "occupation domains" that can be refined and modeled in a manner similar to that for crystalline materials in 3D.[11a,16] However, similar structural investigations have yet to be reported on ternary or higher multinary QCs for which the greater number of crystallographic parameters and the higher probability of mixed site occupancies elicit an additional question about elemental distributions throughout the structure. Nevertheless, an important lesson derived from studying the $YbCd_{5.7}$ i-QC is that the class of CA, which are crystalline phases compositionally close to their QC parents and hypothesized to approximate the structure of a QC, are indeed substructures of the QC structure using hyperspace

crystallography. For example, structural motifs of the CA $YbCd_6$ are found in its i-QC parent

$YbCd_{5.7}$, in agreement with synchrotron diffraction data. Thus, CAs of multinary i-QCs would

likely be substructures of the i-QCs as well. Therefore, to understand more about ternary or

higher multinary i-QCs, the study of their associated CAs remains a paramount investigation.[17]

From the study of CAs of i-QCs, there are currently three known structure types:

Bergman-;[18] Mackay-;[19] and Tsai-types[20]. A characteristic feature of all three motifs is that

atoms arrange in shells of polyhedral clusters in which a 32-atom, rhombic triacontahedral

cluster forms the outermost shell. The Tsai- and Bergman-types, which are more commonly

observed, are structurally similar, with the greatest difference being an innermost disordered

tetrahedral cluster in the Tsai-type and the lack thereof in the Bergman-type. The successfully

modeled binary $YbCd_{5.7}$ i-QC, for example, is associated with the Tsai-type $YbCd_6$ CA.

The so-called rational CAs of i-QCs are classified by an order, "*L/S*" such as "1/1" or

"2/1", based on two consecutive numbers in the Fibonacci sequence and how closely the CA

relates to its QC parent. As the *L/S* designation moves further along the Fibonacci sequence,

the lattice constant of a cubic CA, $a_{L/S}$, steadily increases. Moreover, there is a relationship

between the quasilattice constant a_{QC} for an i-QC and $a_{L/S}$ of the *L/S* CA:

$$a_{QC} = \frac{a_{L/S}(2+\tau)^{1/2}}{2(S+L\tau)}$$

where $\tau \approx 1.618\cdots \left(= \left(\frac{1+\sqrt{5}}{2}\right)\right)$, the golden mean.[21] Therefore, the quasilattice constant for an i-

QC can be estimated from its cubic *L/S* CA lattice parameter, and structural characterization

of the CA may give useful insights into the quasilattice as well as the i-QC structural motifs.

CAs of higher-order feature larger unit cells with greater crystallographic complexities than

lower-order CAs.[21-22] To date, the 2/1 CA structure is the highest order rational approximant reported and the majority of reported CAs are of order 1/1.

Few studies of QCs, however, have identified the lower order 1/0 CA and fewer still include electronic structural analysis. For instance, among Al-based i-QCs, the 1/1 CA is the lowest order approximant reported in the Yb–Au–Al[23] and Al–Mn–Si[24] systems. In the same manner that the aperiodic nature of QCs complicates the solution of its atomic structure, electronic structures based on the use of Bloch's theorem for periodic structures breaks down for QCs. As a result, electronic structural studies of QCs are often performed by extrapolating information gleaned from the electronic structures of their CAs. For example, Hafner et al. have examined $Al_{70}Pd_{20}Mn_{10}$[25] and Li_3CuAl_6[26] 1/1 CAs using tight-binding methods and built up to higher order CA models. However, a thorough electronic structure investigation of the lower order 1/0 CA for these systems has not yet been reported. As part of the general investigation of polar intermetallic compounds, herein we report a new Au-rich i-QC phase, with nominal composition $CaAu_{4.5-x}Al_{1.5+x}$ ($0.11 \leq x \leq 0.40(6)$) (herein referred to as "i-QC"), and its 1/0 CA phase, $CaAu_{3+x}Al_{1-x}$ ($0 \leq x \leq 0.31(1)$) (herein referred to as "1/0 CA"), along with determination of their phase widths and an analysis of the electronic structure of the 1/0 CA.

Experimental Section

Synthesis. Starting elements were obtained as follows: Ca chunks (99.99%, Sigma Aldrich), Au spheres (99.99%, Ames Laboratory) and Al ingots (99.999%, Alfa-Aesar). All were handled in an Ar-filled glovebox with moisture levels less than 0.1 ppm by volume. Each element was weighed to a total sample mass of 300.0(1) mg into tantalum tubes, which were arc-welded shut under argon. To keep the tantalum vessels from oxidizing at high temperature,

they were placed into a secondary silica jacket enclosed under vacuum ($< 10^{-5}$ torr). From there, all reactions were placed into a programmable tube furnace to be heated from room temperature to their reaction temperatures.

The title structures were discovered as part of an exploration of the Ca–Au–Al system around 14–20 atomic percent Ca by varying the Au:Al ratios. In particular, the investigation builds off and adds to previous reports on CaAu$_{3+y}$Ga$_{1-y}$,[27] which suggested that in the Ca-poor/Au-rich region, VEC values less than but near 2.0 e^-/atom, which lies at the border of Hume-Rothery phases, was anticipated to yield an i-QC. Similar results on other Au-rich polar intermetallic i-QCs further supported the investigation of Au-rich compositions near and less than VEC of 2.0 e^-/atom in the Ca–Au–Al system (e.g., see Ca–Au–Sn,[8] Na–Au–Ga,[9] and Sc–Cu–Al/Ga[10]).

As a result of these exploratory syntheses, the refined 1/0 CA phase was obtained from loadings that correspond to a VEC range 1.50–1.60 e^-/atom (1.88–2.00 e^-/electronegative metal Au+Al; ($-0.03(4) \leq x \leq 0.35(4)$)). Loaded CaAu$_{3+x}Al_{1-x}$ ($-0.15(4) \leq x \leq 0.52(4)$) samples (VEC range: 1.40–1.66 e^-/atom or 1.75–2.10 e^-/electronegative metal) were heated to 1000 °C and left to dwell for 24 hours, followed by cooling at 10 °C/hour to 700 °C, at which point they were annealed for a period of 5 days and rapidly quenched to room temperature by submerging the sealed reaction vessels into water. Quasicrystalline samples of loaded compositions CaAu$_{4.5-x}$Al$_{1.5+x}$ ($0.11 \leq x \leq 0.40(6)$), corresponding to VEC values 1.60–1.70 e^-/atom (1.87–1.98 e^-/electronegative metal), were heated to and then annealed at 900 °C for 1–2 days and then rapidly quenched to room temperature by submerging the sealed reaction vessels into water. Synthesis of the i-QC phase requires rapid quenching from its annealing temperature. A longer annealing period followed by slow cooling to room temperature resulted in another

CA phase, a preliminary examination of which suggests a 2/1 crystalline approximant that is still under investigation. Although some thermodynamically stable i-QCs have been reported, e.g., $Al_{65}Cu_{20}Fe_{15}$,[28] $(Yb/Ca)_{15}Cd_{65}Mg_{20}$,[29] binary $(Yb/Ca)_{15}Cd_{85}$,[30] and R–Cd (R = Gd to Tm, Y),[31] the use of rapid quenching — often leading to metastable products — has been reported as a more common route to synthesize i-QCs.[5a, 32] After the course of one year exposure to air and moisture at ambient temperatures, no changes in the products were detected visually or by powder X-ray diffraction.

The target compositions reflect VEC ranges that fall within the polar intermetallic classification between Hume-Rothery and Zintl-Klemm phases, i.e., $2 < VEC \leq 4$, by assigning two electrons to Ca (free atom electronic configuration: $[Ar]4s^2$), one electron to Au (free atom electronic configuration: $[Xe]6s^15d^{10}$) and three electrons to Al (free atom electronic configuration: $[Ne]3s^23p^1$). The targeted VEC ranges, used to determine synthetic loadings, follow the Hume-Rothery VEC mechanism in which the total number of valence electrons is divided by the number of all atoms in the chemical formula.[2b] The use of VEC as a synthetic guide follows previous literature reports, which suggest i-QCs and associated CAs as valence electron compounds that follow the Hume-Rothery electron counting mechanism.[5b] Nevertheless, according to the Zintl-Klemm formalism, if Ca is treated as a formal two-electron "cation," then the corresponding VEC ranges of 1.88–2.00 and 1.87–1.97 e^-/electronegative metal for the CA and i-QC, respectively, also fall within the polar intermetallic classification.

Powder X-ray diffraction. All products were characterized by powder X-ray diffraction data collected on a Stoe Stadi P diffractometer with a position-sensitive image-plate detector at ambient temperature using a Cu $K_{\alpha1}$ radiation source ($\lambda = 1.54060$ Å). Samples were

finely ground using an agate mortar and pestle, homogenously sandwiched between two transparent acetate films held together by a thin layer of vacuum grease and inserted into a Stoe airtight sample holder. For each set of PXRD measurements, the first sample was measured with added Si powder as a standard to ensure that the instrument is aligned. Scans with step sizes of 0.03^o in 2θ were set for all powder X-ray diffraction measurements.

The 1/0 CA phase purity was evaluated by juxtaposing observed powder diffraction data against patterns calculated from refined single-crystal diffraction data (e.g., Figure S1) using the *Powdercell* program.[33] Images from powder diffraction phase width analysis were exported from the *Win*PLOTR program of the *Full*prof suite.[34] Lattice parameters for $CaAu_{3+x}Al_{1-x}$ ($0 \leq x \leq 0.31(1)$) were refined from the seven most intense peaks in the $20-70^o$ 2θ range of the powder diffraction pattern using the *UnitCell* program (Table S1).[35] Additionally, a Rietveld refinement[36] of the lattice parameters and atomic coordinates (without site-occupancy) was performed on the observed PXRD patterns using *Jana2006*.[37]

Powder diffraction patterns of the loaded $CaAu_{4.5-x}Al_{1.5+x}$ ($0.11 \leq x \leq 0.40(6)$) i-QC samples were also analyzed using the *Win*PLOTR program of the *Full*prof suite.[34] By comparison of the powder diffraction patterns at systematic (VEC) loading in the $20-70^o$ 2θ range, which contains distinct features of the i-QC (e.g., Figure 1), the nominal phase width from loadings was estimated.

Single crystal X-ray diffraction. A Bruker *SMART* Apex II diffractometer with a CCD area detector and a Mo $K_{\alpha 1}$ fine-focused radiation source ($\lambda = 0.71073$ Å) was used to collect single-crystal X-ray diffraction data at ambient temperature on the $CaAu_{3+x}Al_{1-x}$ ($0 \leq x \leq 0.31(1)$) crystalline phase. Single crystals of approximate dimensions 30–50 μm × 30–50 μm × 30–50 μm were selected; each crystal was held fixed with grease onto the tip of a glass fiber

and was mounted onto the goniometer head of the diffractometer for data collection. For each

(VEC) sample with the cubic phase as a major component based on PXRD analysis (Figure 1),

at least two single-crystal data sets were collected (e.g., see Tables S1–S2). The *SMART*

software[38] was used to acquire data between one-half and a full sphere of reciprocal space with

0.5° scans in φ and ω at an exposure time of 10–20 seconds per frame. Lorentz and polarization

effects were included using the *SAINT* program. An empirical absorption correction,[39] to

account for the large percent composition of Au, was performed using the program *SADABS*.[40]

Numerical absorption corrections were also carried out for comparison against empirical

absorption corrections using the *X-Red32* and *X-Shape* programs associated with the Stoe IPDS

II program suite.[41] The space group $Pa\overline{3}$ for the 1/0 CA phase, Pearson symbol *cP*40, was

determined using the XPREP[42] program and confirmed using *Jana2006[37]*. The structure was

determined using direct methods and refined in the *SHELXTL 6.14* program suite by the full-

matrix least-squares fitting of observed structure factors.[42] Anisotropic displacement and

secondary extinction parameters were also refined (e.g., see Table S3). Crystallographic sites

are standardized using Vesta.[43] Images of all refined structures were created using the *Crystal*

Impact Diamond 3.2 software.[44]

For the i-QC samples, single-crystal X-ray diffraction data for a full sphere in

reciprocal space were collected on the Stoe IPDS with a Mo $K_{\alpha 1}$ radiation source ($\lambda = 0.71073$

Å) in 200–250 frames for exposure times of 8–10 minutes per frame and a detector-to-sample

distance of 100 mm. Multiple data sets exhibit a 5-fold rotational figure in the 2-dimensional

projected reciprocal space (e.g., see Figures 7a and S8) and could not be indexed by the

program *Recipe 1.18* of the *X-Area 1.52* suite[41] for the Stoe IPDS instrument. These observed

5-fold diffraction patterns provided the initial evidence for the discovery of an icosahedral

quasicrystal. The close resemblance between powder diffraction patterns of the sample and previously reported i-QCs in the literature supported this conjecture.

Further confirmation of the discovery of a Ca–Au–Al i-QC was conducted using an X-ray precession technique[45] at the Advanced Photon Source (APS; Beamline 6ID-D) at Argonne National Laboratory ($\lambda = 0.183520$ Å; 834.2732 mm sample-to-detector distance). At the APS, diffraction data sets were collected along the 2-fold, 3-fold, and 5-fold rotational axes of the sample to verify its identity as an i-QC. The observed peaks were indexed following Cahn's method and the PXRD pattern was simulated to calculate the quasilattice parameter.[46] All high-energy precession images of the quasicrystalline samples were constructed and analyzed using the software *FIT2D* v. 2004 from the *European Synchrotron Radiation Facility*.[47]

Energy dispersive X-ray spectrometry (EDS). Selected crystals as well as their ground products from the sample loaded as 20.32% Ca: 60.46% Au: 19.21% Al (molar ratio: "$Ca_{1.02(2)}Au_{3.04(9)}Al_{0.97(1)}$"; refined as $CaAu_{3.11(4)}Al_{0.89}$ from single-crystal X-ray diffraction, see Table S1) and the sample loaded as 14.43% Ca: 63.30% Au: 22.27% Al ("$CaAu_{4.4}Al_{1.6}$") were mounted onto a double-sided carbon tape stub and their spectra were measured on an FEI TENEO Scanning Electron Microscope (SEM) equipped with an Oxford Instruments Aztec Energy Dispersive Spectrometer (EDS). The SEM was operated under high vacuum using 20 kV; and ~0.4 nA. The analytical working distance is 10 mm. Selected crystals were transferred to the carbon tape using vacuum grease whereas the ground samples were scattered over the carbon tape without grease. Powdered specimens were grounded using an agate mortar and pestle. The use of ground powder for analysis was to expose the sample beyond the surface that may have oxidized or have been covered by grease. From the EDS spectra, atomic

fractions were estimated (see Figures S1–S2 and Table S4 for examples of SEM images and their EDS estimated atomic percent composition breakdown).

Resistivity measurements. Resistivity of selected specimens from the samples loaded as 20.32% Ca: 60.46% Au: 19.21% Al ("$Ca_{1.00(3)}Au_{2.975(5)}Al_{0.95(4)}$"; refined as $CaAu_{3.11(4)}Al_{0.89}$) and the sample loaded as 20.04% Ca: 59.58% Au: 20.38% Al ("$Ca_{1.00(3)}Au_{2.974(6)}Al_{1.02(4)}$"; refined as $CaAu_3Al$) were measured with the standard 4-probe technique using the AC resistivity option of the Quantum Design PPMS instrument at 2–300 K. Measurements from the different sample types were necessary to compare resistivity of disordered (nonstoichiometric) with ordered (stoichiometric) crystallographic refinements. Results were plotted and the RRR values were calculated for selected data sets (see Figure S7).

Electronic structures and site preferences. From the conjecture that $CaAu_{3+x}Al_{1-x}$ ($0 \leq x \leq 0.31(1)$) is a CA phase of the $CaAu_{4.5-x}Al_{1.5+x}$ i-QC, we hypothesize that atomic-site preference and electronic structure conclusions of the CA will give useful insight on the i-QC.

To understand factors that lead to atomic site preferences between Au and Al in the CA, first principles electronic structure calculations using the projected augmented wave method of the Vienna ab-Initio Simulation Package (VASP 4.6.34)[48] were employed to compare the total energies of six models constructed in the observed space group $Pa\overline{3}$ as well as subgroups $Pbca$ and $R\overline{3}$. The generalized gradient approximation with exchange and correlation potentials as constructed by Perdew, Burke, and Ernzerhof (PBE)[49] was used with an energy cutoff at 500 eV and a self-consistent convergence set to 0.01 meV. The orbital basis sets for all calculations were as follows: Ca ($3s^23p^64s^2$), Au ($5d^{10}6s^1$), and Al ($3s^23p^1$). Wyckoff site splitting from the $Pa\overline{3}$ space group to the $Pbca$ and $R\overline{3}$ subgroup models was determined by the *Wycksplit* program on the Bilboa Crystallographic server.[50]

The electronic band structure, density of states (DOS), and crystal orbital Hamilton population (COHP) curves for interatomic interactions up to 3.5 Å were calculated for $CaAu_3Al$ using the Stuttgart tight-binding, linear muffin-tin orbital with the atomic sphere approximation (TB-LMTO-ASA) code[51] without spin polarization (LDA only). Input parameters for $CaAu_3Al$ were those obtained by total energy minimization using all relaxation modes available in VASP. For these calculations, the von Barth-Hedin local exchange-correlation potential and scalar relativistic effects were used.[52] A maximum sphere overlap of 20% (volume overlap of $\leq 9.0\%$) was enforced so that additional empty spheres were not necessary to achieve 100% volume filling of the unit cell in the ASA. The convergence limit was set at 0.01 meV and the following atomic sphere radii with their associated atomic orbital basis sets were employed: Ca: 3.744 Å utilizing $Ca(4s,3d)$ functions with $Ca(4p,4f)$ functions downfolded; Au: 2.925 Å utilizing $Au(6s,6p,5d)$ functions with $Au(5f)$ functions downfolded; and Al: 2.844 Å utilizing $Al(3s,3p)$ functions with $Al(3d)$ functions downfolded.[53] The irreducible wedge from the first Brillouin Zone utilized 3001 ($20 \times 20 \times 20$) k-points for plotting DOS and COHP[54] curves.

Results and Discussion

In the Ca-poor (20 atomic percent) region of the Ca–Au–Al system, the cubic 1/0 CA $CaAu_{3+x}Al_{1-x}$ ($0 \leq x \leq 0.31(1)$) phase ($a = 9.0766(5)–9.1261(8)$ Å; $Pa\overline{3}$ (#205); Pearson symbol $cP40$) was discovered for the VEC range 1.50–1.60 e^-/atom (1.88–2.00 e^-/electronegative metal) following synthesis with a 5-day annealing period at 700 °C. In the 1/0 CA, each of the eight $[Au_{3-x}Al_{1+x}]$ tetrahedra in the unit cell is surrounded by four Ca atoms forming $\{Ca_{4/4}[Au_{3-x}Al_{1+x}]\}$ tetrahedral star substructures, which are condensed via vertex-sharing at the Ca sites. Over multiple single-crystal specimens, Al atoms occupy a single (8c) site of the

cubic unit cell, an outcome that optimizes the total energy according to first principles calculations by optimizing the frequency of heteroatomic (Au–Al) nearest neighbor contacts over homoatomic (Au–Au or Al–Al) ones. Without annealing, i.e., by quenching alone, decreasing the Ca content to 14 atomic percent, giving a VEC range 1.60–1.70 e^-/atom (1.87–1.98 e^-/electronegative metal), leads to the primitive i-QC $CaAu_{4.5-x}Al_{1.5+x}$ ($0.11 \leq x \leq 0.40(6)$) phase ($CaAu_{4.4}Al_{1.6}$: $a_{QC} = 5.383(4)$ Å; $Pm\overline{3}\overline{5}$).

Phase width analysis. Figure 1 and Table 1 show, respectively, the X-ray powder diffraction patterns and analyses of five different loadings that yielded the cubic $CaAu_{3+x}Al_{1-x}$ ($0 \leq x \leq 0.31(1)$) phase as both major and minor products (Table S1 summarizes the data according to VEC and atomic percent breakdown). For the sample loaded as 20.32% Ca: 60.46% Au: 19.21% Al ("$Ca_{1.02(2)}Au_{3.04(9)}Al_{0.97(1)}$"), EDS analysis of grounded polycrystalline products indicate an estimated percent composition corresponding to $Ca_{1.0(1)}Au_{3.1(2)}Al_{0.9(1)}$, which closely agrees with the averaged refined composition from single-crystal X-ray diffraction, $CaAu_{3.11(4)}Al_{0.90}$ (see Figures S1–S2 and Table S4 for EDS results). Table S2 also summarizes the crystallographic results of specimens selected from three $CaAu_{3+x}Al_{1-x}$ samples ($x = 0$, 0.11(4), and 0.21(1)), and Table S3 gives their atomic coordinates and thermal parameters. The observed phase width is similar to that reported for the isotypic phase $CaAu_{3+y}Ga_{1-y}$ ($0 \leq y \leq 0.13$),[27a] although synthetic procedures differ to obtain the respective stoichiometric end members $CaAu_3Al$ and $CaAu_3Ga$. $CaAu_3Al$ was obtained by stoichiometric loadings of "$Ca_{1.0(2)}Au_{3.0(8)}Al_{1.0(2)}$" whereby the Ca:Al ratio is equivalent, whereas $CaAu_3Ga$ could only by obtained from Ga loadings richer than Ca, for example, from "1 Ca: 2.75 Au: 1.25 Ga," to "1 Ca: 2.0 Au: 2.0 Ga".[27a]

Table 1. Phase width analysis of $CaAu_{3+x}Al_{1-x}$ CA and $CaAu_{4.5-x}Al_{1.5+x}$ i-QC samples. Included are loaded molar ratios Ca:Au:Al; average x values ($\langle x \rangle$) in the formulas $CaAu_{3+x}Al_{1-x}$ and $CaAu_{4.5-x}Al_{1.5+x}$; VEC values; phase identification from PXRD; and results from single-crystal XRD refinements.

Figure	Loading Ca: Au: Al mol. %	$\langle x \rangle$	VEC	PXRD	Single-Crystal XRD Refinement Refined	x	VEC
Not shown	19.80: 70.09: 10.11	0.52(4)	1.40	Unknown major phase; possible minor $CaAu_{3+x}Al_{1-x}$	No selected crystals indexed the lattice parameters from $CaAu_{3+x}Al_{1-x}$		
1(a)	20.16: 67.08: 12.76	0.35(4)	1.46	$CaAu_{3+x}Al_{1-x}$ + unknown	$CaAu_{3.314(8)}Al_{0.686}$	0.314(8)	1.48
1(b)	20.04: 64.90: 15.06	0.25(4)	1.50	$CaAu_{3+x}Al_{1-x}$ only	$CaAu_{3.31(1)}Al_{0.69}$	0.31(1)	1.48
1(c)	19.65: 62.40: 17.95	0.15(4)	1.56	$CaAu_{3+x}Al_{1-x}$ only	$CaAu_{3.206(9)}Al_{0.794}$	0.206(9)	1.52
S3	20.32: 60.46: 19.21	−0.03(4)	1.59	$CaAu_{3+x}Al_{1-x}$ only	$CaAu_{3.11(4)}Al_{0.89}$	0.11(4)	1.55
1(d)	20.04: 59.58: 20.38	−0.03(4)	1.61	$CaAu_{3+x}Al_{1-x}$ only	$CaAu_{3.00}Al_{1.00}$	0	1.60
1(e)	19.79: 57.07: 23.14	−0.15(4)	1.66	Minor $CaAu_{3+x}Al_{1-x}$	No selected crystals indexed the lattice parameters from $CaAu_{3+x}Al_{1-x}$		
2(α)	14.43: 63.30: 22.27	0.11(6)	1.60	$CaAu_{4.5-x}Al_{1.5+x}$ only			
2(β)	14.38: 59.78: 25.85	0.34(6)	1.66	$CaAu_{4.5-x}Al_{1.5+x}$ only			
2(γ)	14.14: 58.08: 27.79	0.40(6)	1.70	$CaAu_{4.5-x}Al_{1.5+x}$ only			
2(δ)	14.31: 55.32: 30.37	0.63(5)	1.75	$CaAu_{4.5-x}Al_{1.5+x}$ + minor 2/1 CA			

69
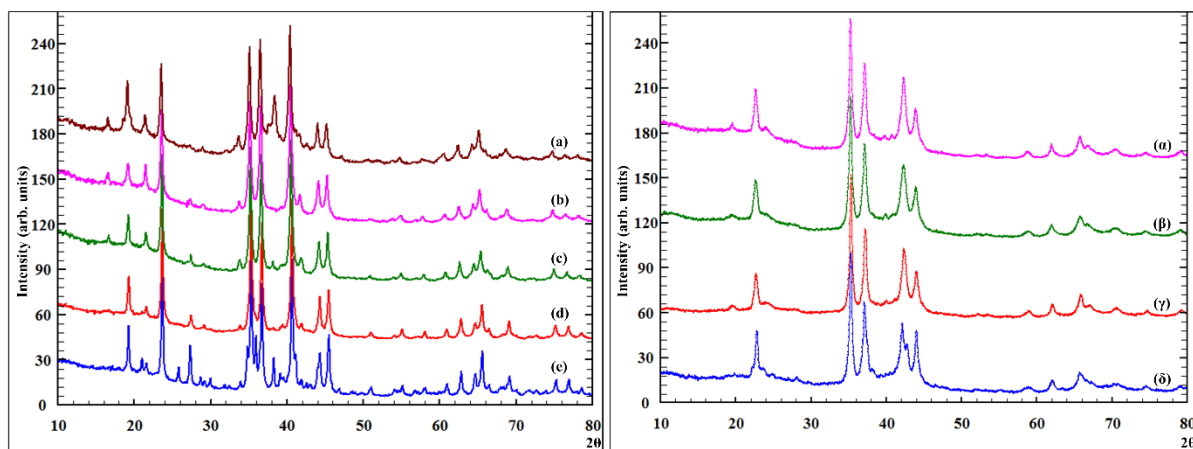
Figure 1. Left: PXRD collected for five products loaded as $CaAu_{3+x}Al_{1-x}$ ($-0.15 \leq x \leq 0.35(4)$): (a) $x = 0.35(4)$; (b) $x = 0.25(4)$; (c) $x = 0.15(4)$; (d) $x = -0.03(4)$; and (e) $x = -0.15(4)$. Right: PXRD patterns for four products loaded as $CaAu_{4.5-x}Al_{1.5+x}$ ($0.11 \leq x \leq 0.40(6)$): (α) $x = 0.11(6)$; (β) $x = 0.34(6)$; (γ) $x = 0.40(6)$ (δ) $x = 0.63(6)$. See Tables S1 and 1.

For comparison with the cubic CA phase, Figure 1 also shows the powder diffraction patterns for loadings corresponding to the i-QC phase, $CaAu_{4.5-x}Al_{1.5+x}$ ($0.11 \leq x \leq 0.40(6)$). Beyond the upper limit, the sample loaded as $Ca_{1.00(4)}Au_{3.866(7)}Al_{2.12(5)}$, corresponding to VEC 1.75 e^-/atom (2.04 e^-/electronegative metal) and $x = 0.63(3)$, yielded the powder diffraction pattern corresponding to a 2/1 CA, which is still under investigation. The shoulder peak at 2θ ~ 42° becomes more pronounced in a phase-pure 2/1 CA phase. EDS analysis of both grounded polycrystalline products and selected "single crystals" from the sample loaded as 14.43% Ca: 63.30% Au: 22.27% Al ("$CaAu_{4.4}Al_{1.6}$") indicate an estimated percent composition, "$Ca_{1.0(1)}Au_{4.5(2)}Al_{1.4(1)}$", which closely matches the loading composition (see Figures S1–S2 and Table S4 for EDS results). From the PXRD patterns and systematic loadings within the VEC range 1.60–1.70 e^-/atom (1.87–1.98 e^-/electronegative metal), the phase width of the i-QC is estimated to be $CaAu_{4.5-x}Al_{1.5+x}$ ($0.11 \leq x \leq 0.40(6)$).

Structure of $CaAu_{3+x}Al_{1-x}$. Figure S3 juxtaposes the measured powder X-ray diffraction pattern from the sample loaded as 20.32% Ca: 60.46% Au: 19.21% Al

Table 2. Refined crystallographic data for CaAu₃Al

instrument	Bruker CCD APEX II
radiation; λ (Å)/ temp.(K)	Mo Kα; 0.71073/298
θ range data collection	3.9°–30.0°
absorp. coeff./ μ (mm^{-1})/ correction	119.21/empirical
meas./ indpnt./ obs. [$I > 2\sigma(I)$]/ para.	14462/369/319/17
$R[F^2 > 2\sigma(F^2)]$/ $wR(F^2)$/ R_{int}/ GOF	0.027/0.060/0.145/1.14
space group/ Pearson symbol	$Pa\overline{3}$ (#205)/ $cP40$
$\Delta\rho_{max}$, $\Delta\rho_{min}$ (e Å^{-3})	1.88, –1.60
dimension a (Å)/ volume (Å^3)/ Z	9.0656(8)/745.1(2)/8
Au (24d)	
x	0.08090(5)
y	0.26068(5)
z	0.35236(5)
U_{iso}/U_{eq}	0.0191 (2)
Ca (8c)	
x	0.3951(3)
y	0.3951(3)
z	0.3951(3)
U_{iso}/U_{eq}	0.0153(8)
Al (8c)	
Al:Au (8c) occupancy	1:0
x	0.0915(4)
y	0.0915(4)
z	0.0915(4)
U_{iso}/U_{eq}	0.013 (1)

"Ca$_{1.02(2)}$Au$_{3.04(9)}$Al$_{0.97(1)}$" against a simulated powder pattern from single-crystal diffraction refined as CaAu$_{3.11(4)}$Al$_{0.89}$. The match between the observed bulk polycrystalline sample and refined single-crystal data indicates that the majority of the product possesses the crystal structure described herein.

The structure of cubic CaAu$_{3+x}$Al$_{1-x}$ is isotypic and nearly isoelectronic to that of NaAu₃Ge/Si[53] and CaAu$_{3+y}$Ga$_{1-y}$ ($0 \leq y \leq 0.13$)[27a]. Table 2 lists significant crystallographic results as well as atomic positions, occupancies, and isotropic displacement parameters for the asymmetric unit of the stoichiometric end-member CaAu₃Al (see Tables S2–S3 for results of other samples). There are three inequivalent sites in the asymmetric unit: Ca atoms at 8c, C_3 point symmetry, surrounded by a 16-vertex Frank Kasper polyhedron; Au atoms at 24d, C_1
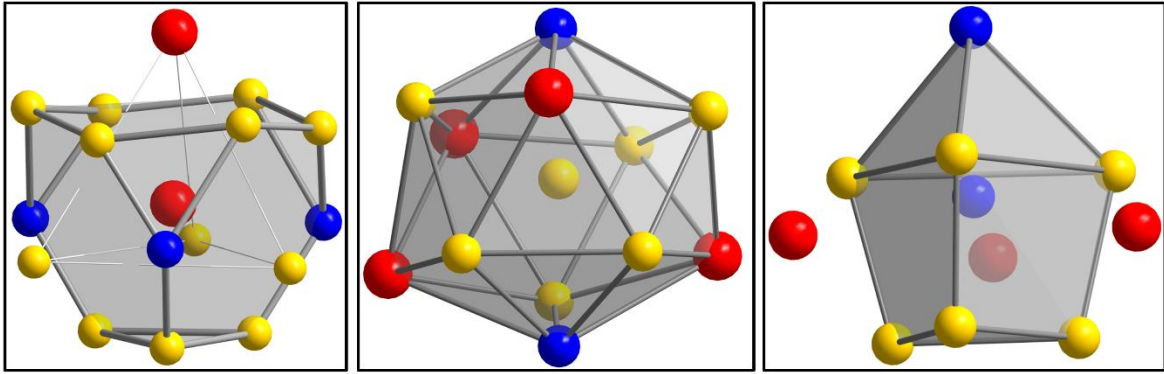
Figure 2. Local environments of independent sites in $CaAu_{3+x}Al_{1-x}$: (left, red) Ca, 16-vertex $[(Au_9Al_3)(CaAu_3)]$ Frank-Kasper polyhedron; (middle, yellow) Au, distorted $[Ca_4Au_6Al_2]$ icosahedron; and (right, blue) Al/Au site, $[Au_6Al](Ca_3)$ monocapped trigonal prism with three additional capping Ca sites.

point symmetry, surrounded by a distorted icosahedron; and Al/Au atoms at $8c$, C_3 point symmetry, surrounded by a capped trigonal prism (see Figure 3). Nonstoichiometric (Au-rich) loadings of $CaAu_{3+x}Al_{1-x}$ led to Al/Au mixed occupancies at a single $8c$ site; this result agrees with the report of Ga/Au mixing in $CaAu_{3+y}Ga_{1-y}$[27a]. On the other hand, only stoichiometric $NaAu_3Ge/Si$ have been reported without any phase width analysis.[55]

The unit cell of the 1/0 CA contains eight equivalent $[Au_{3-x}Al_{1+x}]$ tetrahedra with C_3 point symmetry and each surrounded by four Ca atoms over each face to form tetrahedral stars leading to the structural formulation $\{Ca_{4/4}[Au_{3-x}Al_{1+x}]\}$. In addition, six Au atoms ($24d$ sites) from adjacent tetrahedral stars cap each edge of the $[Au_{3-x}Al_{1+x}]$ tetrahedra to form a distorted octahedron and create a distorted 14-atom $\{[Au_{3-x}Al_{1+x}]Ca_4Au_6\}$ kernel of the typical 26-atom clusters found in Hume-Rothery type γ-brasses.[56] Figure 3 illustrates this perspective of the structure of $CaAu_{3+x}Al_{1-x}$ along the [010] direction.

The various interatomic distances observed in stoichiometric $CaAu_3Al$ are comparable to interatomic distances of isotypic $CaAu_3Ga$ and $NaAu_3Ge/Si$. In general, the Au–X (X = Si/Ge/Al/Ga) distances in the tetrahedral star are the shortest of all followed by either the Au–
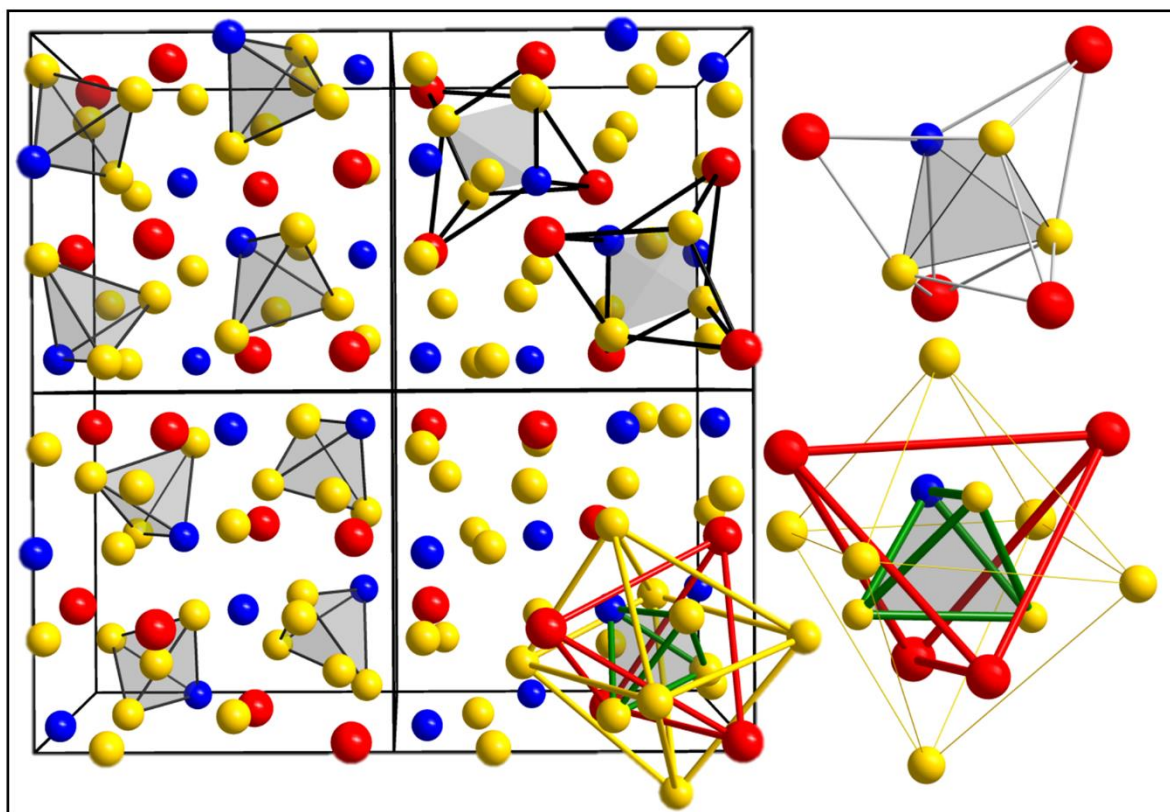
Figure 3. CaAu$_{3+x}$Al$_{1-x}$ drawn across 4 unit cells along the [010] direction depicting different aspects of tetrahedra packing. Left top and bottom respectively: front and back shaded [Au$_{3-x}$Al$_{1+x}$] tetrahedra. Right top: front and back tetrahedral star. Right bottom: 3 innermost shells of the γ-brass cluster. The tetrahedral star and inner shells of the γ-brass cluster are magnified and isolated from the unit cells for visualization.

Au distances or the shortest of the 3 cationic (Na/Ca)–Au distances. Furthermore, among Au–X contacts, the Au–Al (2.817(5) Å (3×)) distance is longest, followed in decreasing order by Au–Ga (2.747(2) Å (3×)), Au–Ge (2.612(9) Å (3×)) and Au–Si Å (2.612(9) Å (3×)). In general, Au–X, (Na/Ca)–X, and Au–Au distances all lengthened on going from Na to Ca. All (Na/Ca)–Au and (Na/Ca)–(Na/Ca) interactions are comparable within the tetrahedral star (see Table S5). Beyond the tetrahedral star, the nearest Na···Na interactions (3.00(1) Å for NaAu$_3$Ge and 3.00(3) Å for NaAu$_3$Si) are also generally shorter than those of Ca···Ca (3.334(4) Å for CaAu$_3$Ga and 3.294(4)–3.397(5) Å for CaAu$_{3+x}$Al$_{1-x}$ (0 ≤ x ≤ 0.31(1)). These formally cationic interactions are discussed at length in both reports of isotypic CaAu$_3$Ga and, more recently,

$AgPd_3Se$,[57] because they form the edges of rhombohedral units that can be related to icosahedral geometry. The structure of $AgPd_3Se$ was reported using powder X-ray diffraction and without phase width for mixed-site occupancy comparisons. From the single reported $AgPd_3Se$ compound, the Ag···Ag contacts (2.729(2) Å) are significantly shorter than all other cationic isotypic interactions discussed herein.[57]

Although the structure of $CaAu_{3+x}Al_{1-x}$ is densely packed with Ca in the voids amongst the network of $[Au_{3-x}Al_{1+x}]$ tetrahedra, the largest isotropic thermal displacement factors occur at the Au (24d) and Al/Au (8c) sites, according to all crystallographic refinements using *Shelxtl* and *Jana2006* software. That $U_{Au}(24d)$ exceeds U_{Ca} in all cases is somewhat surprising given the difference in atomic numbers between Au (79) and Ca (20). Therefore, we have analyzed the refinement outcomes of the 24d site in more detail. Refining the 24d site as mixed Au/Al yields no reasonable solution but assigning it as a possibly split Au/Au site produces viable alternative outcomes to the results presented in Tables 2 and S2–3. Three different refinement strategies for the 24d sites were examined and statistically analyzed: (1) as fully occupied by Au; (2) as two freely occupied split positions without constraints on the individual thermal parameters; and (3) as two equally split sites without constraints on its individual thermal parameters (see Table S3A for a summary of these results). In strategy (2), the two split 24d sites add up to a total occupancy of 0.95(4)–1.09(3) Au with distances between the split positions varying from 0.030(1) to 0.27(4) Å as the composition changes from $CaAu_{2.9(1)}Al$ to $CaAu_{3.60(9)}Al_{0.66}$. The local environment of each Au atom shows no unique differences from that of strategy (1) (i.e., Figure 2 middle). Moreover, U_{Ca} remains lower than U_{Au} on these split 24d sites, as seen in strategy (1). A statistical analysis using the Hamilton test[58] suggests that rejection of the refinement as fully occupied by Au (strategy 1) is significant at the 0.05%–
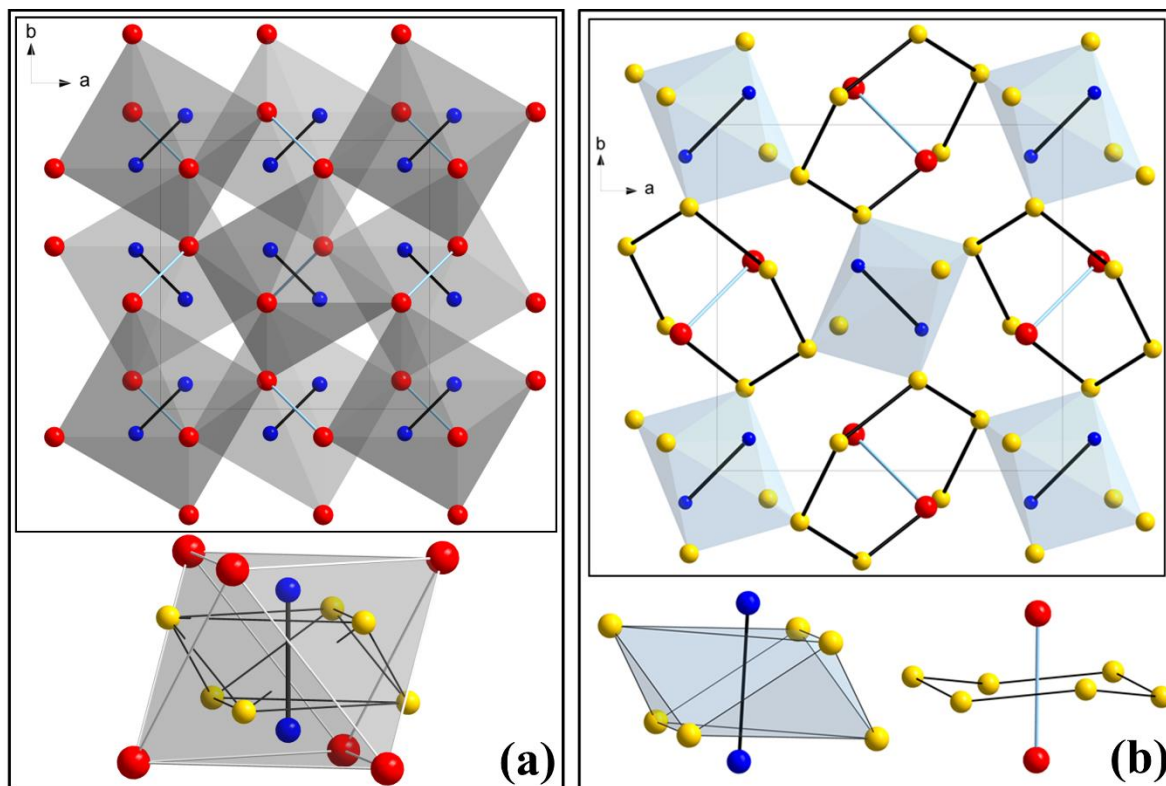
Figure 4. Structure of CaAu$_{3+x}$Al$_{1-x}$ as related to (a) the FeS$_2$-type structure; and (b) the ABX$_3$ perovskite-type structure. Ca atoms (red); Au atoms (yellow); (Al$_{1-x}$Au$_x$) sites (blue).

50% levels. On the other hand, for some refinements using strategy (3), one of the two equally occupied split 24d (Au) sites has U_{Au} less than U_{Ca}, although the other U_{Au} value is significantly larger (2–3× in comparison) than that of the other atomic positions. Furthermore, the distances between the two equally split sites range from 0.007(5) to 0.24(3) Å, which also do not yield unique local environments for these Au atoms. A Hamilton test[58] comparing strategies (2) and (3) suggests that strategy (3) can be rejected up to the 0.05% significance level. In summary, for all 3 refinement strategies, U_{Ca} remains systematically lower than at least one of the split 24d (Au) sites. Increasing the number of refined crystallographic parameters does not suggest that rejection of strategy (1), in which the 24d site is not split and occupied solely by Au atoms yields a statistically significant difference. Therefore, we contend that the structural model for

$CaAu_{3+x}Al_{1-x}$ described in Tables 2 and S2–3 and Figures 2–4 is reasonable for further analysis and bonding interpretation.

Relationship to common structure types. In addition to identification of atomic coordination environments, comparison with isotypic/isoelectronic species, and classification as a polar intermetallic system, the 1/0 CA can be also correlated to more common structure types, two of which are (1) the pyrite-type structure, which possesses the same space group $Pa\overline{3}$ as $CaAu_{3+x}Al_{1-x}$; and (2) the ABX_3 perovskite-type structure, with has the 1:3:1 composition also found in $CaAu_{3+x}Al_{1-x}$. The structure of $CaAu_{3+x}Al_{1-x}$ is related to that of pyrite because the [Al/Au–Al/Au] ($8c$–$8c$) "dimer" units take up the positions of Fe and Ca atoms take up the positions of S in FeS_2, generating a network of "$Ca(Al_{1-x}Au_x)$." The remaining Au atoms form distorted octahedra that interpenetrate the faces of [Ca_6] octahedra (see Figure 4a). Thus, the $CaAu_{3+x}Al_{1-x}$ structure can be described as vertex-sharing [Ca_6] octahedra surrounding [Al/Au–Al/Au] "dimer" units with Au atoms on the faces of the [Ca_6] octahedra. The relationship to perovskite emerges by considering the $CaAu_{3+x}Al_{1-x}$ structure as a network of vertex-sharing [$Au_{6/2}$] units, shaped like "chair cyclohexane," and [$Au_{6/2}$] distorted octahedral units (see Figure 4b). The [$Au_{6/2}$] octahedra surround [Al/Au–Al/Au] "dimers" and the [$Au_{6/2}$] "chair cyclohexane" units bisect [Ca···Ca] groups. The network of vertex-sharing [$Au_{6/2}$] units is reminiscent of the X-framework in ABX_3 perovskite-type structures, but the cuboctahedral voids that are filled by A atoms are empty in $CaAu_{3+x}Al_{1-x}$. The [Al/Au–Al/Au] "dimers" and [Ca···Ca] units occupy the average positions of the single B atoms. Additionally, the equivalent vertex-sharing octahedra [$X_{6/2}$] in perovskite are distorted into alternating [$Au_{6/2}$] octahedra and "chair cyclohexanes."

Table 3. Site preference calculations. Six models and their relative E_{tot} to elucidate Al/Au site preference based on frequency of Au–Al, Au–Au, and Al–Al contacts and their distances.

Label	α	β	γ	δ	ε	ρ
Space group	$Pa\bar{3}$	$R\bar{3}$	$R\bar{3}$	$R\bar{3}$	$Pbca$	$R\bar{3}$
Total # Au–Al	72	72	60	48	72	36
2.551(2) Å	24	12	12	12	8	0
2.817(6) Å	24	12	12	0	8	12
2.828(6) Å	0	12	0	12	16	12
2.883(6) Å	0	0	0	0	0	0
3.067(6) Å	0	12	12	0	16	12
3.079(1) Å	0	12	12	12	16	0
3.423(3) Å	24	12	12	12	8	0
Total # Au–Au	72	77	81	87	76	93
2.551(2) Å	0	12	12	12	16	18
2.817(6) Å	0	12	12	18	16	12
2.828(6) Å	24	12	18	12	8	12
2.883(6) Å	0	3	3	3	4	3
3.067(6) Å	24	12	12	18	8	12
3.079(1) Å	24	12	12	12	8	18
3.423(3) Å	0	12	12	12	16	18
Total # Al–Al	4	1	7	13	0	19
2.551(2) Å	0	0	0	0	0	6
2.817(6) Å	0	0	0	6	0	0
2.828(6) Å	0	0	6	0	0	0
2.883(6) Å	4	1	1	1	0	1
3.067(6) Å	0	0	0	6	0	0
3.079(1) Å	0	0	0	0	0	6
3.423(3) Å	0	0	0	0	0	6
ΔE_{tot}/f.u.(eV)	0	+0.93	+1.05	+1.11	+1.24	+1.48

Atomic site preferences. Among the three sites of the asymmetric unit of $CaAu_{3+x}Al_{1-x}$, the $24d$ site is solely occupied by Au whereas, for nonstoichiometric loadings, an $8c$ site is occupied by a mixture of Au and Al, although mostly Al. For $CaAu_3Al$ in particular, there are seven possible interatomic distances less than 3.5 Å between any two Au atoms, two Al atoms, or an Au atom and an Al atom: 2.551(2) Å ($8c$–$24d$ interactions; 33×), 2.817(6) Å ($8c$–$24d$; 29×), 2.828(6) Å ($24d$–$24d$; 24×), 2.883(6) Å ($8c$–$8c$, 7×) 3.067(6) Å ($24d$–$24d$; 24×), 3.079(1) Å ($24d$–$24d$; 24×), and 3.423(3) Å ($8c$–$24d$; 30×). To understand the site preferences for Au and Al atoms in $CaAu_3Al$, five additional models were constructed by using the maximal non-

isomorphic subgroups of $Pa\bar{3}$, namely *Pbca* and $R\bar{3}$. In *Pbca*, the 24*d* sites become split into three inequivalent 8-fold sites; in $R\bar{3}$, the 24*d* sites are split into four inequivalent 6-fold positions, whereas each 8*c* site splits into a 2-fold and a 6-fold site. Au and Al atoms were then distributed among the various sites keeping the overall composition $CaAu_3Al$. See Table S6 for a summary of the atomic coordinates of all 6 models for $CaAu_3Al$.

Table 3 summarizes the relative total energies evaluated using VASP of these six models, indicated by the labels α, β, γ, δ, ε, and ρ according to increasing energy, and showing the numbers of specific Au–Al, Au–Au, and Al–Al contacts for distances less than 3.5 Å. According to these results, the observed arrangement (model α, space group $Pa\bar{3}$) is most energetically favorable with 72 Au–Al, 72 Au–Au and 4 Al–Al contacts. Although the next most favorable model β has the same number of overall Au–Al contacts to model α, there are fewer nearest neighbor (2.551(2) Å) Au–Al contacts in model β. Therefore, Au and Al atoms prefer optimal nearest-neighbor heteroatomic Au–Al contacts over homoatomic and longer (3.423(3) Å) heteroatomic contacts. This result agrees with previous investigations of various $NaZn_{13}$-type AM_xAl_{13-x} (A = Sr, Ba, La, Ce, Eu; M = Cu, Pd, Ag, Au) phases, in which the atomic distribution shows preference for heteroatomic M–Al contacts over homoatomic Al–Al and M–M bonds.[4b, 59]

Electronic structures & chemical bonding of $CaAu_{3+x}Al_{1-x}$. From the conjecture and classification that $CaAu_{3+x}Al_{1-x}$ is a 1/0 CA of the $CaAu_{4.5-x}Al_{1.5+x}$ i-QC, atomic site preference and electronic structure conclusions obtained for the 1/0 CA may give insight about the i-QC as well. Therefore, although this chemical bonding discussion is specific for $CaAu_3Al$, some generalizations may also be applied to the $CaAu_{3+x}Al_{1-x}$ ($0 \le x \le 0.31(1)$) CA phase region and the $CaAu_{4.5-x}Al_{1.5+x}$ i-QC. However, having additional electronic structures and analysis of

other, higher-order CAs will enhance the correlation between all CAs and the i-QC. At present, therefore, we show results for the lowest order 1/0 CA only and an investigation on higher order CAs is still under way.

The calculated electronic structure and bonding analyses using COHP curves for $CaAu_3Al$ were carried out on the structure optimized using VASP. This exercise led to a 5.0% expansion of the room temperature, experimental unit cell volume, i.e., from 745.1(1) Å^3; $a =$ 9.0656(8) Å to 783.23 Å^3; $a = 9.21784$ Å (see Table S7) with no significant changes in atomic positions and which is 0.08(2) eV/formula unit lower in energy than the experimental structure. The corresponding electronic DOS and selected COHP curves are illustrated in Figure 5.

According to the polar intermetallic description of $CaAu_3Al$, the electronegative metals Au and Al (Pearson $EN_{Au} = 5.77$ eV, $EN_{Al} = 3.23$ eV)[60] form [Au_3Al] tetrahedral clusters that surround the formally electropositive Ca atoms ($EN_{Ca} = 2.2$ eV)[60] by 16-atom Frank-Kasper polyhedra. These Ca atoms formally donate their two 4s valence electrons to the [Au_3Al] clusters and utilized virtual ("empty") 3d orbitals for electronic "back donation" from the same [Au_3Al] clusters via Au 5d and Al 3p orbitals. The DOS and COHP curves (Figures 5, S5, and S6) support this concept of polar intermetallic bonding in $CaAu_3Al$ by showing Ca 3d orbital contributions below the Fermi level (E_F), engaging in bonding interactions mainly with Au atoms, e.g., via 3d–5d interactions, as well as increasing contributions just above E_F. The broad band in the DOS that is ~2.5 to ~6.5 eV below E_F arises primarily from the 5d orbitals of the Au atoms. The Au–Au COHP curves indicate that this large band corresponds to Au–Au bonding interactions at lower energies of the bands and Au–Au antibonding interactions at the higher energies of the bands, although the antibonding overlap is mediated by 6s,6p–6s,6p
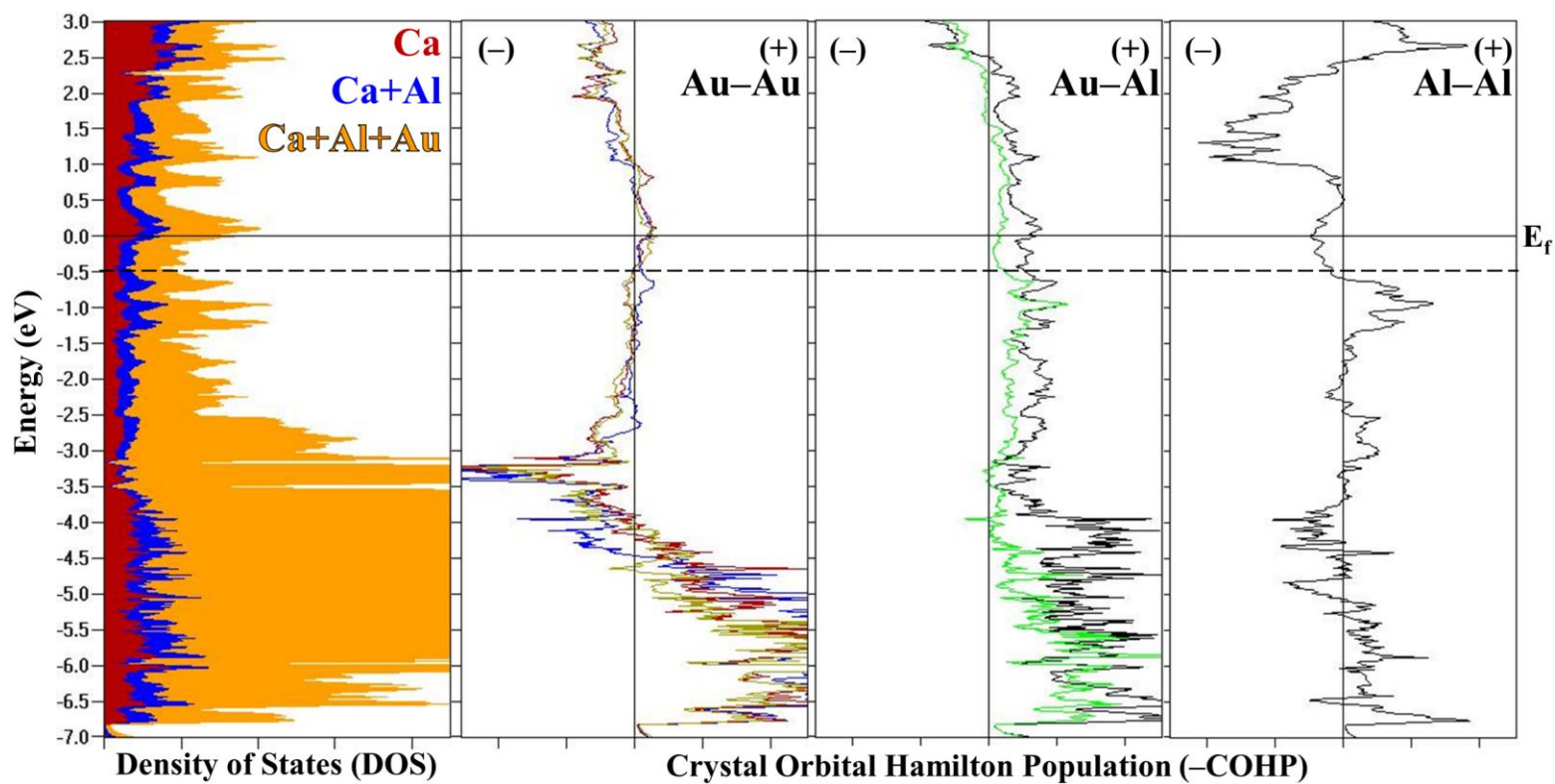
Figure 5. DOS and Au–Au, Au–Al, and Al–Al COHP curves for CaAu$_3$Al after VASP optimization. DOS curves include partial atomic orbital contributions. For all COHP curves, (–) indicates antibonding and (+) indicates bonding and are each plotted for a single interaction. Au–Au COHP curves are for distances: 2.879 Å (blue), 3.123 Å (red) and 3.145 Å (green). Au–Al COHP curves are for distances: 2.590 Å (black) and 2.797 Å (green). Al–Al COHP curve is for distance 3.197 Å (black). The dashed line indicates the experimentally refined CaAu$_{3.31(1)}$Al$_{0.69}$ ($x = 0.31(1)$) composition with maximal Au substitution at the Al/Au 8c site.

interactions to give net Au–Au bonding. In addition, Au–Al and Ca–Au interactions are bonding throughout this 4-eV wide Au $5d$ band.

The DOS curve around the calculated Fermi level (0 eV in Figure 5) of $CaAu_3Al$ shows numerous peaks and valleys (pseudogaps) but no distinctive gaps, as would be anticipated for Zintl-type valence structures. In fact, E_F falls just below a ~0.4 eV wide peak and just above a ~0.5 eV wide valley (pseudogap) in the DOS. Other Au-rich compounds, for instance in the Sr–Au–Al system, also feature E_F just below or above a pseudogap.[7] In isotypic $AgPd_3Se$, for which no corresponding QC has been reported, the E_F is in a pseudogap.[57] However, in isotypic and isoelectronic $CaAu_3Ga$, for which a corresponding i-QC has been identified, the E_F falls in between a pseudogap and a peak in the DOS.[27a] Similarly herein, an i-QC has been identified near to the composition of $CaAu_3Al$. The peak just above E_F corresponds to a band crossing at the Γ point arising primarily from the Ca $3d$ orbitals (see Figure S4 for band structure details).

Further information can be extracted by examining the various COHP curves for $CaAu_3Al$. Figure 5 includes those for significant Au−Au, Au−Al, and Al−Al contacts; those for Ca−Au, Ca−Al, and Ca−Ca contacts are found in Figure S6. As mentioned above, all Au−Au COHP curves show bonding/antibonding interactions within mostly the $5d$ region of the DOS. Near E_F, however, these Au−Au interactions are essentially nonbonding. The Au−Al interactions are weakly bonding around E_F, eventually becoming antibonding ~2.5 eV above E_F. The Al−Al contact reveals orbital interactions that oscillate between bonding and antibonding, falling within an antibonding level at the Fermi level. Lastly, all orbital interactions with Ca atoms are weakly bonding throughout the occupied states, with the strongest interactions being Ca−Au. Indeed, total integrated COHP (ICOHP) values show that, for interactions up to 3.5 Å, 44.8% of all interactions are attributed to Au–Al bonding, followed

by Ca–Au (25.4%), Au–Au (22.3%), Ca–Al (5.1%), Al–Al (2.0%), and Ca–Ca (0.4%). These general percentages further support representing $CaAu_3Al$ as a structure that maximizes the number of heteroatomic Au–Al contacts.

The observed phase width of $CaAu_{3+x}Al_{1-x}$ ($0 \leq x \leq 0.31(1)$) can also be rationalized from some of the subtle features of the Au–Au and Al–Al COHP curves. On increasing the Au content from stoichiometric $CaAu_3Al$, the number of valence electrons would decrease by replacing 3-valent Al atoms with monovalent Au atoms. Lowering the valence electron count, however, would reduce the number of bonding electrons for many interactions, viz., Au–Al, Ca–Au, and Ca–Al contacts. However, antibonding Al–Al states would be depleted. In the Al–Al COHP curve, there is a sharp transition between antibonding and bonding states at ~0.5 eV below E_F, which corresponds to a valence electron count of 37.5 e^-/formula unit, or "$CaAu_{3.25}Al_{0.75}$", corresponding to an estimated maximum x of 0.25. This estimate agrees with the experimental data in which loadings for both $x = 0.35(4)$ and $0.25(4)$ yielded single crystals with $x \leq 0.31(1)$ although "phase-pure" $CaAu_{3+x}Al_{1-x}$ can only be obtained from loading of x up to 0.25(4). On the other hand, increasing the valence electron count could conceivably occur until Au–Au antibonding interactions occur, which are seen at ~0.75 eV above E_F, or a valence electron count of 38.75 e^-/formula unit, or "$CaAu_{2.62}Al_{1.38}$". However, this would entail occupying Al–Al antibonding states. Loadings of negative x beyond –0.3(4), for instance $x =$ –0.15(4) (VEC = 1.40 e^-/atom) however, yielded a different unknown phase so that $CaAu_3Al$ is the end-member of the $CaAu_{3+x}Al_{1-x}$ phase. Therefore, the structural stability of the $CaAu_{3+x}Al_{1-x}$ phase utilizes heteroatomic Au–Al and Ca–Au interactions, but the phase width can be attributed to subtle bonding effects involving the homoatomic Au–Au and Al–Al interactions.

Although no electronic structure calculations were carried out for the $CaAu_{4.5-x}Al_{1.5+x}$ i-QC, we speculate that maximizing the number of Au–Al contacts will also be an important bonding feature of this phase.

$CaAu_{3+x}Al_{1-x}$ as an i-QC "crystalline approximant". Recent reports of isotypic $CaAu_{3+y}Ga_{1-y}$ ($0 \leq y \leq 0.13$)[27a] and $AgPd_3Se$[57] discuss at length the rhombohedra formed by the Ag and Ca atoms, respectively, and these features are also present in $CaAu_{3+x}Al_{1-x}$. Regarding potential relationships to icosahedral quasicrystals, the golden rhombohedron, which has geometric features involving the golden mean $\tau \approx 1.618$, are important building blocks that can fill space without rational translational symmetry, while possessing crystallographically incompatible local 5-fold symmetry. Similarly, i-QCs possess long-range structural order—as demonstrated by observable sharp diffraction peaks—but lack the translational symmetry found in crystals because of its icosahedral symmetry.[61]

Rhombohedral features in the 1/0 CA are observed along the body diagonals of the cubic unit cell. Figure 6a shows a $[Au_{12}(Al/Au)_8]$ prolate rhombohedron, which is comprised of 8 Al/Au atoms at the vertices and 12 Au atoms bisecting the edges, and that interpenetrates a $[Ca_8]$ oblate rhombohedron. Each $[Au_{12}(Al/Au)_8]$ prolate rhombohedron shares its faces with six other oblate $[Au_{12}(Al/Au)_8]$ rhombohedra that cross into adjacent unit cells. Likewise, each $[Ca_8]$ oblate rhombohedron shares faces with six $[Ca_8]$ prolate rhombohedra from adjacent unit cells. Figure 6c shows the two sets of $[Au_{12}Al_8]$ and $[Ca_8]$ rhombohedra that, when juxtaposed, form the unit cell of interpenetrating rhombohedra (seen in Figure 6a).

Between two adjacent $[Au_{12}(Al/Au)_8]$ rhombohedra and bisecting their edges is a distorted $[Ca_4Au_6Al_2]$ icosahedron, which is the local icosahedral environment around the $24d$ Au site (Figure 2, middle image; also Figure 6b). For every pair of one oblate plus one prolate

84
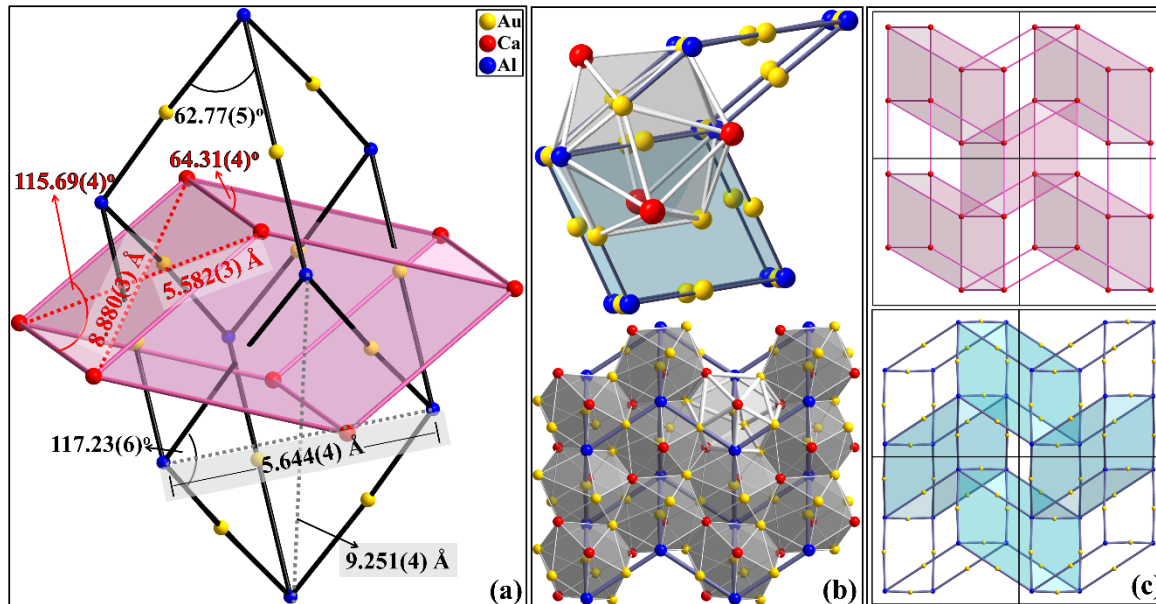
Figure 6. (a) Rhombohedral geometric features as related to the golden rhombohedron. (b) Oblate and prolate rhombi form the skeleton for icosahedra packing (c) Space-filling rhombohedra of Au and Al (blue; bottom) and Ca (red; above) that, when juxtaposed, gives rise to the interpenetrating rhombohedra in (a).

rhombohedra, there are six distorted [Ca$_4$Au$_6$Al$_2$] icosahedra packed by sharing [CaAuAl] triangular faces. Distorted icosahedra are an important component of CAs to i-QCs because they offer a group-subgroup relationship to the $m\overline{3}\overline{5}$ (or I_h) icosahedral symmetry that is incompatible with crystallinity and possessed by i-QCs. In CaAu$_3$Al, the geometric distortion and atomic decorations allow the {[Ca$_4$Au$_6$Al$_2$]@Au} icosahedron to possess C_1 point symmetry. Also, due to the distortion, subunits of [Ca$_4$Au$_6$Al$_2$] icosahedra pack the unit cell (Figure 6b) by sharing [CaAuAl] triangular faces and [CaAu] edges while leaving [CaAu$_2$Al] tetrahedra as voids.

Space-filling rhombohedra in CaAu$_{3+x}$Al$_{1-x}$ exhibit many geometric similarities to the "golden rhombohedra" of the Ammann 3D packing model[62] that fill space in the absence of translational symmetry and exhibit local 5-fold symmetry. Each [Au$_{12}$Al$_8$] prolate rhombus has internal angles of 62.77(5)° and 117.23(6)° (Figure 6a) and a ratio of its rhombic diagonals (9.251(4) Å/5.644(4) Å = 1.639(4)) that is similar to τ ≈ 1.618. In the "golden rhombohedra",
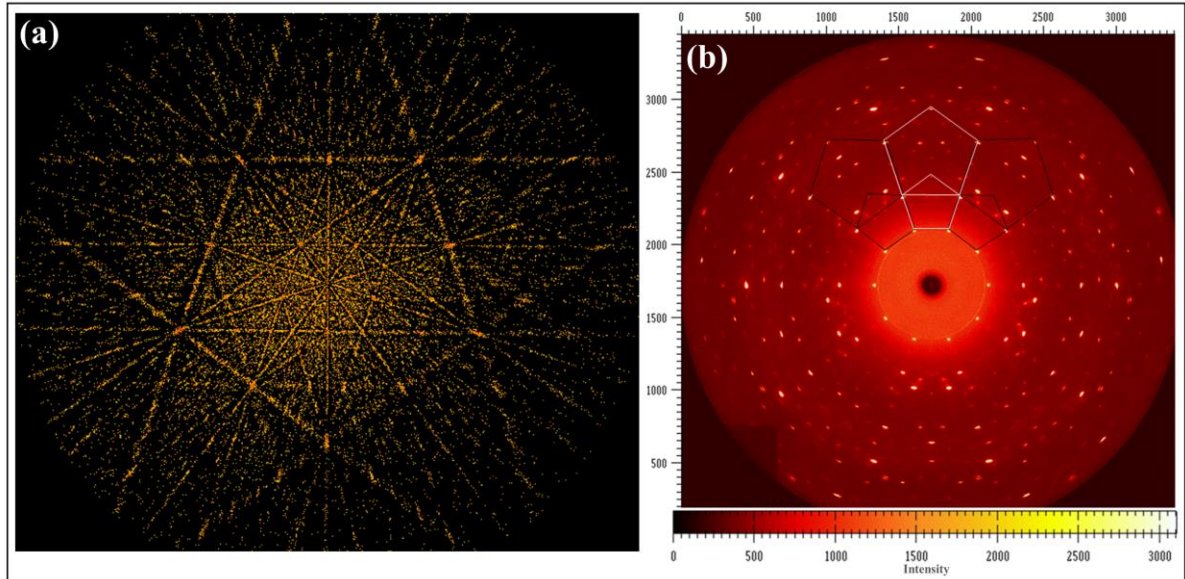
Figure 7. "Single-crystal X-ray diffraction patterns of "CaAu$_{4.4}$Al$_{1.6}$" collected from: (a) conventional single-crystal XRD and (b) high-energy XRD at the APS.

the ratio between two diagonals of a rhombic face is the golden mean, so that these faces have internal angles of $63.435\cdots°$ $\left(=2\arctan\left(\frac{1}{\tau}\right)\right)$ and $116.565\cdots°$ $(=2\arctan(\tau))$. In the 1/0 CA, rhombohedra fill space compatibly with rational translational symmetry, i.e., the rhombohedra are not "golden rhombohedra," and the icosahedral geometry is distorted significantly due to atomic decorations and interatomic distances, hence making CaAu$_{3+x}$Al$_{1-x}$ an "approximant" of an "icosahedral phase".

The classification of CaAu$_{3+x}$Al$_{1-x}$ ($0 \leq x \leq 0.31(1)$) as the 1/0 crystalline approximant phase of an i-QC extends beyond packing of rhombohedra and icosahedra. From the lattice parameters and structural motifs of previously reported 1/1 and 2/1 CAs and their associated i-QCs, the low order 1/0 CA would have an approximate cubic lattice parameter of 8–10 Å. Using the relationship between the quasilattice constant a_{QC} and the lattice constant of the 1/0 CA phases, $a_{1/0} = 9.0766(5)$–$9.1261(8)$ Å for CaAu$_{3+x}$Al$_{1-x}$ ($0 \leq x \leq 0.31(1)$), a_{QC} is estimated to be in the range $5.336(2)$–$5.354(2)$ Å (Table S8). The experimentally determined quasilattice parameter of the sample loaded as 14.43% Ca: 63.30% Au: 22.27% Al "CaAu$_{4.4}$Al$_{1.6}$" i-QC

(sample α in Figure 1) is 5.384(4) Å (see "i-QC Characterization" section), which differs by 0.60–0.90% from the estimated quasilattice range.

However, not all compounds possessing the structure adopted by $CaAu_{3+x}Al_{1-x}$ are classified as 1/0 CAs. For instance, $AgPd_3Se$ and $NaAu_3Ge/Si$ are not yet considered CAs because a corresponding i-QC has not been shown to exist in the Ag–Pd–Se and Na–Au–Ge/Si systems to date.[55, 57]

i-QC characterization. The initial conjecture for the discovery of an i-QC came from single-crystal diffraction data (e.g., see Figures 7a and S8) that could not be indexed following conventional strategies for periodic structures (Figure S8). Then, a reanalysis of the PXRD patterns (Figure 1), which show marking resemblances to previously reported i-QCs (e.g., see refs 9 or 24), provided further indication to classify the loaded compositions $CaAu_{4.5-x}Al_{1.5+x}$ ($0.11 \leq x \leq 0.40(6)$) as an i-QC phase. Further characterization was performed using high-energy X-ray diffraction.

Figure 7b is the zero-level, high-energy precession pattern of an i-QC along the 5-fold direction extracted from the loaded composition 14.43% Ca: 63.30% Au: 22.27% Al ("$CaAu_{4.4}Al_{1.6}$") (sample α in Figure 1 and sample 9C in EDS spectra Figure S2, Table S4) and collected on station 6-ID-D at the Advanced Photon Source in Argonne National Laboratory. In addition to peaks on the zero-level, faint peaks from one level above and one level below are also observed. Self-similarity, a fundamental characteristic of QCs, is illustrated by inflation of the 5-fold rotational symmetry expanding outward from the center of the diffraction pattern.

Diffuse scattering in the pattern where the spots appear "smeared" suggests the presence of phason strain, which in this case can arise from "mistakes" in the tiling.[63] The

result is a broadening of Bragg peaks, as evident in the PXRD patterns of the i-QC phase observed herein (Figure 1). Phason strain is common, suggesting atomic structural rearrangement, and has been reported in other polar intermetallic quasicrystals such as the Na–Au–Ga i-QC.[9]

Within the same sample batch loaded as 14.43% Ca: 63.30% Au: 22.27% Al ("CaAu$_{4.4}$Al$_{1.6}$") (sample α in Figure 1 and sample 9C in EDS spectra Figure S2, Table S4), other randomly selected "crystals" yielded diffraction patterns with even more diffuse scattering and some additional peaks along the 3-fold direction of the 2-fold image. These additional peaks suggest that these crystals may be "higher-order" CAs. Hence, the CaAu$_{4.4}$Al$_{1.6}$ sample may contain both a higher-order CA as well as the i-QC, even though conventional PXRD shows what appears to be a single phase i-QC with broadened peaks (Figure 1). The diffraction images included here (Figures 7b and 8) have less phason strain and more pronounced peaks than the samples suspected as "higher-order" CAs and these peaks can be accounted for by icosahedral symmetry, which verifies the sample as an i-QC.

After confirming the identity of the sample as an i-QC, to determine if the underlying quasilattice is primitive, body-centered, or face-centered requires examination of the sequence of diffraction spots in the 2-fold image, along the 3-fold and the 5-fold directions (Figure 8). Along the 5-fold direction of the 2-fold image, the ratio of distances between two sets of adjacent peaks follows a τ^3-scaling (i.e., 60.85 mm/140.55 mm = 4.29 $\approx \tau^3$), which is indicative of a primitive quasilattice (a face-centered quasilattice would feature τ-scaling of diffraction spots). A primitive quasilattice is common in many i-QCs with 2/1 and 1/1 Tsai-type CAs including the binary Yb–Cd and ternary Yb–Au–Al i-QCs.[14, 23] From this P-centering, it follows that the symmetry of the CaAu$_{4.4}$Al$_{1.6}$ i-QC can be designated as $Pm\overline{3}\overline{5}$.
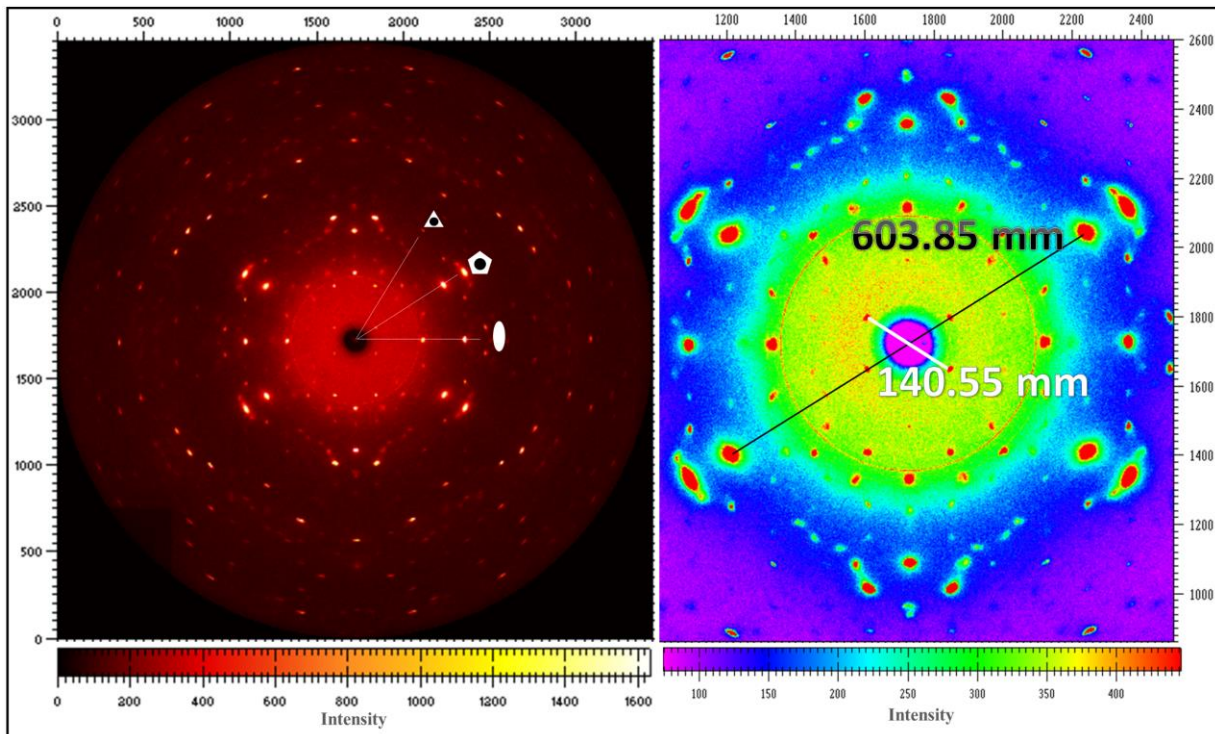
Figure 8. "CaAu$_{4.4}$Al$_{1.6}$" i-QC observed down the 2-fold direction. Left: 2-fold, 3-fold, and 5-fold rotational axes. Right: the ratio of adjacent peaks along any 5-fold provides the underlying quasilattice centering.

Also along the 2-fold image, the quasilattice constant, a_{QC}, can be evaluated to compare against the estimated value obtained from the relationship to the 1/0 CA phases. Following Cahn's indexing method[46] and after simulating the PXRD pattern from the 2-fold image, the quasilattice constant is determined to be $a_{QC} = 5.383(4)$ Å. The quasilattice constant physically represents the edge length of the rhombohedron that repeats in 3D space in an orderly but aperiodic fashion. For comparison, the edge lengths of the cubic CaAu$_3$Al rhombohedra are 5.418(4) Å (+0.64(7)% difference from the a_{QC}) and 5.244(3) Å (–2.61(8)% difference from the a_{QC}), respectively, for the [Au$_{12}$Al$_8$] and [Ca$_8$] rhombohedra (Figure 6). Additionally, the estimated a_{QC} using the cubic lattice of CaAu$_3$Al is 5.3354(1) Å, which is 0.88(7)% lower that the measured value (Table S8). Since the calculated range of quasilattice parameters from the cubic CA phase CaAu$_{3+x}$Al$_{1-x}$ ($0 \leq x \leq 0.31(1)$) closely agrees with the experimentally

determined quasilattice parameter from direct measurement, the relationship between the cubic and the i-QC phase further verifies the structure of the cubic phase as a 1/0 crystalline approximant of the i-QC.

Summary

The 1/0 cubic crystalline approximant phase $CaAu_{3+x}Al_{1-x}$ ($0 \leq x \leq 0.31(1)$); $a = 9.0766(5)–9.1261(8)$ Å; $Pa\bar{3}$ (#205); Pearson symbol $cP40$) along with its primitive icosahedral quasicrystalline parent $CaAu_{4.5-x}Al_{1.5+x}$ ($0.11 \leq x \leq 0.40(6)$); for $CaAu_{4.4}Al_{1.6}$ $a_{QC} = 5.383(4)$; $Pm\bar{3}\bar{5}$) were synthesized in the Ca-poor region of the Ca–Au–Al system using high temperature methods and characterized using powder and single-crystal X-ray diffraction. Based on total energy calculations of $CaAu_3Al$, the site preferences for Au and Al atoms are influenced by creating more Au–Al nearest neighbor atomic interactions over Al–Al or Au–Au interactions. As a CA to an i-QC, similar atomic site preferences and arrangements determined for $CaAu_3Al$ may also be found in the i-QC parent, although atomic site preference and electronic structure of additional, higher-order CAs will be necessary to draw stronger correlations. The cubic phase falls under the broader classification of a polar intermetallic compound, in which the electropositive Ca atoms engage in polar covalent bonding with the more electronegative Au and Al atoms, which fill the unit cell as a network of $[Au_{3-x}Al_{1+x}]$ tetrahedra forming Frank-Kasper polyhedra around each Ca atom. Based on precession high-energy single-crystal X-ray diffraction data of the i-QC, the quasilattice parameter is determined to be $a_{QC} = 5.383(4)$ Å, which is in close agreement to the edge lengths of the $[Au_{12}Al_8]$ and $[Ca_8]$ rhombohedra in cubic $CaAu_{3+x}Al_{1-x}$ and closely agrees with the predicted values ($a_{QC} = 5.336(2)–5.354(2)$) calculated from the lattice parameters ($9.0766(5)–9.1261(8)$

Å) of the 1/0 CA. From the ratios between peaks in the precession diffraction data, the quasicrystal is determined to adopt a primitive quasilattice and possess the symmetry $Pm\overline{3}\overline{5}$.

Supporting Information in APPENDIX B

Tables and figures of (1) loading and refined compositions for the 1/0 CA phase; (2) crystallographic refinement data of selected $CaAu_{3+x}Al_{1-x}$ specimens; (3) Fractional atomic coordinates and displacement (anisotropic and isotropic) parameters of selected $CaAu_{3+x}Al_{1-x}$ crystals and Hamilton test of the split versus full crystallographic models; (4) Scanning Electron Microscopy (SEM) images of $CaAu_{3.11(4)}Al_{0.89}$ and "$CaAu_{4.4}Al_{1.6}$"; (5) SEM-EDS spectra to determine elemental composition; (6) atomic percent breakdown estimates to confirm compositional results: $Ca_{1.0(1)}Au_{3.1(2)}Al_{0.9(1)}$ and $Ca_{1.0(1)}Au_{4.5(2)}Au_{1.4(1)}$; (7) juxtaposed observed and simulated Powder X-ray Diffraction patterns demonstrating phase purity; (8) tetrahedral star distances comparison with isotypic compounds; (9) six models examining total energies, frequency and distances of hetero- versus homoatomic interactions to understand Au and Al site preference; (10) structural relaxation parameters after optimization using VASP; (11) band structure of $CaAu_3Al$ showing band crossings at E_F at Γ; (12) PDOS breakdown according to elemental orbital contribution of Ca, Au, and Al; (13) COHP curves involving Ca showing overall weakly bonding character; (14) comparison of observed and calculated quasilattice calculated from the lattice parameters of the 1/0 CA phase; (15) resistivity measurements on selected crystals from $CaAu_{3.11(4)}Al_{0.89}$ and $CaAu_3Al$ samples indicating a poor metal; (16) quasicrystalline and crystalline raw "single-crystal" diffraction images demonstrating quasiperiodic peak arrangement that cannot be indexed using 3D crystallography in the quasicrystalline sample and periodic peak arrangement in the crystalline approximant sample.

Acknowledgements

References

(1) (a) Whangbo, M.-H.; Lee, C.; Köhler, J., Metal Anions in Metal-Rich Compounds and Polar Intermetallics. *European Journal of Inorganic Chemistry* **2011,** (26), 3841-3847; (b) Corbett, J. D., Exploratory Synthesis: The Fascinating and Diverse Chemistry of Polar Intermetallic Phases[††] This article is based on J. D. Corbett's address upon receipt of the 2008 American Chemical Society's F. Albert Cotton Award in Synthetic Inorganic Chemistry sponsored by the F. Albert Cotton Endowment Fund. *Inorganic Chemistry* **2009,** *49* (1), 13-28.

(2) (a) Hume-Rothery, W., edit: Uichiro Mizutani: Hume-Rothery Rules for Structurally Complex Alloy Phases. *J. Inst. Met.* **1926,** *36*, 295; (b) Mizutani, U., *Hume-Rothery Rules for Structurally Complex Alloy Phases*. CRC Press Taylor & Francis Group: Boca Raton **2010**.

(3) (a) Korber, N., Metal Anions: Defining the Zintl Border. *Zeitschrift für anorganische und allgemeine Chemie* **2012,** *638* (7-8), 1057-1060; (b) Zintl, E., Intermetallische Verbindungen. *Angewandte Chemie* **1939,** *52* (1), 1-6; (c) Corbett, J. D., Polyatomic Zintl anions of the post-transition elements. *Chemical Reviews* **1985,** *85* (5), 383-397.

(4) (a) Nesper, R., Bonding Patterns in Intermetallic Compounds. *Angewandte Chemie International Edition in English* **1991,** *30* (7), 789-817; (b) Miller, G. J. L., C.-S.; Choe, W., Structure and Bonding

Around the Zintl Border. In *Inorganic Chemistry Highlights*, Meyer, G., Naumann, D., Wesemann, L., Wiley-VCH: Wein-heim: Germany, **2002**; pp 21-53; (c) Corbett, J. D., In *Chemistry, Structure, and Bonding of Zintl Phases and Ions*, Kauzlarich, S. M., Ed. VCH: New York, **1996**; p 139.

(5) (a) Janot, C., *Quasicrystals: A Primer*, 2nd *ed.* Clarendon Press. Oxford, 1994; (b) Tsai, A. P., A test of Hume-Rothery rules for stable quasicrystals. *Journal of Non-Crystalline Solids* **2004**, *334–335* (0), 317-322.

(6) Nordell, K. J.; Miller, G. J., Linking Intermetallics and Zintl Compounds: An Investigation of Ternary Trielides (Al, Ga, In) Forming the $NaZn_{13}$ Structure Type. *Inorganic Chemistry* **1999**, *38* (3), 579-590.

(7) Palasyuk, A.; Grin, Y.; Miller, G. J., Turning Gold into "Diamond": A Family of Hexagonal Diamond-Type Au-Frameworks Interconnected by Triangular Clusters in the Sr–Al–Au System. *Journal of the American Chemical Society* **2014**, *136* (8), 3108-3117.

(8) Lin, Q.; Corbett, J. D., Development of an Icosahedral Quasicrystal and Two Approximants in the Ca−Au−Sn System: Syntheses and Structural Analyses. *Inorganic Chemistry* **2010**, *49* (22), 10436-10444.

(9) Smetana, V.; Lin, Q.; Pratt, D.; Kreyssig, A.; Ramazanoglu, M.; Corbett, J.; Goldman, A.; Miller, G., A sodium-containing quasicrystal: using gold to enhance sodium's covalency in intermetallic compounds. *Angewandte Chemie (International ed. in English)* **2012**, *51* (51), 12699-12702.

(10) Honma, T.; Ishimasa, T., New icosahedral quasicrystals formed in Cu-based ternary alloys. *Philosophical Magazine* **2007**, *87* (18-21), 2721-2726.

(11) (a) Bak, P., Icosahedral crystals: Where are the atoms? *Physical Review Letters* **1986**, *56* (8), 861-864; (b) Steurer, W.; Deloudi, S., Fascinating quasicrystals. *Acta Crystallographica Section A* **2008**, *64* (1), 1-11; (c) Steurer, W., Quasicrystals–A Paradigm Shift in Crystallography? *Chimia* **2014**, *68* (1-2), 45-48.

(12) Yamamoto, A., Software package for structure analysis of quasicrystals. *Science and Technology of Advanced Materials* **2008**, *9* (1), 013001.

(13) (a) Hans-Ude Nissen, C. B., Electron Microscopy and Surface Investigation of Quasicrystals. In *Quasicrystals: An Introduction to Structure, Physical Properties, and Applications*, J.-B. Suck, M. S., P. Haussler, Ed. Springer-Verlag Berlin Heidelberg: New York, 2002; pp 115-166; (b) Steinhardt, P. J.; Jeong, H. C.; Saitoh, K.; Tanaka, M.; Abe, E.; Tsai, A. P., Experimental verification of the quasi-unit-cell model of quasicrystal structure. *Nature* **1998**, *396*, 55.

(14) Takakura, H.; Gomez, C. P.; Yamamoto, A.; De Boissieu, M.; Tsai, A. P., Atomic structure of the binary icosahedral Yb-Cd quasicrystal. *Nat Mater* **2007**, *6* (1), 58-63.

(15) Janssen, T., Crystallography of quasi-crystals. *Acta Crystallographica Section A* **1986**, *42* (4), 261-271.

(16) (a) Janot, C., The Crystallography of Quasicrystals. *Proceedings: Mathematical and Physical Sciences* **1993**, *442* (1914), 113-127; (b) Yamamoto, A., Crystallography of Quasiperiodic Crystals. *Acta Crystallographica Section A* **1996**, *52* (4), 509-560.

(17) (a) Abe, E.; Yan, Y.; Pennycook, S. J., Quasicrystals as cluster aggregates. *Nat Mater* **2004,** *3* (11), 759-767; (b) Steurer, W., Why are quasicrystals quasiperiodic? *Chemical Society Reviews* **2012,** *41* (20), 6719-6729.

(18) Bergman, G.; Waugh, J. L. T.; Pauling, L., The crystal structure of the metallic phase $Mg_{32}(Al, Zn)_{49}$. *Acta Crystallographica* **1957,** *10* (4), 254-259.

(19) (a) Mackay, A., A dense non-crystallographic packing of equal spheres. *Acta Crystallographica* **1962,** *15* (9), 916-918; (b) Mackay, A. L., Crystallography and the Penrose pattern. *Physica A: Statistical Mechanics and its Applications* **1982,** *114* (1–3), 609-613; (c) Mackay, A. L., Icosahedra in aluminium/ manganese alloy. *Nature* **1985,** *315* (6021), 636-636.

(20) Tsai, A.-P., "Back to the Future" − An Account Discovery of Stable Quasicrystals. *Accounts of Chemical Research* **2002,** *36* (1), 31-38.

(21) Goldman, A. I.; Kelton, R. F., Quasicrystals and crystalline approximants. *Reviews of Modern Physics* **1993,** *65* (1), 213-230.

(22) Gratias, D.; Katz, A.; Quiquandon, M., Geometry of approximant structures in quasicrystals. *Journal of physics. Condensed matter* **1995,** *7* (48), 9101-9125.

(23) Ishimasa, T.; Tanaka, Y.; Kashimoto, S., Icosahedral quasicrystal and 1/1 cubic approximant in Au–Al–Yb alloys. *Philosophical Magazine* **2011,** *91* (33), 4218-4229.

(24) (a) Elser, V.; Henley, C. L., Crystal and quasicrystal structures in Al-Mn-Si alloys. *Physical Review Letters* **1985,** *55* (26), 2883-2886; (b) Cooper, M.; Robinson, K., The crystal structure of the ternary alloy α(AlMnSi). *Acta Crystallographica* **1966,** *20* (5), 614-617.

(25) Krajčí, M.; Windisch, M.; Hafner, J.; Kresse, G.; Mihalkovič, M., Atomic and electronic structure of icosahedral Al-Pd-Mn alloys and approximant phases. *Physical Review B* **1995,** *51* (24), 17355-17378.

(26) Windisch, M.; Krajci, M.; Hafner, J., Electronic structure in icosahedral AlCuLi quasicrystals and approximant crystals. *Journal of Physics: Condensed Matter* **1994,** *6* (35), 6977.

(27) (a) Lin, Q.; Corbett, J. D., Interpenetrating Networks of Three-Dimensional Penrose Tiles in $CaAu_3Ga$, the Structurally Simplest Cubic Approximant of an Icosahedral Quasicrystal. *Inorganic Chemistry* **2008,** *47* (9), 3462-3464; (b) Lin, Q.; Corbett, J. D., Approximant Phases and an Icosahedral Quasicrystal in the Ca−Au−Ga System: The Influence of Size of Gallium versus Indium. *Inorganic Chemistry* **2008,** *47* (17), 7651-7659.

(28) Tsai, A.-P.; Inoue, A.; Masumoto, T., A Stable Quasicrystal in Al-Cu-Fe System. *Japanese Journal of Applied Physics* **1987,** *26* (9A), L1505.

(29) Guo, J. Q.; Abe, E.; Tsai, A. P., Stable Cd-Mg-Yb and Cd-Mg-Ca icosahedral quasicrystals with wide composition ranges. *Philosophical Magazine Letters* **2002,** *82* (1), 27-35.

(30) Guo, J. Q. A., E.; Tsai, A.P., Stable icosahedral quasicrystals in binary Cd-Ca and Cd-Yb systems. *Physical review. B, Condensed matter* **2000,** *62* (22), R14605.

(31) Alan, I. G.; Tai, K.; Andreas, K.; Anton, J.; Mehmet, R.; Kevin, W. D.; Sergey, L. B. k.; Paul, C. C., A family of binary magnetic icosahedral quasicrystals based on rare earths and cadmium. *Nature Materials* **2013**, *12* (8), 714-718.

(32) Steurer, W., On a Realistic Growth Mechanism for Quasicrystals. *Zeitschrift für anorganische und allgemeine Chemie* **2011,** *637* (13), 1943-1947.

(33) Kraus, W.; Nolze, G., PowderCell - a program for the representation and manipulation of crystal structures and calculation of the resulting X-ray powder patterns. *Journal of Applied Crystallography* **1996,** *29* (3), 301-303.

(34) Roisnel, J. R.-C. T., *Full*Prof.*98 and WinPLOTR: New Windows 95/NT Applications for Diffraction Commission for Powder Diffraction, International Union for Crystallography,* **1998**.

(35) Holland, T. J. B.; Redfern, S. A. T., Unit cell refinement from powder diffraction data; the use of regression diagnostics. *Mineralogical Magazine* **1997,** *61* (1), 65-77.

(36) Rietveld, H., A profile refinement method for nuclear and magnetic structures. *Journal of Applied Crystallography* **1969,** *2* (2), 65-71.

(37) *Jana2006*, Petricek, V., Dusek, M. & Palatinus, L.: **2014**.

(38) *SMART*. version 5 ed.; Bruker AXS: Madison, WI, **2003**.

(39) Blessing, R., An empirical correction for absorption anisotropy. *Acta Crystallographica Section A* **1995,** *51* (1), 33-38.

(40) Sheldrick, G. M. *SADABS*, University of Gottingen: Gottingen, Germany, **2001**.

(41) STOE & Cie GmbH *Stoe . X-SHAPE, X-RED, and X-AREA*, Darmstadt, Germany, **2006**.

(42) Sheldrick, G., *SHELX*. version 6.14 ed.; Bruker AXS: Madison, WI, **2000-2003**.

(43) Momma, K.; Izumi, F., VESTA 3 for three-dimensional visualization of crystal, volumetric and morphology data. *Journal of Applied Crystallography* **2011,** *44* (6), 1272-1276.

(44) Brandenburg, K., *Diamond*. version 3.2i ed.; Crystal Impact Gbr: Bonn, Germany, **2011**.

(45) Goldman, A. I.; Kreyssig, A.; Nandi, S.; Kim, M. G.; Caudle, M. L.; Canfield, P. C., High-energy X-ray diffraction studies of i-Sc12Zn88. *Philosophical Magazine* **2011,** *91* (19-21), 2427-2433.

(46) Cahn, J. W.; Shechtman, D.; Gratias, D., Indexing of icosahedral quasiperiodic crystals. *Journal of Materials Research* **1986,** *1* (01), 13-26.

(47) Hammersley, A. P. *FIT2D V9.129* **1998**.

(48) (a) Blöchl, P. E., *Phys. Rev. B* **1994,** *50*, 17953; (b) Kresse, G.; Hafner, J., *Phys. Rev. B* **1993,** *47*, 558; (c) Kresse, G.; Furthmüller, F., *Comput. Mater. Sci.* **1996,** *6*, 15.

(49) Perdew, J. P.; Burke, K.; Ernzerhof, M., Generalized Gradient Approximation Made Simple. *Phys. Rev. Lett.* **1996,** *77*, 3865.

(50) Aroyo, E. K. *WYCKSPLIT*: a computer program for determination of the relations of Wyckoff positions for a group-subgroup pair. *J. Appl. Cryst.* **1998,** *31*, 646.

(51) Jepson, O. B., A.; Andersen, O.K., *The Program TB-LMTO-ASA,4.7;* **1999,** *Max-Planck-Institut für Festkörperforschung, Stuttgart, Germany*.

(52) (a) Barth, U. v.; Hedin, L., A local exchange-correlation potential for the spin polarized case. i. *Journal of Physics C: Solid State Physics* **1972,** *5* (13), 1629; (b) Koelling, D. D.; Harmon, B. N., A technique for relativistic spin-polarised calculations. *Journal of Physics C: Solid State Physics* **1977,** *10* (16), 3107.

(53) Lambrecht, W. R. L.; Andersen, O. K., Minimal basis sets in the linear muffin-tin orbital method: Application to the diamond-structure crystals C, Si, and Ge. *Physical Review B* **1986,** *34* (4), 2439-2449.

(54) Dronskowski, R.; Bloechl, P. E., Crystal orbital Hamilton populations (COHP): energy-resolved visualization of chemical bonding in solids based on density-functional calculations. *The Journal of Physical Chemistry* **1993,** *97* (33), 8617-8624.

(55) Doering, W.; Schuster, H.-U., Preparation and structure of NaAu3Si and NaAu3Ge. *Zeitschrift für Naturforschung. Teil b, Anorganische Chemie, organische Chemie* **1980,** *35B* (11), 1482.

(56) Hume-Rothery, W. R., G. V., *The Structure of Metals and Alloys. 1st ed.* Institute of Metals, London, **1936**.

(57) Laufek, F.; Vymazalová, A.; Chareev, D. A.; Kristavchuk, A. V.; Lin, Q.; Drahokoupil, J.; Vasilchikova, T. M., Crystal and electronic structure study of AgPd3Se. *Journal of Solid State Chemistry* **2011,** *184* (10), 2794-2798.

(58) Hamilton, W., Significance tests on the crystallographic R factor. *Acta Crystallographica* **1965,** *18* (3), 502-510.

(59) Nordell, K., Exploring aluminum-rich intermetallics with experiment and theory (aluminides, gold, trielides). Dissertation. Iowa State University. **1997**.

(60) Pearson, R. G., Absolute electronegativity and hardness: application to inorganic chemistry. *Inorganic Chemistry* **1988,** *27* (4), 734-740.

(61) Ogawa, T., Three-dimensional Penrose transformation and the ideal quasicrystals. **1986**.

(62) (a) Senechal, M., Donald and the Golden Rhombohedra. *The Coxeter Legacy* **2006,** *AMS Fields, Providence*; (b) Senechal, M., The Mysterious Mr. Ammann. *The Mathematical Intelligencer* **2004,** *26* (4), 10-21.

(63) Socolar, J. E.; Socolar, J. E. S., Phason Strain in Quasicrystals. *Journal de physique. Colloque* **1986,** *47* (C3), C3-C3-226.

CHAPTER 5

FROM QUASICRYSTALS TO CRYSTALS WITH INTERPENETRATING ICOSAHEDRA IN Ca–Au–Al: IN-SITU VARIABLE-TEMPERATURE TRANSFORMATION

Modified from a manuscript submitted (09/2017) to *Journal of the American Chemical Society*

Joyce Pham,[†] Fanqiang Meng,[§] Matthew J. Lynn,[§] Tao Ma,[§] Andreas Kreyssig,[§,‡] Matthew J. Kramer,[§] Alan I. Goldman,[§,‡] and Gordon J. Miller,[,†,§]*

[†]Departments of Chemistry, and [‡] Physics and Astronomy, Iowa State University, [§]U.S. Department of Energy, Ames Laboratory, Ames, Iowa, 50011–3111
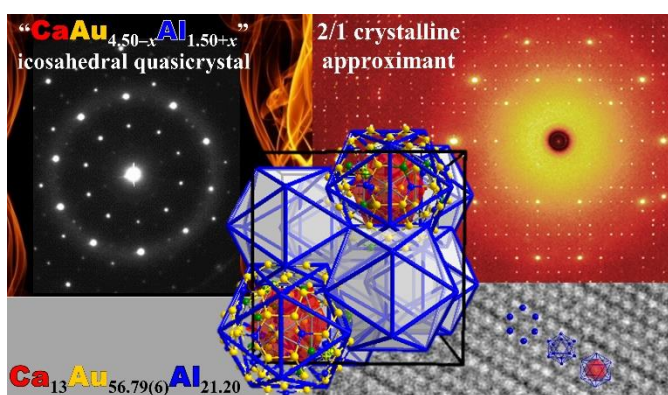
Abstract

The irreversible transformation from an icosahedral quasicrystal (i-QC) $CaAu_{4.39}Al_{1.61}$ to its cubic 2/1 crystalline approximant (CA) $Ca_{13}Au_{56.79(6)}Al_{21.20}$ ($CaAu_{4.37(1)}Al_{1.63}$, $Pa\bar{3}$ (No. 205); Pearson symbol: $cP728$; $a = 23.8918(2)$), starting at ~570 °C and complete by ~650 °C, is discovered from *in-situ*, high-energy, variable-temperature powder X-ray diffraction (PXRD), thereby providing direct experimental evidence for the relationship between QCs and their associated CAs. The new cubic phase crystallizes in a Tsai-type approximant structure under the broader classification of polar intermetallic compounds, in which atoms of different electronegativities, viz., electronegative Au + Al vs. electropositive Ca, are arranged in concentric shells. From a structural chemical perspective, the outermost shell of this cubic approximant may be described as interpenetrating and edge-sharing icosahedra, a perspective

that is obtained by splitting the traditional structural description of this shell as a 92-atom rhombic triacontahedron into an 80-vertex cage of primarily Au [$Au_{59.94(2)}Al_{17.07}\square_{3.00}$] and an icosahedral shell of only Al [$Al_{10.5}\square_{1.5}$], in which $\square$ represents the structural voids. Following the proposal that the cubic 2/1 CA approximates the structure of the i-QC and based on the observed transformation, an atomic site analysis of the 2/1 CA, which shows a preference to maximize the number of heteroatomic Au–Al nearest neighbor contacts over homoatomic Al–Al contacts, implies a similar outcome for the i-QC structure. Analysis of the most intense reflections in the diffraction pattern of the cubic 2/1 CA that changed during the phase transformation shows correlations with icosahedral symmetry and the stability of this cubic phase is assessed using valence electron counts. According to electronic structure calculations, a cubic 1/1 CA, "$Ca_{24}Au_{88}Al_{64}$" ($CaAu_{3.67}Al_{2.67}$) is proposed.

Introduction

From the conventional classification of solids using symmetry and atomic arrangements in real space, quasicrystals (QCs) occur between disordered amorphous materials and ordered, periodic crystalline solids because they are well-ordered but aperiodic, arising from their short-range, "crystallographically incompatible" five-, seven-, eight-, or higher-order rotational symmetry.[1] The periodicity of crystalline solids is exploited for diffraction analyses and structural determinations, whereas analogous 3-dimensional (3D) crystallographic analysis is unable to achieve a similar level of characterization for most QCs. Of the known QC classes, icosahedral QCs (i-QCs) form one of the most complex ones because icosahedral symmetry results in quasiperiodicity in 3D space unlike, for instance, decagonal QCs, which are quasiperiodic only in 2D and have been structurally described as stackings of quasiperiodic layers or quasiperiodic packings of overlapping columnar clusters.[2] The

predominance of i-QCs over the other QC classes seemingly correlates with the predominance of the 12-atom pseudo-icosahedral local environments within many complex intermetallic compounds, and the complexity of i-QCs, especially among multinary systems, suggests the need for more structural research.[3] Crystalline phases that are nearby in composition to corresponding QCs are coined "crystalline approximants" (CAs) because they are proposed to approximate the structures of related i-QCs, and are good starting points for study.[4]

There are three primary cubic CA classifications that are typically represented as clusters of concentric shells[5]: Mackay-,[6] Bergman-,[7] and Tsai-types,[8] with the two latter types more commonly observed. The Mackay-type features three shells with icosahedra as the inner and outermost shells and a 30-atom icosidodecahedron as the second, middle shell. The Bergman-type is similar to the Mackay-type but has a dodecahedron as the second shell and a 60-atom Buckminsterfullerene-type truncated icosahedron as an additional fourth shell. The Tsai-type mostly resembles the Bergman-type, but contains disordered tetrahedral clusters as the innermost shell and an icosidodecahedral fourth shell of atoms. Recent literature represents the fifth outermost shell of Tsai-type CAs as a 92-atom rhombic triacontahedron with rhombohedra between these triacontahedral clusters.[2b, 4c, 9]

A given CA is close in chemical composition to a related QC and is proposed to approximate the local atomic structure of the QC, a conjecture that has become universally accepted since the discovery of the first Mn–Al i-QC and its associated CAs.[4a, 4b] Even results from electronic structure calculations, valence electron concentrations (VECs), and metallic radius ratios are used to establish relationships among various CAs and identify some features important for bonding and stability of related QCs.[10] As part of the conjecture that CA phases are "approximate phases" of QCs, CAs are classified by a rational order "*L/S*," which is a ratio

of two consecutive numbers in the Fibonacci sequence. The *L/S* CA lattice constant ($a_{L/S}$)

relates to the quasilattice constant (a_{QC}) of the QC and the golden mean ($\tau = \left(\frac{1+\sqrt{5}}{2}\right) = 1.618...$)

following Equation (1),[4a] so that the higher the CA *L/S* order, the closer is its relationship to

the QC.

$$a_{QC} = \frac{a_{L/S}(2 + \tau)^{1/2}}{2(S + L\tau)} \qquad (1)$$

In general, Bergman- and Tsai-type approximants are more commonly observed and

their cubic 2/1 CAs are the highest order cases thus far reported with structural details. The

majority of cubic CA structural reports are for the order 1/1. Additionally, Tsai-type CAs

usually occur for i-QCs with primitive quasilattices, instead of body (I)- or face(F)-centered

quasilattices, as in the Yb–Au–Al,[9b] (Yb/Ca)–Cd,[8, 11] and Yb–Ag–In[12] systems.

One means of classifying QCs and CAs from a chemical perspective utilizes VEC,

which is also expressed as an e/a ratio and counts only the total number of valence *s* and *p*

electrons in a chemical formula divided by the number of atoms. In this prescription, valence

d and *f* electrons are ignored because either they contribute very little toward chemical bonding

and cohesion, or their respective bands are filled. Many QCs are found with *e/a* values ranging

from ~1.75 to ~2.00 electrons/atom. Among crystalline intermetallic compounds, these *e/a*

values fall near the upper end of Hume-Rothery phases, which occur for $1.00 \leq e/a \leq 2.00$,

and just below polar intermetallic compounds, which occur for $2.00 < e/a < 4.00$.[13] Hume-

Rothery phases are densely packed structures with atoms of similar sizes and

electronegativities from among the late- and post-transition metals. One example is the class

of γ-brasses (*e/a* = ~1.60—~1.75), which are body-centered cubic packings of 26-atom clusters

involving four fused icosahedra.[14] Polar intermetallics, on the other hand, involve

combinations of electropositive alkali, alkaline-earth, or rare earth metals with the more electronegative late and/or post-transition metals. The polar-covalent interactions between these different elements lead to complex networks of electronegative metals encapsulating electropositive metals with high coordination numbers, both of which are features of many i-QCs and their CAs.

The proposed relationships between QCs and CAs are widely accepted, given the structural and electron counting schemes mentioned above. Studies using variable temperature and/or pressure to induce transformations between QCs and their CAs can further corroborate their relationships, although not all transformations have led strictly to the expected CA. For the temperature-induced in-situ transformation of hexagonal $MgYZn_3$ to the i-QC Mg_3YZn_6 ($e/a = 2.10$), electron microscopy provided insights about atomic clustering in the i-QC during nucleation of the hexagonal crystal in a Mg matrix that led to i-QCs at Mg_3YZn_6/Mg interfaces. However, the starting $MgYZn_3$ crystal in the study was not strictly a CA of the corresponding i-QC because the hypothetical 2/1 CA would have a composition $Mg_{18}Y_9Zn_{58}$ (= $Mg_2YZn_{6.44}$).[15] Formation and transformation studies of an Al–Cu–Fe i-QC using mechanical milling[16] and variable temperature,[17] pressure,[18] or both[19] have shown that, whereas increasing temperature reversibly transforms the i-QC to rhombohedral, orthorhombic, and pentagonal[17b] "CA" phases, of which the resulting structures are not one of the three typical CA types, increasing pressure or both pressure and temperature inhibits the formation of any known CA phases. Increasing temperature on the i-QC $Al_{60.3}Cu_{30}Fe_{9.7}$ leading to "CA" phases that are not one of the primary CA types is intriguing, given the generally accepted relationships between the known CA structure types and i-QCs.[17b] This variety of outcomes showing both relationships between CAs and QCs as well as crystalline phases not classified as approximants

suggests that the view for what constitutes a CA of a QC may be too narrow. Formation of a Mg–Al–Zn QC and CA by mechanical alloying with thermal data analyses shows correlations between known CAs and QCs, although in the same study there was no structural information about the resulting CA phase.[20] Subsequently, the structure of the 1/1 CA $Mg_{2-y}(Zn_xAl_{1-x})_{3+y}$ was elucidated using a combination of single-crystal and powder neutron XRD, EDS, densities, and theoretical modeling.[21] Thus, in addition to discrete, sharp diffraction peaks indicating QCs to be more closely related to periodic solids than amorphous structures, reports of transformations between crystalline and quasicrystalline phases provide additional evidence for their relationships. However, identifying the features of crystalline structures that give rise to a QC or vice versa remains speculative, since not all QCs transform to their related or known CA structure type.

In an attempt to better probe this transformation, we examine and report the discovery of a crystalline structure in close composition to the i-QC in the Ca–Au–Al system, namely, a cubic 2/1 CA. Herein, we report an in-situ transformation of the i-QC $CaAu_{4.50-x}Al_{1.50+x}$ phase, specifically $\langle x \rangle$ = 0.32(6) and 0.40(6), to its cubic 2/1 CA $Ca_{13}Au_{56.79(6)}Al_{21.20}$ ($CaAu_{4.37(1)}Al_{1.63}$) from direct observation of the changes in synchrotron PXRD patterns, and identify the crystallographic solution of the 2/1 CA as an overall packing of interpenetrating and edge-sharing icosahedra. Additionally, we examine the most intense PXRD reflections in the resulting 2/1 CA that arise during the transformation to identify clear correlations between the i-QC and the CA. Lastly, using electronic structure theory and data on the 1/0[22] and 2/1 CAs of the Ca–Au–Al system, we propose a hypothetical 1/1 CA and rationalize the chemical stability of the i-QC from its valence electron count based on a Hume-Rothery mechanism.

Experimental Section

Synthesis. $Ca_{1.00(4)}Au_{4.50-x}Al_{1.50+x}$ $(0.11(6) \leq x \leq 0.63(6))$ samples were synthesized from elemental Ca chunks (99.99%, Sigma Aldrich), Au spheres (99.99% Ames Laboratory), and Al ingots (99.999%, Alfa-Aesar) with compositions loaded corresponding to targeted e/a values of 1.60–1.75. Elemental mixtures were sealed in tantalum tubes under argon, then enclosed in secondary silica jackets under vacuum, and then heated to 900 °C at 180 °C/h in a programmable tube furnace. The samples characterized as quasicrystalline were quenched from 900 °C after heating for one day by rapid submersion of the reaction vessels into room temperature water; the 2/1 CA samples were also quenched to room temperature from 900 °C after heating for one day, but they were subsequently heated to 650 °C for a 1-week annealing period, after which they were quenched or naturally cooled to room temperature by turning off the furnace. At the targeted e/a values of 1.75, which is above the nominal loading phase width that resulted in the 2/1 CA, annealing led to multiple phases, which may include the 2/1 CA or i-QC as a minor component, whereas quenching led to the i-QC with traces of the 2/1 CA.

Single crystal X-ray diffraction. Single-crystal XRD data of the 2/1 CA were collected using the program SMART[23] at ~25 °C on the Bruker APEX3 with a high-focused beam (Mo $K_{\alpha 1}$; $\lambda = 0.71073$ Å) from irregular, block-shaped specimens with longest cross-sectional length of 80–100 μm that were mounted onto the tips of glass fibers and held fixed by grease. Only those specimens that gave data sets containing greater than 95% of the total number of reflections indexing as cubic with a lattice parameter ~23.5–24.0 Å via a preliminary scan were examined in more detail. On average, at least ten crystal specimens from each sample loading were tested. Empirical absorption corrections were performed using the program SADABS[24] of the APEX3 suite; the $Pa\bar{3}$ space group was determined using the

program XPREP; and the crystal structure was solved using direct methods with subsequent refinements using the SHELXTL suite.[25]

High-energy XRD data using the X-ray precession technique at the Advanced Photon Source (APS; Beamline 6ID-D) at Argonne National Laboratory (ANL; $\lambda = 0.183520$ Å) were collected at room temperature to compare the single-grained diffraction patterns of the 2/1 CA and associated i-QC along the ([1 0 0]) 2-fold, ([1 1 1]) $\bar{3}$-fold, and ([3 0 5] pseudo)-$\bar{5}$-fold axes.[26] Precession diffraction images were processed using the FIT2D program, v. 2004 from the *European Synchrotron Radiation Facility*.[27]

Thermal analysis. Thermal analysis of the powdered i-QC sample loaded as $Ca_{1.00(4)}Au_{4.158(8)}Al_{1.80(6)}$ ($x = 0.32(6)$ in $Ca_{1.00(4)}Au_{4.50-x}Al_{1.50+x}$) was performed on a Netzsch STA 449 F3 Jupiter instrument using an alumina crucible and under a flow of nitrogen at 20 ml/min. A calibration run of the empty alumina was performed first prior to the run with the i-QC sample. The temperature profile, with all ramp rates at 10 °C/min, was (1) heating from 27 °C to 900 °C for 10 min; (2) cooling to 400 °C for 30 min; (3) heating back to 900 °C; and (4) cooling down to ~90 °C.

Powder X-ray diffraction. PXRD data for phase analysis at ~25 °C were collected on a STOE STADI P diffractometer (Cu $K_{\alpha1}$; $\lambda = 1.54060$ Å) with a step size of 0.03° in 2θ for a 1-hour scan. Ground polycrystalline samples were dispersed onto and sandwiched between two transparent films with the use of vacuum grease. Diffraction images were processed using the *FullProf* suite[28] and the software WinXPOW.[29] Rietveld refinements[30] of lattice parameters and atomic positions were carried out on the observed PXRD patterns using Jana2006.[31] To study the transformation from i-QC–to–2/1 CA, ground products (~30–50 mg) were loaded into a 1-mm diameter silica capillary and sealed under helium to avoid oxidation during

heating. An IR furnace was used for *in-situ* heating of the powdered products at various heating rates up to ~750 °C. The specific heating profile for the sample $x = 0.32(6)$ in $Ca_{1.00(4)}Au_{4.50-x}Al_{1.50+x}$, discussed in the main text, is as follows: from room temperature to ~400 °C the sample was heated at 40 °C/min, and from 400 °C to ~750 °C, the sample was heated at 10 °C/min. From ~750 °C to room temperature, the sample was cooled at a rate of 100 °C/min. (See SI for *in-situ* PXRD of additional heating profiles with isothermal holds and various heating and cooling rates and for PXRD data of the sample $x = 0.40(6)$ in $Ca_{1.00(4)}Au_{4.50-x}Al_{1.50+x}$.) To monitor the temperature of the IR furnace, one end of a thermocouple was placed underneath and touching the silica capillary tube to achieve closest contact to the ground polycrystalline sample and the other end was connected to the temperature controller.

In-situ, high-energy, variable-temperature PXRD data were collected at the Advanced Photon Source (APS) at Argonne National Laboratory ($\lambda = 0.17712$ Å; Beamline-1D) with a data acquisition time of 11 s/scan including 5 seconds of exposure and ~6 seconds for data processing. All collected temperature data were calibrated against a sample of $Al_{90}Sm_{10}$ (at %) metallic glass of known melting temperature. Peak-fitting from 23–32 nm^{-1} using a Lorentzian function, in which the area of each peak is calculated as a product of the full-width at half-maximum and the peak height, was evaluated as a function of temperature to analyze peak splitting throughout the transformation.

Transmission electron microscopy (TEM). Samples of the i-QC and 2/1 CA were prepared for TEM using a Thermo Fischer Scientific (FEI) Helios NanoLab G3 UC with EasyLift micromanipulator and MultiChem Gas Injection System, and employing standard *in-situ* lift-out techniques.[32] Selected area electron diffraction (SAED) patterns of the i-QC and 2/1 CA samples were taken using the FEI Tecnai (G2-F20) TEM equipped with a field

emission gun (FEG), under an accelerating voltage of 200 kV. Each sample was mounted on an FEI double-tilt holder, which enabled precise sample tilting along the main axes and its perpendicular direction (~±30°). The sample was then tilted to the 2-, $\bar{3}$-, and (pseudo) $\bar{5}$-fold zone axes while the Kikuchi pattern was monitored. The high (atomic)-resolution high-angle annular dark field (HAADF) images were collected using a Titan Themis 300 probe-corrected scanning transmission electron microscope (STEM).

Electronic structure calculations. The electronic density of states and band structure of a hypothetical cubic 1/1 CA "$Ca_{24}Au_{88}Al_{64}$" were calculated using the projected augmented wave method of the Vienna Ab-initio Simulation Package (VASP 4.6.34)[33] in the space group $I23$ (No. 197), based on data from the 1/1 CA $Ca_3Au_{12.07}Ga_{6.93}$ (space group: $Im\bar{3}$, No. 204).[10c] Following the Tsai-type structural prescription of the experimentally determined cubic 2/1 CA $Ca_{13}Au_{56.79(6)}Al_{21.20}$, the innermost shell of the hypothetical model was simplified to a single, fully-occupied Al_4 tetrahedron from the 12 partially occupied positions that generally averaged as 3 tetrahedra, and was then shifted to the center of the concentric shells. The hypothetical cubic lattice ($a_{1/1} = 14.8181$ Å) was calculated following Equation (1) and using the quasilattice constant a_{QC} determined from a single quasicrystal. The model contains 11 atoms in the asymmetric unit for a total of 176 atoms in the unit cell. All calculations used the generalized gradient approximation (GGA) for exchange and correlation potentials as constructed by Perdew, Burke, and Ernzerhof (PBE) with a 500 eV energy cutoff, a 0.01 meV self-consistent convergence criterion, and an orbital basis set as follows: Ca ($3s^23p^64s^2$), Au ($5d^{10}6s^1$), and Al ($3s^23p^1$).[34]

Table 1. $Ca_{1.00(4)}Au_{4.5-x}Al_{1.5+x}$ $(0.11(6) \leq \langle x \rangle \leq 0.44(6))$ i-QC and 2/1 CA phases, compositions, and lattice parameters

	actual loading	target $\langle VEC \rangle$	$\langle x \rangle$	identified phases	a (Å) powder XRD	specimen composition	a (Å) single-crystal XRD
annealed	$Ca_{13.0(5)}Au_{59.4(1)}Al_{18.5(7)}$	1.55	−0.05(6)	unknown[a] + possible 2/1 CA traces			
	$Ca_{13.0(5)}Au_{57.1(1)}Al_{20.9(8)}$	1.60	0.11(6)		23.8917(7)	no selected crystals	
	$Ca_{13.1(5)}Au_{55.0(1)}Al_{23.5(7)}$	1.65	0.30(6)		23.8915(6)	no selected crystals	
	$Ca_{13.0(5)}Au_{52.8(1)}Al_{25.3(7)}$	1.70	0.44(6)	2/1 CA major phase	23.893(1)	$Ca_{13}Au_{56.79(6)}Al_{21.20}$[b] $Ca_{13}Au_{57.02(6)}Al_{20.99}$[b] $Ca_{13}Au_{57.04(6)}Al_{20.96}$[b]	23.8918(2) 23.914(1) 23.8950(6)
	$Ca_{13.0(5)}Au_{50.4(1)}Al_{27.4(7)}$	1.75	0.62(6)	unknown[a] + possible 2/1 CA or i-QC traces			
quenched	$Ca_{13.0(5)}Au_{57.3(1)}Al_{20.1(8)}$	1.60	0.11(6)		$a_{QC} =$ 5.393(6)	$Ca_{1.0(1)}Au_{4.5(2)}Al_{1.4(1)}$[c]	$a_{QC} =$ 5.383(4)
	$Ca_{13.2(5)}Au_{55.0(1)}Al_{23.8(7)}$	1.65	0.32(6)	i-QC major phase	$a_{QC} = 5.387(7)$		
	$Ca_{12.8(5)}Au_{52.6(1)}Al_{25.2(7)}$	1.70	0.40(6)		$a_{QC} = 5.378(6)$		
	$Ca_{13.0(5)}Au_{50.38(9)}Al_{27.7(7)}$	1.75	0.63(6)	i-QC + possible 2/1 CA traces			

[a] Not 1/1 CA. See Figure 1. [b] Single-crystal XRD. See Tables S3–S6. [c] EDS. See Reference 22.

Table 2. Selected refined crystallographic data of 2/1 CA $Ca_{13}Au_{56.79(6)}Al_{21.20}$

loaded (VEC)	$Ca_{13.0(5)}Au_{52.8(1)}Al_{25.3(7)}$ (1.70 e/a)
crystal color / appearance / size (μm)	gray / irreg. blocks / 40–50 × 60–80 × 20–30
refined composition (VEC)	$Ca_{13}Au_{56.79(6)}Al_{21.20}$ (1.61 e/a)
refined nominal composition	$CaAu_{4.37(1)}Al_{1.63}$
instrument	Bruker APEX III
radiation; λ (Å) / temp.(K)	Mo K_{a1}; 0.71073 / 298
θ range data collection	2.4°–27.5°
absorp. coeff. μ (mm^{-1}) / correction	122.87 / empirical
meas. / indpnt. / obs. [I > 2σ(I)] / param. / rest.	124424 / 5216 / 3252/ 331 / 1
R[$F^2 > 2\sigma(F^2)$] / wR(F^2) / R_{int} / GOF	0.069 / 0.170 / 0.185 / 1.03
space group / Pearson symbol	$Pa\bar{3}$ (#205) / $cP728$
$\Delta\rho_{max}$, $\Delta\rho_{min}$ (e Å^{-3})	8.43, −2.99
a (Å)	23.8918(2)
$a_{Reitveld}$ (Å) (Table S2)	23.893(1)
volume (Å^3) / Z	13637.9(2) / 8
index ranges	$-31 \leq h \leq 31$; $-30 \leq k \leq 30$; $-31 \leq l \leq 30$

Results and Discussion
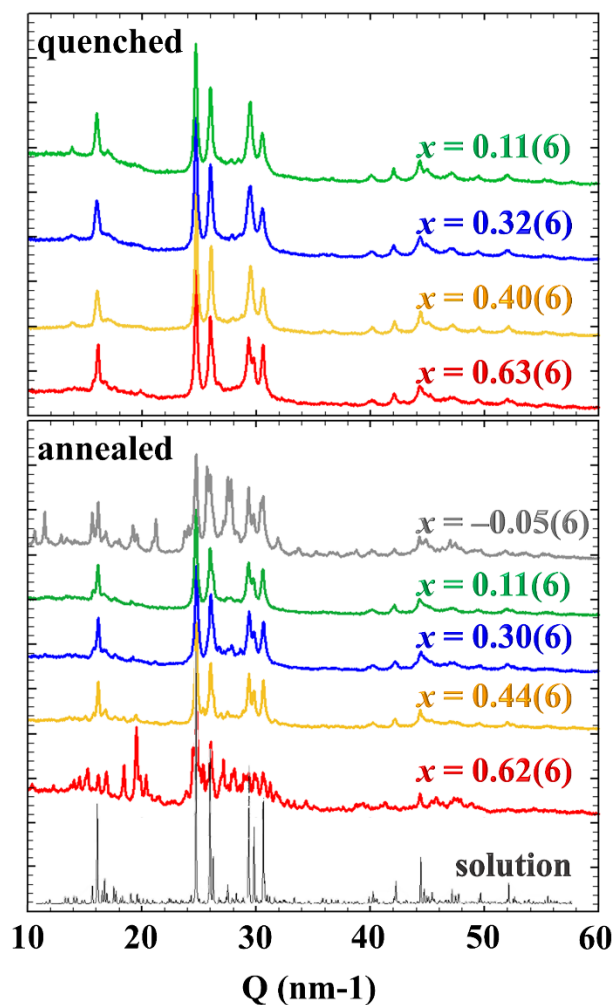
Figure 1. PXRD patterns at ~25 ºC from loadings of $CaAu_{4.50-x}Al_{1.50+x}$ i-QC (targeted e/a = 1.60–1.75; top), and cubic 2/1 CA (targeted e/a = 1.55–1.75; bottom), with theoretical pattern from single-crystal XRD refinement, $Ca_{13}Au_{56.79(6)}Al_{21.20}$ ($CaAu_{4.37(1)}Al_{1.63}$).

Phase analysis. At 14.3(1) atomic percent Ca, nine Ca–Au–Al samples were loaded with e/a values ranging from 1.55 to 1.75 and heated to 900 °C. Of these, five were then annealed for one week at 650 °C and four were quenched to room temperature. The results of these synthetic procedures are summarized in Table 1, in which $<x>$ was calculated by first dividing the reported composition by 13 to obtain the nominal composition per Ca, and by subsequently summing the electronegative Au + Al elements so that $<x>$ show their

compositional relationship. According to PXRD (see Figure 1), only loadings with e/a values 1.60–1.70 yielded as major phases either an i-QC or the 2/1 CA depending upon whether the sample was quenched or annealed, respectively. Targeted compositions with e/a values of 1.55 and 1.75, which represent the upper and lower bounds of sample loadings, yielded either a different phase or the 2/1 CA as a minor phase after annealing (Figure 1). On the other hand, the i-QC $CaAu_{4.50-x}Al_{1.50+x}$ was only observed upon quenching after heating for 1 day at 900 °C for compositions corresponding to e/a values of 1.60–1.70 (i.e., $0.11(6) \leq x \leq 0.40(6)$). For the quenched sample loaded with $e/a = 1.75$, the observed PXRD pattern shows resemblances to the 2/1 CA. Rietveld refinements of lattice constants for the 2/1 CA from three PXRD patterns of the annealed samples ($e/a = 1.60$–1.70) remain essentially equal within standard deviation ($a_{2/1} = 23.8917(7)$–23.893(1) Å) and suggest that the actual phase width of the 2/1 CA may, in fact, be smaller than the variation in loading compositions (Table S1 and Figure S1). From these refined lattice constants and using Equation (1), the quasilattice parameter of the corresponding i-QC is estimated to be $a_{QCcalc.} = 5.3640$–5.3643 Å, which is close, but slightly smaller than quasilattice parameters refined from PXRD patterns (5.378(6)–5.393(6) Å) or from single-crystal XRD patterns ($a_{QC} = 5.383(4)$ Å) (Table S2). The quasilattice parameters were evaluated from the PXRD patterns following Cahn's indexing method [35] from the 12 most intense peaks in 10–50 nm^{-1}.

As part of the conjecture that a CA approximates the structure of a QC, some diffraction features found for the CA are also likely present in the QC in corresponding geometrical relationships. High-energy, single-crystal precession XRD data of the cubic 2/1 CA $Ca_{13}Au_{56.79(6)}Al_{21.20}$ ($CaAu_{4.37(1)}Al_{1.63}$) and the i-QC "$CaAu_{4.39}Al_{1.61}$" show resemblances along the ([1 0 0]) 2-fold and ([1 1 1]) $\bar{3}$-fold axes, but display stark differences along the $\bar{5}$-fold
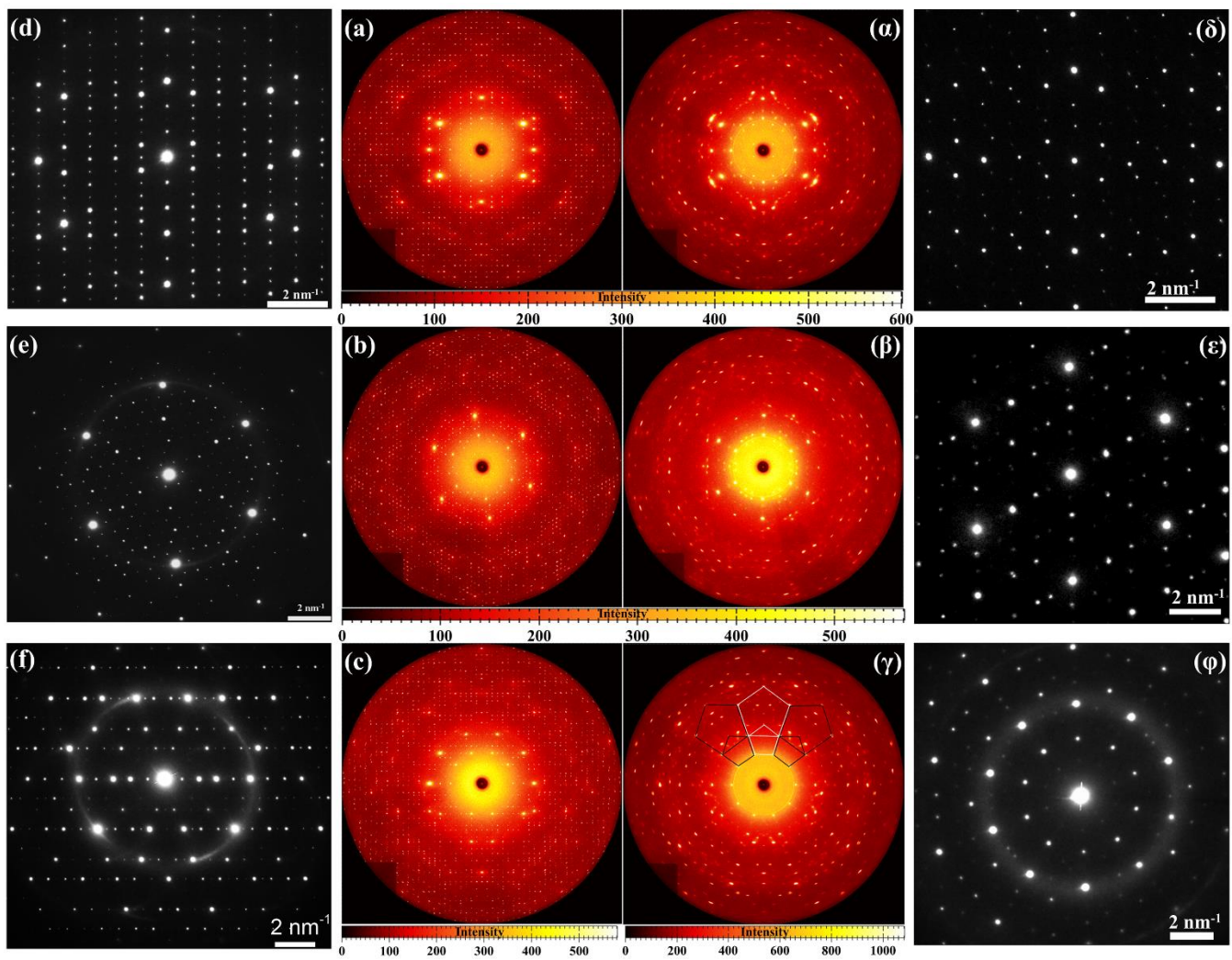
Figure 2. CaAu$_{4.50-x}$Al$_{1.50-x}$ precession diffraction images and TEM SAED patterns of the 2/1 CA, $x = 0.44(6)$ (a–c; d–f), and the i-QC, $x = 0.11(6)$ (α–γ (Ref. 22); ε–φ), along the 2-fold [1 0 0] (top), $\bar{3}$-fold [1 1 1] (middle), and (pseudo)-$\bar{5}$-fold [3 0 5] (bottom) directions.
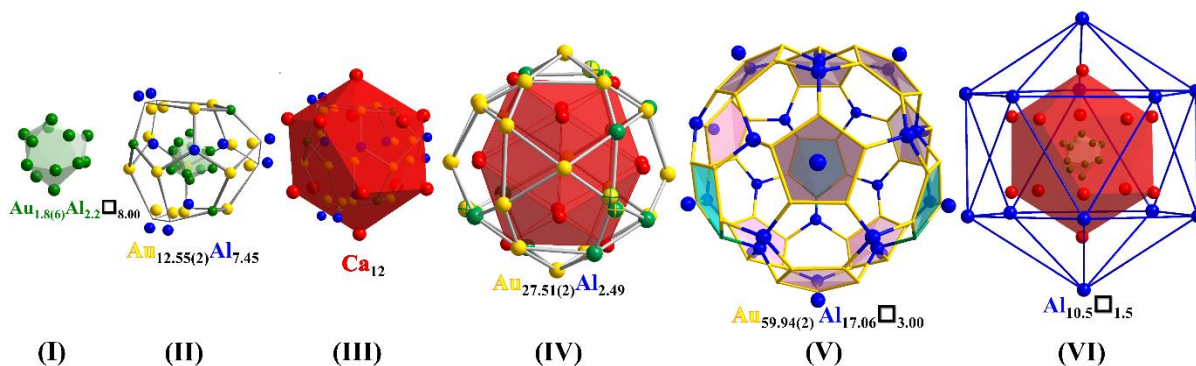
Figure 3. Concentric shells of the 2/1 CA $Ca_{13}Au_{56.79(6)}Al_{21.20}$. Au/Al mixed sites are in green, Au atoms are in dark yellow, Al atoms in blue, Ca atoms are in red, and voids are in □.

direction of the i-QC (Figure 2γ), which only displays mirror symmetry along the analogous direction ([3 0 5]) of the cubic 2/1 CA (Figure 2c). Additionally, icosahedral symmetry of the QC and lack thereof in the 2/1 CA is verified from TEM SAED patterns (Figure 2d–f, δ–φ), which exhibit good correlations to the XRD patterns. The partial rings in the SAED patterns are from surface oxidation due to sample thinning preparation for atomic-resolution imaging (see Figure S2), with results which show atomic cluster arrangements suggesting phason strain within the structure, as also seen in the i-QC. [22]

Crystal structure of the 2/1 CA. Crystals selected from the sample loaded as $Ca_{1.00(4)}Au_{4.062(8)}Al_{1.95(6)}$ ($x = 0.44(6)$; $e/a = 1.70$) met the criteria for further examination by single-crystal diffraction methods. Three crystalline specimens were measured, all of which gave lattice parameters 23.8918(2)–23.914(1) Å and an average refined composition of $Ca_{13}Au_{56.95(10)}Al_{21.05} = CaAu_{4.38(1)}Al_{1.62}$ ($x = 0.12$; $e/a = 1.61$). The structure of this cubic 2/1 CA can be described by six concentric atomic shells following the Tsai-type prescription, but with features that have not been previously mentioned (Figure 3). The centers of the shells lie at the 8c sites (0.152, 0.152, 0.152) of the cubic cell in space group $Pa\overline{3}$, so that there are 8 total sets of concentric atomic shells ($Z = 8$). Therefore, the refined composition, $Ca_{13}Au_{56.79(6)}Al_{21.20}$, can be multiplied by 8 to obtain the full unit cell contents, or be divided

by 13 to obtain the nominal composition per Ca ($CaAu_{4.37(1)}Al_{1.63}$). A summary of the crystallographic refinement for the sample refining as $Ca_{13}Au_{56.79(6)}Al_{21.20}$, with all atoms in the asymmetric unit labeled for the various shells, is listed in Tables 2–3 (see Tables S3–S6 for the results of the other two crystals).

These distinct atomic shells are (see Figure 3):

(I) *Spatially disordered "tetrahedron" [$Au_{1.8(6)}Al_{2.2}\square_{8.00}$]*. The innermost shell is comprised of four mixed Au/Al independent sites that take up 12 partially occupied positions arranged in a distorted icosahedron, but with occupancies that may geometrically suggest disordered and distorted tetrahedra, so that the overall composition is [$Au_{1.8(6)}Al_{2.2}\square_{8.00}$], and in which $\square$ represents the structural voids. From the center to the 12 Au/Al sites, the distances range from 1.37(2)–1.55(3) Å, which means that having all 12 positions fully occupied is unrealistic. A structural refinement omitting electron densities from this shell provides an incomplete model because the observed electron densities can account for 12 positions fully occupied by Al atoms, a result that is not possible due to the distances noted above. Hence, the inner shell is refined as four mixed Au/Al sites (24d Au/Al25–28 in Table 3) each 1/3 occupied. The equivalent isotropic thermal parameters associated with these sites are the largest of all the positions in the asymmetric unit by a factor of ~2–3. For the prototypic Tsai-type cubic 2/1 CA (Yb/Ca)$_{13}$Cd$_{64}$, which shows somewhat longer distances of 1.734(6)–1.98(1) Å from the center to the 12 partially occupied Cd sites at ambient conditions, a refinement outcome of spatially disordered, distorted tetrahedra is one of the hallmarks of the Tsai-type CA.[8b] In this case, to obtain tetrahedra from the 12 positions in the shell, the atoms would be unrealistically close to one another ($\leq 2.00(4)$ Å) and therefore, although this shell may be geometrically seen as 4 spatially disordered tetrahedra, from XRD, the only chemical conclusion is that there are

Table 3A. Selected structural parameters of $Ca_{13}Au_{56.79(6)}Al_{21.20}$

shell	atom	Wyck.	sym.	x	y	z	frac. occ.	U_{iso}/U_{eq}
(I)	Au/ Al25	24d	1	0.1231 (3)	0.1528 (3)	0.2061 (3)	0.226(8)/ 0.107	0.047 (3)
	Au/ Al26	24d	1	0.1463 (7)	0.2126 (6)	0.1707 (8)	0.20(1)/ 0.14	0.17 (1)
	Au/ Al27	24d	1	0.1007 (8)	0.1264 (9)	0.1502 (7)	0.11(2)/ 0.23	0.06 (1)
	Au/ Al28	24d	1	0.0908 (9)	0.159 (2)	0.131 (1)	0.05(2)/ 0.28	0.06 (1)
(II)	Au1	24d	1	0.15384 (5)	0.21407 (5)	0.30212 (5)		0.0301 (3)
	Au2	24d	1	0.00314 (5)	0.15588 (5)	0.21045 (5)		0.0298 (3)
	Au3	8c	.3.	0.06226 (5)	0.06226 (5)	0.06226 (5)		0.0297 (5)
	Au/ Al4	24d	1	0.0633 (2)	0.2514 (2)	0.2387 (2)	0.278(7)/ 0.722	0.052 (2)
	Au5	24d	1	0.05599 (9)	0.24381 (8)	0.06618 (8)	0.734 (6)	0.0382 (7)
	Al5	24d	1	0.024 (2)	0.276 (2)	0.054 (2)	0.266 (6)	
	Au6	24d	1	0.1678 (4)	0.4123 (4)	0.4988 (4)	0.186 (8)	0.030 (3)
	Al6	24d	1	0.0144 (7)	0.1555 (7)	0.1003 (7)	0.814 (8)	
	Au7	24d	1	0.0903 (1)	0.3022 (1)	0.1579 (1)	0.651 (6)	0.0415 (9)
	Al7	24d	1	0.062 (2)	0.337 (2)	0.153 (1)	0.349 (6)	
	Al1	24d	1	0.2355 (5)	0.2355 (5)	0.2355 (5)		0.040 (5)
(III)	Ca1	24d	1	0.1542 (3)	0.3437 (3)	0.2702 (3)		0.027 (1)
	Ca2	24d	1	0.2700 (3)	0.3443 (3)	0.4614 (3)		0.027 (1)
	Ca3	24d	1	0.0366 (2)	0.3446 (3)	0.4659 (3)		0.025 (1)
	Ca4	24d	1	0.0383 (3)	0.1514 (3)	0.3426 (3)		0.026 (1)

4 Au/Al sites split among 12 positions. Another hallmark of the Tsai-type structure is the pentagonal dodecahedral shell that encapsulates this tetrahedron.

(II) *Disordered, distorted dodecahedron [Au$_{12.55(2)}$Al$_{7.45}$] with split-sites.* The disordered, distorted pentagonal dodecahedron[Au$_{12.55(2)}$Al$_{7.45}$] consists of eight independent sites: three are fully occupied Au sites; one is a fully occupied Al site; three are split 24d Au or Al sites constrained to a total occupancy of 100%; and one is a mixed but not split Au/Al site. The distances from the center of the dodecahedron to the atoms range from 3.46(1) Å to 4.91(3) Å so that the interatomic edge lengths range from 2.33(1) Å to 3.72(3) Å. Refinement of the three split positions relies on observed electron densities near the respective sites. The resulting distances between each of the split sites are: 0.56(2) Å; 1.07(3) Å; and 1.11(4) Å, for which the sites split by the two longer distances contain predominantly Au (0.651(6)/0.349 Au7/Al7 and 0.734(6)/0.266 Au5/Al5, respectively) and the one separated by the shortest distance is predominantly Al (0.186(8)/0.814 Au6/Al6).

(III) *Distorted icosahedron [Ca$_{12}$].* The [Ca$_{12}$] icosahedral shell is comprised of four independent Ca 24d sites with a center-to-atom distance range of 5.232(6)–5.381(7) Å, and caps the distorted pentagonal faces of the dodecahedral shell within. The triangular faces related by the 3-fold axis also bisect the Au/Al split-sites of the dodecahedral [Au$_{12.55(2)}$Al$_{7.45}$] shell.

(IV) *Icosidodecahedron [Au$_{27.51(2)}$Al$_{2.49}$].* The [Au$_{27.51(2)}$Al$_{2.49}$] icosidodecahedral shell is comprised of 10 independent 24d sites, of which six are Au, three are mixed Au/Al, and one is a mixed and split position (0.433(3)Au/0.17Al + 0.410(4) Au) with a refinement restraint that forces 100% total occupation by Au and Al atoms because the split sites are just 0.931(6) Å apart. The center-to-atom distances range from 5.878(2)–6.121(2) Å, so that the edge lengths of the icosidodecahedron fall between 2.966(2) and 4.405(2) Å.

Table 3B. Selected structural parameters for shells IV–VI

shell	atom	*Wyck.*	*sym.*	x	y	z	frac. occ.	U_{iso}/U_{eq}
(IV) (V)	Au9	24*d*	1	0.24399 (5)	0.28291 (5)	0.34450 (6)		0.0310 (3)
	Au10	24*d*	1	0.06149 (5)	0.28293 (5)	0.34882 (6)		0.0313 (3)
	Au11	24*d*	1	0.21349 (5)	0.45980 (5)	0.24362 (5)		0.0305 (3)
	Au12	24*d*	1	0.08754 (6)	0.46472 (5)	0.44312 (5)		0.0302 (3)
	Au13	24*d*	1	0.15181 (6)	0.36313 (6)	0.40349 (6)		0.0356 (3)
	Au14	24*d*	1	0.14572 (7)	0.40813 (6)	0.15382 (6)		0.0403 (4)
(IV)	Au/ Al15	24*d*	1	0.02592 (9)	0.3476 (1)	0.24052 (9)	0.640(7)/ 0.360	0.0448 (8)
(IV) (V)	Au/ Al16	24*d*	1	0.06706 (6)	0.21611 (6)	0.45349 (7)	0.981(7)/ 0.019	0.0406 (6)
(IV)	Au/ Al17	24*d*	1	0.2233 (1)	0.46635 (9)	0.44842 (9)	0.699(7)/ 0.301	0.0530 (9)
	Au/ Al18	24*d*	1	0.0224 (1)	0.3476 (2)	0.0602 (2)	0.433(3)/ 0.157	0.0421 (8)
	Au19	24*d*	1	0.0356 (2)	0.3673 (2)	0.0911 (2)	0.410 (4)	
(V)	Al2	4*a*	.–3.	0	0	0		0.025 (5)
	Al3	24*d*	1	0.1565 (5)	0.2556 (5)	0.4012 (4)		0.039 (3)
	Au20	24*d*	1	0.24856 (5)	0.40520 (5)	0.34474 (5)		0.0273 (3)
	Au21	24*d*	1	0.05482 (5)	0.40266 (5)	0.34346 (5)		0.0291 (3)
	Au22	24*d*	1	0.08942 (5)	0.45975 (5)	0.24608 (6)		0.0306 (3)
	Au23	24*d*	1	0.34363 (6)	0.44329 (6)	0.40394 (6)		0.0356 (3)
	Au24	24*d*	1	0.05716 (6)	0.09442 (6)	0.46367 (6)		0.0421 (4)
(V) (VI)	Al8	24*d*	1	0.1527 (4)	0.4618 (4)	0.3434 (4)		0.027 (2)
	Al9	8*c*	.3.	0.3432 (4)	0.3432 (4)	0.3432 (4)		0.020 (3)
	Al10	24*d*	1	0.0386 (7)	0.461 (1)	0.1525 (9)	0.50	0.036 (5)
voids (VII)	Ca5	8*c*	.3.	0.4594 (3)	0.4594 (3)	0.4594 (3)		0.032 (3)

(V) *C_{80}-like [$Au_{59.94(2)}Al_{17.07}\square_{3.00}$] polyhedral cluster*. The typical description of the fifth shell of a Tsai-type CA is a rhombic triacontahedron with 32 atoms at each of the vertices and 60 atoms sitting midway along each edge as reported for the 2/1 CAs $Sc_{11.18(9)}Mg_{2.5(1)}Zn_{73.6(2)}$,[36] (Yb/Ca)$_{13}Cd_{76}$,[8b] and 1/1 CAs $Yb_{14}Au_{51}Al_{35}$,[9b] and RE–Au–SM (RE = Yb, Gd and SM = Si, Ge).[9a] However, to assign atoms at the vertices only, as consistently portrayed in all inner shells, the 92-atom rhombic triacontahedron can be split into an 80-vertex atom cage and a 12-vertex icosahedral shell. Therefore, in $Ca_{13}Au_{56.79(6)}Al_{21.20}$, the fifth shell is a defect-80-atom cage [$Au_{59.94(2)}Al_{17.07}\square_{3.00}$], consisting of 12 pentagonal and 30 hexagonal faces, as found for C_{80} clusters such as (Gd$_3$N)@C_{80}.[37] There are no split sites in this 80-vertex cage and one independent Au-rich mixed Au/Al site (0.981(7)/0.019 Au/Al) that comprises 3 atoms of the cage. The interatomic distances making up the C_{80}-like polyhedral edges range from 2.54(2) Å to 2.977(2) Å, of which Au–Au distances are 2.776(2) Å or longer and Au–Al (or Au/Al–Al) distances are 2.77(1) Å or shorter, so that within standard deviation, the 2.77(1) Å edges feature 3 Au–Al distances and 3 Au–Au distances within this shell.

(VI) *Distorted icosahedron [$Al_{10.5}\square_{1.5}$]*. The last shell is a partially occupied icosahedron [$Al_{10.5}\square_{1.5}$] that caps the pentagonal faces of the 80-vertex [$Au_{59.94(2)}Al_{17.07}\square_{3.00}$] fifth shell and aligns with the innermost distorted tetrahedron and the third shell of the distorted icosahedron [Ca_{12}]. Each [$Al_{10.5}\square_{1.5}$] icosahedron interpenetrates seven other [$Al_{10.5}\square_{1.5}$] icosahedra and shares edges with six additional [$Al_{10.5}\square_{1.5}$] icosahedra in which the voids of a resulting 3-edge sharing icosahedral set are filled by distorted Ca-centered [$Al_{6.5}\square_{1.5}$] tetrahedral stars (Figure 4). The center-to-atom distances of this last shell range from 8.58(1) to 8.70(1) Å, so that the 30 Al···Al edge lengths vary from 9.01(2) Å to 9.19(2) Å.
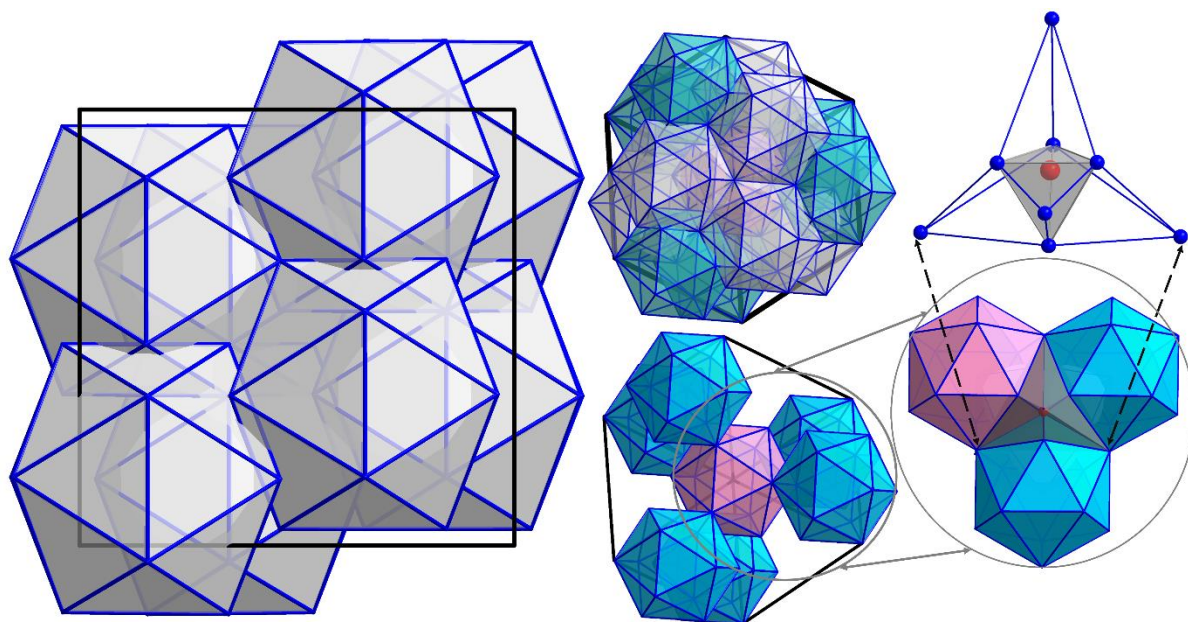
Figure 4. Packing of icosahedra in the 2/1 CA $Ca_{13}Au_{56.79(6)}Al_{21.20}$. Left: Eight total interpenetrating $[Al_{10.5}\square_{1.5}]$ icosahedra fill the unit cell. Along the [111] direction (middle): for any single icosahedron (pink), there are 7 other interpenetrating icosahedra (gray) and 6 edge-sharing icosahedra (blue). Right: Each set of 3-edge sharing icosahedra forms a Ca-centered $[Al_{6.5}\square_{1.5}]$ tetrahedral star (top right).

By splitting the 92-atom triacontahedron into two shells (V) and (VI), the 80-vertex shell is now comprised of predominantly Au whereas the icosahedron shell is only Al. In the structural description of both $Sc_{11.18(9)}Mg_{2.5(1)}Zn_{73.6(2)}$[36] and $(Yb/Ca)_{13}Cd_{76}$,[8b] the triacontahedral shell is comprised of only Zn and Cd, respectively, and as such, dividing the shells into an 80-atom vertex cage and an icosahedron as shown here is not as chemically relevant. However, in $Yb_{1.083}Au_{4.477}Ge_{1.304}$, the Au/Ge 12$e$ forms its own $[Au_{0.10}Ge_{11.90}]$ icosahedron, separate from the Au-rich 80-vertex $[Au_{62.84}Ge_{11.90}\square_{5.26}]$ shell. Many other Tsai-type structures, such as $Yb_{14}Au_{51}Al_{35}$,[9b] $Gd_{1.008}Au_{4.723}Ge_{1.301}$,[9a] and $Gd_1Au_{4.922}Si_{1.123}$,[9a] may benefit from a structural chemical representation that separates the typical triacontahedral shell into an 80-vertex Au-rich cage and a 12-vertex icosahedral shell with elements of only or predominantly the p-block.

Table 4. Coordination spheres of split-sites according to distances

shell	site	total coordination	< 2.70 Å	2.70–3.00 Å	≤ 3.41 Å
(II)	Al7	$CaAu_{5.146(7)}Al_{2.005}$	$Au_{3.134(7)}Al_{0.517}$	$CaAu_{0.278(7)}Al_{0.988}$	$Au_{1.734(6)}Al_{0.5}$
	Au7	$Ca_3Au_{4.92(1)}Al_{2.10}$	$Au_{0.89(1)}Al_{1.21}$	$Au_{3.600(8)}Al_{0.467}$	$Ca_3Au_{0.433(6)}Al_{0.423}$
	Al5	$CaAu_{5.094(7)}Al_{2.140(8)}$	$Au_{3.257(7)}Al_{0.477}$	$CaAu_{0.186(6)}Al_{0.349(6)}$	$Au_{1.651(6)}Al_{1.313(8)}$
	Au5	$Ca_3Au_{4.95(2)}Al_{2.66}$	$Au_{0.67(2)}Al_{1.52}$	$Au_{3.67(2)}Al_{0.66}$	$Ca_3Au_{0.61(1)}Al_{0.49(1)}$
	Al6	$Ca_3Au_{5.89(2)}Al_{1.31}$	$Au_{3.19(2)}Al_{0.74}$	$Au_{2.699(7)}Al_{0.301}$	$Ca_3Al_{0.266(6)}$
	Au6	$Ca_2Au_{5.70(2)}Al_{2.12}$	$Au_{3.48(2)}Al_{1.40}$	$AuAl_{0.226(6)}$	$Ca_2Au_{1.22(2)}Al_{0.46}$
(IV)	Au/Al18	$Ca_3Au_{6.776(7)}Al_{1.134}$	$Au_{1.144(6)}Al_{0.615(6)}$	$Au_2Al_{0.5}$	$Ca_3Au_{3.632(7)}Al_{0.019}$
	Au19	$Ca_3Au_{6.818(6)}Al_{1.272(6)}$	$Au_{1.084(6)}Al_{1.272(6)}$	Au_2	$Ca_3Au_{3.734(6)}$

In total, there are four split positions involving Au and Al in the structure of the 2/1 CA refined as $Ca_{13}Au_{56.79(6)}Al_{21.20}$ (the other two crystals yielded similar refinements with slightly different parameters; see Tables S3–S6 for details.) Three (Au/Al7, Au/Al5, Au/Al6) of these are in the second dodecahedral shell (II) and one [(Au/Al18)/Au19] occupies the fourth icosidodecahedral shell (IV). A summary of the coordination environments of these sites up to a radius of 3.41 Å, which is the longest distance expected between any two heteroatomic atoms based on their metallic radii (R_{Ca} = 1.97 Å, R_{Au} = 1.44 Å, R_{Al} = 1.43 Å)[38], is given in Table 4. In the closest coordination sphere designated as distances less than 2.70 Å, which is slightly longer than the predicted Au–Al distance (2.665 Å) when taking into account metallic valence, bond number, and electronegativity corrections as performed by Pauling,[39] the split sites of the cubic 2/1 CA occupied by Al generally prefer more Au contacts. For instance, Al7 and Al5 of the dodecahedral shell (II) and Al(/Au)18 of the icosidodecahedral shell (IV) all have more Au than Al nearest neighbors. Analogously, those split sites occupied by Au generally exhibit more shorter distances to Al than to Au as shown by the environments of the Au7, Au5, and Au19 sites. This general trend follows the site preference energy calculations for Au and Al atoms in the cubic 1/0 CA $CaAu_3Al$, which show that the structure maximizes the number of heteroatomic Au–Al nearest neighbor contacts over homoatomic Au–Au or Al–Al contacts.[22] An anomaly to this behavior occurs for the Au/Al6 split site in the 2/1 CA, a site which shows Al6 closer (< 2.70 Å) to more Au than Al atoms, but Au6 is closer to more Au than Al atoms.

Additionally, the total compositions at each of the refined split sites in the 2/1 CA feature more heteroatomic than homoatomic contacts. For instance, surrounding Al7, Al5, and Al6, there are more combined (Ca + Au) atoms than Al atoms in the following ratios, respectively: 6.146(7)/2.005, 6.094(7)/2.140(8), and 8.89(2)/1.31(2) (Ca + Au)/Al. Although detailed structural information remains unknown for the corresponding Ca–Au–Al i-QC, these features of the 2/1 CA suggest that general avoidance of homoatomic nearest neighbor interactions of the minor components Al and Ca may also occur within the structure of the i-QC.

Transformation of the i-QC into 2/1 CA. That the i-QC $CaAu_{4.50-x}Al_{1.50+x}$ can only be synthesized from quenching suggests that it is metastable. Therefore, given the close chemical compositions and similar room-temperature PXRD patterns for the i-QC and 2/1 CA $CaAu_{4.50-x}Al_{1.50+x}$ phases (Figure 1), *in-situ* high-energy, variable-temperature PXRD was carried out on the i-QC samples loaded as $Ca_{13.2(5)}Au_{55.0(1)}Al_{23.8(7)}$ and $Ca_{12.8(5)}Au_{52.6(1)}Al_{25.2(7)}$ ($x = 0.32(6)$ and $0.40(6)$ in $CaAu_{4.50-x}Al_{1.50+x}$) to examine a possible structural evolution of the i-QC as a function of temperature. The PXRD patterns of the i-QC sample $x = 0.32(6)$ (Figure 5) begins to transform at ~570 °C with the peak at ~29.25 nm^{-1} first broadening and increasing in intensity before splitting at ~640 °C. Also, the peak at 25.8 nm^{-1} first increases in intensity before splitting at ~650 °C. (See Figures S3–S7 for additional PXRD patterns of i-QC sample $x = 0.40(6)$).

The intensities and positions of the main peaks that split during the i-QC–to–2/1 CA transformation ($Q = 25.4$–26 nm^{-1} and 28.2–29.6 nm^{-1}) have been evaluated as a function of temperature (Figure S8). In both regions, the sum of the intensities of the individual peaks
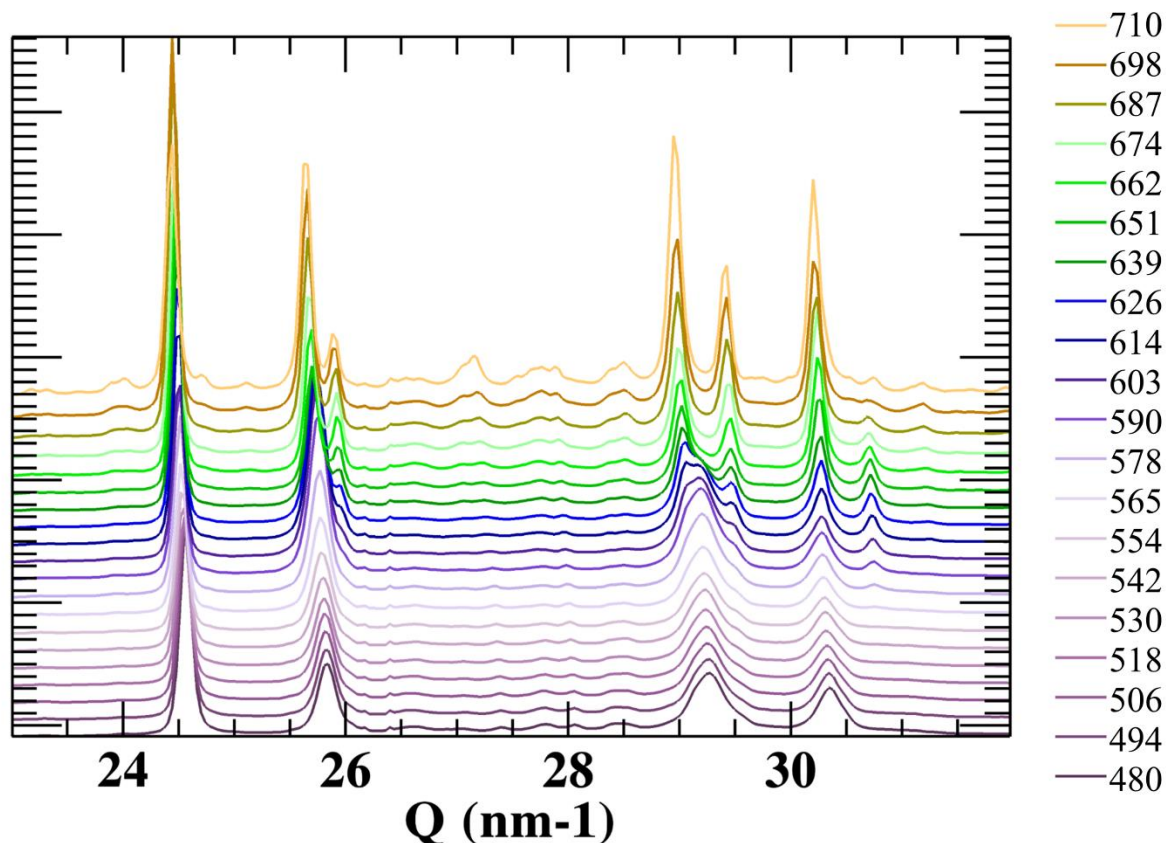
Figure 5. Variable-temperature PXRD patterns of the CaAu$_{4.50-x}$Al$_{1.50+x}$ i-QC ($x = 0.32(6)$) showing transformation from the i-QC to its 2/1 CA for increasing temperature starting ~570 °C and complete by ~650 °C.

appearing after the transformation equals that of the peak immediately prior to the splitting, which suggests a direct transformation in the temperature range ~570–~650 °C. After the transformation, increasing temperature results in decreasing Q-values of all peak positions and thus validates thermal expansion of the crystal.

Analysis of the positions in reciprocal space of the diffraction peaks observed in this Q-range further confirm the close structural relationship between the i-QC and the 2/1 CA (see Figure 6). The peaks indexed as (2 1 1 1 1 1) and (3 1 1 1 1 1) for the i-QC remain single peaks in the PXRD pattern of the 2/1 CA and are indexed respectively as {5 0 8} and {6 0 10}, both of which have 12-fold multiplicities in $Pa\overline{3}$ arranged as distorted icosahedra. The peak
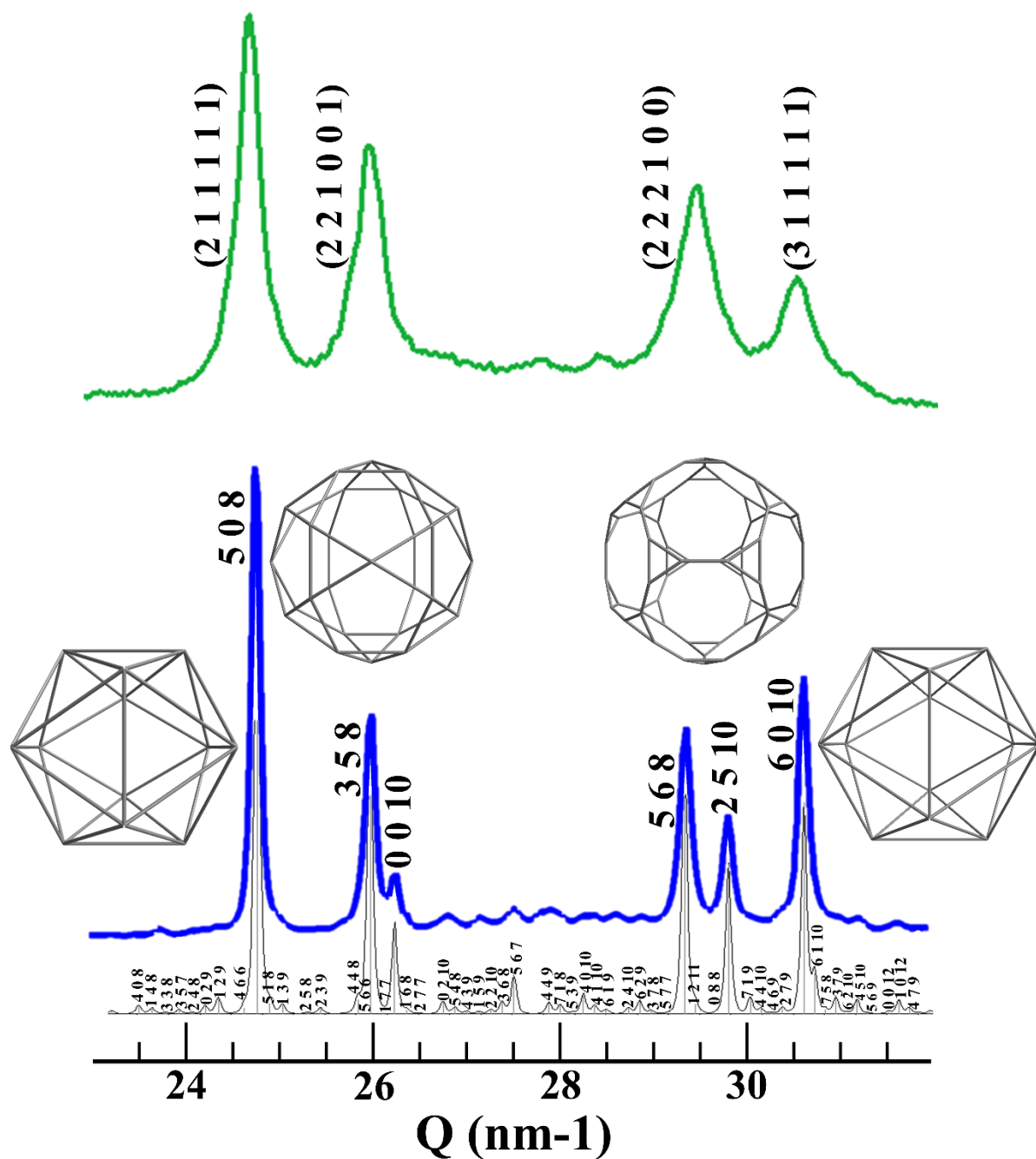
Figure 6. Indexed PXRD patterns of CaAu$_{4.50-x}$Al$_{1.50+x}$ i-QC ($x = 0.11(6)$; top) and cubic 2/1 CA ($x = 0.30(6)$; bottom) with simulated pattern from single-crystal XRD refinement, Ca$_{13}$Au$_{56.79(6)}$Al$_{21.20}$. The most intense reflection indices and multiplicities of the cubic phase are drawn and show correlations to icosahedral symmetry.

at 25.8 nm^{-1} of the i-QC, indexed as (2 2 1 0 0 1) splits into 24-fold {5 6 8} and 6-fold (0 0

10). These 30 positions in reciprocal space form a slightly distorted icosidodecahedron.

Lastly, the (2 2 2 1 0 0) peak of the i-QC at 29.25 nm^{-1} separates into 24-fold {5 6 8} + 12-fold {0 2 11} + 24-fold {2 5 10} peaks for the 2/1 CA, and form an irregular truncated dodecahedron in reciprocal space. Thus, all of the most intense peaks observed in the PXRD pattern of the 2/1 CA can be mapped into 3D reciprocal space to form a polyhedral arrangement that is slightly distorted from a polyhedron that can adopt icosahedral symmetry.

For one of the prototypic Tsai-type examples in the Ca–Cd system, transformation of the cubic 2/1 CA $Ca_{13}Cd_{76}$ to the corresponding i-QC "$Ca_{15}Cd_{85}$" [8a] would merge the most intense peak in the 2/1 CA PXRD pattern ({3 8 5}; 24.55 nm^{-1}) with the {0 0 10} peaks (24.80 nm^{-1}) based on comparisons of the i-QC and CA PXRD patterns. For the $CaAu_{4.50-x}Al_{1.50+x}$ i-QC, however, the most intense peak {5 0 8} of the PXRD does not split during the phase transformation. Additionally, the i-QC $CaAu_{4.50-x}Al_{1.50+x}$ exhibits two sets of doublet peaks at ~23–27 nm^{-1} and ~28–32 nm^{-1}, whereas the analogous region (~27–29 nm^{-1}) for the "$Ca_{15}Cd_{85}$" i-QC possesses three peaks as also seen for its 2/1 CA. In fact, the PXRD pattern of the $CaAu_{4.50-x}Al_{1.50+x}$ i-QC bears more resemblance to that of the i-QC "$Yb_{16}Cd_{84}$" and its corresponding 2/1 CA $Yb_{13}Cd_{76}$.[8a]

This transition from the i-QC to the 2/1 CA $CaAu_{4.50-x}Al_{1.50+x}$, however, is not reversible on cooling because the PXRD pattern of the 2/1 CA does not revert back into the i-QC pattern. From thermal analysis of the i-QC sample loaded as $Ca_{1.00(4)}Au_{4.158(8)}Al_{1.80(6)}$ (e/a = 1.66) (Figure 1: i-QC sample x = 0.32(6)), there is a small endothermic event at ~575 °C in the first heating cycle (Figure S9: enlarged inset) but is absent in the second heating cycle, a result which is indicative of an irreversible transformation and supports the *in-situ*, high-energy, variable-temperature PXRD data. In addition, heating the 2/1 CA sample from room temperature (~25 °C) to 725 °C, close to its melting temperature of 755 °C, and cooling down

to room temperature do not reveal any observable structural transition (Figures S10–S11), which implies that the cubic 2/1 CA phase is more stable than its i-QC counterpart.

Valence electron count evaluation. After the discovery of stable i-QCs, e.g., in the (Ca/Yb)–Ag–In and (Ca/Yb)–Cd systems among others, Tsai proposed applying Hume-Rothery-type rules, which consider atomic size, electronegativities, and valence electron concentrations, to identify compositions of stable QCs.[40] Based on the nearly free-electron model according to Mott and Jones, the structure of a Hume-Rothery phase is influenced by the number of valence electrons that fill the electronic density of states (DOS).[41] Within the free electron model, the number of valence electrons per unit cell (*e/a* value) sets the Fermi wavevector k_f. If k_f lies close to Brillouin-zone boundaries, i.e., if $k_f \sim |K_{hkl}|/2$, then interactions between states at the Fermi surface can open a pseudogap in the DOS, so-called Brillouin-zone, Fermi surface (BZ-FS) interactions.[41] In general, the largest structure factors (*hkl*) in a PXRD pattern identify the Brillouin-zone boundaries $K_{hkl}/2$ leading to the most significant BZ-FS interactions. A survey of some reported CAs, e.g., $Mg_{27}Al_{10.7}Zn_{47.3}$,[42] $Sc_{11.18}Mg_{2.5}Zn_{73.6}$,[36] $Ca_3Au_{12.07}Ga_{6.93}$,[10c] and $(Yb/Ca)_{13}Cd_{76}$),[8b] shows that, when considering peaks above 20% relative to the maximum intensity with *d*-spacings < 3.0 Å, the average VEC is 1.967 *e/a* (Table S7). For the cubic 2/1 CA $Ca_{13}Au_{56.79(6)}Al_{21.20}$, the most intense PXRD peaks fall in the region 24.81–30.67 nm^{-1} and lead to VEC values spanning 1.208 to 2.108 *e/a*, averaging 1.814 *e/a*, which corresponds to a composition $Ca_{13}Au_{47.46}Al_{30.54}$ (Table S7). These VEC values fall at the border between Hume-Rothery and polar intermetallic classifications[13] even though not all the compounds evaluated contain elements that may participate in polar-covalent interactions as typically found for polar intermetallics.

The i-QC and its cubic 2/1 CA $CaAu_{4.50-x}Al_{1.50+x}$ also exhibit general chemical features similar to previously reported systems. Many Tsai-type CAs and i-QCs have the condensed formulation $AB_{5.3-6.0}$ where "A" represents an active, electropositive metal and "B" is either a group 12 element or a combination of late d-block and early p-block elements as seen in polar intermetallics. In many cases, "A" is a divalent or trivalent metal and "B" is Cd or a combination of a group 11 element with a group 13/14 element. For example, $(Ca/Yb)_{13}Cd_{76}$[8b] (VEC = 2.00 e/a) and $Sc_{16}Cu_{46}Al_{38}$ i-QC (VEC = 2.08 e/a)[43] can be formulated, respectively, as $(Ca/Yb)Cd_{5.846}$ and $Sc(Cu_{0.548}Al_{0.452})_{5.25}$. For a few examples of Bergman-type CAs with a monovalent active metal, the condensed formulation is $AB_{2.0-2.4}$. For instance, the i-QCs Li_3CuAl_6[44] (VEC = 2.20 e/a) and $Na_{13}Au_{12}Ga_{15}$[45] (VEC = 1.75 e/a) can be reformulated, respectively, as $Li(Cu_{0.143}Al_{0.857})_{2.33}$ and $Na(Au_{0.444}Ga_{0.556})_{2.08}$. Many of these Bergman- and Tsai-type CAs and i-QCs fall under the larger umbrella of polar intermetallic compounds based on their chemical compositions, even though they may span both the Hume-Rothery and polar intermetallics classifications based on VEC alone (Table S8). Thus, $Ca_{13}Au_{56.79(6)}Al_{21.20}$, reformulated as $Ca(Au_{0.73}Al_{0.27})_6$, also follows the "polar intermetallics" classification, in which (Au + Al) atoms are the more electronegative species that generally share the same shells and Ca atoms form their own shell as previously described (Figure 3).

Prediction of a 1/1 Ca–Au–Al CA using Electronic Structure Theory. From the experimentally determined quasilattice (a_{QC} = 5.383(4) Å) and using Equation (1), a hypothetical Ca–Au–Al 1/1 CA would have a cubic lattice of $a_{1/1}$ = ~14.818 Å. Using the sequence of atomic clusters in the Tsai-type 2/1 CA, in which the innermost shell is simplified to a single, fully occupied tetrahedron, and the atomic coordinates of the 1/1 CA $Ca_3Au_{12.07}Ga_{6.93}$ (space group $Im\bar{3}$, No. 204),[10c] a 1/1 CA "$Ca_{24}Au_{88}Al_{64}$" (VEC = 1.86 e/a)

hypothetical model was derived in the subgroup $I23$ (No. 197) (Table S9). Although the calculated total DOS of "Ca$_{24}$Au$_{88}$Al$_{64}$" shows no obvious gaps or pseudogaps (Figure S12), the band structure near the zone center shows gaps for energy ranges corresponding to valence electron counts of 1.966–1.993 e/a, i.e., "Ca$_{24}$Au$_{79.00-x}$Al$_{73.00+x}$" ($0 \le x \le 2.375$), 1.847–1.864 e/a, i.e., "Ca$_{24}$Au$_{89.50-x}$Al$_{62.50+x}$" ($0 \le x \le 1.50$), and 1.759–1.774 e/a, i.e., "Ca$_{24}$Au$_{97.25-x}$Al$_{54.75+x}$" ($0 \le x \le 1.375$). Therefore, theoretically, these predicted compositions are a good starting target for synthesizing the 1/1 CA.

Summary

For the targeted compositions Ca$_{1.00(4)}$Au$_{4.50-x}$Al$_{1.50(6)+x}$ ($0.11(6) \le x \le 0.44$) (VEC = 1.60–1.70 e/a), a primitive i-QC was produced from quenching, and its cubic 2/1 CA was discovered from annealing. The cubic 2/1 CA Ca$_{13}$Au$_{56.79(6)}$Al$_{21.20}$ (CaAu$_{4.37(1)}$Al$_{1.63}$; $Pa\bar{3}$ (No. 205); Pearson symbol: $cP728$; $a = 23.8918(2)$ Å) crystallizes in a series of concentric shells following the Tsai-type prescription, but with its outermost shell described as interpenetrating and edge-sharing icosahedra. Furthermore, the minor components Ca and Al generally prefer to avoid nearest neighbor homoatomic Ca−Ca and Al−Al contacts based on analysis of site occupancies and their various coordination environments. This i-QC and its cubic 2/1 CA belong to the general category of polar intermetallics in which the electronegative metals (Au + Al) share atomic shells and the formally electropositive Ca atoms form their own intervening shells to create significant polar-covalent Ca−(Au+Al) interactions for structural cohesion. Single-crystal XRD data obtained by the precession technique at the synchrotron APS show correlations between the primitive i-QC and its cubic 2/1 CA along the ([1 0 0]) 2- and ([1 1 1]) $\bar{3}$-fold rotational axes but the $\bar{5}$-fold rotational axis of the i-QC is no longer observed along the analogous direction ([3 0 5]) of the 2/1 CA. TEM SAED patterns of the three zone axes

provide further confirmation for the icosahedral symmetry in the i-QC and the lack thereof in the 2/1 CA. *In-situ*, variable-temperature PXRD data collected at the APS demonstrate that the i-QC irreversibly transforms into its cubic 2/1 CA starting at ~570 °C and completing at ~650 °C, based on peak splitting analysis in the regions of scattering lengths ~25–26 nm^{-1} and ~28–30 nm^{-1}. The stability of the cubic 2/1 CA $Ca_{13}Au_{56.79(6)}Al_{21.20}$ can be rationalized via a Hume-Rothery mechanism using VEC evaluated from the most intense peaks in the PXRD patterns, so that the hypothetical average composition that may lead to a pseudogap in the DOS is $Ca_{104.01}Au_{379.70}Al_{244.29}$ (VEC = 1.814 *e/a*). Using electronic structure calculations, a hypothetical cubic 1/1 CA was examined and the composition "$Ca_{24}Au_{88}Al_{64}$" is proposed as a good starting point to prepare a 1/1 CA of the i-QC.

Supporting Information in APPENDIX C

Supporting Information (SI) with the following is available: Rietveld refinements of the atomic coordinates and lattice parameters of the observed PXRD patterns; Calculated and experimentally determined quasilattices and lattices of all known CAs in Ca–Au–Al; Refined crystallographic data of the 2/1 CA for all atoms in the asymmetric unit; High-(atomic) resolution images of the 2/1 CA along the $\bar{3}$-fold axis; *In-situ*, high-energy, variable-temperature PXRD patterns of the i-QC–to–2/1 CA transformation; Fitting of the PXRD peak intensity, position, and area in the regions that showed the i-QC–to–2/1 CA transformation; Thermal analysis of an i-QC sample; *In-situ*, variable-temperature PXRD of the 2/1 CA; Survey of CAs and their *e/a* and i-QCs with condensed compositions; and Crystallographic information, DOS, and band structure for a hypothetical 1/1 CA "$Ca_{24}Au_{88}Al_{64}$".

Acknowledgements

References

1. (a) Levine, D.; Steinhardt, P. J., Quasicrystals: A new class of ordered structures. *Physical Review Letters* **1984**, *53* (26), 2477-2480; (b) Levine, D.; Steinhardt, P. J.; Quasicrystals, I., Definition and structure. *Phys. Rev. B* **1986**, *34*, 596; (c) Shechtman, D.; Blech, I.; Gratias, D.; Cahn, J. W., Metallic phase with long-range orientational order and no translational symmetry. *Physical Review Letters* **1984**, *53* (20), 1951-1953.

2. (a) Steurer, W.; Deloudi, S., Decagonal quasicrystals–What has been achieved? *Comptes Rendus Physique* **2014**, *15* (1), 40-47; (b) Steurer, W., Why are quasicrystals quasiperiodic? *Chemical Society Reviews* **2012**, *41* (20), 6719-6729.

3. Steurer, W.; Deloudi, S., Fascinating quasicrystals. *Acta Crystallographica Section A* **2008**, *64* (1), 1-11.

4. (a) Goldman, A. I.; Kelton, R. F., Quasicrystals and crystalline approximants. *Reviews of Modern Physics* **1993**, *65* (1), 213-230; (b) Dong, C., The concept of the approximants of quasicrystals. *Scripta Metallurgica et Materialia* **1995**, *33* (2), 239-243; (c) Gómez, C. P.; Tsai, A. P., Crystal chemistry and chemical order in ternary quasicrystals and approximants. *Comptes Rendus Physique* **2014**, *15* (1), 30-39.

5. (a) Steurer, W., Stable clusters in quasicrystals: fact or fiction? *Philosophical Magazine* **2006**, *86* (6-8), 1105-1113; (b) Guyot, P.; Audier, M., Quasicrystals and atomic clusters. *Comptes Rendus Physique* **2014**, *15* (1), 12-17.

6. Mackay, A., A dense non-crystallographic packing of equal spheres. *Acta Crystallographica* **1962**, *15* (9), 916-918.

7. Bergman, G.; Waugh, J. L. T.; Pauling, L., The crystal structure of the metallic phase $Mg_{32}(Al, Zn)_{49}$. *Acta Crystallographica* **1957**, *10* (4), 254-259.

8. (a) Guo, J. Q.; Abe, E.; Tsai, A. P., Stable icosahedral quasicrystals in binary Cd–Ca and Cd–Yb systems. *Physical Review B*: *Condensed Matter and Materials Physics* **2000**, *62* (22); (b) Gómez, C. P.; Lidin, S., Structure of $Ca_{13}Cd_{76}$: A novel approximant to the $MCd_{5.7}$ quasicrystals (M=Ca, Yb). *Angewandte Chemie International Edition* **2001**, *40* (21), 4037-4039.

9. (a) Gebresenbut, G. H.; Tamura, R.; Eklöf, D.; Gómez, C. P., Syntheses, optimization, structural, and thermoelectric properties of 1/1 Tsai-type quasicrystal approximants in RE–Au–SM systems (RE = Yb, Gd and SM = Si, Ge). *Journal of Physics: Condensed Matter* **2013**, *25* (13), 135402; (b) Ishimasa, T.; Tanaka, Y.; Kashimoto, S., Icosahedral quasicrystal and 1/1 cubic approximant in Au–Al–Yb alloys. *Philosophical Magazine* **2011**, *91* (33), 4218-4229.

10. (a) Hafner, J.; Krajcí, M., Electronic structure of rational approximants to icosahedral quasi-crystals. *EPL (Europhysics Letters)* **1992**, *17* (2), 145; (b) Mizutani, U.; Sato, H., The physics of the Hume-Rothery electron concentration rule. *Crystals* **2017**, *7* (1), 9; (c) Lin, Q.; Corbett, J. D., Approximant phases and an icosahedral quasicrystal in the Ca−Au−Ga system: The influence of size of Gallium versus Indium. *Inorganic Chemistry* **2008**, *47* (17), 7651-7659; (d) Nayak, J.; Maniraj, M.; Gloskovskii, A.; Krajčí, M.; Sebastian, S.; Fisher, I. R.; Horn, K.; Barman, S. R., Bulk electronic structure of Zn–Mg–Y and Zn–Mg–Dy icosahedral quasicrystals. *Physical Review B: Condensed Matter Materials Physics* **2015**, *91* (23), 235116; (e) Mihalkovič, M.; Richmond-Decker, J.; Henley, C. L.; Oxborrow, M., Ab-initio tiling and atomic structure for decagonal ZnMgY quasicrystal. *Philosophical Magazine* **2014**, *94* (14), 1529-1541; (f) Fujiwara, T., Electronic structure in the Al–Mn alloy crystalline analog of quasicrystals. *Physical Review B: Condensed Matter Materials Physics* **1989**, *40* (2), 942-946.

11. Takakura, H.; Gómez, C. P.; Yamamoto, A.; De Boissieu, M.; Tsai, A. P., Atomic structure of the binary icosahedral Yb–Cd quasicrystal. *Nature Materials* **2007**, *6* (1), 58-63.

12. Cui, C.; Shimoda, M.; Tsai, A. P., Studies on icosahedral Ag–In–Yb: A prototype for Tsai-type quasicrystal. *RSC Advances* **2014**, *4*, 46907-46921.

13. Miller, G. J.; Reedijk, J.; Poeppelmeier, K. R., Metal-rich compounds of the *d*-metals. *Comprehensive Inorganic Chemistry II* **2013**, *2*, 311-357.

14. Mizutani, U. Crystal Structures of Gamma-Brasses. In *Hume-Rothery Rules for Structurally Complex Alloy Phases*; CRC Press Taylor & Francis Group: Boca Raton, FL., USA **2010**; pp 299-324.

15. Liu, J.-F.; Yang, Z.-Q.; Ye, H.-Q., Direct observation of solid-state reversed transformation from crystals to quasicrystals in a Mg alloy. *Scientific Reports* **2015**, *5*, 9816.

16. Travessa, D. N.; Cardoso, K. R.; Wolf, W.; Jorge Junior, A. M.; Botta, W. J., The formation of quasicrystal phase in Al–Cu–Fe system by mechanical alloying. *Materials Research* **2012**, *15*, 749-752.

17. (a) Shalaeva, E. V.; Prekul, A. F., Structural phase transformations in quasicrystal-forming Al–Cu–Fe alloys and defects of the icosahedral phase. *The Physics of Metals and Metallography* **2010**, *109* (4), 392-401; (b) Quiquandon, M.; Quivy, A.; Devaud, J.; Faudot, F.; Lefebvre, S.; Bessière, M.; Calvayrac, Y., Quasicrystal and approximant structures in the Al–Cu–Fe system. *Journal of Physics: Condensed Matter* **1996**, *8* (15), 2487.

18. (a) Joulaud, J. L.; Capitán, M. J.; Haüsermann, D.; Lefebvre, S.; Calvayrac, Y., Structural study of approximant phases of Al–Cu–Fe quasicrystals under high pressure. *Physical Review B: Condensed Matter Materials Physics* **1999**, *59* (5), 3521-3526; (b) Lefebvre, S.; Bessièref, M.; Calvayrac, Y.; ltié, J. P.; Polian, A.; Sadoc, A., Stability of icosahedral Al–Cu–Fe and two approximant phases under high pressure up to 35 GPa. *Philosophical Magazine* **1995**, *72* (1), 101-113.

19. Stagno, V.; Bindi, L.; Shibazaki, Y.; Tange, Y.; Higo, Y.; Mao, H. K.; Steinhardt, P. J.; Fei, Y., Icosahedral AlCuFe quasicrystal at high pressure and temperature and its implications for the stability of icosahedrite. *Scientific Reports* **2014**, 4, 5869.

20. Takeuchi, T.; Murasaki, S.; Matsumuro, A.; Mizutani, U., Formation of quasicrystals and approximant crystals by mechanical alloying in Mg–Al–Zn alloy system. *Journal of Non-Crystalline Solids* **1993**, *156*, 914-917.

21. Lee, C.-S.; Miller, G. J., Where are the elements in complex aluminides? An experimental and theoretical investigation of the quasicrystalline approximants, $Mg_{2-y}(Zn_xAl_{1-x})_{3+y}$. *Journal of the American Chemical Society* **2000**, *122* (20), 4937-4947.

22. Pham, J.; Kreyssig, A.; Goldman, A. I.; Miller, G. J., An icosahedral quasicrystal and its 1/0 crystalline approximant in the Ca–Au–Al System. *Inorganic Chemistry* **2016**, *55* (20), 10425-10437.

23. SMART, version 5; Bruker AXS: Madison, WI, USA, **2003**.

24. Sheldrick, G. M. SADABS; University of Gottingen: Gottingen, Germany, **2001**.

25. (a) Sheldrick, G., A short history of SHELX. *Acta Crystallographica Section A* **2008**, *64* (1), 112-122; (b) Sheldrick, G., SHELX, version 6.14; Bruker AXS: Madison, WI, USA, **2000-2003**.

26. Goldman, A. I.; Kreyssig, A.; Nandi, S.; Kim, M. G.; Caudle, M. L.; Canfield, P. C., High-energy X-ray diffraction studies of i-$Sc_{12}Zn_{88}$. *Philosophical Magazine* **2011**, *91* (19-21), 2427-2433.

27. Hammersley, A. P. FIT2D, version 9.129; ESRF: Grenoble, France, **1998**.

28. Roisnel, J. R.-C. T., *FullProf*.98 and WinPLOTR: New Windows 95/NT Applications for Diffraction Commission for Powder Diffraction, International Union for Crystallography: London, **1998**.

29. WinXPOW; STOE & Cie GmbH: Darmstadt, Germany, **2006**.

30. Rietveld, H., A profile refinement method for nuclear and magnetic structures. *Journal of Applied Crystallography* **1969**, *2* (2), 65-71.

31. Petricek, V.; Dusek, M.; Palatinus, L., Jana2006; International Union for Crystallography: London, **2014**.

32. (a) Yaguchi, T.; Kamino, T.; Ishitani, T.; Urao, R., Method for cross-sectional transmission electron microscopy specimen preparation of composite materials using a dedicated focused ion beam system. *Microscopy and Microanalysis* **2002**, *5* (5), 365-370; (b) Giannuzzi, L. A.; Kempshall, B. W.; Schwarz, S. M.; Lomness, J. K.; Prenitzer, B. I.; Stevie, F. A., FIB lift-out specimen preparation techniques. In *Introduction to Focused Ion Beams: Instrumentation, Theory, Techniques and Practice*, Eds. Giannuzzi, L. A.; Stevie, F. A., Springer: Boston, MA, USA, **2005**; pp 201-228.

33. (a) Blöchl, P. E., *Physical Review B: Condensed Matter Materials Physics* **1994**, *50*, 17953; (b) Kresse, G.; Hafner, J., *Physical Review B: Condensed Matter Materials Physics* **1993**, *47*, 558; (c) Kresse, G.; Furthmüller, F., *Computational Materials Science* **1996**, *6*, 15.

34. Perdew, J. P.; Burke, K.; Ernzerhof, M., Generalized gradient approximation made simple. *Physical Review Letters* **1996**, *77*, 3865.

35. Cahn, J. W.; Shechtman, D.; Gratias, D., Indexing of icosahedral quasiperiodic crystals. *Journal of Materials Research* **1986**, *1*, 13-26.

36. Lin, Q.; Corbett, J. D., The 1/1 and 2/1 Approximants in the Sc–Mg–Zn quasicrystal system: Triacontahedral clusters as fundamental building blocks. *Journal of the American Chemical Society* **2006**, *128* (40), 13268-13273.

37. Stevenson, S.; Phillips, J. P.; Reid, J. E.; Olmstead, M. M.; Rath, S. P.; Balch, A. L., Pyramidalization of Gd_3N inside a C_{80} cage. The synthesis and structure of $Gd_3N@C_{80}$. *Chemical Communications* **2004**, (24), 2814-2815.

38. Porterfield, W. W., *Inorganic chemistry: A unified approach*. Addison Wesley Pub. Co.: Reading, MA, USA, **1984**.

39. Pauling, L., The nature of the chemical bond and the structure of molecules and crystals: An introduction to modern structural chemistry. 3rd ed.; Cornell University Press: Ithaca, NY, USA, **1960**.

40. Tsai, A. P., A test of Hume-Rothery rules for stable quasicrystals. *Journal of Non-Crystalline Solids* **2004**, 317-322.

41. Berger, R. F.; Walters, P. L.; Lee, S.; Hoffmann, R., Connecting the chemical and physical viewpoints of what determines structure: From 1-D chains to γ-brasses. *Chemical Reviews* **2011**, *111* (8), 4522-4545.

42. Lin, Q.; Corbett, J. D., New building blocks in the 2/1 crystalline approximant of a Bergman-type icosahedral quasicrystal. *Proceedings of the National Academy of Sciences* **2006**, *103* (37), 13589-13594.

43. Honma, T.; Ishimasa, T., New icosahedral quasicrystals formed in Cu-based ternary alloys. *Philosophical Magazine* **2007**, *87* (18-21), 2721-2726.

44. Audier, M.; Pannetier, J.; Leblanc, M.; Janot, C.; Lang, J.-M.; Dubost, B., An approach to the structure of quasicrystals: A single-crystal X-ray and neutron diffraction study of the R-Al$_5$CuLi$_3$ phase. *Physica B: Condensed Matter* **1988**, *153* (1–3), 136-142.

45. Smetana, V.; Lin, Q.; Pratt, D.; Kreyssig, A.; Ramazanoglu, M.; Corbett, J.D.; Goldman, A.I.; Miller, G.J., A sodium-containing quasicrystal: using gold to enhance sodium's covalency in intermetallic compounds. *Angewandte Chemie International Edition* **2012**, *51* (51), 12699-12702.

CHAPTER 6

AAuAl (A = Ca, Sc, AND Ti): PEIERLS DISTORTION, ATOMIC COLORING, AND STRUCTURAL COMPETITION

To be submitted for publication in spring 2018

Joyce Pham[†] and Gordon J. Miller[*, †, §]

[†]Department of Chemistry, Iowa State University,
[§]U.S. Department of Energy, Ames Laboratory, Ames, Iowa, 50011–3111
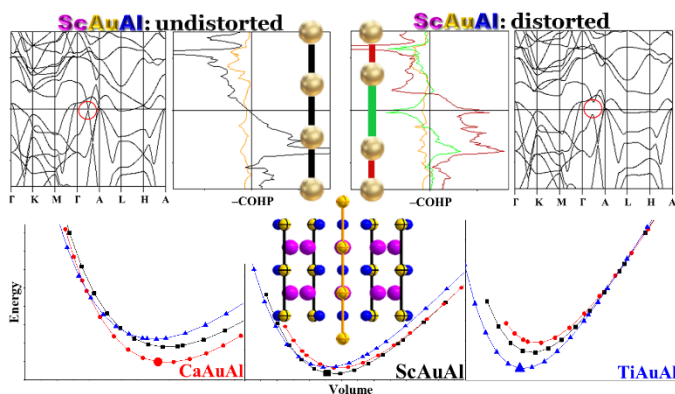
Abstract

Using density functional theory, the crystal structure variation of AAuAl (A = Ca, Sc, and Ti) from orthorhombic Co_2Si-type to distorted hexagonal Fe_2P- and then Ni_2In-structure types is shown to correlate with their electronic structures and valence electron counts, sizes of the active metals A, and site preferences for Au and Al atoms, which are arranged to maximize Au−Al nearest neighbor contacts. An evaluation of chemical pressure imposed by the varying A metals using total energy vs. volume calculations indicates that larger unit cell volumes favor the orthorhombic structure whereas smaller volumes favor the hexagonal structures. The electronic origin of the Mg_2Ga-type crystal structure of ScAuAl, refined as a distorted Fe_2P-type supercell doubled along the c-axis, indicates a Peierls-type distortion mechanism of the Au-chains along the *c*-axis.

Introduction

Polar intermetallic compounds containing Au exhibit diverse structures ranging from large clusters and networks of complex polyhedra and even quasicrystals,[1] to smaller atomic coordination spheres and 2-dimensional building blocks.[2] A defining characteristic of this class is the occurrence of polar-covalent interactions between the formally electropositive metals from groups 1–4 including rare-earth elements, and the more electronegative elements from the late transition metals and early p-block. The more electronegative metals form complex clusters or networks with large voids that are filled by the electropositive metals for structural cohesion.[3] To date, there lacks a holistic set of fundamental algorithms to predict and rationalize the diverse structures observed for polar intermetallic compounds, such as those like the octet rule, valence electron-to-atom (e/a) values, or metallic radius ratios proposed for Zintl-Klemm or Hume-Rothery phases.[4]

A widely used "rule of thumb" to categorize polar intermetallic structures involves using valence electron concentrations (VECs), which are evaluated as the sum of the total number of valence ($s+p+d$) electrons per formula unit (e^-/fu). For the simplest ternary stoichiometry 1:1:1, there are already more than 2000 polar intermetallic compounds reported with many containing Au because it is the most electronegative metal according to Mulliken and Pauling electronegative values.[5] Some of the commonly observed structures and their corresponding VEC values for 1:1:1 compounds are as follows:[5-6] (1) orthorhombic TiNiSi (Co_2Si-derivative)-type with 15–18e^-/fu, and is considered one of the most ubiquitous structure types discussed herein; (2) hexagonal Fe_2P-type with 15–19e^-/fu but observed mostly for compositions with 18e^-/fu; and (3) hexagonal $CaIn_2$- and Ni_2In-type structures, which are observed for compounds with 13–18e^-/fu. For the 1:1:1 compositions containing Au in the

Inorganic Chemistry Structural Database (ICSD), there are 15 compounds in the Fe_2P-type structure, and all except for LuAuAl ($17e^-/fu$) and MgAuGa ($16e^-/fu$) are reported with In. If Al replaces In in these compounds, the TiNiSi-type structure is observed instead, and of these 21 compounds with Au, 15 contain both Au and Al, in which all except for CaAuAl ($16e^-/fu$) contains $17e^-/fu$. In total, there are 62 compounds containing Au in the $CaIn_2$- or Ni_2In-type structure, in which only TiAuAl (Ni_2In-type; $18e^-/fu$) contains both Au and Al so that 50 of the 62 compounds all contain $18e^-/fu$. From these VEC trends, it seems that most 1:1:1 polar intermetallic compounds containing both Au and In would crystallize in the Fe_2P-type structure, but that those with both Au and Al would more likely crystallize in the TiNiSi-type, although the Ni_2In-type is plausible as well. However, VEC does not solely distinguish any of these common structure types (Co_2Si/TiNiSi, Fe_2P, and Ni_2In or $CaIn_2$), so that other factors contributing to the structural variation may be size effects, an understanding of which may be fruitful for investigations using variable pressure to induce structural transitions.

In addition to relationships between VECs and the structure-types discussed above, variations of atomic coordinates in the structure types due to distortions or atomic arrangements ("coloring")[7] on going from binary to ternary phases lead to additional structural derivatives. For instance, the Mg_2Ga-type ($hP18$) structure is a subtly distorted supercell of the Fe_2P-type with a doubled c-axis, so that ZrNiAl and HfRhSn are ternary derivatives of Fe_2P and Mg_2Ga, respectively.[8] The question remains about the factors influencing the occurrence of Mg_2Ga-type over its more popular Fe_2P-type subcell. Similarly, within the $CaIn_2$ family, the isopointal NdPtSb and LiGaGe structures differ in their interlayer interactions along the c-axis so that even though both possess hexagonal chair conformations ($[Pt_3Sb_3]$ and $[Ga_3Ge_3]$, respectively) within the puckered honeycomb net of electronegative metal/metalloid atoms,

the former exhibits 2-dimensional characteristics whereas the latter features a 3-dimensional tetrahedral network. Again, what factors give rise to these two isopoints within the $CaIn_2$ structure type?

To contribute to an understanding of the diverse structures among such 1:1:1 polar intermetallics, herein we examine the ScAuAl structure (distorted Fe_2P-type; $17e^-/fu$), which was recently reported to adopt the HfRhSn structure-type (Mg_2Ga ternary derivative).[9] We discuss its bonding features, electronic structure and stability, atomic size effects and site preferences, and compare its energetics with competing structure types to rationalize the existence of ScAuAl in the Fe_2P-type and its distortion to the Mg_2Ga supercell as opposed to the TiNiSi- , Ni_2In-, and Ca_2In-type structures. Moreover, we perform analogous studies on its neighbors TiNiSi-type CaAuAl ($16e^-/fu$) and Ni_2In-type TiAuAl ($18e^-/fu$).

Experimental Section

Synthesis. ScAuAl was initially found as a product in the search for quasicrystals and their crystalline approximants within the Sc–Au–Al system. A stoichiometric loading confirms its formation using an annealing heating scheme in contrast to the report of its existence from an arc melting synthesis.

Sc chunks (99.9%, APL-Aldrich), Au spheres (99.99%, Ames Laboratory), and Al ingots (99.999% Alfa-Aesar) were weighed for molar ratios 1Sc: 2Au: 5Al and 1Sc: 1Au: 1Al, with sample sizes totaling 300.0(1) mg. Reaction mixtures were loaded into tantalum ampoules in a glovebox under argon atmosphere, with moisture levels at ≤ 0.1 ppm. The tantalum reaction vessels were then arc-welded shut and subsequently sealed under vacuum in a secondary silica jacket to avoid oxidation of the tantalum during heating to reaction temperatures. All reactions were heated in a tube furnace to 1050 ℃ for 30 hours, slowly

cooled at 10 ºC/h to 700 ºC and held at this temperature for 15 days, after which they were quenched by rapid submersion into room temperature water.

Powder X-ray diffraction. Phase analysis was carried out using powder X-ray diffraction (PXRD) data collected on the Stoe Stadi P diffractometer equipped with a position-sensitive image-plate detector and a Cu $K_{\alpha 1}$ radiation source ($\lambda = 1.54060$ Å). Ground samples were dispersed onto and sandwiched between two transparent acetate films with the aid of vacuum grease. To ensure instrument alignment, a Si powder standard (to compare against sample ICSD # 53783) was mixed with each preliminary scan of the specimen.[10] Data were acquired over a 1-hr exposure period with step sizes of 0.03º in 2θ, and were analyzed by juxtaposing the observed PXRD patterns against theoretical PXRD patterns calculated from single-crystal XRD refined models and those of reported binary compounds containing the constituent elements.

Single crystal X-ray diffraction. Diffraction data for selected crystals were collected on a Bruker SMART[11] APEX II CCD diffractometer with graphite-monochromatized Mo $K_{\alpha 1}$ radiation ($\lambda = 0.71073$ Å) at ambient conditions between one hemisphere to a full sphere in reciprocal space in ω at 20–30 s exposure time per frame.

For the sample chosen from the 1:2:5 loading included in the main text, 2160 frames were collected over an 18 h exposure period and these frames were integrated using the Bruker SAINT software package, which yielded 7792 total peaks in the hexagonal unit cell for θ_{max} of 31.27º (0.68 Å resolution). The final unit cell parameters were based upon refinements of XYZ-centroids of the 2268 reflections with intensities exceeding $20\sigma(I)$ and scattering angles 2θ between 11.26º and 62.05º. Data were corrected empirically for absorption using the multi-scan method in the program SADABS,[12] from which the ratio of maximum transparent

transmission was 0.446.[13] Analogously, for the sample chosen from the 1:1:1 loading in the main text, 1800 frames were collected with a total exposure time of 15 h that yielded 4550 total peaks in the hexagonal unit cell for θ_{max} of 28.87º (0.74 Å resolution). The unit cell parameters were calculated from refinements of *XYZ*-centroids of the 1329 reflections in scattering angles 2θ between 11.25º and 56.62º with a ratio of 0.438 maximum transmission.

Using the program XPREP,[14] determination of the space group $P\bar{6}2m$ emerged for ScAuAl crystals selected for samples loaded as 1Sc: 2Au: 5Al, so that doubling the *c*-axis to achieve the space group $P\bar{6}2c$ was performed manually. Using the same software, the space group $P\bar{6}2c$ was selected for crystals from sample loadings 1Sc: 1Au: 1Al. All structural models were solved in the SHELXTL 6.14 program suite[15] using direct methods and refined from the full-matrix least-squares fitting of observed structure factors with final refinements that included anisotropic displacements and secondary extinction parameters. The absolute structural parameters were refined to account for the non-centrosymmetric characteristics of $P\bar{6}2m$ and $P\bar{6}2c$.[16] Structure Tidy of the WinGX-Platon program suite was used to standardize the crystallographic sites and to invert and realign the origin of the raw/observed *hkl* data.

Atomic site preference, Bader charge analysis, formation energy, and electronic structure. To rationalize the ScAuAl atomic arrangement ("coloring"), first principles electronic structure calculations using VASP 5.2 was carried out on its subcell (Fe_2P-type).[17] The projected augmented wave GGA-PBE method (generalized gradient approximation with exchange correlation potentials as constructed by Perdew, Burke, and Ernzerhof)[18] was employed for six different isocompositional coloring models and their total energies were calculated and compared. For all calculations, the energy cutoff was 500 eV, the self-consistent convergence criterion was 0.01 meV, and the orbital basis set included $Sc(3p^6 4s^2 3d^1)$,

$Au(5d^{10}6s^1)$, and $Al(3s^23p^1)$. For each model, the numbers of various interatomic interactions (i.e., Sc–Au/Al, Sc–Sc, and Al/Au–Al/Au,) were assessed to rationalize the atomic site preference of the experimental ScAuAl subcell. Analogous site-preference studies were also performed on the CaAuAl and TiAuAl neighbors with additional orbital bases $Ca(3s^23p^64s^2)$ and $Ti(3p^64s^23d^1)$.[19] To further assess the ordering of Au and Al atoms in ScAuAl, a Bader charge analysis from the results of VASP structural optimizations was carried out on the experimental model of ScAuAl and on "$ScCd_2$," in which the atomic sites with the greatest charge were assigned to the more electronegative metal Au.[20]

The AAuAl (A = Ca, Sc, Ti) formation energies ($\Delta E_{reaction}$) were calculated from the respective elements and reported binary structures Au_2Al, $AuAl_2$, AAu_2, Au_2A (A = Sc only), AAl_2, and A_2Al (A = Sc only) after VASP optimization.[21] Additionally, structural optimizations and total energy calculations were carried out for the competing structures: TiNiSi (Co_2Si-derived); NdPtSb, LiGaGe and ScAuSi (all $CaIn_2$-derived); Ni_2In; and Cu_2Sb.[22] For all models, the numbers of interatomic interactions (A–Au/Al, A–A, and Al/Au–Al/Au) per formula unit were evaluated to rationalize the observed AAuAl (A = Ca, Sc, Ti) structural trend. Additionally, chemical pressure effects were investigated using calculated total energies as a function of unit cell volume for the competing structures CaAuAl (R_{Ca} = 1.97 Å; TiNiSi-type), ScAuAl (R_{Sc} = 1.64 Å; Fe_2P substructure), and TiAuAl (R_{Ti} = 1.47 Å; Ni_2In-type). Data were fitted using the Murnaghan potential to extract the volumes with lowest energies and their associated bulk moduli.

The electronic band structures, densities of states (DOS), and crystal orbital Hamilton population (COHP)[23] curves for pair-wise interactions less than 3.5 Å apart were calculated for AAuAl and their various competing structure types using the Stuttgart Tight-Binding

Linear Muffin-Tin Orbital Atomic Sphere Approximation (TB-LMTO-ASA) code, with scalar relativistic effects and the von Barth-Hedin local exchange-correlation potential,[24] but without spin-polarization or spin-orbit coupling. Input structural parameters for the TB-LMTO-ASA calculations of ScAuAl used the VASP optimized model of the experimental subcell (Fe_2P-type), whereas those of CaAuAl, TiAuAl, and the other competing structural models were taken from the experimentally reported structures directly.[19] The self-consistent calculation convergence limit was 0.01 meV, the maximum overlap before empty spheres were introduced was 18.7%, and the atomic orbital basis sets contained: Ca($4s$, $3d$) and Ca($4p$, $4f$) downfolded; Sc($4s$,$3d$) and Sc($4p$) downfolded; Ti($4s$, $4p$, $3d$); Au($6s$,$6p$,$5d$), and Au($5f$) downfolded, Al($3s$,$3p$) and Al($3d$) downfolded. The irreducible wedges of the first Brillouin zones used for plotting the DOS and subsequent COHP curves contained 3001 or 5001 k-points. See Table S13 for respective atomic Wigner-Seitz radii of each model.[25]

Results and Discussion

During the search for polar intermetallic quasicrystals and their crystalline approximants in the Ca–Au–Al system[1b] and as part of a broader investigation on the effects of atomic sizes (chemical pressure) and valence electron counts in such compounds, the Sc-poor region of the Sc–Au–Al system was examined. The loaded molar ratio 1Sc: 2Au: 5Al led to ScAuAl as the major phase with probable traces of at most two of Sc_2Al, ScAl, and $ScAl_2$ (unequivocal determination of the precise trace phase(s) cannot be made by X-ray powder diffraction). ScAuAl sits at the center of the Sc–Au–Al existence triangle (Figure 1), as well as a hexagon formed by tetragonal $MoSi_2$-type $ScAu_2$[21a] and Au_2Al;[26] cubic $MgCu_2$-type $ScAl_2$[21b] and CaF_2-type $AuAl_2$;[27] hexagonal Ni_2In-type Sc_2Al;[28] and orthorhombic Co_2Si-type Sc_2Au.[29] The only other Sc–Au–Al compound reported in the ICSD is the Heusler ($AlCu_2Mn$)-
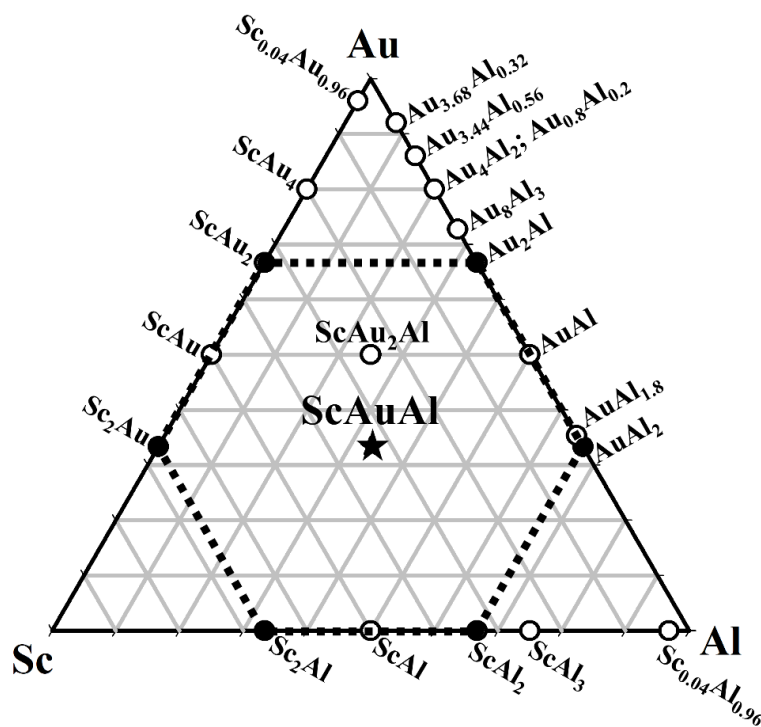
Figure 1. ScAuAl existence triangle showing ScAuAl sitting at the center of the MoSi$_2$-type ScAu$_2$, cubic MgCu$_2$-type ScAl$_2$, Ni$_2$In-type Sc$_2$Al, MoSi$_2$-type Au$_2$Al, Co$_2$Si-type Sc$_2$Au and CaF$_2$-type AuAl$_2$ hexagon.

type ScAu$_2$Al, which bisects the CsCl-type ScAu and AuAl along the 50% Au-content line.[30]

In the PXRD pattern from products of the 1Sc: 2Au: 5Al synthesis, the minor phases were assigned as follows: the two peaks at 2θ values ~26–27° were identified as belonging to Sc$_2$Al[28] and ScAl,[31] respectively, and those around 39° and 41° can be indexed for Sc$_2$Al and ScAl$_2$,[21b] respectively. However, no single binary or ternary compound from the Sc–Au–Al system could be conclusively assigned to all peaks, a result which calls for analysis using single-crystal XRD for possible new phase(s).

Three crystals were randomly selected from the product of the 1Sc: 2Au: 5Al loading and all crystallographic solutions refined initially to the composition ScAuAl, so that subsequent synthesis of this refined composition and single-crystal XRD analysis of randomly selected specimens from the sample confirmed its formation. However, preliminary structural
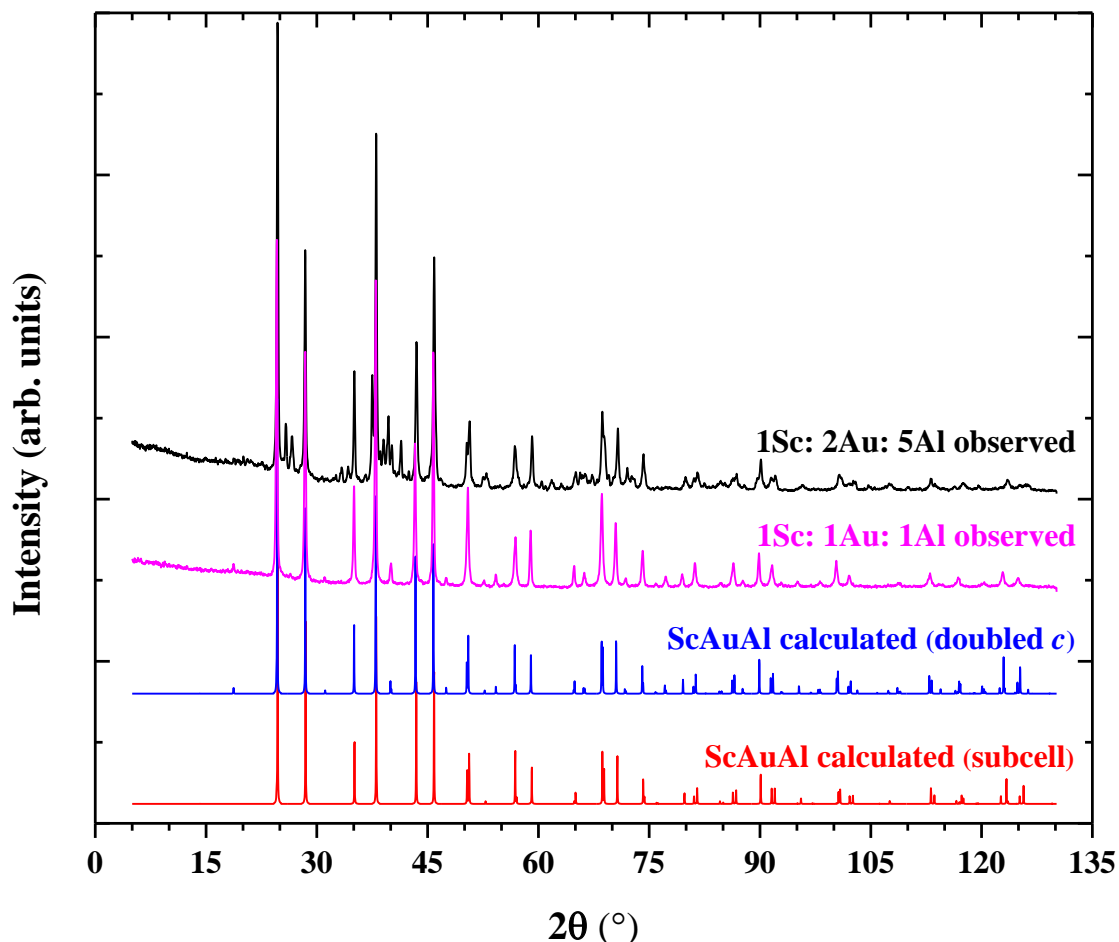
Figure 2. Observed and simulated PXRD patterns from refined single-crystal XRD data for both supercell (Mg$_2$Ga-type) and subcell (Fe$_2$P-type) in Sc–Au–Al.

solutions of crystals selected from the 1Sc: 1Au: 1Al loading differ from the 1Sc: 2Au: 5Al synthesis by a doubling of the unit cell along the *c*-axis in the pure phase sample (see Figure 2 for PXRD patterns). In the PXRD pattern of the doubled *c*-axis structure, the less intense peaks at 2θ values ~19°, 31°, 40°, 48°, 54°, 66°, 72°, and 77° are not clearly visible in the corresponding pattern for the product of the 1Sc: 2Au: 5Al loading. Therefore, subsequent investigations were aimed at assessing the origin of this structural variation by crystallographic refinements and electronic structural studies.

Crystallographic refinement and structure. During preliminary stages of this investigation, the structure of ScAuAl was reported to crystallize in the HfRhSn-type structure,

Table 1. ScAuAl selected crystallographic refinement parameters.

refined composition	ScAu$_{1.017(3)}$Al$_{0.983}$			ScAuAl		
instrument		Bruker CCD APEX II				
radiation; λ (Å)/ temp.(K)		Mo Kα; 0.71073/298				
space group/ Pearson symbol		$P\bar{6}2c$/ hP18				
loading	1Sc: 2Au: 5Al			1Sc: 1Au: 1Al		
θ range data collection/ param.	3.3°–31.3°/ 23			3.3°–29.0°/ 19		
absorp. coeff. μ (mm^{-1})/ correction	71.83/ empirical			69.90/ empirical		
meas./ indpnt./ obs. [I > 2σ(I)]/	7249/ 383/ 229			4550/ 307/ 291		
R[F^2 > 2σ(F^2)]/ wR(F^2)/ R_{int}/ GOF	0.015/ 0.039/ 0.035/ 1.05			0.018/ 0.036/ 0.035/ 1.15		
Δρ$_{max}$, Δρ$_{min}$ (e Å^{-3})	1.13, −0.96			1.35, −1.33		
dimensions (Å)	a = 7.2074(6); c = 7.2443(6)			a = 7.2362(10); c = 7.2448(10)		
volume (Å^3)/ Z	325.90(6)/ 6			328.53(10)/ 6		
index ranges	−10 ≤ h, k ≤ 10; −5 ≤ l ≤ 5			−9 ≤ h, k, l ≤ 9		
absolute structure parameter	0.00(3)			0.03(3)		
2b, x, y, z, U_{iso}	Au1	0, 0, 1/4	0.0092(2)	Au1	0, 0, 1/4	0.0077(2)
4f, x, y, z, U_{iso}	Au2 (0.54(2))	1/3, 2/3, 0.0195(9)	0.0100(5)	Au2	1/3, 2/3, 0.02100(6)	0.0079(2)
	Au3 (0.42(2))	2/3, 1/3, 0.0214(9)	0.0100(5)	--	--	--
6g, x, y, z, U_{iso}	Al/0.016(3)Au	0.2645(5), 0, 0	0.012(1)	Al	0.2628(6), 0, 0	0.0080(7)
6h, x, y, z, U_{iso}	Sc	0.4019(7), 0.4024(7), 1/4	0.0137(4)	Sc	0.4096(4), 0.3947(4), 1/4	0.0075(5)
2b–2b (c-axis), 2b–6g, 2b–6h	3.6221(3)	2.629(1)	2.899(6)	3.6224(5)	2.626(2)	2.912(3)
4f–4f (c-axis), 4f–6g, 4f–6h	3.312(9), 3.905(9)	2.689(2)	2.753(5), 2.942(6)	3.3181(8), 3.9267(8)	2.708(2)	2.831(2), 2.887(2)

which is a derivative of the Mg_2Ga-type and is a slightly distorted superstructure of the Fe_2P-type with a doubled c-axis caused by alternating long-short Au–Au chains along the c-direction.[8b, 9] ScAuAl specimens from the sample loaded as 1Sc: 2Au: 5Al yielded structures that can be refined in the Fe_2P-type with acceptable statistical assessment values ($R = 0.016$ for $F^2 > 2s(F^2)$; $wR(F^2) = 0.040$; $R_{int} = 0.032$; and GOF = 1.21; see Table S1). For this solution, there are four sites in the asymmetric unit: Au1($1a$), Au2($2d$), Al($3f$, $x = 0.2642(5)$), and Sc($3g$, $x = 0.5979(3)$), in which Au2($2d$) and Al($3f$) lie in the same plane, the $2d$–$2d$ Au2–Au2 distances along the c-axis are 3.6217(3) Å, and the $2d$–$3f$ Au2–Al distances in the ab-plane are 2.687(4) Å, but the U_{eq} value for the Au2($2d$) sites is substantially larger by factors of 1.9–2.3 over those for the Au1($1a$) and Al($3f$) sites. Manually doubling the unit cell, revising the space group to $P\bar{6}2c$, and assigning the Au2 sites to two $4f$ sites, each partially occupied but constrained to a total of 4 atoms, led to a refinement with the corresponding z-coordinates of the Au2($4f$) sites shifted 0.141(7) Å and 0.155(7) Å in opposite directions out of the Au-Al planes along c and resulting in Au–Au distances of 3.312(9) and 3.905(9) Å. Moreover, the occupancy factor of the Al($6h$) site was refined, resulting in 98.4(3)% Al/1.6% Au, and the U_{eq} of all sites were mutually similar in magnitudes. A statistical Hamilton test based on the number of parameters and weighted R-refinement values of the two models show that refinement of the subcell can be rejected at the 75% confidence level.[32] Thus, this optimal refinement yields $ScAu_{1.017(3)}Al_{0.983}$ in a disordered Mg_2Ga-type structure.

On the other hand, three specimens selected from the 1Sc: 1Au: 1Al loading can be refined directly in the Mg_2Ga-type superstructure with the Au2 ($4f$) and Al ($6g$) in the same plane, $4f$–$4f$ Au2–Au2 distances alternating at 3.3325(8) and 3.9162(8) Å (average: 3.6244(8)

Å) along c, and $4f$–$6g$ Au2–Al distances of 2.705(2) Å in the ab-plane. See Tables S2 and S4 for a crystallographic refinement summary.

According to the ICSD, ScAuAl is the only polar intermetallic compound with both Au and Al that crystallizes in the Mg_2Ga-type superstructure and LuAuAl is the only other polar intermetallic with Au and Al adopting the Fe_2P-type substructure. All other members of the LnAuAl series (Ln = Y, Ce to Yb) crystallize in the orthorhombic TiNiSi-type instead, which is also the structure reported for CaAuAl, to be discussed later.[33] The metallic radius of Lu (R_{Lu} = 1.73 Å) is smaller than that of the other lanthanides (Ln = Y, Ce−Yb), which vary from 1.75–2.04 Å (R_{Tm} = 1.75 Å, R_{Eu} = 2.04 Å), so that atomic size seems to play an important factor in the structural variation of A^{III}AuAl (A^{III} = trivalent electropositive metal), which favors the formation of the TiNiSi-type structure for larger electropositive metals, the Fe_2P-type for slightly smaller ones, and the Mg_2Ga-type for the smallest trivalent electropositive atom Sc (R_{Sc} = 1.64 Å). Therefore, the unit cell volume of the ScAuAl subcell is smaller (162.90(2) Å^3) than that of Fe_2P-type LuAuAl (177.36Å^3), a result arising mainly from a shortening of the c-axis, whereas the a- and b-axes lengthen (from 7.1033(4) Å to 7.2067(6) Å). Additionally, all interatomic contacts shorten on going from LuAuAl to ScAuAl, except the Al–Al interactions, which extend from 3.0758(2) Å to 3.2966(3) Å, and form the triangles of the [$Al_3(Au1)_2$] trigonal bipyramids in their structures.[33] To highlight the interactions between Au and Al atoms, which are more electronegative than Sc, there are also [$Al_3(Au2)_2$+Al1] "half-chair conformers" within the ScAuAl Fe_2P-substructure, features which are related to the [Au_3Ge_3] "chair conformers" in $18e^-/fu$ ScAuGe (LiGaGe-type.)[22e] On the other hand, for $16e^-/fu$ CaAuAl, the orthorhombic TiNiSi-type structure occurs, as seen for LnAuAl (Ln = Y, Ce−Yb), whereas $18e^-/fu$ TiAuAl adopts the hexagonal Ni_2In-type structure.[19] Therefore, the structural

Table 2. ScAuAl Bader charge analysis

	site	ScAuAl	"ScCd$_2$"	atom
	3g	1.65	1.93	Sc
Fe$_2$P	1a	13.94	12.50	Au1
	2d	13.26	12.76	Au2
	3f	1.86	12.40	Al
	6h	1.64	1.91	Sc
Mg$_2$Ga	2b	13.82	12.44	Au1
	4f	13.30	12.77	Au2
	6g	1.88	12.43	Al

variation from CaAuAl to ScAuAl to TiAuAl follows along TiNiSi-type to Mg$_2$Ga-type (Fe$_2$P-superstructure) to Ni$_2$In-type, which changes directly with decreasing metallic radius in the electropositive element (R_{Ca} = 1.97 Å, R_{Sc} = 1.64 Å, R_{Ti} = 1.47 Å).

Atomic site preference. Since the crystallographic refinements of ScAuAl yield structures that are subtle distortions from the hexagonal Fe$_2$P-type, the site preferences for different elements were analyzed using the smaller subcell (the calculated total energy of the experimental structure is just 6 meV lower than that of the Fe$_2$P model). Evaluating atomic colorings of a structural network involves evaluating factors contributing to the site energy and bond energy terms of the total band energy.[7] The site energy term can be qualitatively assessed using a Bader charge analysis on models that use the same atomic potentials for the sites being examined for differentiation. For ScAuAl, a Bader charge analyses of ScAuAl and hypothetical "ScCd$_2$" in both the Fe$_2$P- and Mg$_2$Ga-type structures corroborate the experimental coloring (see Table 2). For all models, the charges on the 1a (2b) and 2d (4f) sites are greater than those on the 3f (6g) sites and indicate their respective preferences for Au and Al based on their relative electronegativities.

To examine the bond energy term in ScAuAl, interatomic distances less than 3.4 Å, which is 0.12 Å greater than the Sc–Sc distances in hcp Sc, were taken into account in the

Table 3. ScAuAl atomic site preference from isocompositional coloring models.

(Å)	Experiment	α	β	γ	δ	ε
< 2.7	Au–Al (12×)	Au–Al (12×)	Sc–Au (12×)	Sc–Au (12×)	Sc–Al (12×)	Sc–Al (12×)
< 2.9	Sc–Au (15×)	Sc–Al (15×)	Au–Al (15×)	Sc–Al (15×)	Au–Al (15×)	Sc–Au (15×)
< 3.2	Sc–Al (18×)	Sc–Au (18×)	Sc–Al (16×)	Au–Al (16×)	Sc–Au (18×)	Au–Al (18×)
< 3.4	Al–Al (3×)	Au–Au (3×)	Sc–Sc (3×)	Au–Au (3×)	Sc–Sc (3×)	Al–Al (3×)
eV/f.u.	0	+0.347	+0.960	+1.480	+1.759	+2.112

Fe$_2$P-type model. Thus, there are seven different interatomic contacts (2.638(5), 2.681(1), 2.848(5), 2.893(5), 3.005(6), 3.125(3), and 3.331(2) Å) to account for in ScAuAl, and, for space group $P\bar{6}2m$ (no. 189), there are six different atomic arrangements that can be generated by switching elements among the various crystallographic sites to maintain the overall composition ScAuAl. According to the results of VASP total energy calculations for each coloring, listed in Table 2 (and Table S5), the lowest energy occurs for the experimental model, which maximizes the number of shortest Au–Al interactions, followed by the next shortest distances of Sc–Au interactions so that Sc–Al and Al–Al distances are respectively longer. The next most energetically competitive model in this set (coloring α in Table 2) also has shortest Au–Al interactions, but the next shortest distances are Sc–Al contacts rather than Sc–Au. Therefore, ScAuAl prefers shorter Sc–Au over Sc–Al contacts, which can be influenced by the greater polar character of Sc−Au over Sc−Al interactions, as well as stabilizing Sc−Au interactions between nearly empty 3d atomic orbitals of Sc with formally filled 5d AOs of Au. Model β has overall more total Au–Al interactions (15×) at distances less than 3.4 Å than both the experimental and α model, but these interactions are not amongst the shortest distances, which suggests that ScAuAl prefers to maximize the number of *shortest* Au–Al interactions over a *greater frequency* of Au–Al interactions at longer averaged distances, in general, and that the next shortest distances favor Sc–Au over Sc–Al contacts. This atomic site preference analysis based on interatomic interactions also supports a structure that can be broken up into
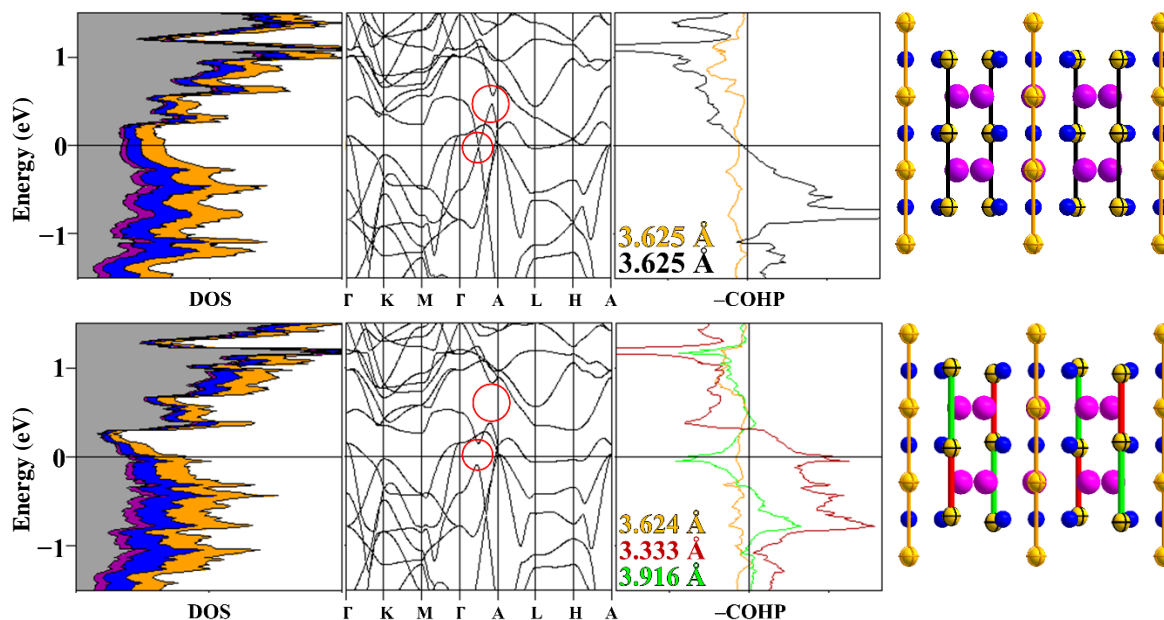
Figure 3. ScAuAl electronic structures in the Fe_2P-type subcell (top) and Mg_2Ga-type supercell (bottom) with Au–Au pseudo Peierl's distortion. For all COHP curves, (–) and (+) indicate antibonding and bonding, respectively, for contacts < 3.5 Å.

"planes" of $[(Au2)_2Al_3]$ and $[Sc_3(Au1)]$ stacked alternately along the c-axis as mentioned in the atomic structure discussion.

Like ScAuAl, TiNiSi-type CaAuAl also exhibits shortest Au–Al distances followed by Ca–Au, with longer Ca–Al distances.[19a] In TiAuAl, Au–Al distances are also the shortest, whereas Ti–Ti and Ti–Au/Al are comparable,[19b] which implies enhanced A−A (Ti−Ti) bonding than in the other AAuAl structures (A = Ca or Sc). In the structures of many ternary polar intermetallic compounds, such as these AAuAl examples with two different electronegative metallic components, maximizing the number of shortest distances between the more electronegative elements, i.e., Au and Al, while manifesting a large number of stabilizing polar-covalent A–(Au+Al) interactions subject to the size constraints of A reflects one of the hallmarks of this compound class.[1b, 4a]

Table 4. AAuAl (A = Ca, Sc, Ti) formation energies (*eV/f.u.*)

Sc + Au + Al ⟶ ScAuAl	−2.308
$\frac{1}{2}$ ScAu$_2$ + $\frac{1}{2}$ ScAl$_2$ ⟶ ScAuAl	−0.348
$\frac{1}{2}$ Sc$_2$Al + $\frac{1}{2}$ Au$_2$Al ⟶ ScAuAl	−1.313
$\frac{1}{2}$ Sc$_2$Au + $\frac{1}{2}$ AuAl$_2$ ⟶ ScAuAl	−0.663
Ca + Au + Al ⟶ CaAuAl	−2.142
$\frac{1}{2}$ CaAu$_2$ + $\frac{1}{2}$ CaAl$_2$ ⟶ CaAuAl	−0.569
Ti + Au + Al ⟶ TiAuAl	−1.522
$\frac{1}{2}$ TiAu$_2$ + $\frac{1}{2}$ TiAl$_2$ ⟶ TiAuAl	−0.226

Electronic origins of the distortion from Fe$_2$P-type to Mg$_2$Ga-type in ScAuAl. As indicated by our crystallographic refinements and a previous investigation,[9] ScAuAl is slightly distorted from the Fe$_2$P-type structure. The calculated electronic DOS curve, band structure, and Au–Au COHP curves (see Figure 3) for Fe$_2$P-type ScAuAl reveal distinct similarities to a Peierls-like distortion, because at the Fermi level the band structure shows a degeneracy via band crossing near the midpoint wavevector between the Γ(0,0,0) and A(0,0,$c^*/2$) and the Au2–Au2 COHP curve crosses from bonding states below to antibonding states above the Fermi level. Upon distortion of the structure to create alternating Au−Au distances along the *c*-axis, the degeneracy is broken in the band structure, the Fermi level falls within the gap for these states at $\boldsymbol{k} \sim (0, 0, c^*/4)$, and, as seen in the COHP curve (Figure 3), the shorter and longer Au−Au distances give, respectively, occupied bonding and antibonding states at the Fermi level.

Formation energies. The theoretical energy of formation provides information on the stability of a compound and the feasibility of assembling the structure from its constituent starting reagents. AAuAl (A = Ca, Sc, Ti) formation energies calculated from the elements and their corresponding binaries ½ AAu$_2$ + ½ AAl$_2$ show that, in general, the formations of the ternaries are all energetically favorable (Table 4), and that computational studies and
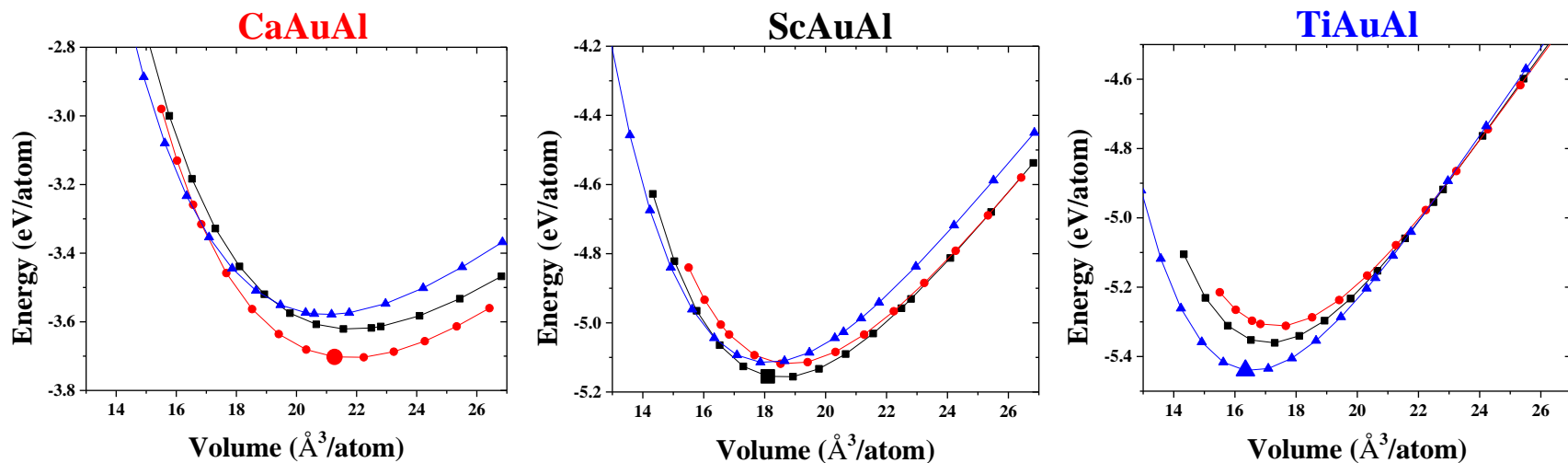
Figure 4. AAuAl total energies as a function of volume in competing models: TiNiSi as observed for CaAuAl in red; Fe_2P refined for ScAuAl in black, and Ni_2In as observed for TiAuAl in blue. For each, the experimental model is shown as a larger data point.

Table 5. Calculated Murnaghan minimum energy E_0 (eV/atom), volume V_0 (Å^3/atom), and bulk modulus B_0 (Mbar)

		Compound		
		CaAuAl	ScAuAl	TiAuAl
Type	TiNiSi	–3.705; 21.850; 0.6744	–5.118; 18.773; 1.0506	–5.314; 17.322; 1.3159
	Fe2P	–3.622; 21.920; 0.6411	–5.155; 18.508; 1.0496	–5.361; 17.019; 1.3038
	Ni2In	–3.580; 21.137; 0.6599	–5.110; 18.138; 1.0105	–5.437; 16.474; 1.2757

experimental structural reports of AAuAl corroborate one another. Additionally, whereas the formation of ScAuAl from the elements is most energetically favorable in comparison to that of (Ca/Ti)AuAl, formation of CaAuAl from $CaAu_2$ and $CaAl_2$ is more favorable than formation of (Sc/Ti)AuAl from their binaries. This type of calculation provides some insight into the potential use of binary precursors for the synthesis of a ternary compound.

Competing structural models. Differences in AAuAl (A = Ca, Sc, Ti) formation energies are much larger than differences in energies between related structures, so that, in general, the factors giving rise to a compound in a specific structure is an investigation that utilizes and analyzes calculated electronic structures, atomic site preferences, and relative atomic characteristics such as size and electronegativity.

From CaAuAl to ScAuAl to TiAuAl, the overall decreasing unit cell volume (V_{CaAuAl} = 21.324 Å^3/atom; V_{ScAuAl} = 18.103 Å^3/atom; and V_{TiAuAl} = 16.344 Å^3/atom) reflects the decreasing metallic radius of the formally electropositive element ($R_{Ca,Sc,Ti}$ = 1.97, 1.64, 1.47 Å). For the elements themselves, these decreasing metallic radii correspond to filling metal–metal bonding states of the $3d$ band, so we may anticipate similar features for the electronic structures of these ternary intermetallics. The size effect from the electropositive metal is also demonstrated by LnAuAl (Ln = rare-earth metals) adopting the orthorhombic TiNiSi-type as opposed to hexagonal Mg_2Ga- (doubled, distorted Fe_2P-) type for ScAuAl. To examine this size effect of the A elements, total energy vs. volume, $E(V)$, curves were

calculated for AAuAl (A = Ca, Sc, Ti) in the three competing TiNiSi-, Fe_2P-, and Ni_2In-type models (Figure 4), all of which show smaller energy differences among the three structures than the calculated total energies of formation. For each AAuAl, the crystallographically determined structure type gives the lowest overall energy and the corresponding unit cell volume agrees with the experimental value. A comparison of the three sets of $E(V)$ curves indicates that the sizes of the electropositive A metals play a significant role for the structures of these 16–$18e^-/fu$ AAuAl compounds: (a) at large volumes, the TiNiSi-type structure is favorable (it becomes energetically competitive for ScAuAl at ~10% above V_{exp} and for TiAuAl at ~11% above V_{exp}); and (b) at small volumes, the hexagonal Ni_2In-type structure is favorable (it becomes competitive for ScAuAl at ~3% below V_{exp} and for CaAuAl at ~7% below V_{exp}). These results imply that under pressure, ScAuAl may transform into a hexagonal Ni_2In-type; CaAuAl is also susceptible to this transformation but the pressure would be much higher than for ScAuAl. Furthermore, fitting all curves using a Murnaghan form (Table 5) shows that the bulk moduli for all TiNiSi-type curves are the largest.

Besides atomic size effects, analysis of interatomic interactions arising from atomic site preferences in the observed and competing models provide effective rationale for the observed structural variations. These are obtained by calculated electronic DOS and COHP curves for nearest pairwise interactions for distances less than 3.5 Å. Since the observed structures (TiNiSi-type for $16e^-/fu$ CaAuAl; distorted Fe_2P-type for $17e^-/fu$ ScAuAl; and Ni_2In-type for $18e^-/fu$ TiAuAl) all contain [AuAl] networks involving $[Au_3Al_3]$ alternant hexagonal rings, three additional structure types based upon the hexagonal $CaIn_2$-type were examined: (1) NdPtSb-type, observed for CeAuGe, but contains no Au−Ge interactions along

Table 6. AAuAl competing models, total energies, and integrated COHP < 3.5 Å

ScAuAl (Fe₂P-type)

	TiNiSi	Fe₂P	Ni₂In	NdPtSb	LiGaGe	ScAuSi
$\Delta E(eV/f.u.)$	+0.031	**0.000**	+0.081	+0.077	+0.079	+0.140
a (Å)	6.674	**7.287**	4.467	4.459	4.459	4.427
b (Å)	4.378					
c (Å)	7.636	**3.625**	6.389	6.419	6.428	6.623
V (Å³/f.u.)	55.779	**55.563**	55.191	55.257	55.333	56.213
Sc–Au	27.95	**19.12**	30.24	29.23	29.26	37.36
Sc–Al	23.16	**15.33**	26.99	26.74	23.83	31.47
Sc–Sc	4.59	**--**	--	--	1.54	4.48
Au–Al	38.73	**64.39**	42.77	44.03	45.38	22.52
Al–Al	--	**1.16**	--	--	--	2.36
Au–Au	5.57	**--**	--	--	--	1.80

(Left label for the above ICOHP rows: –ICOHP (%))

CaAuAl (TiNiSi-type)

	TiNiSi	Fe₂P	Ni₂In	NdPtSb	LiGaGe	ScAuSi
$\Delta E(eV/f.u.)$	**0.000**	+0.138	+0.216	+0.213	+0.217	+0.212
a (Å)	**7.337**	7.255	4.548	4.563	4.564	4.536
b (Å)	**4.552**					
c (Å)	**7.824**	4.310	7.597	7.526	7.513	7.703
V (Å³/f.u.)	**65.319**	65.485	68.043	67.836	67.752	68.642
Ca–Au	**21.83**	14.59	28.35	27.09	23.31	34.55
Ca–Al	**19.94**	13.36	26.12	25.27	21.60	30.57
Ca–Ca	**--**	--	--	--	1.03	2.89
Au–Al	**55.93**	70.73	45.53	47.65	52.05	26.97
Al–Al	**2.31**	1.32	--	--	--	2.98
Au–Au	**--**	--	--	--	--	2.04

(Left label for the above ICOHP rows: –ICOHP (%))

TiAuAl (Ni₂In-type)

	TiNiSi	Fe₂P	Ni₂In	NdPtSb	LiGaGe	ScAuSi
$\Delta E(eV/f.u.)$	+0.234	+0.157	**0.000**	+0.020	+0.024	+0.121
a (Å)	6.516	6.694	**4.461**	4.365	4.363	4.395
b (Å)	4.001					
c (Å)	7.747	3.977	**5.740**	6.150	6.161	6.025
V (Å³/f.u.)	50.494	51.435	**49.452**	50.740	50.788	50.392
Ti–Au	33.83	24.72	**34.01**	39.69	35.05	40.21
Ti–Al	27.78	21.33	**27.62**	32.19	28.66	34.51
Ti–Ti	5.43	--	**6.65**	--	4.25	8.98
Au–Al	28.50	52.98	**31.72**	28.12	32.04	13.97
Al–Al	--	0.97	**--**	--	--	1.26
Au–Au	4.46	--	**--**	--	--	1.06

(Left label for the above ICOHP rows: –ICOHP (%))

the *c*-direction yielding essentially separated puckered hexagonal [Au₃Ge₃] layers; (2) LiGaGe-type, which occurs for ScAuGe, and have a 3D tetrahedral framework with only Au−Ge contacts; and (3) ScAuSi features [Au₃Si₃] puckered hexagons stacked directly on top of one another with distances that suggest Au–Au and Si–Si interlayer interactions.[22]

Geometrically, the hexagonal layers of the electronegative metal/metalloid network in $CaIn_2$-type derivatives are puckered in a chair-conformation; those in Ni_2In-type (TiAuAl) are planar; and those in the distorted Fe_2P-type (ScAuAl) are half-chair conformers.

Table 6 summarizes the total energies, relative to the lowest energy structure, calculated unit cell parameters, and percent integrated Hamilton populations (ICOHPs) evaluated for all interactions within 3.5 Å for AAuAl (A = Ca, Sc, and Ti) in the various competing models (see Tables S6–S11 for more details). Some general observations of the results in Table 6 include: (i) for all AAuAl, the total energies for hexagonal Ni_2In- and $CaIn_2$-derivatives, except for the ScAuSi-type, fall within a few millivolts of each other; (ii) the lowest energy structures for CaAuAl and TiAuAl exhibit the smallest unit cell volumes per formula unit; and (iii) the Fe_2P-structure type always shows the greatest polar-covalent bonding contributions coming from Au−Al contacts for all AAuAl cases.

Examination of the DOS and COHP curves for these cases can illuminate these outcomes. Figure 5 shows these curves for $17e^-/fu$ ScAuAl in Fe_2P-, TiNiSi-, and Ni_2In-type arrangements. The different structures significantly affect the shapes of the DOS curves. For the Fe_2P-type, there are no clear gaps in the DOS, although the Au $5d$ band is clearly seen at 5 eV below the Fermi level and is about 1.5 eV wide. At the Fermi level, there is a pseudogap arising from the general crossing of Sc $3d$ states with Au $6s$ and $6p$ orbitals (the rationale for the distortion of ScAuAl was given earlier). This pseudogap region also corresponds to essentially optimized Au−Al interactions, but there remain Sc−Au and Sc−Al bonding states above E_F as seen in their COHP curves in Figure 5. By applying a rigid-band approximation to these curves, for $16e^-/fu$, significant Au−Al states would be depleted, whereas for $18e^-/fu$, Au−Al antibonding states would be populated. The DOS curves for ScAuAl in the TiNiSi- and
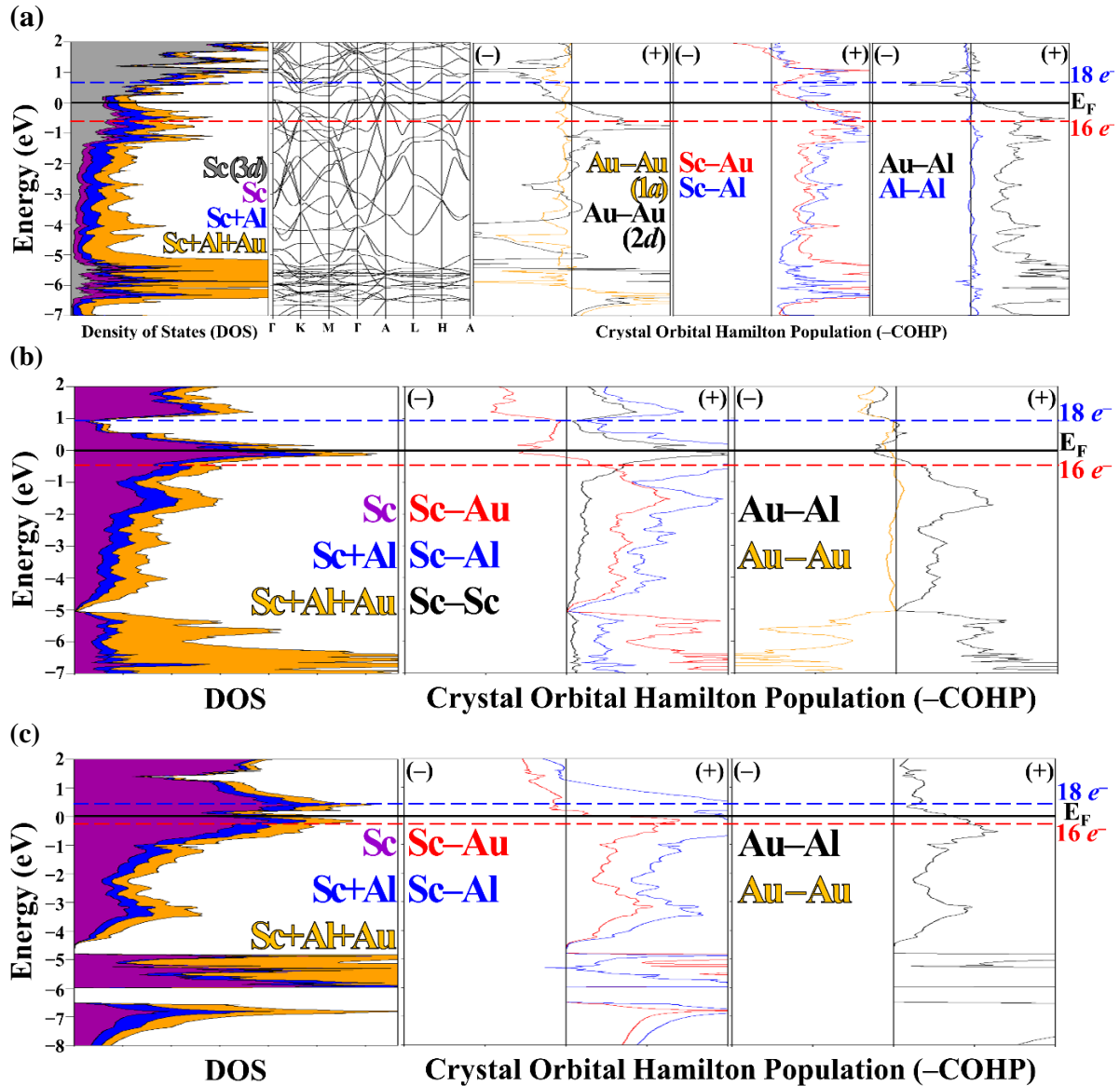
Figure 5. ScAuAl in the (a) experimental, (b) TiNiSi-type and (c) Ni$_2$In-type as respectively seen for CaAuAl and TiAuAl. For all COHP curves, (−) and (+) indicate antibonding and bonding, respectively for contacts < 3.5 Å

Ni$_2$In-alternatives show distinct (pseudo)gaps for 12 electrons, which correspond to formally filling one *s*-band and the Au 5*d* band with electrons. The Fermi levels for 17 *e⁻/fu* both lie close or on peaks in the DOS curve, and the Ni$_2$In-type DOS shows considerable contributions from Sc wavefunctions among the occupied states. Therefore, the Fe$_2$P-related structure

adopted by ScAuAl optimizes Au–Al interactions while avoiding Sc–Au antibonding interactions, which are indicated for TiNiSi-type "ScAuAl" in its COHP curve.

Analogous analyses are afforded for the (Ca/Ti)AuAl neighbors to rationalize features stabilizing their observed structures. In TiNiSi-type CaAuAl, the next most competitive model to the experimental one is the Fe_2P-type structure; in both, Au–Al interactions contribute the most to the total ICOHP value, as in ScAuAl. (See Tables S8–S9 for summaries and Figures S3 for electronic structures of CaAuAl in competing structure types.) Also like ScAuAl, there are overall bonding Ca–Au and Ca–Al interactions at the Fermi level, but unlike ScAuAl the Au–Al interactions are not optimized. The small volume of the unit cell relative to the other structural models reflects that there may be significant stabilization arising from charge transfer from Ca to the electronegative Au and Al atoms in this structure. In Ni_2In-type TiAuAl, the observed Ni_2In- and $CaIn_2$-type models are energetically close, which is somewhat surprising given that the $[Au_3Al_3]$ hexagons in the $CaIn_2$-type variants are puckered whereas those in the Ni_2In-type are planar. For the observed structure of TiAuAl, the Au–Al distances are the shortest (2.5448(5) Å), followed by the Ti–Ti distances (2.9145(5) Å) (See Tables S10–S11 for summaries of TiAuAl and its competing structure types and Figure S4 for electronic structures.) According to analysis of the ICOHPs (Table 6), the Ni_2In-type structure yields a nearly even distribution in bonding contributions from Au–Al, Ti–Au, and Ti–Al interactions, while also providing some Ti–Ti bonding. The $CaIn_2$-types show similar characteristics, but with some subtle redistribution in bonding contributions, results which rationalize the similar total energies to the Ni_2In-type model. On the other hand, the relative destabilization of TiNiSi- and Fe_2P-types occurs, respectively, by introducing either Au–Au interactions or reducing the contributions of Ti–Au and Ti–Al to the total bond energy term.

Conclusions

AAuAl (A = Ca, Sc, Ti) compounds with consecutively increasing valence electron concentration (16–18e^-/fu) and decreasing atomic radius crystallize in different structure types: orthorhombic TiNiSi-type CaAuAl; hexagonal Mg_2Ga-type ScAuAl (a distorted superstructure of Fe_2P-type); and hexagonal Ni_2In-type TiAuAl. Density functional theory and atomic site preference investigations using total energy calculations show that this structural variation is related to both chemical pressure effects, results indicating larger unit cells favoring the orthorhombic TiNiSi structure and smaller unit cells favoring the hexagonal Fe_2P- or Ni_2In-type structure, as well as atomic arrangements that maximize the number of Au–Al nearest neighbor contacts. Electronic DOS and COHP plots highlight the polar covalent A–(Au+Al) interactions, which are also necessary for structural cohesion. For the ScAuAl structure specifically, the electronic band structure and Au–Au COHP curves indicate that the refined Mg_2Ga-type structure arises from a Peierls-like distortion of the Au-chains along the c-axis, which gives rise to the doubled c-axis on going from the Fe_2P to Mg_2Ga-type structures.

Supporting Information in APPENDIX D

The following are included in the SI: Selected crystallographic parameters of ScAuAl refined in the Fe_2P-structure as selected from the 1Sc: 2Au: 5Al molar loading as well as the Mg_2Ga-structure as selected from the 1Sc: 1Au: 1Al molar loading; Environment of each atom in the ScAuAl asymmetric unit of Fe_2P structure; ScAuAl (Fe_2P-structure), CaAuAl (TiNiSi-structure), and TiAuAl (Ni_2In-structure) relative total formation energies and energies of competing structures with numbers of selected interatomic distances; ScAuAl structural parameters after VASP optimization used for subsequent electronic calculations; Ca, Sc, Ti, Au, and Al Wigner Seitz radii; DOS and COHP curves of AAuAl in competing structure types.

Acknowledgements

References

1. (a) Miller, G. J.; Thimmaiah, S.; Smetana, V.; Palasyuk, A.; Lin, Q., Gold's structural versatility within complex intermetallics: From Hume-Rothery to Zintl and even quasicrystals. *MRS Online Proceedings Library Archive* **2013,** *1517*; (b) Pham, J.; Kreyssig, A.; Goldman, A. I.; Miller, G. J., An icosahedral quasicrystal and its 1/0 crystalline approximant in the Ca–Au–Al System. *Inorganic Chemistry* **2016,** *55* (20), 10425-10437.

2. Palasyuk, A.; Grin, Y.; Miller, G. J., Turning gold into "diamond": A family of hexagonal diamond-type Au-frameworks interconnected by triangular clusters in the Sr–Al–Au system. *Journal of the American Chemical Society* **2014,** *136* (8), 3108-3117.

3. (a) Miller, G. J.; Lee, C.-S.; Choe, W., Structure and bonding around the Zintl border. *Inorganic Chemistry Highlights*, Ed. Meyer, G.; Naumann, D.; Wesemann, L.; Wiley-VCH: Wein-heim: Germany, **2002**; 21-53; (b) Miller, G.; Schmidt, M.; Wang, F.; You, T.-S., Quantitative advances in the Zintl–Klemm formalism. *Structure and Bonding* **2011,** *139* (Zintl Phases), 1-55.

4. (a) Miller, G. J.; Reedijk, J.; Poeppelmeier, K.R., Metal-rich compounds of the *d*-metals. *Comprehensive Inorganic Chemistry II (Second Edition)*, **2013**, *2*, 311-357; (b) Nesper, R., Bonding patterns in intermetallic compounds. *Angewandte Chemie International Edition*,**1991,** *30* (7), 789-817.

5. (a) Dshemuchadse, J.; Steurer, W., More statistics on intermetallic compounds–ternary phases. *Acta Crystallographica Section A* **2015,** *71* (3), 335-345; (b) Bojin, M. D.; Hoffmann, R., The RE–M–E phases-overview. *Helvetica Chimica Acta* **2003,** *86* (5), 1653-1682.

6. (a) Bojin, M. D.; Hoffmann, R., The RE–M–E phases–What's possible. *Helvetica Chimica Acta* **2003,** *86* (5), 1683-1708; (b) Seibel, E. M.; Schoop, L. M.; Xie, W.; Gibson, Q. D.; Webb, J. B.; Fuccillo, M. K.; Krizan, J. W.; Cava, R. J., Gold–Gold bonding: The key to stabilizing the 19-electron ternary phases LnAuSb (Ln = La–Nd and Sm). *Journal of the American Chemical Society* **2015,** *137* (3), 1282-1289.

7. Miller, G. J., The "Coloring Problem" in solids: How it affects structure, composition and properties. *European Journal of Inorganic Chemistry* **1998,** *1998* (5), 523-536.

8. (a) Zumdick Markus, F.; Hoffmann, R.-D.; Pöttgen, R., The intermetallic Zirconium compounds ZrNiAl, ZrRhSn, and ZrPtGa–Structural distortions and metal-metal bonding in Fe_2P related

compounds. *Zeitschrift für Naturforschung B*, **1999**, *54b*, 45-53; (b) Zumdick, M. F. R. P., Determination of the superstructures for the stannides ZrIrSn, HfCoSn, and HfRhSn. *Zeitschrift für Kristallographie–Crystalline Materials*, **1999**, *214*, 90-97.

9. Radzieowski, M.; Benndorf, C.; Haverkamp, S.; Eckert, H.; Janka, O., On new ternary equiatomic scandium transition metal aluminum compounds ScTAl with T = Cr, Ru, Ag, Re, Pt, and Au. *Zeitschrift für Naturforschung B*, **2016**, *71 (5)b*, 553-566.

10. Kuestner, H. R., H., Struktur des Siliziums. *Physikalische Zeitschrift* **1923,** *24*, 25-29.

11. *SMART*. version 5; Bruker AXS: Madison, WI, **2003**.

12. Sheldrick, G. M. *SADABS*, University of Gottingen: Gottingen, Germany, **2001**.

13. Blessing, R., An empirical correction for absorption anisotropy. *Acta Crystallographica Section A* **1995,** *51* (1), 33-38.

14. Sheldrick, G., *SHELX*. version 6.14 ed.; Bruker AXS: Madison, WI, **2000-2003**.

15. Sheldrick, G., A short history of SHELX. *Acta Crystallographica Section A* **2008,** *64* (1), 112-122.

16. Parsons, S.; Flack, H. D.; Wagner, T., Use of intensity quotients and differences in absolute structure refinement. *Acta Crystallographica Section B* **2013,** *69* (3), 249-259.

17. (a) Blöchl, P. E., *Phys. Rev. B* **1994,** *50*, 17953; (b) Kresse, G.; Hafner, J., *Phys. Rev. B* **1993,** *47*, 558; (c) Kresse, G.; Furthmüller, F., *Comput. Mater. Sci.* **1996,** *6*, 15.

18. Perdew, J. P.; Burke, K.; Ernzerhof, M., Generalized gradient approximation made simple, *Phys. Rev. Lett.* **1996,** *77*, 3865.

19. (a) Cordier, G.; Friedrich, T., Crystal structure of calcium gold aluminium (1/1/1), CaAuAl. *Zeitschrift für Kristallographie–Crystalline Materials*, **1992**, *201*, 304-305; (b) Jorda, J. L.; Muller, J.; Braun, H. F.; Susz, C., Phase relationships in the ternary system Ti-Au-Al at 775 K. *Journal of the Less Common Metals* **1987,** *134* (1), 99-107.

20. Bader, R. F. W., *Atoms in Molecules: A Quantum Theory*. Clarendon Press: **1994**.

21. (a) Reule, H.; Steeb, S.; Donolato, C., Structure of the compounds Ag_4Sc, Ag_2Sc, Au_4Sc, Au_2Sc, and Ag_3Yb. *Journal of the Less Common Metals* **1971,** *24* (1), 108-112; (b) Schuster, J. C.; Bauer, J., The ternary systems Sc–Al–N and Y–Al–N. *Journal of the Less Common Metals* **1985,** *109* (2), 345-350; (c) Zachwieja, U., Synthesis and structure of $CaAu_2$ and $SrAu_2$. *Journal of Alloys and Compounds* **1996,** *235* (1), 12-14; (d) Nowotny, H.; Mohrnheim, A., Die Kristallstruktur von Al_2Ca, *Zeitschrift fuer Kristallographie, Kristallgeometrie, Kristallphysik, Kristallchemie* **1939,** (100), 540-542; (e) Pietrokowsky, P., The partial constutional diagram $TiAu_2$–Au: Lattice parameters of the alpha solid solutions and the intermediate phase $TiAu_4$. *Journal of the Institute of Metals* **1962,** *90*, 434-438; (f) Schuster, J. C.; Ipser, H., Phases and phase relations in the partial system $TiAl_3$ – TiAl. *Zeitschrift fuer Metallkunde* **1990,** *81* (6), 389-396.

22. (a) Fornasini, M. L.; Iandelli, A.; Pani, M., Different stacking of the gold and silicon atoms in the phases RAuSi (R = Sc, Y, Lu). *Journal of Alloys and Compounds* **1992,** *187* (1), 243-247; (b) Bockelmann, W.; Schuster, H.-U., *Z. Anorg. Allg. Chem.* **1974,** *410*; (c) Bockelmann, W.; Jacobs, H.;

Schuster, H.-U., *Z. Naturforsch. B* **1970,** *25*; (d) Wenski, G.; Mewis, A., REPtX compounds with structures related to AlB$_2$- and MgAgAs-type (RE = Y, Rare earth element; X = P, As, Sb), *Zeitschrift für Kristallographie*, **1986**, *(176)*, 125-134; (e) Pöttgen, R.; Borrmann, H.; Felser, C.; Jepsen, O.; Henn, R.; Kremer, R. K.; Simon, A., Crystal and electronic structures of ScAuGe, CeAuGe, and LuAuGe: a transition from two- to three-dimensional [AuGe] polyanions. *Journal of Alloys and Compounds* **1996,** *235* (2), 170-175; (f) Hoffmann, R. D.; Pöttgen, R., AlB$_2$-related intermetallic compounds–a comprehensive view based on group-subgroup relations. In *Zeitschrift für Kristallographie–Crystalline Materials*, **2001**, *(216)*, 127-145.

23. Dronskowski, R.; Bloechl, P. E., Crystal orbital Hamilton populations (COHP): Energy-resolved visualization of chemical bonding in solids based on density-functional calculations. *The Journal of Physical Chemistry* **1993,** *97* (33), 8617-8624.

24. Jepson, O. B., A.; Andersen, O.K., *The Program TB-LMTO-ASA,4.7;* **1999,** *Max-Planck-Institut für Festkörperforschung, Stuttgart, Germany*.

25. Lambrecht, W. R. L.; Andersen, O. K., Minimal basis sets in the linear muffin-tin orbital method: Application to the diamond-structure crystals C, Si, and Ge. *Physical Review B* **1986,** *34* (4), 2439-2449.

26. Pušelj, M.; Schubert, K., Kristallstrukturen der Phasen Au$_2$Al(h), Au$_2$Al$_1$−(r) und Au$_2$Al$_1$+(r). *Journal of the Less Common Metals* **1974,** *35* (2), 259-266.

27. West, C. D.; Peterson, A. W., The crystal structure of AuAl$_2$. *Zeitschrift fuer Kristallographie, Kristallgeometrie, Kristallphysik,* **1934,** *88*, 93-94.

28. Eymond, S.; Parthé, E., Sc$_2$Al with Ni$_2$ln structure type. *Journal of the Less Common Metals* **1969,** *19* (4), 441-443.

29. Palenzona, A.; Manfrinetti, P., The phase diagram of the Sc–Au system. *Journal of Alloys and Compounds* **1997,** *257* (1), 224-226.

30. (a) Frank, K.; Schubert, K., Kristallstruktur von AuAl. *Journal of the Less Common Metals* **1970,** *22* (3), 349-354; (b) Aldred, A. T., Intermediate phases involving scandium. *Transactions of the Metallurgical Society of Aime* **1962,** *224*, 1082-1083; (c) Dwight, A. E.; Kimball, C. W., ScT$_2$X and LnT$_2$X compounds with the MnCu$_2$Al-type structure. *Journal of the Less Common Metals* **1987,** *127* (0), 179-182.

31. Schob, O.; Parthe, E., AB compounds with Sc, Y and rare earth metals. I. Scandium and yttrium compounds with CrB and CsCl structure. *Acta Crystallographica* **1965,** *19* (2), 214-224.

32. Hamilton, W., Significance tests on the crystallographic R factor. *Acta Crystallographica* **1965,** *18* (3), 502-510.

33. Hulliger, F., On new rare earth gold aluminides LnAuAl. *Journal of Alloys and Compounds* **1993,** *200* (1), 75-78.

CHAPTER 7

Y/Gd–Au–Al 1/1 CRYSTALLINE APPROXIMANTS, STRUCTURES WITH HEXAGONAL STARS AND NONCENTROSYMMETRY

All Y/Gd–Au–Al crystallographic structures tabulated here are from products synthesized by heating to 1050 $^{\circ}$C for 24–40 hours, slowly (5–7 $^{\circ}$C/hr) cooling to 700 $^{\circ}$C and annealing there for 5 days, and then quenching by rapid submersion into room-temperature water.

In previous chapters examining various electropositive active metals with Au and Al, divalent Ca (R_{Ca} = 1.97 Å) led to i-QCs in the synthetic compositional range 1:5.3–1.60 Ca:(Au+Al), whereas trivalent Sc (R_{Ca} = 1.64 Å) did not. Preliminary crystallographic data with Y/Gd ($R_{Y,Gd}$ = 1.80 Å) show Tsai-type 1/1 CAs ($Y_3Au_{14.08(2)}Al_{4.49(1)}$ and $Gd_3Au_{14.10(2)}Al_{4.47}$), so that additional electronic tuning and synthesis without annealing may lead to i-QCs, as seen in the Ca–Au–Al system (see Section 7.1).

The ~1:3:1 loading compositions of Y/Gd–Au–Al that led to the 1/0 CA phase $CaAu_{3+x}Al_{1-x}$ (0 ≤ x ≤ 0.31(1)) yielded $(Y/Gd)Au_{2.929(4)}Al_{0.659}$ with structures that can be described as layers of hexagonal stars following the $GdAg_{3.6}$-structure type,[1] or three distinct space-filling Y/Gd-centered polyhedra following the polar intermetallics depiction that highlights Y/Gd–(Au+Al) polar-covalent interactions (see Section 7.2).

In the Al-rich region of the Y/Gd–Au–Al phase-spaces, a noncentrosymmetric structure was discovered in $(Gd/Y)_4Au_{9.00(3)}Al_{13}$ that shows two face-sharing $Au_{2.98(2)}Al_6$ octahedral building blocks (see Section 7.3). Preliminary data of these new compounds and their structures further represent the diversity and complexity within the family of polar intermetallic compounds that can use more in-depth analysis and electronic structural studies as performed in previous chapters of this dissertation.

1/1 Crystalline Approximants $Y_3Au_{14.08(2)}Al_{4.49(1)}$ and $Gd_3Au_{14.10(2)}Al_{4.47}$

Table 1. Selected refined crystallographic data of 1/1 CA $Y_3Au_{14.08(2)}Al_{4.49(1)}$

loaded (VEC)	$Y_{1.00(2)}Au_{4.94(1)}Al_{1.97(7)}$ (1.75 e^-)	$Gd_{1.00(1)}Au_{5.07(1)}Al_{1.95(8)}$ (1.75 e^-)
refined composition (VEC, e/a)	$Y_3Au_{14.08(2)}Al_{4.49(1)}$	$Gd_3Au_{14.10(2)}Al_{4.47}$
refined empirical composition	$YAu_{4.49}Al_{1.50}$	$GdAu_{4.70}Al_{1.49}$
instrument	Bruker CCD APEX II	
radiation; λ (Å)/ temp.(K)	Mo $K_{\alpha1}$; 0.71073/ 298	
θ range data collection	2.0º–30.0º	
absorp. coeff. μ (mm^{-1})/ correction	141.59/ empirical	141.28/ empirical
meas./ indpnt./ obs. [I > 2σ(I)]/ para./ rest.	50432/ 862/ 753/ 52/ 0	46082/865/683/53/0
R[F^2 > 2σ(F^2)]/ wR(F^2)/ R$_{int}$/ GOF	0.035/ 0.087/ 0.187/ 1.05	0.032/ 0.078/ 0.201/ 1.03
space group/ Pearson symbol	$Im\overline{3}$ (#204)/ cI192	
$\Delta\rho_{max}$, $\Delta\rho_{min}$ (e Å^{-3})	4.11, –4.38	3.58, –4.51
a (Å)	14.662(2)	14.7081(4)
a_{PXRD} (Å)	14.657(7)	14.717(7)
volume (Å^3)/ Z	3151.1(11)/ 8	3181.8(3)
index ranges	$-20 \le h, k, l \le 20$	

Table 2. $Y_3Au_{14.08(2)}Al_{4.49(1)}$ selected crystallographic parameters

	Wyck.	*x*	*y*	*z*	*Uiso*	Occ. (<1)
Au1	24g	1/2	0.14793(4)	0.09515(4)	0.0096(2)	
Au2	48h	0.39510(3)	0.30182(3)	0.15879(3)	0.0100(2)	
Au3	16f	0.34970(3)	0.34970(3)	0.34970(3)	0.0134(2)	
Au4	12d	0.4028(1)	0	0	0.0332(6)	0.772(7)
Al4						0.228(7)
Y1	24g	0.3057(1)	0.1889(1)	0	0.0080(3)	
Au5	24g	0.2425(2)	0	0.0778(1)	0.0281(6)	0.452(5)
Al5						0.548(5)
Al2	12e	1/2	0	0.1928(5)	0.009(2)	
Al3	8c	1/4	1/4	1/4	0.013(2)	
Au6	24g	0.0625(9)	0	0.0779(7)	0.091(4)	0.189(5)
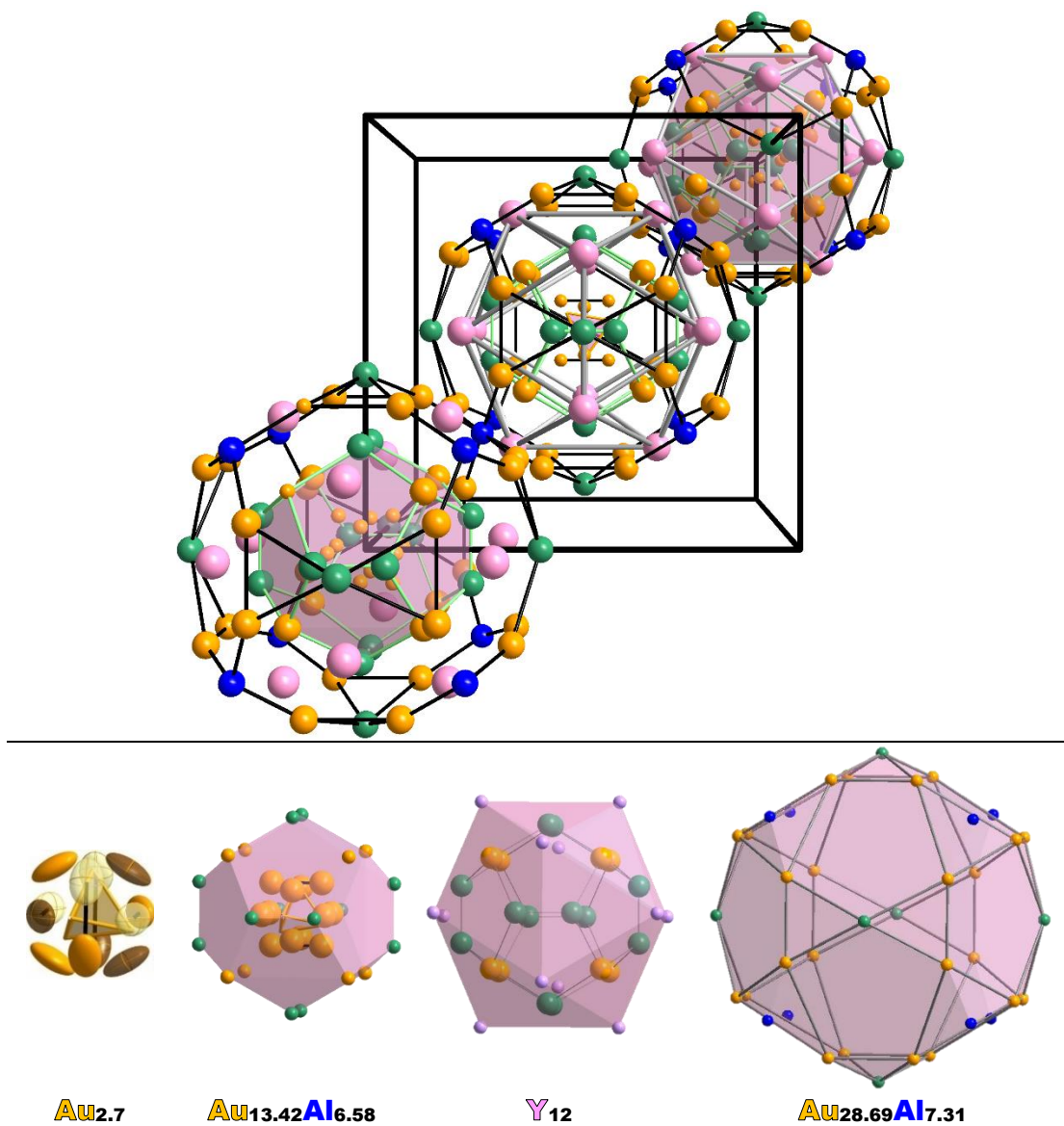
Figure 1. Y₃Au₁₄.₀₈₍₂₎Al₄.₄₉₍₁₎ overall structure (top) with concentric shells (bottom) following the Tsai-type crystalline approximant. Y atoms are in pink; Au are dark yellow; Al are blue; and sites of Au/Al mixtures are green.

162
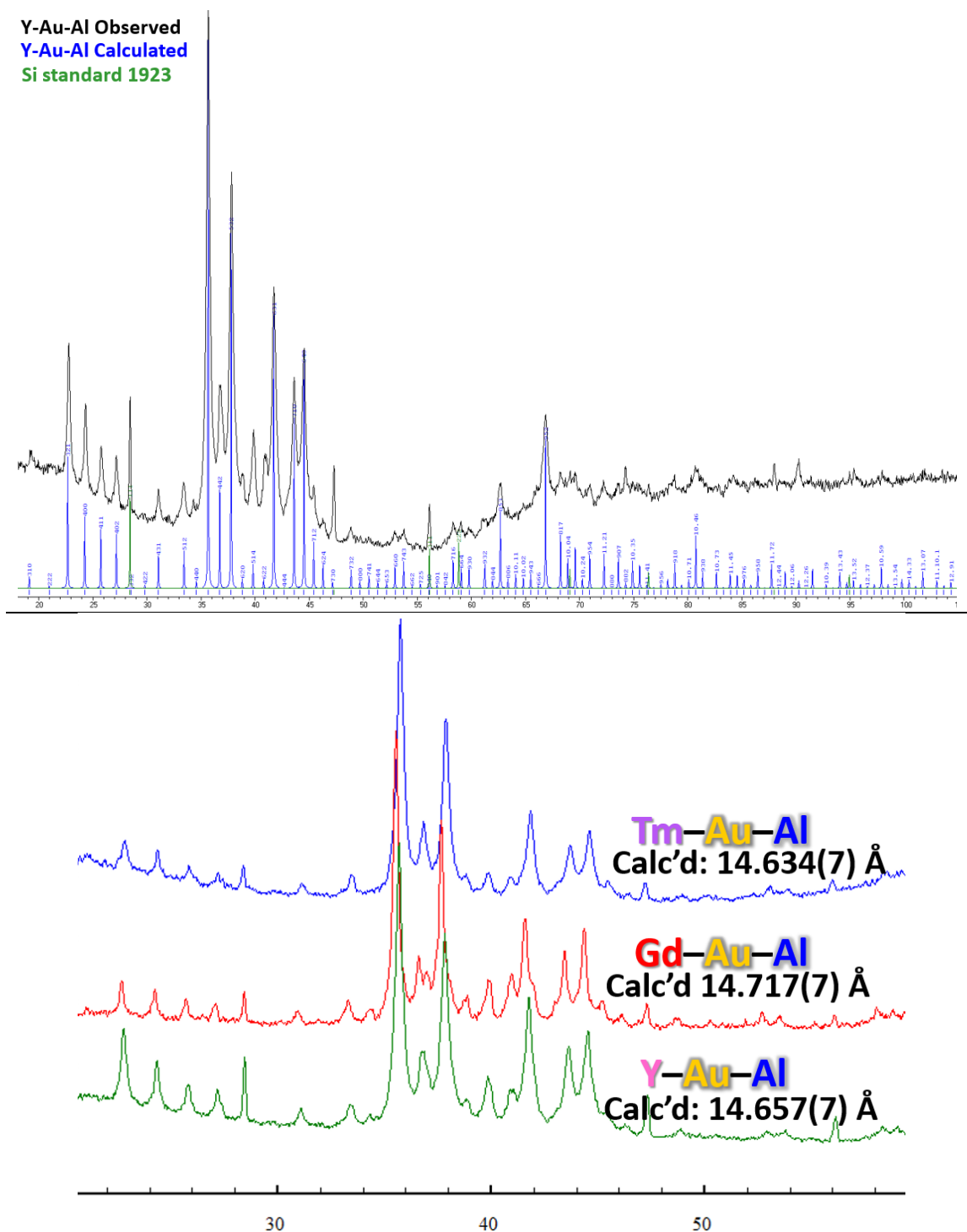
Figure 2. Y₃Au₁₄.₀₈₍₂₎Al₄.₄₉₍₁₎ 1/1 CA simulated PXRD pattern from single-crystal XRD refinement and from "Y₁.₀₀₍₂₎Au₄.₉₄₍₁₎Al₁.₉₇₍₇₎" loading (top). PXRD of 1/1 crystalline approximants in Y/Gd/Tm–Au–Al with calculated cubic lattice parameters from Le Bail decomposition.

(Y/Gd)Au$_{2.929(4)}$Al$_{0.659}$ Hexagonal Stars in GdAg$_{3.6}$-Type

Table 3. YAu$_{2.929(4)}$Al$_{0.659}$ Selected refined crystallographic data

loading	"YAu$_3$Al"
refined composition	YAu$_{2.929(4)}$Al$_{0.659}$
instrument	Bruker CCD APEX II
radiation; λ (Å)/ temp.(K)	Mo K$_{\alpha1}$; 0.71073/ 298
θ range data collection	1.9°–29.6°
absorp. coeff. μ (mm^{-1})/	120.42/
correction	empirical
meas./ indpnt./ obs. [I > 2σ(I)]/ para./ rest.	27083/ 1244/ 1028/ 68/ 0
R[F^2 > 2σ(F^2)]/ wR(F^2)/ R$_{int}$/ GOF	0.044/ 0.089/ 0.159/ 1.10
space group; Pearson	P6/m ^{2}; 2; hP64
Δρ$_{max}$, Δρ$_{min}$ (e Å^{-3})	3.59, –2.78
a (Å)	12.515(2)
c (Å)	9.112(2)
volume (Å^3)/ Z	1236.0(5)/ 14
index ranges	–17 ≤ h, k ≤ 17; –12 ≤ l ≤ 12

Table 4. YAu$_{2.929(4)}$Al$_{0.659}$ selected crystallographic parameters

	Wyck.	x	y	z	U$_{iso}$	Occ. (<1)
Au1	12l	0.66734(6)	0.10725(6)	0.33621(6)	0.0167(2)	
Au/Al2	12l	0.73135(7)	0.92800(6)	0.23315(8)	0.0206(3)	0.871(5)/0.129
Au/Al3	4h	2/3	1/3	0.3017(1)	0.0256(5)	0.818(7)/0.182
Au/Al4	12l	0.50327(8)	0.88180(8)	0.14726(10)	0.0275(3)	0.762(4)/0.238
Au/Al5	6k	0.8316(1)	0.0563(1)	1/2	0.0171(5)	0.524(6)/0.476
Au/Al6	2c	2/3	1/3	0	0.026(1)	0.401(9)/0.599
Au7	6j	0.8980(4)	0.0343(4)	0	0.043(1)	0.372(5)
Y1	6k	0.4702(2)	0.1393(2)	1/2	0.0158(4)	
Y2	2e	0	0	0.2979(4)	0.0138(7)	
Y3	6j	0.7252(3)	0.1116(2)	0	0.0319(6)	
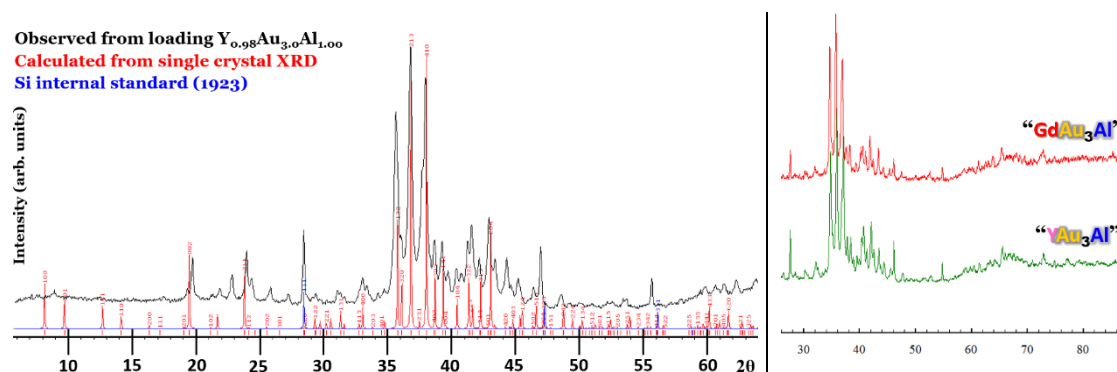
Figure 3. Simulated powder diffraction patterns of preliminary refined YAu$_{2.929(4)}$Al$_{0.659}$ showing phase match (left) also observed for the "GdAu$_3$Al" loading (left).
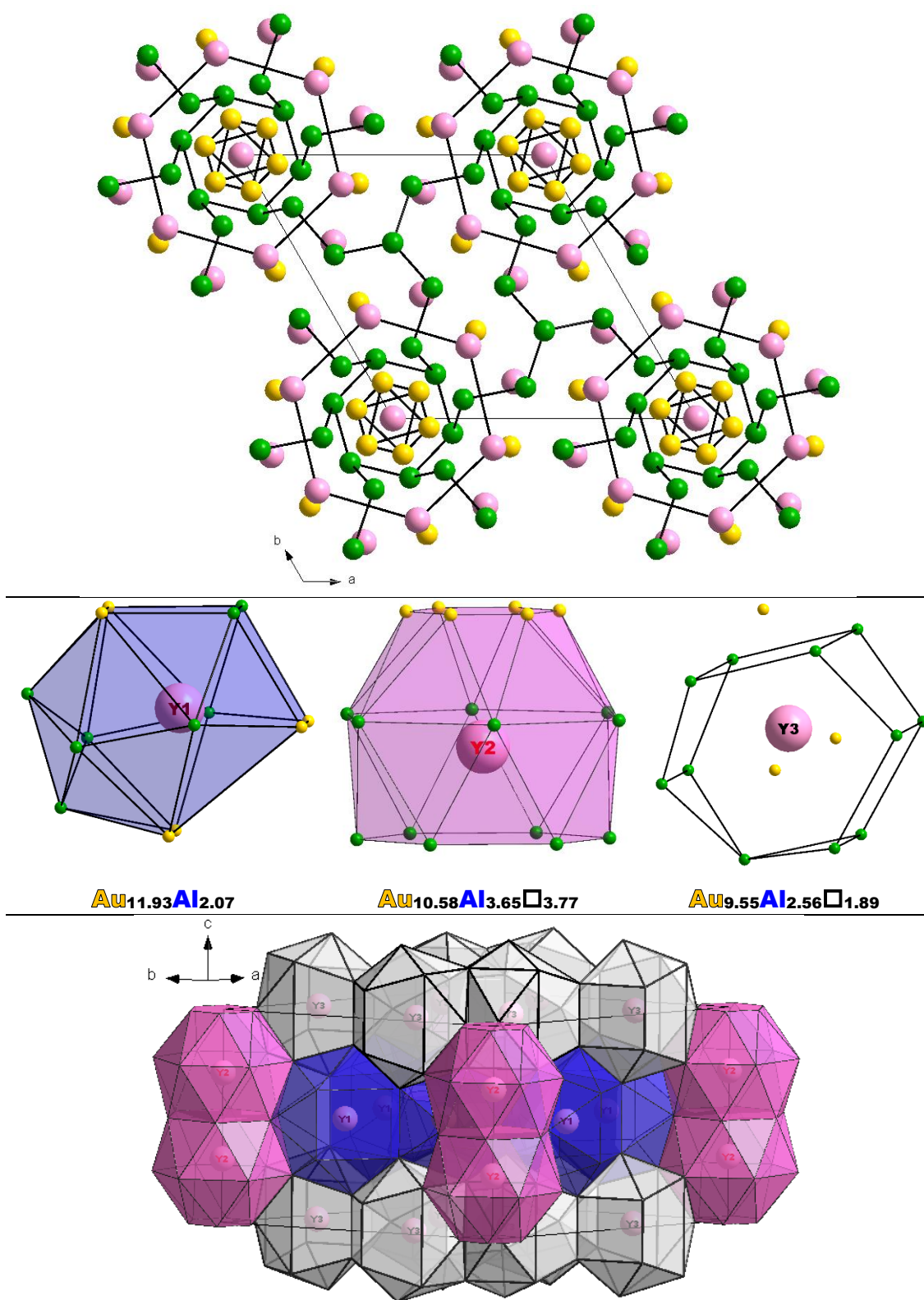
Figure 4. YAu$_{2.929(4)}$Al$_{0.659}$ drawn as layers of hexagonal stars (top), polyhedral coordination spheres of the three independent Y sites (middle), and polyhedral packing of the unit cell from the Y coodination spheres (bottom).

Noncentrosymmetric (Gd/Y)₄Au₉.₀₀₍₃₎Al₁₃

Table 5. Selected refined crystallographic data of Y₄Au₈.₉₉₍₃₎Al₁₃ and Gd₄Au₈.₉₈₍₂₎Al₁₃

Loading	"YAu₂Al₅"	"GdAu₂Al₅"
refined composition	Y₄Au₈.₉₉₍₃₎Al₁₃	Gd₄Au₈.₉₈₍₂₎Al₁₃
instrument	Bruker CCD APEX II	
radiation; λ (Å)/ temp.(K)	Mo K$_{\alpha1}$; 0.71073/ 298	
θ range data collection	2.0°–30.1°	
absorp. coeff. μ (mm^{-1})/ correction	36.76/ empirical	37.26/ empirical
meas./ indpnt./ obs. [I > 2σ(I)]/ para./ rest.	14473/ 609/ 596/ 38/ 0	11136/609/593/38/0
R[F² > 2σ(F²)]/ wR(F²)/ R$_{int}$/ GOF	0.018/ 0.033/ 0.072/ 1.03	0.025/ 0.059/ 0.105/ 1.06
space group/ Pearson symbol	$P\bar{6}m2$ (#167)/ hP26	
Δρ$_{max}$, Δρ$_{min}$ (e Å^{-3})	1.35, –1.41	1.97, –2.54
Absolute structure parameter	0.00(2)	0.02(3)
a (Å)	11.6463(9)	11.6314(5)
c (Å)	4.0970(3)	4.1330(2)
volume (Å³)/ Z	481.25(8)/ 1	484.24(5)/ 1
index ranges	−16 ≤ h, k ≤ 16 −5 ≤ l ≤ 5	

Table 6. Gd₄Au₈.₉₈₍₂₎Al₁₃ selected crystallographic parameters

	Wyck.	x	y	z	U$_{iso}$	Occ. (<1)
Au1	3j	0.21261(5)	0.4252(1)	0	0.0070(3)	
Au2	3k	0.9114(1)	0.45569(6)	1/2	0.0075(3)	
Gd1	1d	1/3	2/3	1/2	0.0066(5)	
Gd2	3j	0.79552(7)	0.20448(7)	0	0.0076(4)	
Au5	3k	0.91376(5)	0.08624(5)	1/2	0.0077(3)	0.992 (6)
Al1	6m	0.0493(6)	0.7056(6)	1/2	0.008(1)	
Al2	3j	0.0849(4)	0.1699(9)	0	0.007(2)	
Al3	1f	2/3	1/3	1/2	0.015(4)	
Al4	3j	0.4679(4)	0.5321(4)	0	0.009(2)	
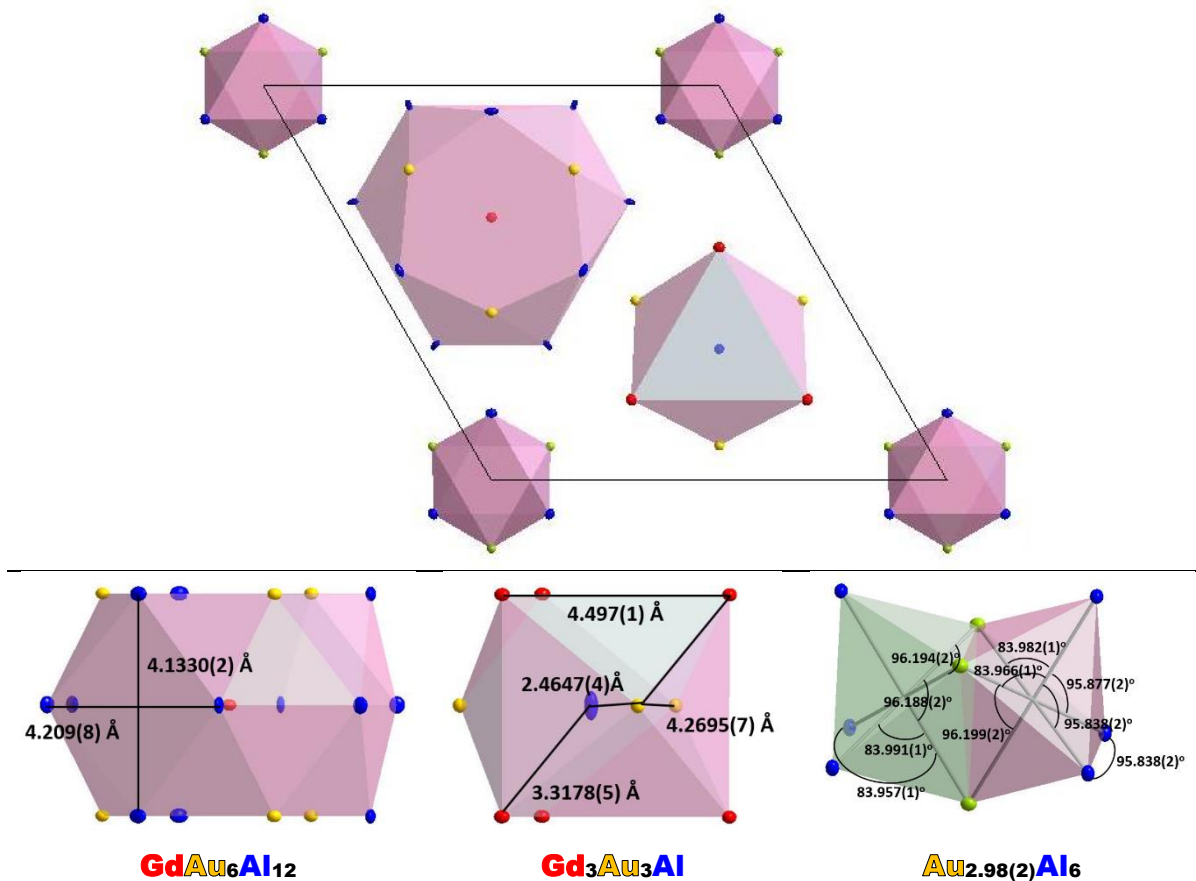
Figure 5. Gd$_4$Au$_{8.98(2)}$Al$_{13}$ drawn as three different polyhedra with two face-sharing octahedra of Au$_{2.98(2)}$Al$_6$ as building units.

Reference

1. Bailey, D. M.; Kline, G. R., The crystal structure of GdAg$_{3.6}$. *Acta Crystallographica Section B* **1971,** *27* (3), 650-653.

CHAPTER 8

SUMMARY AND FUTURE DIRECTIONS

To contribute to a "localized", electronic, perspective of metals and main-group intermetallics, this dissertation primarily researched polar intermetallic compounds by focusing on two main questions: (1) Where are the atoms, based on observed electron densities via diffraction? (2) What gives rise to the observed structures, based on chemical bonding and electronic structure theory?

From investigations of the Ca–Au–Al system using X-ray diffraction, we learn that with variation in temperature, metastable polar intermetallic i-QCs can irreversibly transform into their 2/1 CAs, which thus provided experimental corroboration for the proposal that a CA "approximates" the local structure of a QC. In the study of multinary phases, as seen in the structures herein, to answer question (1) of this dissertation, there is an additional subset of problems to address "which atom is where?", such as the investigation of site distributions between Au and Al within the same structural framework.

To elucidate the structure of an i-QC beyond approximations via CAs, decreasing the number of parameters in a system from a ternary phase space to binary may be important so that atomic mixed occupancies and site preferences may be minimized. Tsai- and Bergman-type CAs are structurally similar, with the greatest difference being the central tetrahedra in the former and the lack thereof in the latter. Whereas Tsai-type CAs and i-QCs have the condensed composition $AB_{5.3-6.0}$ with "A" as the active metal and "B" as either a group 12 element or a combination of elements to achieve a polar-intermetallic compound, many Bergman-type compounds have the condensed composition $AB_{2.0-3.0}$. The "A" for most Tsai-type phases are either divalent or trivalent, as also seen in this dissertation with the Ca/Y/Gd–

Au–Al systems, which all produced Tsai-type CA structures, whereas monovalent "A" of Bergman-type phases have been reported. Both the Tsai- and Bergman-type CAs have reported using a combination of groups 11 and 13/14 elements for "B" so that polar-intermetallic Tsai- and Bergman-types have both been produced. Whereas the Tsai-type binaries report using Cd for "B", there is no report on the investigation of Bergman-type binaries using Cd for "B". Also, whereas the Bergman-type utilizes Na for "A", there is no report on the investigation of monovalent Na in the Tsai-type for "A", which begs the question on whether valence electron tuning to target compositions of the Na–Cd system may lead to i-QCs and CAs that would minimize atomic mixed occupancies and disorders. This proposed direction would examine Zintl-Klemm-like i-QCs and CAs, which, if exist, may not help elucidate chemical bonding features of polar intermetallic compounds, but may contribute to answering question (1) of the dissertation: where are the atoms, specifically, in i-QCs?

From general bonding features and atomic site preference analysis of the polar intermetallic systems in this dissertation, we learn that (AE/RE/TM^{III-IV})–(Au+Al) polar-covalent interactions contribute to structural cohesion, which is also influenced by maximizing nearest neighbor orbital interactions between Au and Al. Maximizing Au–Al nearest contacts may be at the expense of Au–Au contacts, which may lead to structural distortions, as shown in the cubic- to tetragonal- to monoclinic- $NaZn_{13}$ derivatives of $SrAu_xAl_{13-x}$, and also in the electronic pseudo-Peierls distortion of ScAuAl that resulted in alternating long-short Au–Au chains with overall longer averaged Au–Au distances than in the "undistorted" structure.

Electronically, the progression from AE to RE and TM^{III-IV} active metals generally correlates with the increased contribution of d valence electrons overall. Ca ([Ar]$4s^2$) and Sr ([Kr]$5s^2$) have virtual $3d$ and $4d$ orbitals, respectively. Moving from Ca to Sc ([Ar]$3d^14s^2$) and

from Sr to Y ([Kr]$4d^1 5s^2$), the effects of one additional d electron were examined, and finally to Ti ([Ar]$3d^2 4s^2$), with now two $3d$ valence electrons. With Gd ([Xe]$4f^7 5d^1 6s^2$), pseudo-core $4f$ electrons were introduced, which generally do not engage in sufficient interatomic orbital overlap, but more importantly the effects of $5d$–$5d$ orbital interactions between Gd and Au are to be examined. Structurally, chemical pressure side effects by changing the active metal with differing radii were examined ($R_{Sr,Ca}$ = 2.15, 1.97 Å; $R_{Y,Sc}$ = 1.80, 1.64 Å; R_{Ti} = 1.47 Å; R_{Gd} = 1.80 Å).

Generally, variation of the active metal showed that increasing d orbital contribution in polar intermetallics seems to correlate with a progression from Hume-Rothery features to more Zintl-Klemm structural subtleties within the comparative systems. In Ca/Sr–Au–Al, large polyhedra comprised of discrete (Au+Al) atoms, and intervening (Ca/Sr) atoms with also large coordination spheres, are ubiquitous. In these systems, valence electronic tuning, to target compositions for experimental synthesis, utilized the Hume-Rothery valence-electron counting mechanism to observe subtle phase changes. Moving to Sc/Ti–Au–Al with additional $3d$ electrons in the active metal, rather than large atomic coordination spheres and polyhedra, which are structural hallmarks of H-R phases, we instead observe 2-dimensional networks formed by Au and Al atoms. For a more standardized compositional comparison, this general trend is more relevant in the study of AAuAl (A = Ca, Sc, and Ti). In moving from Ca to Sc and Ti, the structures of the respective compounds go from mostly 3-dimensional in CaAuAl of the TiNiSi-type with [Au$_3$Al$_3$] "chair" conformations, to completely 2-dimensional in TiAuAl of the Ni$_2$In-type (AlB$_2$-like) with now planar hexagons of [Au$_3$Al$_3$] and intervening layers of Ti. This d-orbital contribution generality can be further studied by observing effects of the d electrons in p-block elements of polar intermetallic compounds, for instance by

replacing Ga–Tl for Al, in which case: What are the atomic and electronic structural effects of d "core" electrons in p-block elements of polar intermetallic compounds?

Finally, the Y/Gd–Au–Al systems show significant structural similarities in the compounds discussed in this dissertation, specifically the 1/1 CAs $Y_3Au_{14.08(2)}Al_{4.49(1)}$ and $Gd_3Au_{14.10(2)}Al_{4.47}$; and the hexagonal $(Y/Gd)Au_{2.929(4)}Al_{0.659}$ and $(Gd/Y)_4Au_{9.00(3)}Al_{13}$. Electronically, Gd and Y differ in that Gd possesses unpaired electrons in the pseudo-core f-orbitals, whereas Y has virtual f orbitals, but they both contain 1 electron in their respective $5d$ and $4d$ orbitals. Presumably, whereas Ca/Y–Au–Al i-QCs are non-magnetic, Gd–Au–Al i-QCs would be magnetic. How, then, do unpaired electronic spins contribute to the observed structures of polar intermetallic compounds?

APPENDIX A

CHAPTER 3 SUPPORTING INFORMATION

Structure-Composition Subtleties in NaZn$_{13}$-type Derivatives of Sr/Ca(Au$_x$Al$_{1-x}$)$_{12-13}$

Table S1. Summary of crystallographic refinements for Ca(Au$_x$Al$_{1-x}$)$_{12.10-12.21(4)}$

instrument	Bruker CCD APEX II		
radiation; λ (Å)/ temp.(K)	Mo $K\alpha_1$; 0.71073/ 298		
loading composition	Ca$_{1.00(6)}$Au$_{5.99(1)}$Al$_{5.86(8)}$	Ca$_{1.04(6)}$Au$_{6.69(1)}$Al$_{6.27(8)}$	Ca$_{1.01(6)}$Au$_{6.01(1)}$Al$_{7.04(8)}$
refined composition	CaAu$_{6.09(2)}$Al$_{6.01(1)}$	CaAu$_{6.14(4)}$Al$_{6.05(3)}$	CaAu$_{6.16(2)}$Al$_{6.05(2)}$
θ range data collection	1.6–27.8°	1.7–33.3°	1.6–29.3°
absorp. coeff. μ (mm^{-1})/ correction	96.46/ empirical	96.91/ empirical	96.67/ empirical
meas./ indpnt./ obs. [I > 2σ(I)]/ para.	22258/ 2192/ 1513/ 138	24745/ 3516/ 2435/ 138	26135/ 2600/ 1985/ 138
R[F^2 > 2σ(F^2)]/ wR(F^2)/ R$_{int}$/ GOF	0.038/ 0.077/ 0.111/1.00	0.056/ 0.121/ 0.131/ 1.09	0.075/ 0.116/ 0.112/ 1.27
space group/ Pearson symbol	*Pbcm* (no. 57)/ *oP*108		
Δρ$_{max}$, Δρ$_{min}$ (e Å^{-3})	2.82, –2.77	5.22, –4.57	4.25, –4.18
dimensions (Å)	a = 12.4481(4) b = 12.2776(4) c = 12.2096(5)	a = 12.2321(8) b = 12.4512(8) c = 12.2898(7)	a = 12.481(2) b = 12.299(2) c = 12.256(2)
dimensions (Å) (PXRD; Cu $K\alpha_1$)	a = 12.4484(4) b = 12.2792(6) c = 12.2145(7)	a = 12.052(4) b = 12.273(5) c = 12.142(5)	a = 12.451(4) b = 12.286(4) c = 12.223(4)
volume (Å^3)/ Z	1866.03(1)/ 8	1871.8(2)	1881.4(6)
index ranges	$-15 \le h, k \le 15$ $-15 \le l \le 12$	$-18 \le h, k, l \le 18$	$-17 \le h \le 17$ $-16 \le k, l \le 16$
Al7 (4d): stuffed icosahedron occ.	0.20(3)	0.37(5)	0.40(7)
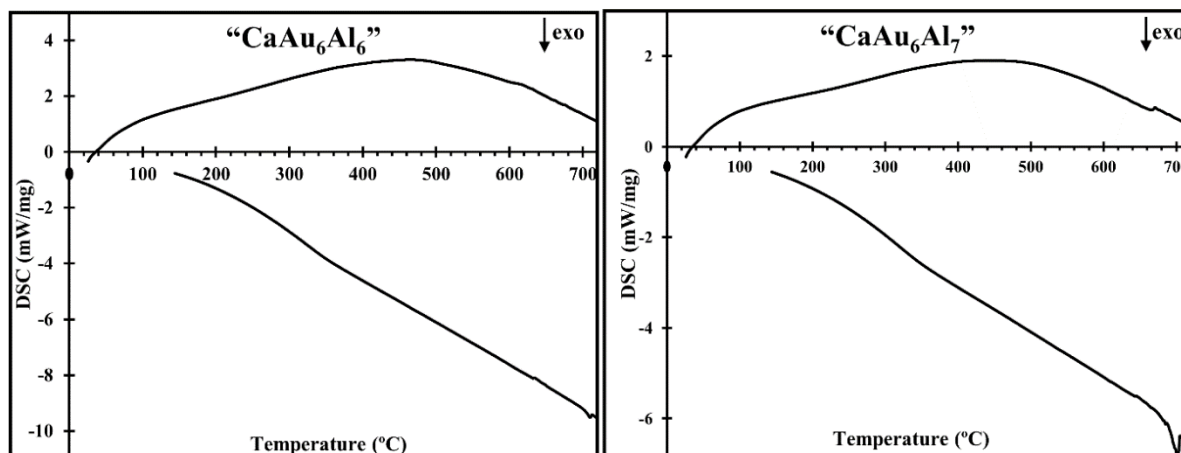
Figure S1. Thermal analysis from loadings "CaAu$_6$Al$_6$" and "CaAu$_6$Al$_7$" that guides the quenching synthesis due to a small peak ~625°C on cooling for both.

Table S2. Crystallographic parameters from specimens in Table S1

atom	wyck	sym	CaAu$_{6.07}$Al$_{6.05}$					CaAu$_{6.04}$Al$_{6.06}$				
			x	y	z	U$_{iso}$/U$_{eq}$	occ. (<1)	x	y	z	U$_{iso}$/U$_{eq}$	occ. (<1)
Au1	4d	..m	0.38680(6)	0.31861(6)	1/4	0.0188(2)		0.38665(3)	0.31840(3)	1/4	0.01155(7)	
Au2	4d	..m	0.63413(6)	0.15682(6)	1/4	0.0191(2)		0.63386(3)	0.15665(3)	1/4	0.01151(8)	
Au3	8e	1	0.06756(4)	0.52039(5)	0.11328(5)	0.0210(2)		0.06744(2)	0.52056(3)	0.11337(3)	0.01366(6)	
Au4	4d	..m	0.08700(7)	0.13722(7)	1/4	0.0221(2)		0.08752(4)	0.13722(4)	1/4	0.01416(8)	
Au5	4d	..m	0.05672(6)	0.87008(7)	1/4	0.0219(2)		0.05679(4)	0.87006(4)	1/4	0.01473(8)	
Au6	8e	1	0.37633(5)	0.00262(4)	0.08001(5)	0.0207(2)		0.37619(3)	0.00308(2)	0.08044(3)	0.01284(6)	
Au7	8e	1	0.75428(4)	0.31429(5)	0.12327(5)	0.0200(2)		0.75420(2)	0.31425(2)	0.12326(3)	0.01259(6)	
Au8	8e	1	0.24517(4)	0.38076(5)	0.06873(5)	0.0196(2)		0.24513(2)	0.38081(2)	0.06885(2)	0.01216(6)	
Au/Al9	4d	..m	0.4305(4)	0.1149(4)	1/4	0.016(2)	0.045(5)/0.955	0.4315(2)	0.1152(2)	1/4	0.0112(9)	0.034(3)/0.966
Au/Al10	8e	1	0.2556(3)	0.1828(3)	0.1335(3)	0.018(1)	0.043(4)/0.957	0.2553(2)	0.1830(2)	0.1333(2)	0.0101(7)	0.026(3)/0.974
Ca1	4c	2..	0.0042(3)	1/4	0	0.0230(9)		0.0043(2)	1/4	0	0.0169(4)	
Ca2	4c	2..	0.5068(4)	1/4	0	0.0266(9)		0.5068(2)	1/4	0	0.0194(5)	
Al1	8e	1	0.2516(3)	0.6117(4)	0.0704(4)	0.0161(9)		0.2514(2)	0.6114(2)	0.0708(2)	0.0102(4)	
Al2	4d	..m	0.5893(5)	0.3744(5)	1/4	0.018(1)		0.5888(3)	0.3739(3)	1/4	0.0114(6)	
Al3	4d	..m	0.1446(5)	0.3508(5)	1/4	0.019(1)		0.1438(3)	0.3511(3)	1/4	0.0118(6)	
Al4	8e	1	0.4243(3)	0.4894(3)	0.1295(4)	0.0169(9)		0.4250(2)	0.4891(2)	0.1290(2)	0.0104(4)	
Al5	4d	..m	0.1260(5)	0.6765(5)	1/4	0.022(1)		0.1252(3)	0.6765(3)	1/4	0.0144(6)	
Al6	8e	1	0.1378(4)	0.5042(3)	0.5891(4)	0.0204(9)		0.1377(2)	0.5043(2)	0.5895(2)	0.0130(4)	
Al7	4d	..m	0.250(2)	0.006(2)	1/4	0.008(8)	0.23(3)	0.246(1)	0.005(1)	1/4	0.000(4)	0.21(2)

Table S3. Orthorhombic ~CaAu$_6$Al$_6$ from the loading "CaAu$_6$Al$_6$"

instrument	Bruker CCD APEX II		
radiation; λ (Å)/ temp.(K)	Mo Kα; 0.71073/298		
θ range data collection	1.6º–31.1º	1.6º–37.6º	1.6–27.8º
absorp. coeff. μ (mm^{-1})/ correction	95.06/ empirical	95.86/ empirical	96.46/ empirical
meas./ indpnt./ obs. [I > 2σ(I)]/ para.	20725/ 3051/ 2598/ 138	85902/ 5048/ 4207/ 138	22258/ 2192/ 1513/ 138
R[F^2 > 2σ(F^2)]/ wR(F^2)/ R$_{int}$/ GOF	0.047/ 0.108/ 0.127/ 1.09	0.035/ 0.081/ 0.115/ 1.04	0.038/ 0.077/ 0.111/1.00
space group/ Pearson symbol	*Pbcm* (#57)/ *oP*108		
Δρ$_{max}$, Δρ$_{min}$ (e Å^{-3})	3.60, −3.40	4.31, −3.62	2.82, −2.77
dimensions (Å)	a = 12.497(7) b = 12.307(7) c = 12.259(7)	a = 12.446(2) b = 12.266(2) c = 12.206(2)	a = 12.4481(4) b = 12.2776(4) c = 12.2096(5)
volume (Å^3)/ Z	1885.6(2)/ 8	1863.4(4)/ 8	1866.03(1)/ 8
index ranges	−17 ≤ h, k ≤ 17 −17 ≤ l ≤ 16	−21 ≤ h ≤ 21 −20 ≤ k, l ≤ 20	−15 ≤ h, k ≤ 15 −15 ≤ l ≤ 12
	CaAu$_{6.07}$Al$_{6.05}$	**CaAu$_{6.04}$Al$_{6.06}$**	**CaAu$_{6.09}$Al$_{6.01}$**

Table S4. Summary of crystallographic refinements for Sr(Au$_x$Al$_{1-x}$)$_{12-13}$

instrument	Bruker CCD APEX I					
radiation; λ (Å) /temp.(K)	Mo Ka_1; 0.71073/ 298					
loading composition	SrAu$_{6.7}$Al$_{6.3}$	SrAu$_{6.8}$Al$_{5.2}$	SrAu$_{7.3}$Al$_{8.3}$	SrAu$_{5.8}$Al$_{5.8}$	SrAu$_6$Al$_7$	SrAu$_{5.5}$Al$_{6.5}$
refined composition	SrAu$_{6.68(2)}$Al$_{6.32}$	SrAu$_{7.24(2)}$Al$_{5.76}$	SrAu$_{6.59(1)}$Al$_{6.41}$	SrAu$_{6.35(3)}$Al$_{6.65}$	SrAu$_{6.10(3)}$Al$_{6.40}$	SrAu$_{5.75(2)}$Al$_{6.25}$
θ range data collection	3.3–23.2º	3.3–23.1º	1.6–23.1º	1.6–23.3º	1.7–23.3º	1.6–23.3º
absorp. coeff. μ (mm^{-1})	106.29/ empirical	113.41/ empirical	105.72/ empirical	100.85/ empirical	100.78/ empirical	95.71/ empirical
meas./ indpnt./ obs. [I > 2σ(I)]/ para.	2230/ 71/ 67/ 11	2340/ 71/ 68/ 11	5733/ 388/ 323/ 49	5320/ 392/ 359/ 49	9987/ 2494/ 1695/ 251	5329/ 385/ 355/ 44
R[F^2 > 2σ(F^2)]/ wR(F^2)/ R$_{int}$/ GOF	0.021/ 0.049/ 0.062/1.38	0.23/ 0.048/ 0.058/ 1.21	0.039/ 0.078/ 0.094/ 1.21	0.060/ 0.134/ 0.103/ 1.31	0.055/ 0.116/ 0.088/ 1.05	0.023/ 0.048/ 0.061/ 1.07
space group/ Pearson symbol	$Fm\bar{3}c$ (no. 226)/ cF112		$P4/nbm$ (no. 125)/ tP56		$P2/c$ (no. 13)/ mP108	$P4/nbm$ (no. 125)/ tP52
Δρ$_{max}$, Δρ$_{min}$ (e Å^{-3})	1.06, –1.20	0.84, –1.02	1.92, –1.50	–2.41, 2.22	–3.16, 3.01	–1.09, 1.05
dimensions (Å)	$a=b=c=$ 12.482(2)	$a=b=c=$ 12.528(2)	$a=b=8.789(3)$ $c=12.505(6)$	$a=b=8.842(3)$ $c=12.505(6)$	$a=12.260(8)$ $b=12.470(9)$ $\beta=90.26(2)$ $c=12.320(9)$	$a=b=8.698(2)$ $c=12.397(6)$
volume (Å^3)/ Z	1944.7(6)/ 8	1966.5(6)/ 8	965.9(7)/ 4	977.7(6)/ 4	1883(2)/ 8	937.9(6)/ 4
index ranges	-13 ≤ h, k, l ≤ 13		$-9 ≤ h, k ≤ 9$ $-13 ≤ l ≤ 13$	$-9 ≤ h, k ≤ 9$ $-13 ≤ l ≤ 13$	13 ≤ h, k, l ≤ 13	$-9 ≤ h, k ≤ 9$ $-13 ≤ l ≤ 13$
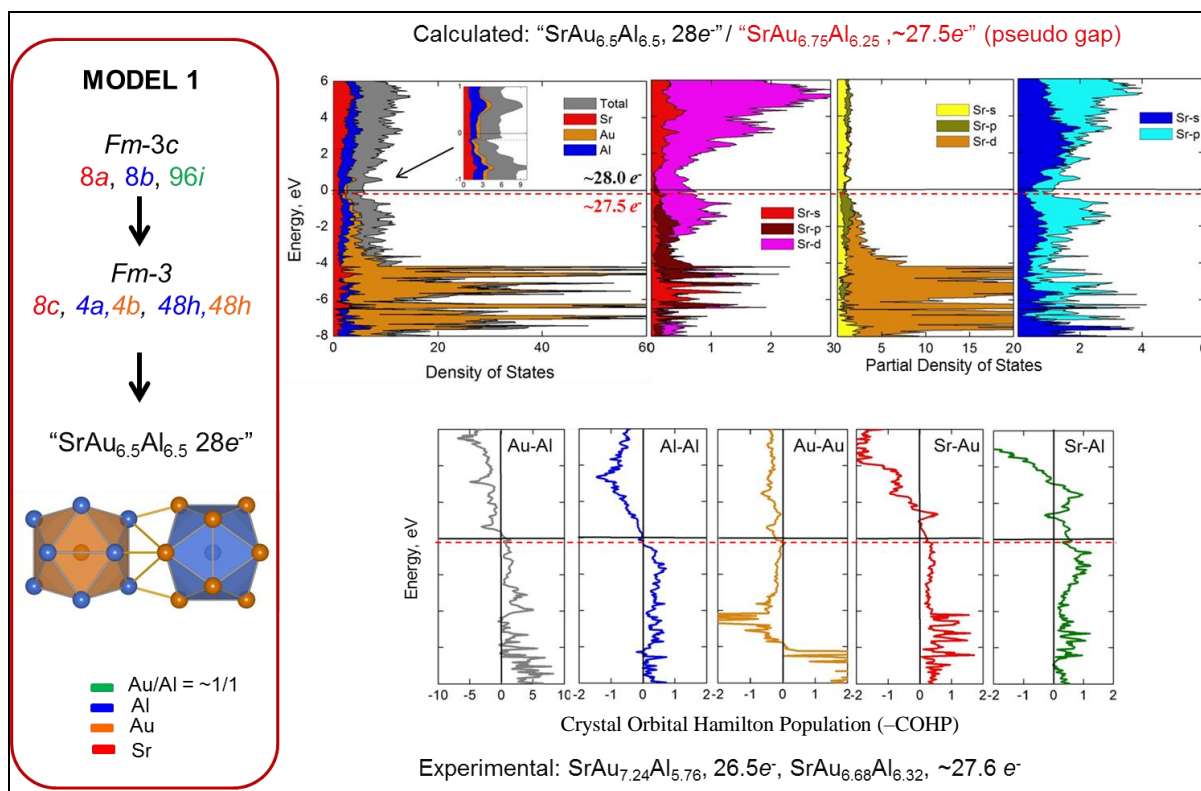
Figure S2. Electronic structures of cubic "SrAu$_{6.5}$Al$_{6.5}$" with partial atomic orbital contributions and nearest pair-wise interactions.
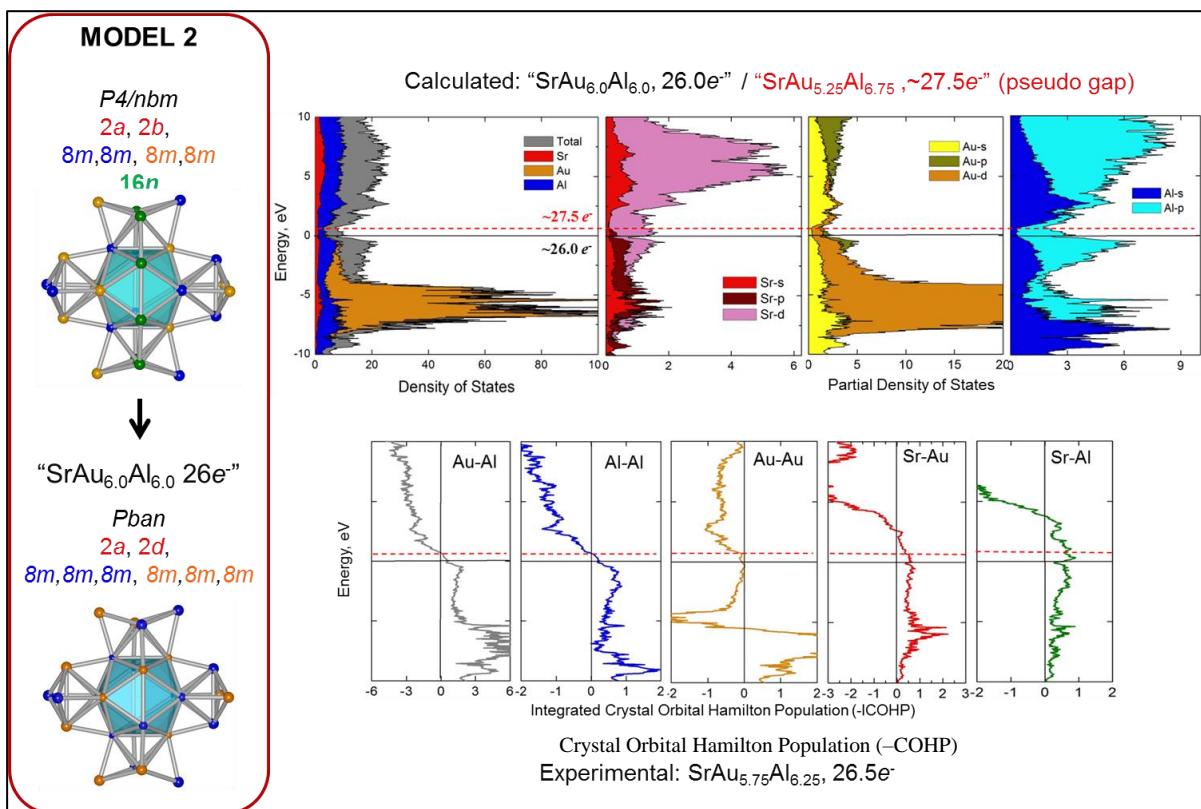
Figure S3. Electronic structures of tetragonal "SrAu$_{6.0}$Al$_{6.0}$" with empty icosahedra.

APPENDIX B

CHAPTER 4 SUPPORTING INFORMATION

An Icosahedral Quasicrystal and Its 1/0 Crystalline Approximant in the Ca–Au–Al System

Contents

Table S1. Loading and refined compositions from single-crystal X-ray diffraction of $CaAu_{3+x}Al_{1-x}$ ($0 \leq x \leq 0.31(1)$)

Loading molar % Ca:Au:Al	Loading "ratio" (per Ca atom)	VEC	$\langle x \rangle$	Refined	VEC	x	%Au	%Al	Single crystal XRD a (Å)	Powder XRD (7 I_{max} peaks) a (Å)	Powder XRD (Rietveld) a (Å)
20.16: 67.08: 12.76	$Ca_{1.00(3)}Au_{3.327(6)}Al_{0.63(4)}$	1.457	0.35(4)	$CaAu_{3.315(7)}Al_{0.685}$	1.474	0.315(7)	66.300	13.700	9.112(1)	9.109(4)	9.1261(8)
20.04: 64.90: 15.06	$Ca_{1.00(3)}Au_{3.238(6)}Al_{0.75(4)}$	1.502	0.25(4)	$CaAu_{3.291(7)}Al_{0.709}$	1.484	0.291(6)	65.820	14.180	9.112(8)	9.102(4)	9.1152(5)
19.65: 62.40: 17.95	$Ca_{1.00(3)}Au_{3.176(6)}Al_{0.91(4)}$	1.555	0.15(4)	$CaAu_{3.207(6)}Al_{0.793}$	1.518	0.207(4)	64.125	15.875	9.087(4)	9.118(4)	9.1003(4)
20.32: 60.46: 19.21	$Ca_{1.00(3)}Au_{2.975(5)}Al_{0.95(4)}$	1.587	–0.03(4)	$CaAu_{3.11(4)}Al_{0.89}$	1.555	0.11(4)	62.250	17.750	9.0772(2)	9.078(4)	9.0795(3)
20.04: 59.58: 20.38	$Ca_{1.00(3)}Au_{2.974(6)}Al_{1.02(4)}$	1.608	–0.03(4)	$CaAu_{3.00}Al_{1.00}$	1.600	0	60.000	20.000	9.0656(8)	9.077(4)	9.0766(5)

Table S2. Selected refined crystallographic data of a few CaAu$_{3+x}$Al$_{1-x}$ (0 ≤ x ≤ 0.31(1)) crystals

	CaAu$_{3.00}$Al$_{1.00}$	CaAu$_{3.11(4)}$Al$_{0.89}$	CaAu$_{3.207(6)}$Al$_{0.793}$	CaAu$_{3.291(7)}$Al$_{0.709}$	CaAu$_{3.314(7)}$Al$_{0.686}$
instrument	Bruker CCD APEX II	Bruker CCD APEX II	Bruker CCD APEX II	Bruker CCD APEX II	Bruker CCD APEX II
radiation; λ (Å)/ temp.(K)	Mo Kα; 0.71073/298	Mo Kα; 0.71073/298	Mo Kα; 0.71073/298	Mo Kα; 0.71073/298	Mo Kα; 0.71073/298
θ range data collection	3.9º–30.0º	3.9º–32.3º	3.9º–30.1º	3.9º – 29.1º	3.9º–29.1º
absorp.coeff./ μ (mm-1)/ correction	119.21	123.11	126.14	128.48	129.38
absorp. correction	Empirical	empirical & numerical	empirical	empirical	empirical
meas./ indpnt./ obs. [I > 2σ(I)]/ para.	14462/369/319/17	4099/435/376/18	23098/374/289/18	6189/338/297/18	6177/339/270/18
R[F2 > 2σ(F2)]/ wR(F2)/ Rint/ GOF	0.027/0.060/0.145/1.14	0.031/0.055/0.053/1.11	0.030/0.064/0.183/1.07	0.031/0.059/0.076/1.15	0.036/0.081/0.101/1.07
space group/ Pearson symbol	$Pa\overline{3}$ (#205)/$cP40$	$Pa\overline{3}$ (#205)/$cP40$	$Pa\overline{3}$ (#205)/$cP40$	$Pa\overline{3}$ (#205)/$cP40$	$Pa\overline{3}$ (#205)/$cP40$
Δρ$_{max}$, Δρ$_{min}$ (e Å^{-3})	1.88, −1.60	2.59, −2.45	1.66, −1.51	3.31, − 2.51	2.68, −2.11
dimension a (Å)/ volume (Å^3)/ Z	9.0656(8)/745.1(2)/8	9.0772(2)/747.92(3)/8	9.087(4)/750.4(1)/8	9.112(8)/756.6/8	9.112(2)/756.6(4)/8
Au:Al (8c) occupancy	0/1	0.112(5)/0.888	0.201(6)/0.799	0.289(6)/0.711	0.312(7)/0.688

Table S3. Fractional atomic coordinates and displacement parameters of selected $CaAu_{3+x}Al_{1-x}$ ($0 \leq x \leq 0.31(1)$) crystals

	atom	*wyck*	sym	x	y	z	Frac. occ.	U_{iso}/U_{eq}	U_{11}	U_{22}	U_{33}	U_{12}	U_{13}	U_{23}
$CaAu_{3.00}Al_{1.00}$	Au	24*d*	1	0.08090 (5)	0.26068 (5)	0.35236 (5)	1	0.0191 (2)	0.0171 (3)	0.0232 (3)	0.0172 (3)	−0.0025 (2)	−0.0027 (2)	0.0019 (2)
	Ca	8*c*	.3.	0.3951 (3)	0.3951 (3)	0.3951 (3)	1	0.0153 (8)	0.0153 (8)	0.0153 (8)	0.0153 (8)	−0.0001 (9)	−0.0001 (9)	−0.0001 (9)
	Au/Al	8*c*	.3.	0.0915 (5)	0.0915 (5)	0.0915 (5)	0/1	0.013 (2)	0.013 (2)	0.013 (2)	0.013 (2)	0.011 (1)	0.011 (1)	0.011 (1)
$CaAu_{3.11(4)}Al_{0.89}$	Au	24*d*	1	0.08026 (4)	0.25968 (4)	0.35145 (4)	1	0.0111 (2)	0.0079 (2)	0.0162 (2)	0.0093 (2)	−0.0031 (1)	−0.0028 (1)	0.0030 (2)
	Ca	8*c*	.3.	0.3947 (2)	0.3947 (2)	0.3947 (2)	1	0.0069 (6)	0.0069 (6)	0.0069 (6)	0.0069 (6)	0.0000 (7)	0.0000 (7)	0.0000 (7)
	Au/Al	8*c*	.3.	0.0868 (3)	0.0868 (3)	0.0868 (3)	0.112(5)/ 0.888	0.023 (1)	0.023 (1)	0.023 (1)	0.023 (1)	0.014 (1)	0.014 (1)	0.014 (1)
$CaAu_{3.207(6)}Al_{0.793}$	Au	24*d*	1	0.07975 (5)	0.25753 (6)	0.34989 (6)	1	0.0267 (2)	0.0220 (3)	0.0339 (3)	0.0243 (3)	−0.0044 (2)	−0.0040 (2)	0.0058 (2)
	Ca	8*c*	.3.	0.3933 (3)	0.3933 (3)	0.3933 (3)	1	0.0208 (9)	0.0208 (9)	0.0208 (9)	0.0208 (9)	−0.0019 (9)	−0.0019 (9)	−0.0019 (9)
	Au/Al	8*c*	.3.	0.0812 (2)	0.0812 (2)	0.0812 (2)	0.201(6)/ 0.799	0.037 (1)	0.037 (1)	0.037 (1)	0.037 (1)	0.013 (1)	0.013 (1)	0.013 (1)
$CaAu_{3.291(7)}Al_{0.709}$	Au	24*d*	1	0.07949 (5)	0.25540 (6)	0.34789 (5)	1	0.0184 (2)	0.0124 (3)	0.0272 (3)	0.0158 (3)	−0.0060 (2)	−0.0047 (2)	0.0073 (2)
	Ca	8*c*	.3.	0.3930 (2)	0.3930 (2)	0.3930 (2)	1	0.0106 (8)	0.0106 (8)	0.0106 (8)	0.0106 (8)	−0.0022 (8)	−0.0022 (8)	−0.0022 (8)
	Au/Al	8*c*	.3.	0.0760 (2)	0.0760 (2)	0.0760 (2)	0.289(6)/ 0.711	0.0254 (9)	0.0254 (9)	0.0254 (9)	0.0254 (9)	−0.0022 (8)	−0.0022 (8)	−0.0022 (8)
$CaAu_{3.314(7)}Al_{0.686}$	Au	24*d*	1	0.07937 (6)	0.25497 (7)	0.34759 (6)	1	0.0197 (3)	0.0133 (4)	0.0290 (4)	0.0167 (4)	−0.0061 (2)	−0.0050 (2)	0.0079 (3)
	Ca	8*c*	.3.	0.3932 (3)	0.3932 (3)	0.3932 (3)	1	0.011 (2)	0.011 (2)	0.011 (2)	0.011 (2)	−0.002 (1)	−0.002 (1)	−0.002 (1)
	Au/Al	8*c*	.3.	0.0751 (2)	0.0751 (2)	0.0751 (2)	0.312(7)/ 0.688	0.027 (1)	0.027 (1)	0.027 (1)	0.027 (1)	−0.002 (1)	−0.002 (1)	−0.002 (1)

Table S3A. Hamilton test[*] of the 24*d* site: "split" versus "fully" occupied Au.

Refined composition with Au "full"	Refined composition with Au "split" free	Ca U_{iso}/U_{eq}	Au split U_{iso}/U_{eq}	Au full Frac. Occ.	Hypothesis: The 24*d* site is comprised of a "full Au" instead of 2 freely split Au.	Refined composition with Au "split" 0.5	Ca U_{iso}/U_{eq}	Au split U_{iso}/U_{eq}	Hypothesis: the 24*d* site is comprised of 2 Au split at 0.5 occ. each instead of 2 freely split Au.
$CaAu_{3.00}Al_{1.00}$	$CaAu_{2.9(1)}Al$	0.018(1)	0.19(2); 0.021(2)	0.54(4); 0.41(4)	Hypothesis can be rejected up to the 2.5% significance level.	$CaAu_{3.00}Al_{1.00}$	0.0200(8)	0.051(2); 0.0104(6)	Hypothesis can be rejected up to the 0.05% significance level.
$CaAu_{3.11(4)}Al_{0.89}$	$CaAu_{3.18(6)}Al_{0.88}$	0.008(1)	0.8(4); 0.0110(2)	0.020(9); 0.98(2)	Hypothesis can be rejected up to the 0.05% significance level.	$CaAu_{3.11(4)}Al_{0.89}$	0.0072(4)	0.017(1); 0.0068(9)	Hypothesis can be rejected up to the 0.05% significance level.
$CaAu_{3.207(6)}Al_{0.793}$	$CaAu_{3.3(1)}Al_{0.8}$	0.020(1)	0.0219(8); 0.031(2)	0.54(4); 0.48(4)	Hypothesis can be rejected up to the 0.05% significance level.	$CaAu_{3.192(7)}Al_{0.808}$	0.0318(7)	0.067(2); 0.0200(6)	Hypothesis can be rejected up to the 0.05% significance level.
$CaAu_{3.291(7)}Al_{0.709}$	$CaAu_{3.4(1)}Al_{0.7}$	0.010(1)	0.011(2); 0.022(1)	0.28(4); 0.72(4)	Hypothesis can be rejected up to the 50% significance level	$CaAu_{3.29(5)}Al_{0.71}$	0.0108(5)	0.026(2); 0.013(1)	Hypothesis can be rejected up to the 0.05% significance level.
$CaAu_{3.314(7)}Al_{0.686}$	$CaAu_{3.60(9)}Al_{066}$	0.009(2)	0.19(7); 0.0185(5)	0.07(2); 1.02(3)	Hypothesis can be rejected up to the 0.05% significance level.	$CaAu_{3.316(7)}Al_{0.684}$	0.0106(6)	0.016(2); 0.012(2)	Hypothesis can be rejected up to the 0.05% significance level.

* Hamilton, W. *Acta Crystallographica* **1965**, *18*, 502.
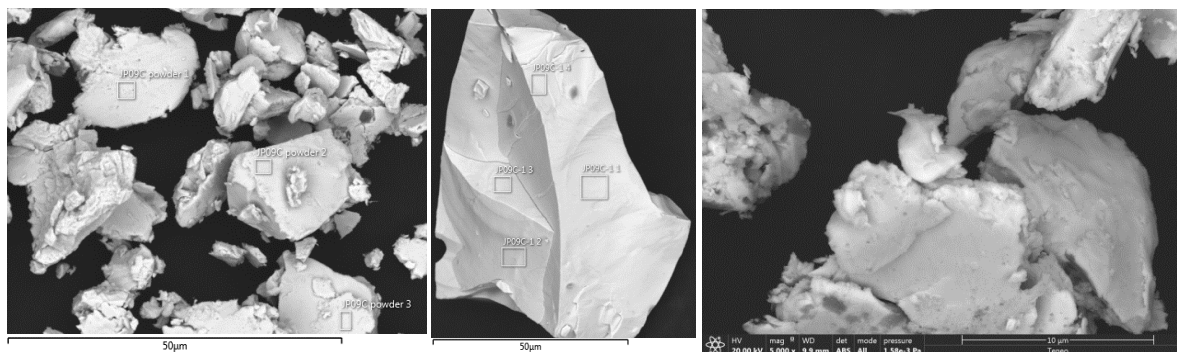
Figure S1. SEM images and locations of where the estimated compositions from EDS are scanned. Left and middle respectively: ground quasicrystalline products and single crystal from the loading 14.43% Ca: 63.30% Au: 22.27% Al ("CaAu$_{4.4}$Al$_{1.6}$" in main text). Right: back-scattering electron image of the ground crystalline approximant sample loaded as 20.32% Ca: 60.46% Au: 19.21% Al (refined as CaAu$_{3.11(4)}$Al$_{0.89}$).
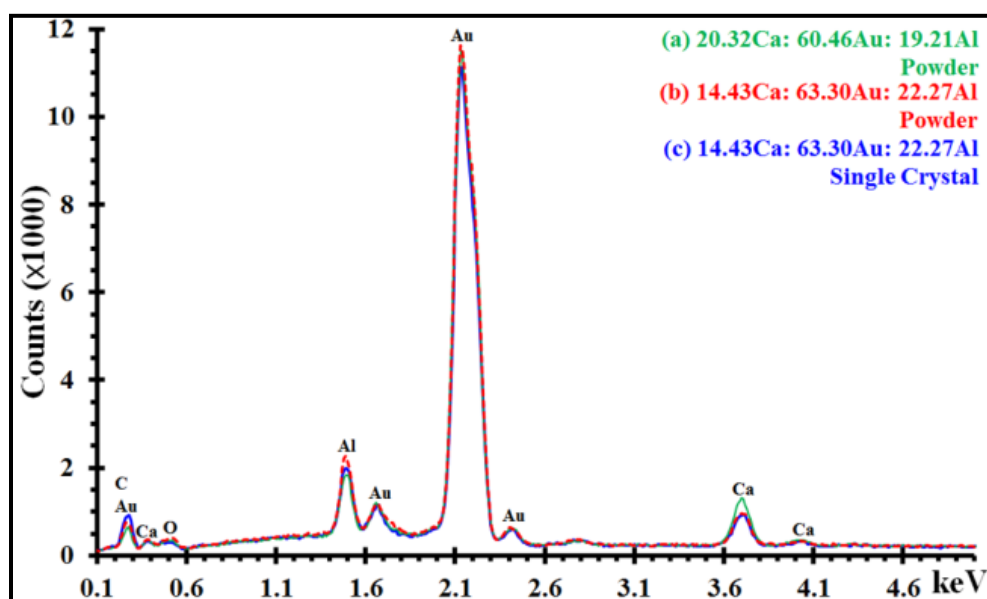
Figure S2. Combined EDS spectra of selected specimens. See accompanying Table S4 for atomic percent estimations according to the spectra.

Table S4. EDS estimation of atomic percent composition. When normalized without oxygen, the crystalline approximant and quasicrystalline compositions are respectively: Ca$_{1.0(1)}$Au$_{3.1(2)}$Al$_{0.9(1)}$ (refined: CaAu$_{3.11(4)}$Al$_{0.89}$) and Ca$_{1.0(1)}$Au$_{4.5(2)}$Au$_{1.4(1)}$ (loaded: "CaAu$_{4.4}$Al$_{1.6}$")

Figure S1 label	Atomic %				Molar ratios		
	O	Al	Ca	Au	Ca	Au	Al
JP09C-1 1	**10.6**	**18.5**	**12.9**	**57.9**	**1**	**4.5**	**1.4**
JP09C-2	14.3	17.7	12.3	55.7	1	4.5	1.4
JP09C-APS_Xtra_redo	15.0	17.8	12.2	55.0	1	4.5	1.5
JP09C_powder 1	**18.1**	**17.9**	**11.6**	**52.3**	**1**	**4.5**	**1.5**
JP09C powder 2	9.7	20.1	13.2	57.1	1	4.3	1.5
JP09C powder 3	8.9	19.0	13.6	58.6	1	4.3	1.4
JP005_powder 1	**15.7**	**14.7**	**17.2**	**52.5**	**1**	**3.1**	**0.9**
JP005_powder 2	19.2	13.8	16.2	50.8	1	3.1	0.9
JP005_powder 3	13.9	14.7	17.3	54.2	1	3.1	0.9
Precision sigma					0.1	0.2	0.1
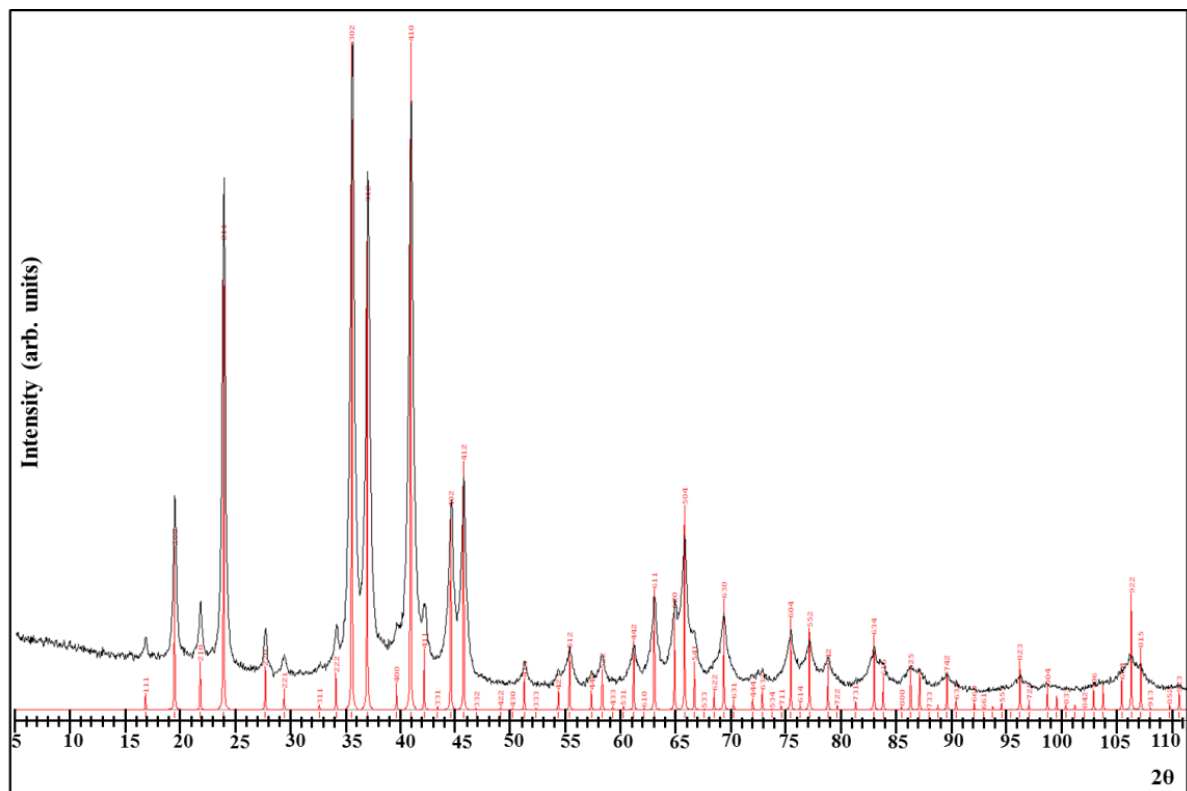
Figure S3a. Observed Powder X-ray diffraction pattern (black) for sample loading 20.32% Ca: 60.46% Au: 19.21% Al juxtaposed against simulated pattern (red) from single-crystal X-ray diffraction refinement $CaAu_{3.11(4)}Al_{0.89}$.
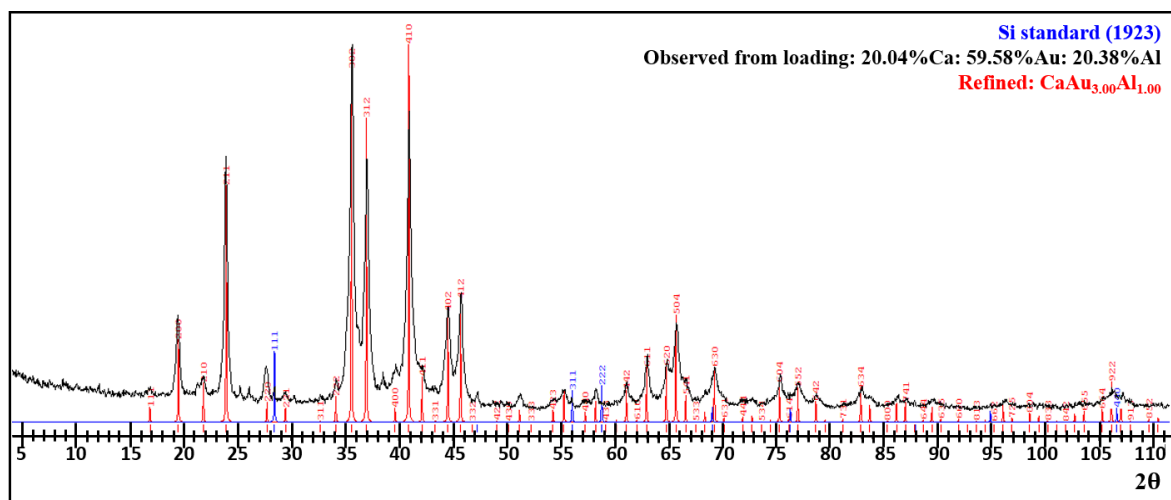
Figure S3b. Observed PXRD pattern of sample loading 20.04% Ca: 59.58% Au: 20.38% Al measured with added Si powder as a standard and juxtaposed against refined single-crystal XRD, $CaAu_{3.00}Al_{1.00}$.
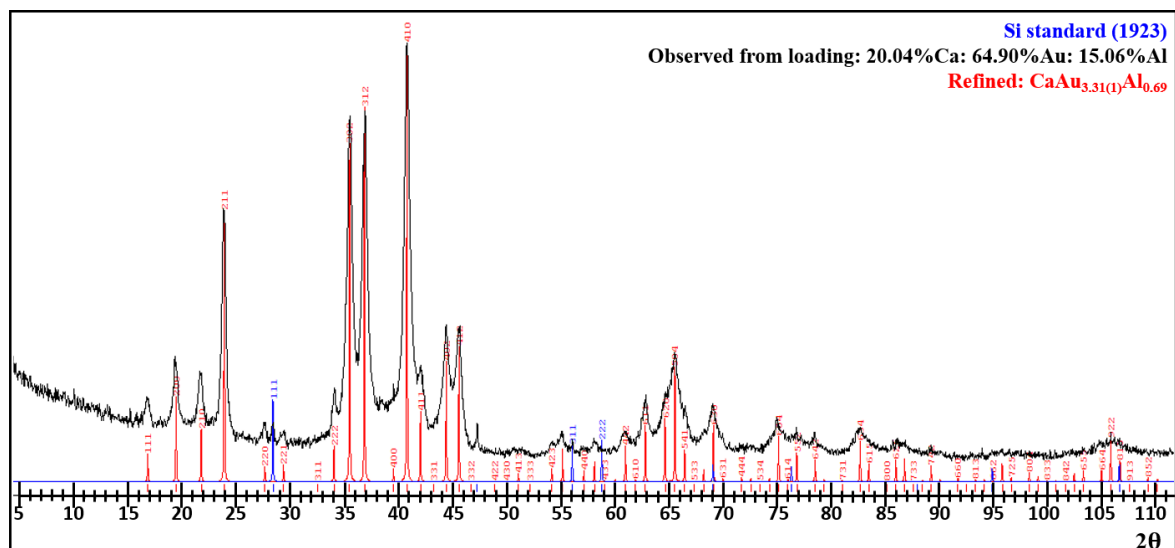
Figure S3c. Observed PXRD pattern of sample loading 20.04% Ca: 64.90% Au: 15.06% Al measured with added Si powder as a standard and juxtaposed against refined single-crystal XRD, $CaAu_{3.00}Al_{1.00}$.

Table S5. Tetrahedral star interactions: comparison of distances with isotypic, stoichiometric compounds in the literature[*] where X = Ge, Si, Ga or Al.
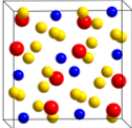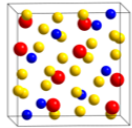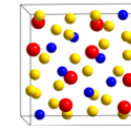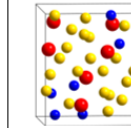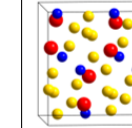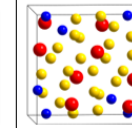
Interaction	$NaAu_3Ge$ (Å)	$NaAu_3Si$ (Å)	$CaAu_3Ga$ (Å)	$CaAu_3Al$ (Å)
Na/Ca–Au	3.103(9) (3×)	3.01(2) (3×)	3.079(3) (3×)	3.059(3) (3×)
	3.152(9) (3×)	3.12(2) (3×)	3.122(3) (3×)	3.122(3) (3×)
	3.325(9) (3×)	3.32(2) (3×)	3.352(3) (3×)	3.344(3) (3×)
<Na/Ca–Au>	3.193(9)	3.15(2)	3.184(3)	3.175(3)
Na/Ca–X	3.24(2) (3×)	3.19(2) (3×)	3.264(3) (3×)	3.279(5) (3×)
Au–Au	3.025(3) (3×)	3.040(1) (3×)	3.1069(7) (3×)	3.0669(8) (3×)
Au–X	2.67(2) (3×)	2.612(9) (3×)	2.747(2) (3×)	2.817(5) (3×)
Na/Ca–Na/Ca	5.30(1) (3×)	5.23(3) (3×)	5.245(4) (3×)	5.241(4) (3×)
	5.57(1) (3×)	5.51(3) (3×)	5.587(4) (3×)	5.575(4) (3×)

* (a) $NaAn_3Ge$/Si: Doering, W.; Schuster, H.-U., *Zeitschrift für Naturforschung. Teil b, Anorganische Chemie, organische Chemie* **1980**, *35B*, 1482. (b) $CaAu_3Ga$: Lin, Q.; Corbett, J. D., *Inorganic Chemistry* **2008**, *47*, 3462.

Table S7. Structural relaxation from experimental data using VASP for CaAu₃Al. The output parameters are used for subsequent LMTO calculations.

Parameter	Experimental input	Output after structural relaxation from VASP
a (Å)	9.0656	9.21784
b (Å)	9.0656	9.21784
c (Å)	9.0656	9.21784
Volume (Å³)	745.06	783.23 (+5.0% diff. from expt.)
Au1 (x,y,z)	0.08089, 0.26071, 0.35238	0.08186, 0.26227, 0.35589
Ca1 (x,y,z)	0.39512, 0.39512, 0.39512	0.39434, 0.39434, 0.39434
Al1 (x,y,z)	0.09170, 0.09170, 0.09170	0.89988, 0.89988, 0.89988
Au–Al ($24d$–$8c$)	2.551 Å	2.589 Å (+1.5% diff. from expt.)
	2.817 Å	2.795 Å (–0.8% diff. from expt.)
	3.433 Å	3.563 Å (+3.7% diff. from expt.)
Au–Au ($24d$–$24d$)	2.828 Å	2.880 Å (+1.8% diff. from expt.)
	3.067 Å	3.122 Å (+1.8% diff. from expt.)
	3.079 Å	3.149 Å (+2.2% diff. from expt.)
Al–Al ($8c$–$8c$)	2.883(6) Å	3.206 Å (+10.6% diff. from expt.)
E_{tot}/f.u. (eV)	–18.66(2)	–18.74(2) (–0.4% diff. from expt.)

183

Table S6. Six models and total energy differences illustrating possible arrangements of Au and Al for CaAu₃Al. The number of Au–Au, Au–Al and Al–Al interactions and their distances give insight into structural preference for Au–Al nearest neighbor contacts.

Label	α		β		Γ		δ		ε		ρ	
Depiction												
Space group	$Pa\bar{3}$		$R\bar{3}$		$R\bar{3}$		$R\bar{3}$		$Pbca$		$R\bar{3}$	
Sites	atom (wyck.)	coord.	atom (wyck.)	coord.	atom (wyck.)	coord.	atom (wyck.)	coord.	atom (wyck.)	coord.	atom (wyck.)	coord.
			Au1 (6f)	0.26071 0.35238 0.08089	Au1 (6f)	0.26071 0.35238 0.08089	**Al3 (6f)**	**0.26071 0.35238 0.08089**	Au1 (8c)	0.26071 0.35238 0.08089	**Au1 (6f)**	**0.26071 0.35238 0.08089**
	Au1 (24d)	0.08089 0.26071 0.35238	Au2 (6f)	0.23929 0.64762 0.58089	**Al3 (6f)**	**0.23929 0.64762 0.58089**	Au1 (6f)	0.23929 0.64762 0.58089	Au2 (8c)	0.08089 0.26071 0.35238	Au2 (6f)	0.23929 0.64762 0.58089
			Al3 (6f)	**0.73929 0.85238 0.41911**	Au2 (6f)	0.73929 0.85238 0.41911	Au2 (6f)	0.73929 0.85238 0.41911			Au3 (6f)	0.73929 0.85238 0.41911
			Au3 (6f)	0.76071 0.14762 0.91911	Au3 (6f)	0.76071 0.14762 0.91911	Au3 (6f)	0.76071 0.14762 0.91911	**Al3 (8c)**	**0.35238 0.08089 0.26071**	**Al3 (6f)**	**0.76071 0.14762 0.91911**
	Ca1 (8c)	0.39512 0.39512 0.39512	Ca1 (2c)	0.39512 0.39512 0.39512	Ca1 (2c)	0.39512 0.39512 0.39512	Ca1 (2c)	0.39512 0.39512 0.39512	Ca1 (8c)	0.39512 0.39512 0.39512	Ca1 (2c)	0.39512 0.39512 0.39512
			Ca2 (6f)	0.10488 0.60488 0.89512	Ca2 (6f)	0.10488 0.60488 0.89512	Ca2 (6f)	0.10488 0.60488 0.89512			Ca2 (6f)	0.10488 0.60488 0.89512
	Al1 (8c)	0.09180 0.09180 0.09180	Al4 (2c)	0.09180 0.09180 0.09180	Al4 (2c)	0.09180 0.09180 0.09180	Al4 (2c)	0.09180 0.09180 0.09180	Au4 (8c)	**0.09180 0.09180 0.09180**	Al4 (2c)	0.09180 0.09180 0.09180
			Au4 (6f)	**0.59177 0.09177 0.40823**	**Au4 (6f)**	**0.59177 0.09177 0.40823**	**Au4 (6f)**	**0.59177 0.09177 0.40823**			**Au4 (6f)**	**0.59177 0.09177 0.40823**
Total # Au–Al	72		72		60		48		72		36	
2.551(2) Å	24		12		12		12		8		0	
2.817(6) Å	24		12		12		0		8		12	
2.828(6) Å	0		12		0		12		16		12	
2.883(6) Å	0		0		0		0		0		0	
3.067(6) Å	0		12		12		0		16		12	
3.079(1) Å	0		12		12		12		16		0	
3.423(3) Å	24		12		12		12		8		0	
Total # Au–Au	72		75		81		87		76		93	
2.551(2) Å	0		12		12		12		16		18	
2.817(6) Å	0		12		12		18		16		12	
2.828(6) Å	24		12		18		12		8		12	
2.883(6) Å	0		3		3		3		4		3	
3.067(6) Å	24		12		12		18		8		12	
3.079(1) Å	24		12		12		12		8		18	
3.423(3) Å	0		12		12		12		16		18	
Total # Al–Al	4		1		7		13		0		19	
2.551(2) Å	0		0		0		0		0		6	
2.817(6) Å	0		0		0		6		0		0	
2.828(6) Å	0		0		6		0		0		0	
2.883(6) Å	4		1		1		1		0		1	
3.067(6) Å	0		0		0		6		0		0	
3.079(1) Å	0		0		0		0		0		6	
3.423(3) Å	0		0		0		0		0		6	
ΔE_{tot}/f.u. (eV)	0		+0.932		+1.049		+1.111		+1.237		+1.476	

Figure S4. Band structure of CaAu₃Al. Band crossings at E_f open up between M and X ~0.5 eV above and below E_f corresponding to 0.75 e^-/f.u. more or 0.5 e^-/f.u. less respectively.
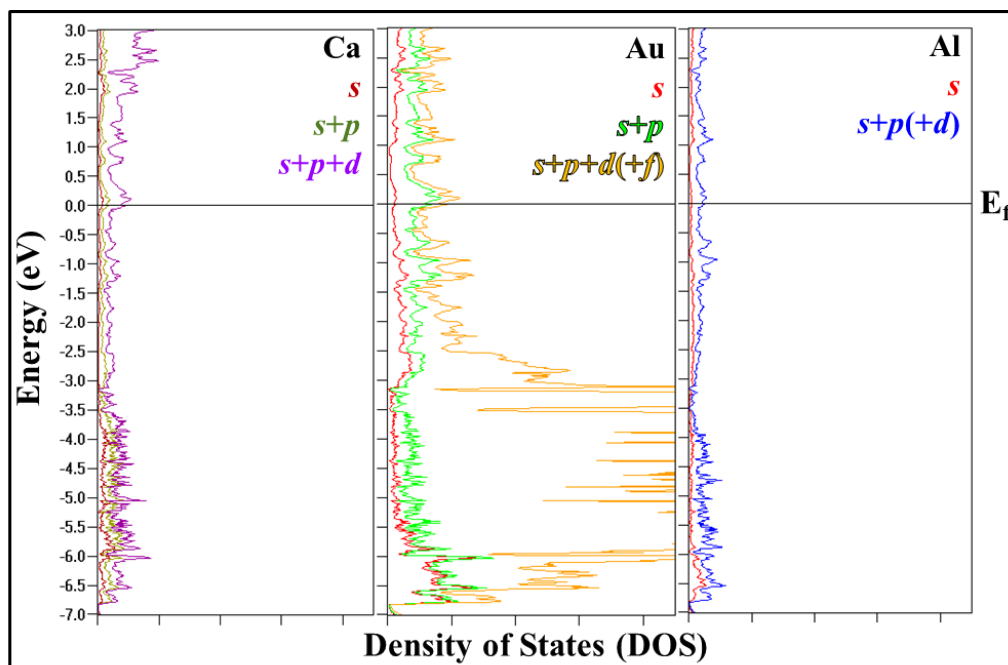
Figure S5. Partial DOS orbital breakdown for CaAu₃Al. The large band ~3 eV below E_F corresponds mainly to the Au $5d$ – Ca $3d$ orbital interactions. Ca $3d$ orbitals also lie above E_F available for accepting electrons. Together, the $5d$–$3d$ bonding and $3d$ empty states give rise to the "polar-covalent interaction" of the "polar intermetallic" CaAu₃Al classification.
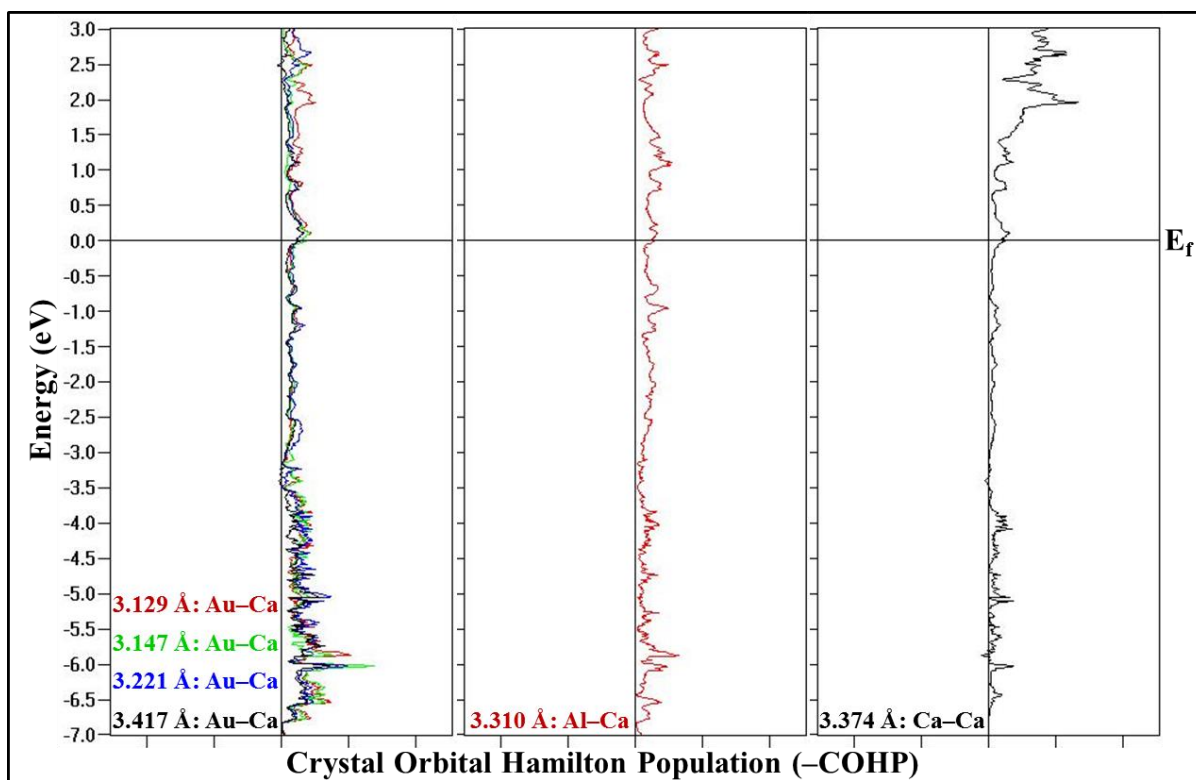
Figure S6. CaAu$_3$Al COHP curves for all Ca interactions up to 3.5 Å away showing all weakly bonding interactions whereby, on average, Ca–Au interactions dominate.

Table S8. Calculated and observed a_{QC}. The calculation is based on the classification that CaAu$_{3+x}$Al$_{1-x}$ is a 1/0 crystalline approximant of the icosahedral quasicrystal

CaAu$_{3+x}$Al$_{1-x}$ $a_{L/S}$ (Å)	L/S	Calculated a_{QC} (Å)	Observed a_{QC} (Å) for CaAu$_{4.4}$Al$_{1.6}$
9.078(4)–9.109(4)	1/0	5.336(2)–5.354(2)	5.384(4) (0.60–0.90% difference)
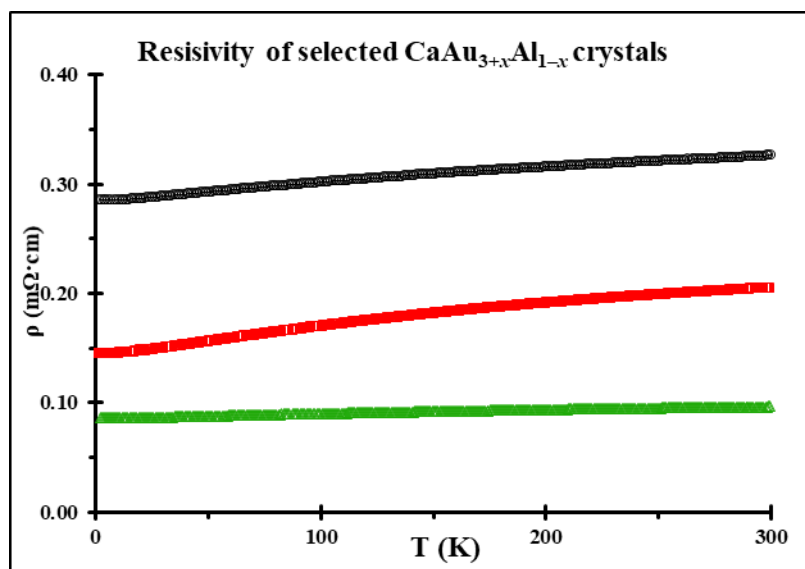
Figure S7. Resistivity of selected crystals from samples $CaAu_{3.11(4)}Al_{0.89}$ (black) and $CaAu_3Al$ (red and green). All RRR values are around 1.0 (black: 1.14; red: 1.47; green: 1.12), indicating a poor metal with structural disorder, which corroborate the structural disorder described herein.
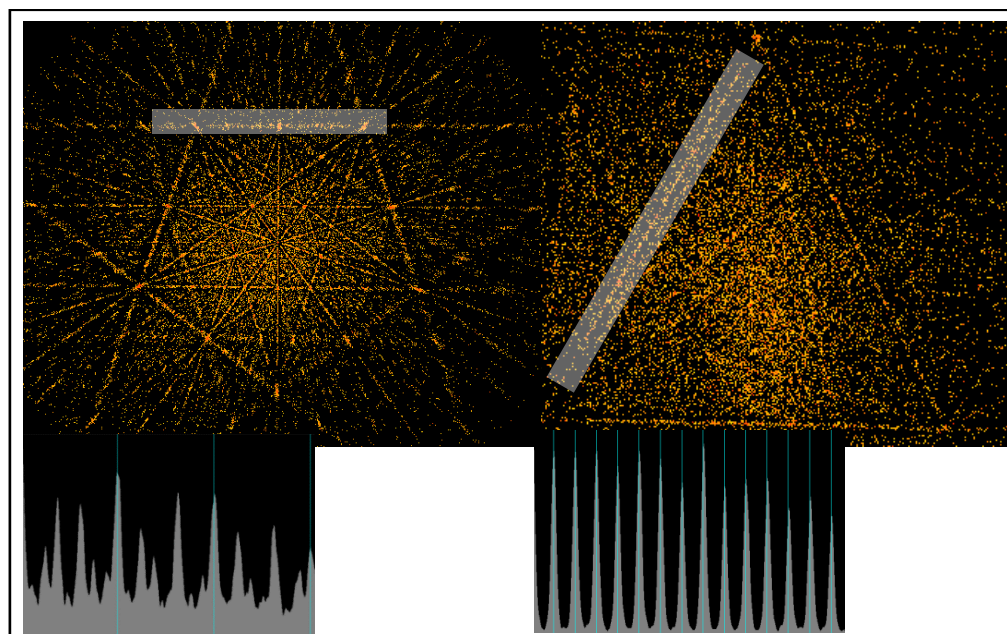
Figure S8. Single crystal diffraction images of quasicrystalline "$CaAu_{4.4}Al_{1.6}$" (left) in which peaks are arranged aperiodically and cannot be indexed using 3D crystallography; and crystalline (approximant) $CaAu_{3.11(4)}Al_{0.89}$ (right), in which peaks are arranged periodically and can be indexed cubic.

APPENDIX C

CHAPTER 5 SUPPORTING INFORMATION

From Quasicrystals to Crystals with Interpenetrating Icosahedra in Ca–Au–Al: *In-Situ* Variable-Temperature Transformation

Contents:

Table S1. Selected Rietveld refinement data of atomic coordinates and lattice parameters.

Table S2. Quasilattice and crystalline approximant lattice summary for the Ca–Au–Al system using equation (1).

Table S3. Selected refined crystallographic data of the 2/1 CA.

Figures S1: Rietveld refinement PXRD patterns juxtaposing single-crystal XRD refinement (as shown in Table S1) against bulk observed PXRD patterns.

Figure S2. High (atomic)-resolution images along the $\bar{3}$-fold axis of the 2/1 CA.

Table S4–S6: Fractional atomic coordinates of the 2/1 CA from refinements from Table S3.

Figure S3. High-energy, *in-situ*, variable-temperature PXRD patterns of the i-QC sample e/a = 1.66. Part of this sample batch was taken for thermal analysis (Figure S9).

Figures S4–S7: *In-situ*, variable-temperature PXRD patterns of the i-QC sample e/a = 1.70 using various heating schemes.

Figure S8. Fitting of the intensities, areas (Lorentzian Function), and positions of the main peaks that split in the i-QC–to–2/1 CA transformation according to in-situ, variable temperature PXRD.

Figure S9. Thermal analysis of the i-QC sample e/a = 1.66.

Figures S10–S11: *In-situ*, variable-temperature PXRD patterns of the 2/1 CA to show the irreversibility of the transformation from the i-QC to the 2/1 CA.

Table S7. Survey of some CAs and their VECs following the Hume-Rothery VEC prescription.

Table S8. Some reported i-QCs and their condensed compositions.

Table S9. Crystallographic information for the proposed hypothetical 1/1 CA $Ca_{24}Au_{88}Al_{64}$.

Figure S12. Band structure and DOS of the hypothetical 1/1 CA "$Ca_{24}Au_{88}Al_{64}$" in space group $I23$.

Table S1. Selected Rietveld refinement data of lattice parameters and coordinates

loaded	$Ca_{13.0(5)}Au_{52.8(1)}Al_{25.3(7)}$	$Ca_{13.1(5)}Au_{55.0(1)}Al_{23.5(7)}$	$Ca_{13.0(5)}Au_{57.1(1)}Al_{20.9(8)}$
loaded (empirical)	$Ca_{1.00(4)}Au_{4.062(8)}Al_{1.95(6)}$	$Ca_{1.00(4)}Au_{4.187(8)}Al_{1.79(6)}$	$Ca_{1.00(4)}Au_{4.410(8)}Al_{1.62(6)}$
loaded VEC (e/a)	1.70	1.66	1.60
PXRD pattern	Figure S1 top	Figure S1 middle	Figure S1 bottom
instrument/ radiation; λ (Å)/ temp.(K)	Stoe Stadi-P/ Cu $K_{\alpha1}$; 1.54060/298		
background Legendre polynomials	36	20	20
profile refinement/software	Le Bail decomposition; Jana2006		
counts observed/calculated	83783/82961	71595/71936	101070/101766
R_p/ wR_p/ GOF	1.19/ 1.62/1.47	1.16/1.57/1.51	1.08/1.47/1.69
a	23.893(1)	23.8915(6)	23.8917(7)

Table S2. Crystalline approximant lattice relationship to the i-QC quasilattice using equation (1)

	1/0 CA	2/1 CA	i-QC
loading composition	$CaAu_{3+x}Al_{1-x}$ $(-0.03 \leq \langle x \rangle \leq 0.35(4))$	$CaAu_{4.50-x}Al_{1.50+x}$ $(0.11 \leq \langle x \rangle \leq 0.44(6))$	"$CaAu_{4.50-x}Al_{1.50+x}$ $(0.11 \leq x \leq 0.40(6))$"
loading VEC (e/a)	1.50–1.60	1.60–1.70	1.60–1.70
refined composition	$CaAu_{3+x}Al_{1-x}$ $(0 \leq x \leq 0.31(1))$	$CaAu_{4.50-x}Al_{1.50+x}$ $(0.113 \leq x \leq 0.131(5))$ (from sample loaded: $Ca_{1.00(4)}Au_{4.062(8)}Al_{1.95(6)}$)	
refined VEC (e/a)	1.47–1.60	1.60–1.62 (from sample loaded: $Ca_{1.00(4)}Au_{4.062(8)}Al_{1.95(6)}$)	
$a_{L/S}$ (observed from PXRD)	9.0766(5)–9.1261(8)	23.8915(6)–23.893(1)	
$a_{L/S}$ (calculated from QC)	9.1581	23.9762	
a_{QC} (sing-crystal XRD)			5.383(4)
a_{QC} (calculated from CA)	5.3351–5.3642	5.3640–5.3643	
a_{QC} (observed from PXRD)			5.378(6)–5.393(6)

Table S3. Selected refined crystallographic data of CaAu$_{4.50-x}$Al$_{1.50-x}$ crystalline approximant

loaded (VEC)	Ca$_{13.0(5)}$Au$_{52.8(1)}$Al$_{25.3(7)}$ (1.70 e^-/a)		
refined composition (VEC, e/a)	Ca$_{13}$Au$_{56.79(6)}$Al$_{21.20}$ (1.61)	Ca$_{13}$Au$_{57.02(6)}$Al$_{20.99}$ (1.60)	Ca$_{13}$Au$_{57.04(6)}$Al$_{20.96}$ (1.62)
refined empirical composition	CaAu$_{4.369(5)}$Al$_{1.631}$	CaAu$_{4.386(5)}$Al$_{1.614}$	CaAu$_{4.387(5)}$Al$_{1.613}$
atomic coordinates	Table S4	Table S5	Table S6
instrument	Bruker APEX III Multi-focused		Bruker Apex II CCD
radiation; λ (Å)/ temp.(K)	Mo K$_{\alpha1}$; 0.71073/298		
θ range data collection	2.4º–27.5º	2.4º–27.5º	1.5–27.5º
absorp. coeff./ μ (mm^{-1})/ correction	122.87/empirical	123.00/empirical	123.34/empirical
meas./ indpnt./ obs. [I > 2σ(I)]/ para./rest.	124424/5216/3252/331/1	100569/5245/2795/331/1	186300/5220/2235/331/1
R[F^2 > 2σ(F^2)]/ wR(F^2)/ R$_{int}$/ GOF	0.069/0.170/0.185/1.03	0.063/0.164/0.289/1.01	0.062/0.176/0.394/0.94
space group/ Pearson symbol	$Pa\overline{3}$ (#205)/ cP728		
Δρ$_{max}$, Δρ$_{min}$ (e Å^{-3})	8.43, −2.99	7.95, −2.91	7.28, −3.46
a	23.8918(2)	23.914(1)	23.8950(6)
$a_{Reitveld}$ (Table S1)	23.893(1)		
volume (Å^3)/ Z	13637.9(2)/8	1367(1)/8	13643.3(6)/8
index ranges	−31 ≤ h ≤ 31 −30 ≤ k ≤ 30 −31 ≤ l ≤ 30	−27 ≤ h ≤ 31 −24 ≤ k ≤ 26 −31 ≤ l ≤ 31	−31 ≤ h ≤ 31 −30 ≤ k ≤ 31 −31 ≤ l ≤ 31

Figure S1. Rietveld refinement for lattice parameters and atomic positions (no occupancy) of the 2/1 CA using single-crystal data refinement (Table S1) as a model. The calculated patterns are in dots and the observed patterns are in solids.
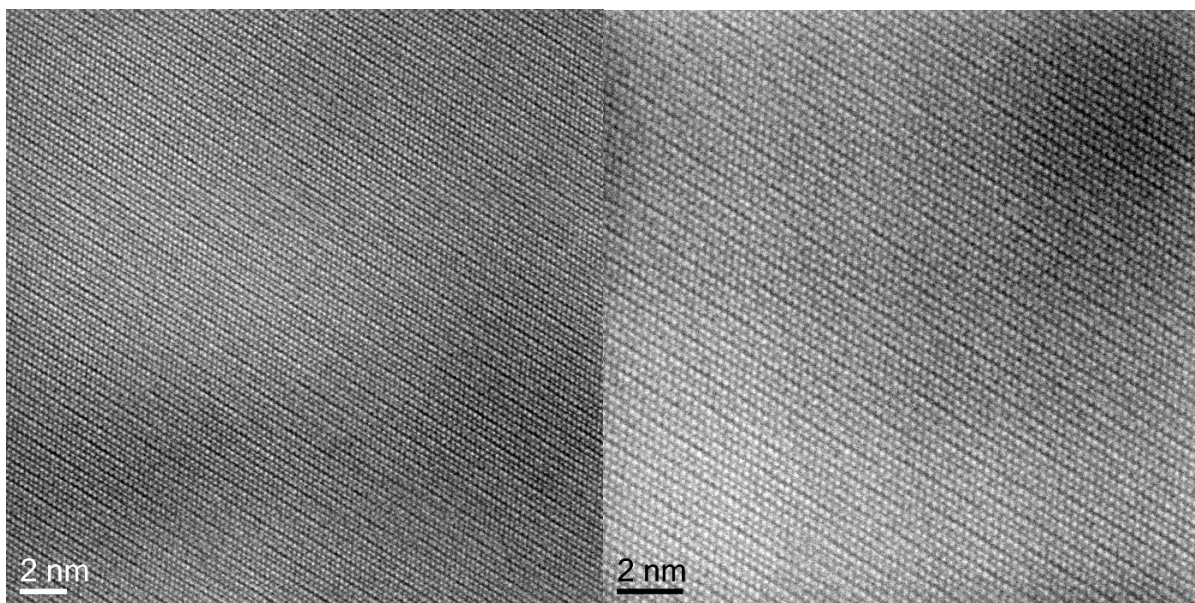
Figure S2. Atomic-resolution images of the 2/1 CA collected along the $\bar{3}$-fold axis. A magnified image is included in the Table of Contents figure.

Table S4. Fractional atomic coordinates and displacement parameters of Ca$_{13}$Au$_{56.79(6)}$Al$_{21.20}$

atom	wyck	sym	x	y	z	frac. occ.	U$_{iso}$	U$_{11}$	U$_{22}$	U$_{33}$	U$_{12}$	U$_{13}$	U$_{23}$
Au/Al25	24d	1	0.1231 (3)	0.1528 (3)	0.2061 (3)	0.226(8)/ 0.107	0.047 (3)	0.058 (5)	0.044 (4)	0.041 (4)	−0.001 (3)	−0.003 (3)	0.005 (3)
Au/Al26	24d	1	0.1463 (7)	0.2126 (6)	0.1707 (8)	0.20(1)/ 0.14	0.17 (1)	0.18 (1)	0.13 (1)	0.19 (2)	−0.11 (1)	0.14 (1)	−0.12 (1)
Au/Al27	24d	1	0.1007 (8)	0.1264 (9)	0.1502 (7)	0.11(2)/ 0.23	0.06 (1)	0.09 (1)	0.05 (2)	0.04 (1)	−0.03 (1)	0.026 (8)	−0.001 (8)
Au/Al28	24d	1	0.0908 (9)	0.159 (2)	0.131 (1)	0.05(2)/ 0.28	0.06 (1)	0.02 (1)	0.07 (2)	0.08 (1)	−0.03 (1)	−0.02 (1)	0.04 (1)
Au1	24d	1	0.15384 (5)	0.21407 (5)	0.30212 (5)		0.0301 (3)	0.0286 (6)	0.0301 (7)	0.0316 (7)	−0.0018 (5)	−0.0017 (6)	0.0001 (5)
Au2	24d	1	0.00314 (5)	0.15588 (5)	0.21045 (5)		0.0298 (3)	0.0304 (7)	0.0298 (7)	0.0292 (6)	−0.0016 (5)	−0.0014 (5)	0.0007 (5)
Au3	8c	.3.	0.06226 (5)	0.06226 (5)	0.06226 (5)		0.0297 (5)	0.0297 (5)	0.0297 (5)	0.0297 (5)	0.0007 (5)	0.0007 (5)	0.0007 (5)
Au/Al4	24d	1	0.0633 (2)	0.2514 (2)	0.2387 (2)	0.278(7)/ 0.722	0.052 (2)	0.035 (2)	0.086 (4)	0.033 (2)	−0.027 (2)	−0.009 (2)	0.007 (2)
Al5	24d	1	0.024 (2)	0.276 (2)	0.054 (2)	0.266 (6)	0.0382 (7)	0.045 (1)	0.036 (1)	0.034 (1)	−0.0017 (9)	0.0112 (9)	−0.0002 (8)
Au5	24d	1	0.05599 (9)	0.24381 (8)	0.06618 (8)	0.734 (6)							
Au6	24d	1	0.1678 (4)	0.4123 (4)	0.4988 (4)	0.186 (8)	0.030 (3)	0.036 (5)	0.025 (4)	0.030 (4)	0.003 (3)	−0.007 (3)	−0.008 (3)
Al6	24d	1	0.0144 (7)	0.1555 (7)	0.1003 (7)	0.814 (8)							
Al7	24d	1	0.062 (2)	0.337 (2)	0.153 (1)	0.349 (6)	0.0415 (9)	0.037 (1)	0.046 (2)	0.042 (1)	−0.019 (1)	−0.007 (1)	0.009 (1)
Au7	24d	1	0.0903 (1)	0.3022 (1)	0.1579 (1)	0.651 (6)							
Al1	24d	1	0.2355 (5)	0.2355 (5)	0.2355 (5)		0.040 (5)	0.040 (5)	0.040 (5)	0.040 (5)	0.023 (6)	0.023 (6)	0.023 (6)
Ca1	24d	1	0.1542 (3)	0.3437 (3)	0.2702 (3)		0.027 (1)	0.025 (3)	0.024 (3)	0.030 (3)	0.000 (3)	0.002 (3)	−0.003 (3)
Ca2	24d	1	0.2700 (3)	0.3443 (3)	0.4614 (3)		0.027 (1)	0.026 (3)	0.031 (3)	0.024 (3)	0.001 (3)	0.000 (3)	0.003 (3)
Ca3	24d	1	0.0366 (2)	0.3446 (3)	0.4659 (3)		0.025 (1)	0.020 (3)	0.028 (3)	0.027 (3)	0.000 (3)	−0.001 (2)	0.002 (3)
Ca4	24d	1	0.0383 (3)	0.1514 (3)	0.3426 (3)		0.026 (1)	0.025 (3)	0.026 (3)	0.028 (3)	0.000 (3)	−0.001 (3)	−0.005 (3)
Au9	24d	1	0.24399 (5)	0.28291 (5)	0.34450 (6)		0.0310 (3)	0.0283 (6)	0.0281 (7)	0.0364 (7)	−0.0035 (5)	−0.0040 (6)	−0.0009 (6)
Au10	24d	1	0.06149 (5)	0.28293 (5)	0.34882 (6)		0.0313 (3)	0.0286 (7)	0.0281 (6)	0.0373 (7)	−0.0001 (5)	0.0004 (6)	−0.0008 (6)
Au11	24d	1	0.21349 (5)	0.45980 (5)	0.24362 (5)		0.0305 (3)	0.0295 (7)	0.0324 (7)	0.0296 (7)	0.0024 (5)	0.0013 (5)	0.0034 (6)
Au12	24d	1	0.08754 (6)	0.46472 (5)	0.44312 (5)		0.0302 (3)	0.0343 (7)	0.0274 (7)	0.0290 (7)	−0.0009 (5)	0.0046 (5)	−0.0010 (5)
Au13	24d	1	0.15181 (6)	0.36313 (6)	0.40349 (6)		0.0356 (3)	0.0287 (7)	0.0384 (8)	0.0398 (8)	0.0041 (6)	0.0034 (6)	0.0125 (6)
Au14	24d	1	0.14572 (7)	0.40813 (6)	0.15382 (6)		0.0403 (4)	0.0524 (9)	0.0366 (8)	0.0319 (7)	0.0077 (6)	0.0018 (7)	−0.0045 (6)
Au/Al15	24d	1	0.02592 (9)	0.3476 (1)	0.24052 (9)	0.640(7)/ 0.360	0.0448 (8)	0.032 (1)	0.056 (2)	0.046 (1)	0.001 (1)	−0.0078 (9)	−0.020 (1)
Au/Al16	24d	1	0.06706 (6)	0.21611 (6)	0.45349 (7)	0.981(7)/ 0.019	0.0406 (6)	0.0404 (9)	0.0324 (9)	0.049 (1)	0.0054 (6)	−0.0157 (7)	−0.0042 (7)
Au/Al17	24d	1	0.2233 (1)	0.46635 (9)	0.44842 (9)	0.699(7)/ 0.301	0.0530 (9)	0.074 (2)	0.039 (1)	0.046 (1)	0.024 (1)	0.018 (1)	0.007 (1)
Au/Al18	24d	1	0.0224 (1)	0.3476 (2)	0.0602 (2)	0.433(3)/ 0.157	0.0421 (8)	0.0356 (1)	0.044 (2)	0.047 (2)	0.006 (1)	0.006 (1)	0.005 (1)
Au19	24d	1	0.0356 (2)	0.3673 (2)	0.0911 (2)	0.410 (4)							
Al2	4a	.−3.	0	0	0		0.025 (5)	0.025 (5)	0.025 (5)	0.025 (5)	−0.001 (5)	−0.001 (5)	−0.001 (5)
Al3	24d	1	0.1565 (5)	0.2556 (5)	0.4012 (4)		0.039 (3)	0.053 (7)	0.042 (6)	0.022 (5)	−0.009 (6)	−0.002 (5)	0.003 (4)
Au20	24d	1	0.24856 (5)	0.40520 (5)	0.34474 (5)		0.0273 (3)	0.0250 (6)	0.0299 (6)	0.0272 (6)	−0.0015 (5)	−0.0008 (6)	0.0005 (6)
Au21	24d	1	0.05482 (5)	0.40266 (5)	0.34346 (5)		0.0291 (3)	0.0307 (7)	0.0285 (6)	0.0281 (6)	−0.0003 (5)	0.0031 (5)	0.0010 (5)

Table S4 (continued).

atom	wyck.	sym	x	y	z	frac. occ.	U_{iso}	U_{11}	U_{22}	U_{33}	U_{12}	U_{13}	U_{23}
Au22	24d	1	0.08942 (5)	0.45975 (5)	0.24608 (6)		0.0306 (3)	0.0317 (7)	0.0277 (6)	0.0325 (7)	0.0004 (5)	0.0036 (6)	0.0004 (6)
Au23	24d	1	0.34363 (6)	0.44329 (6)	0.40394 (6)		0.0356 (3)	0.0314 (7)	0.0390 (8)	0.0364 (7)	−0.0025 (6)	−0.0066 (6)	−0.0059 (6)
Au24	24d	1	0.05716 (6)	0.09442 (6)	0.46367 (6)		0.0421 (4)	0.0452 (9)	0.0397 (8)	0.0415 (8)	−0.0097 (7)	−0.0030 (7)	0.0052 (6)
Al8	24d	1	0.1527 (4)	0.4618 (4)	0.3434 (4)		0.027 (2)	0.021 (4)	0.033 (5)	0.027 (5)	−0.001 (4)	−0.001 (4)	−0.003 (4)
Al9	8c	.3.	0.3432 (4)	0.3432 (4)	0.3432 (4)		0.020 (3)	0.020 (3)	0.020 (3)	0.020 (3)	0.001 (4)	0.001 (4)	0.001 (4)
Al10	24d	1	0.0386 (7)	0.461 (1)	0.1525 (9)	0.50	0.036 (5)	0.011 (8)	0.06 (1)	0.03 (1)	−0.022 (9)	−0.010 (8)	0.01 (1)
Ca5	8c	.3.	0.4594 (3)	0.4594 (3)	0.4594 (3)		0.032 (3)	0.032 (3)	0.032 (3)	0.032 (3)	−0.003 (3)	−0.003 (3)	−0.003 (3)

Table S5. Fractional atomic coordinates and displacement parameters of Ca$_{13}$Au$_{57.02(6)}$Al$_{20.99}$

atom	wyck.	sym	x	y	z	frac. occ.	U_{iso}	U_{11}	U_{22}	U_{33}	U_{12}	U_{13}	U_{23}
Au/ Al25	24d	1	0.1231 (4)	0.1521 (4)	0.2066 (4)	0.24(1)/ 0.09	0.057 (4)	0.060 (7)	0.057 (5)	0.054 (5)	−0.008 (5)	−0.005 (4)	−0.003 (4)
Au/ Al26	24d	1	0.1468 (8)	0.2115 (7)	0.172 (1)	0.19(1)/ 0.14	0.15 (1)	0.17 (2)	0.13 (2)	0.18 (2)	−0.10 (1)	0.11 (2)	−0.12 (2)
Au/ Al27	24d	1	0.10 (1)	0.126 (2)	0.1498 (9)	0.13(2)/ 0.21	0.08 (2)	0.10 (2)	0.12 (3)	0.03 (1)	−0.06 (2)	0.03 (1)	−0.01 (1)
Au/ Al28	24d	1	0.091 (1)	0.159 (2)	0.132 (2)	0.03(2)/ 0.30	0.07 (2)	0.03 (2)	0.14 (4)	0.05 (2)	−0.04 (2)	−0.00 (2)	0.08 (3)
Au1	24d	1	0.15388 (7)	0.21394 (6)	0.30204 (7)		0.0334 (4)	0.0326 (8)	0.0313 (8)	0.0363 (9)	−0.0016 (8)	−0.0023 (8)	−0.0006 (6)
Au2	24d	1	0.00328 (6)	0.15587 (7)	0.21063 (6)		0.0330 (4)	0.0314 (8)	0.0332 (8)	0.0343 (8)	−0.0010 (7)	−0.0008 (6)	−0.0001 (6)
Au3	8c	.3.	0.06227 (7)	0.06227 (7)	0.06227 (7)		0.0332 (6)	0.0332 (6)	0.0332 (6)	0.0332 (6)	0.0010 (7)	0.0010 (7)	0.0010 (7)
Au4	24d	1	0.0634 (2)	0.2512 (3)	0.2385 (2)	0.282(8)/ 0.718	0.051 (2)	0.038 (3)	0.081 (4)	0.032 (3)	−0.028 (3)	−0.006 (2)	0.006 (3)
Al5	24d	1	0.025 (2)	0.278 (2)	0.053 (2)	0.268 (7)	0.0417 (9)	0.051 (2)	0.037 (2)	0.037 (1)	−0.001 (1)	0.011 (1)	−0.002 (1)
Au5	24d	1	0.0561 (1)	0.2438 (1)	0.0661 (1)	0.732 (7)							
Au6	24d	1	0.1666 (5)	0.4118 (4)	0.4997 (4)	0.201 (9)	0.041 (4)	0.060 (8)	0.029 (5)	0.034 (5)	0.006 (4)	−0.017 (5)	−0.011 (4)
Al6	24d	1	0.015 (1)	0.155 (1)	0.1006 (9)	0.799 (9)							
Al7	24d	1	0.063 (2)	0.338 (2)	0.153 (2)	0.347 (7)	0.045 (1)	0.041 (2)	0.047 (2)	0.047 (2)	−0.019 (1)	−0.010 (1)	0.011 (1)
Au7	24d	1	0.0903 (1)	0.3024 (1)	0.1578 (1)	0.653 (7)							
Al1	24d	1	0.2358 (7)	0.2358 (7)	0.2358 (7)		0.052 (7)	0.052 (7)	0.052 (7)	0.052 (7)	0.004 (8)	0.004 (8)	0.004 (8)
Ca1	24d	1	0.1536 (3)	0.3436 (3)	0.2699 (3)		0.027 (2)	0.024 (4)	0.023 (4)	0.033 (4)	0.002 (4)	−0.005 (3)	−0.002 (3)
Ca2	24d	1	0.2709 (3)	0.3437 (3)	0.4611 (3)		0.023 (2)	0.026 (4)	0.020 (4)	0.021 (4)	−0.004 (3)	−0.013 (3)	0.004 (3)
Ca3	24d	1	0.0367 (3)	0.3447 (3)	0.4651 (3)		0.026 (2)	0.028 (4)	0.026 (4)	0.025 (4)	−0.012 (4)	0.004 (3)	0.005 (3)
Ca4	24d	1	0.0383 (3)	0.1517 (3)	0.3429 (3)		0.029 (2)	0.031 (4)	0.023 (4)	0.033 (4)	0.002 (3)	0.007 (3)	−0.003 (4)
Au9	24d	1	0.24400 (6)	0.28295 (6)	0.34476 (6)		0.0330 (4)	0.0302 (8)	0.0300 (8)	0.0387 (9)	−0.0026 (8)	−0.0017 (8)	0.0000 (8)
Au10	24d	1	0.06147 (6)	0.28295 (6)	0.34867 (8)		0.0341 (4)	0.0300 (8)	0.0319 (8)	0.0405 (9)	−0.0008 (6)	0.0004 (8)	−0.0016 (8)
Au11	24d	1	0.21364 (7)	0.45970 (7)	0.24379 (7)		0.0334 (4)	0.0335 (9)	0.0339 (9)	0.0328 (9)	0.0018 (7)	0.0002 (7)	0.0051 (7)
Au12	24d	1	0.08768 (7)	0.46476 (7)	0.44325 (7)		0.0330 (4)	0.0383 (9)	0.0305 (9)	0.0301 (9)	−0.0025 (7)	0.0038 (7)	−0.0009 (7)
Au13	24d	1	0.15213 (7)	0.36306 (7)	0.40339 (7)		0.0385 (4)	0.0302 (8)	0.0430 (10)	0.0423 (9)	0.0028 (8)	0.0025 (8)	0.0139 (7)
Au14	24d	1	0.14550 (8)	0.40807 (7)	0.15384 (7)		0.0429 (4)	0.055 (1)	0.0408 (9)	0.0330 (9)	0.0086 (8)	0.0024 (9)	−0.0033 (8)
Au/ Al15	24d	1	0.0260 (1)	0.3474 (1)	0.2405 (1)	0.652(8)/ 0.348	0.050 (1)	0.034 (2)	0.062 (2)	0.053 (2)	0.003 (1)	−0.010 (1)	−0.022 (2)

Table S5 (continued).

atom	Wyck.	sym	x	y	z	frac. occ.	U_{iso}	U_{11}	U_{22}	U_{33}	U_{12}	U_{13}	U_{23}
Au/Al16	24d	1	0.06689(8)	0.21606(8)	0.45360(8)	0.984(8)/0.016	0.0452(7)	0.045(1)	0.036(1)	0.054(1)	0.0056(8)	−0.0176(9)	−0.0053(9)
Au/Al17	24d	1	0.2233(1)	0.4663(1)	0.4483(1)	0.712(9)/0.288	0.060(1)	0.084(2)	0.046(2)	0.051(2)	0.027(2)	0.020(2)	0.007(1)
Au/Al18	24d	1	0.0225(2)	0.3475(2)	0.0606(2)	0.450(3)/0.132	0.0461(9)	0.03(2)	0.053(2)	0.051(2)	0.002(2)	0.005(2)	0.006(2)
Au19	24d	1	0.0359(2)	0.3676(2)	0.0910(2)	0.418(5)							
Al2	4a	.−3.	0	0	0		0.035(7)	0.035(7)	0.035(7)	0.035(7)	−0.006(7)	−0.006(7)	−0.006(7)
Al3	24d	1	0.1563(6)	0.2544(6)	0.4020(6)		0.047(3)	0.059(9)	0.038(7)	0.044(8)	−0.003(8)	−0.007(8)	−0.006(6)
Au20	24d	1	0.24840(6)	0.40517(6)	0.34470(6)		0.0281(3)	0.0268(7)	0.0302(7)	0.0272(7)	−0.0019(6)	−0.0011(8)	0.0002(8)
Au21	24d	1	0.05481(7)	0.40289(6)	0.34355(6)		0.0304(4)	0.0322(8)	0.0297(8)	0.0293(8)	0.0006(6)	0.0031(8)	0.0001(7)
Au22	24d	1	0.08969(7)	0.46005(7)	0.24622(7)		0.0338(4)	0.0355(9)	0.0322(8)	0.0337(9)	0.0009(7)	0.0050(7)	0.0011(8)
Au23	24d	1	0.34390(8)	0.44314(7)	0.40414(7)		0.0380(4)	0.0326(9)	0.041(1)	0.041(1)	−0.0023(9)	−0.0070(8)	−0.0058(7)
Au24	24d	1	0.05732(9)	0.09440(8)	0.46347(8)		0.0463(5)	0.051(1)	0.045(1)	0.043(1)	−0.0094(9)	−0.0042(9)	0.0056(9)
Al8	24d	1	0.1523(6)	0.4616(5)	0.3436(6)		0.042(3)	0.046(7)	0.041(7)	0.038(7)	0.008(7)	−0.006(8)	−0.006(6)
Al9	8c	.3.	0.3435(4)	0.3435(4)	0.3435(4)		0.027(4)	0.027(4)	0.027(4)	0.027(4)	−0.010(5)	−0.010(5)	−0.010(5)
Al10	24d	1	0.0380(8)	0.462(1)	0.153(1)	0.50	0.033(6)	0.01(1)	0.05(2)	0.04(1)	−0.01(1)	−0.01(1)	−0.01(1)
Ca5	8c	.3.	0.4611(3)	0.4611(3)	0.4611(3)		0.026(3)	0.026(3)	0.026(3)	0.026(3)	0.001(3)	0.001(3)	0.001(3)

Table S6. Fractional atomic coordinates and displacement parameters of Ca$_{13}$Au$_{57.04(6)}$Al$_{20.96}$

atom	Wyck.	sym	x	y	z	frac. occ.	U_{iso}	U_{11}	U_{22}	U_{33}	U_{12}	U_{13}	U_{23}
Au/Al25	24d	1	0.1238(3)	0.1524(3)	0.2062(3)	0.247(8)/0.086	0.058(3)	0.060(5)	0.065(5)	0.049(4)	−0.008(4)	−0.001(3)	0.000(3)
Au/Al26	24d	1	0.1462(6)	0.2113(6)	0.1725(7)	0.176(9)/0.157	0.145(9)	0.15(1)	0.13(1)	0.15(2)	−0.10(1)	0.11(1)	−0.10(1)
Au/Al27	24d	1	0.1031(7)	0.1247(8)	0.1506(7)	0.12(2)/0.21	0.07(1)	0.08(1)	0.07(2)	0.058(9)	−0.04(1)	0.003(8)	0.011(9)
Au/Al28	24d	1	0.0880(9)	0.159(2)	0.1331(8)	0.04(2)/0.29	0.05(1)	0.02(1)	0.08(2)	0.05(2)	−0.01(1)	−0.003(9)	0.03(1)
Au1	24d	1	0.15384(5)	0.21399(5)	0.30209(5)		0.0339(3)	0.0323(7)	0.0337(7)	0.0358(7)	−0.0008(6)	−0.0025(6)	−0.0007(5)
Au2	24d	1	0.00326(5)	0.15588(5)	0.21048(5)		0.0334(3)	0.0324(7)	0.0335(7)	0.0342(7)	−0.0016(6)	−0.0009(5)	−0.0001(6)
Au3	8c	.3.	0.06233(5)	0.06233(5)	0.06233(5)		0.0338(5)	0.0338(5)	0.0338(5)	0.0338(5)	0.0009(6)	0.0009(6)	0.0009(6)
Au/Al4	24d	1	0.0634(2)	0.2512(2)	0.2389(2)	0.290(7)/0.710	0.057(2)	0.039(3)	0.093(4)	0.040(3)	−0.026(2)	−0.005(2)	0.005(2)
Al5	24d	1	0.024(2)	0.276(2)	0.054(2)	0.270(6)	0.0413(8)	0.050(1)	0.038(1)	0.037(1)	−0.0028(9)	0.0117(9)	−0.0026(8)
Au5	24d	1	0.05592(8)	0.24381(8)	0.06608(8)	0.730(6)							
Au6	24d	1	0.1668(4)	0.4125(3)	0.4993(3)	0.208(8)	0.042(3)	0.056(5)	0.036(4)	0.035(4)	0.007(3)	−0.011(3)	−0.006(3)
Al6	24d	1	0.0162(9)	0.1558(8)	0.1010(8)	0.792(8)							
Al7	24d	1	0.062(1)	0.337(2)	0.153(1)	0.346(6)	0.0454(9)	0.039(1)	0.051(2)	0.047(1)	−0.018(1)	−0.008(1)	0.010(1)
Au7	24d	1	0.09035(9)	0.3024(1)	0.15800(9)	0.654(6)							
Al1	24d	1	0.2354(5)	0.2354(5)	0.2354(5)		0.041(5)	0.041(5)	0.041(5)	0.041(5)	0.013(5)	0.013(5)	0.013(5)
Ca1	24d	1	0.1540(2)	0.3433(2)	0.2704(3)		0.028(1)	0.024(3)	0.025(3)	0.033(3)	0.001(3)	0.002(3)	0.000(3)
Ca2	24d	1	0.2704(2)	0.3444(3)	0.4618(3)		0.02(1)	0.027(3)	0.031(3)	0.028(3)	0.004(3)	0.000(2)	−0.003(3)
Ca3	24d	1	0.0371(3)	0.3450(3)	0.4656(2)		0.029(2)	0.028(3)	0.030(3)	0.029(3)	0.002(3)	0.003(3)	0.001(3)
Ca4	24d	1	0.0385(2)	0.1518(3)	0.3430(3)		0.029(2)	0.029(3)	0.029(3)	0.029(3)	0.002(3)	0.002(3)	−0.004(3)
Au9	24d	1	0.24407(5)	0.28288(5)	0.34455(6)		0.0339(3)	0.0302(7)	0.0321(7)	0.0393(7)	−0.0028(5)	−0.0028(6)	−0.0012(6)

Table S6 (continued).

			x	y	z	occ.	U_{11}	U_{22}	U_{33}	U_{12}	U_{13}	U_{23}
Au10	24d	1	0.06144(5)	0.28286(5)	0.34880(6)		0.0342(3)	0.0316(7)	0.0303(7)	0.0408(7)	−0.0011(5)	0.0011(6)	−0.0002(6)
Au11	24d	1	0.21351(5)	0.45976(5)	0.24368(5)		0.0339(3)	0.0325(7)	0.0361(7)	0.0331(7)	0.0022(6)	0.0012(6)	0.0025(6)
Au12	24d	1	0.08758(5)	0.46473(5)	0.44321(5)		0.0333(3)	0.0373(7)	0.0306(7)	0.0321(7)	−0.0011(6)	0.0047(6)	−0.0006(5)
Au13	24d	1	0.15196(6)	0.36314(6)	0.40341(6)		0.0391(3)	0.031(7)	0.042(8)	0.043(8)	0.0033(6)	0.0044(6)	0.0133(6)
Au14	24d	1	0.14567(6)	0.40810(6)	0.15382(6)		0.0436(4)	0.0551(9)	0.0400(8)	0.0356(7)	0.0083(6)	0.0026(7)	−0.0037(6)
Au/Al15	24d	1	0.02601(8)	0.3475(1)	0.24048(9)	0.658(6)/0.342	0.0504(9)	0.036(1)	0.062(2)	0.054(2)	0.001(1)	−0.0072(9)	−0.021(1)
Au/Al16	24d	1	0.06697(6)	0.21608(6)	0.45359(6)	0.974(6)/0.026	0.0441(6)	0.044(1)	0.0354(9)	0.0531(1)	0.0057(6)	−0.0164(7)	−0.0041(7)
Au/Al17	24d	1	0.2232(1)	0.46635(9)	0.44836(5)	0.702(7)/0.298	0.0562(9)	0.080(2)	0.043(1)	0.046(1)	0.024(1)	0.020(1)	0.007(1)
Au/Al18	24d	1	0.0225(1)	0.3476(2)	0.0603(2)	0.449(3)/0.130	0.0481(8)	0.039(2)	0.055(2)	0.050(2)	0.0085(1)	0.004(1)	0.007(1)
Au19	24d	1	0.0357(2)	0.3674(2)	0.0913(2)	0.420(4)							
Al2	4a	.−3.	0	0	0		0.033(5)	0.033(5)	0.033(5)	0.033(5)	0.003(6)	0.003(6)	0.003(6)
Al3	24d	1	0.1562(5)	0.2559(5)	0.4011(4)		0.044(3)	0.044(6)	0.051(7)	0.039(6)	−0.001(5)	−0.004(6)	−0.002(5)
Au20	24d	1	0.24840(5)	0.40516(5)	0.34466(5)		0.0300(3)	0.0283(6)	0.0321(6)	0.0296(6)	−0.0016(5)	0.0001(6)	0.0008(6)
Au21	24d	1	0.05487(5)	0.40281(5)	0.34350(5)		0.0320(3)	0.0336(7)	0.0315(7)	0.0308(7)	0.0006(5)	0.0021(6)	−0.0001(6)
Au22	24d	1	0.08950(5)	0.45978(5)	0.24613(6)		0.0340(3)	0.0351(7)	0.0321(7)	0.0349(7)	0.0012(6)	0.0055(6)	0.0007(6)
Au23	24d	1	0.34374(6)	0.44323(6)	0.40398(6)		0.0386(3)	0.0351(7)	0.0402(8)	0.0405(8)	−0.0024(6)	−0.0074(6)	−0.0055(6)
Au24	24d	1	0.05709(6)	0.09442(6)	0.46364(6)		0.0460(4)	0.0478(9)	0.0449(9)	0.0452(9)	−0.0095(7)	−0.0041(7)	0.0060(7)
Al8	24d	1	0.1525(4)	0.4620(4)	0.3437(4)		0.032(2)	0.029(5)	0.025(5)	0.042(5)	0.007(4)	−0.001(5)	0.000(4)
Al9	8c	.3.	0.3430(3)	0.3430(3)	0.3430(3)		0.025(3)	0.025(3)	0.025(3)	0.025(3)	−0.001(4)	−0.001(4)	−0.001(4)
Al10	24d	1	0.0378(7)	0.462(1)	0.1531(9)	0.50	0.042(6)	0.018(9)	0.07(2)	0.04(1)	−0.02(1)	−0.030(9)	0.03(1)
Ca5	8c	.3.	0.4599(2)	0.4599(2)	0.4599(2)		0.032(3)	0.032(3)	0.032(3)	0.032(3)	−0.006(3)	−0.006(3)	−0.006(3)

In the following *in-situ*, variable-temperature PXRD patterns: Figure S3 refers to one sample at a constant heating rate; Figures S4–S7 refer to another sample at various heating rates and isothermal holds. The objective was to examine the effects of temperature (T) and time (*t*) on the transformation.
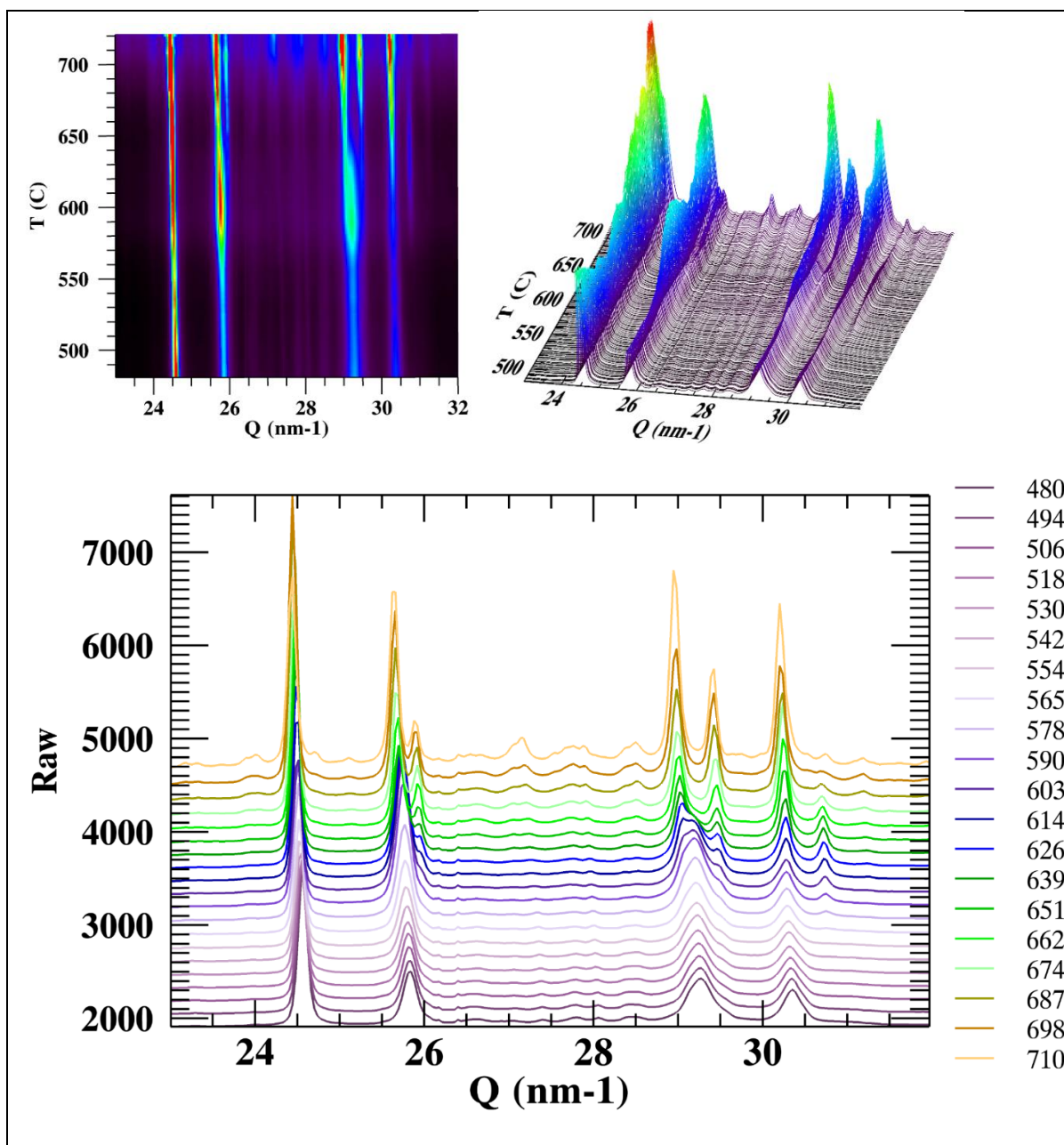
Figure S3 (and Figure 5). *In-situ*, variable-temperature PXRD patterns measured using an IR furnace at the APS at a constant heating rate of 10º C/min from 480–720 ºC for sample loading Ca$_{13.2(5)}$Au$_{55.0(1)}$Al$_{23.8(8)}$ (= Ca$_{1.00(4)}$Au$_{4.158(8)}$Al$_{1.80(6)}$, *e/a*: 1.66).
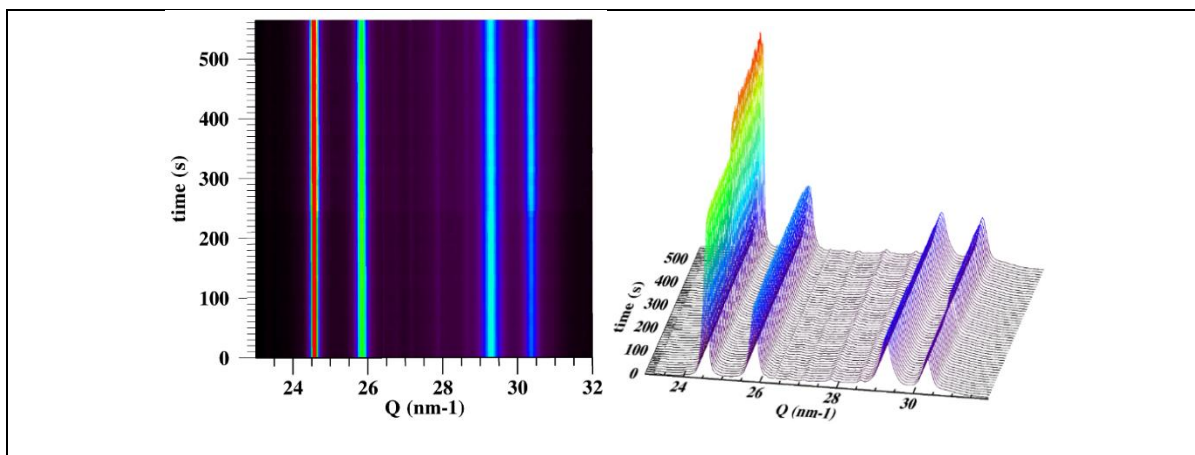
Figure S4. PXRD patterns of quasicrystalline sample loaded as $Ca_{12.8(5)}Au_{52.6(1)}Al_{25.2(8)}$ (= $Ca_{1.00(4)}Au_{4.108(8)}Al_{1.97(6)}$, e/a = 1.70) dwelling at 530 ºC for 10 min and showing no detectable phase change.
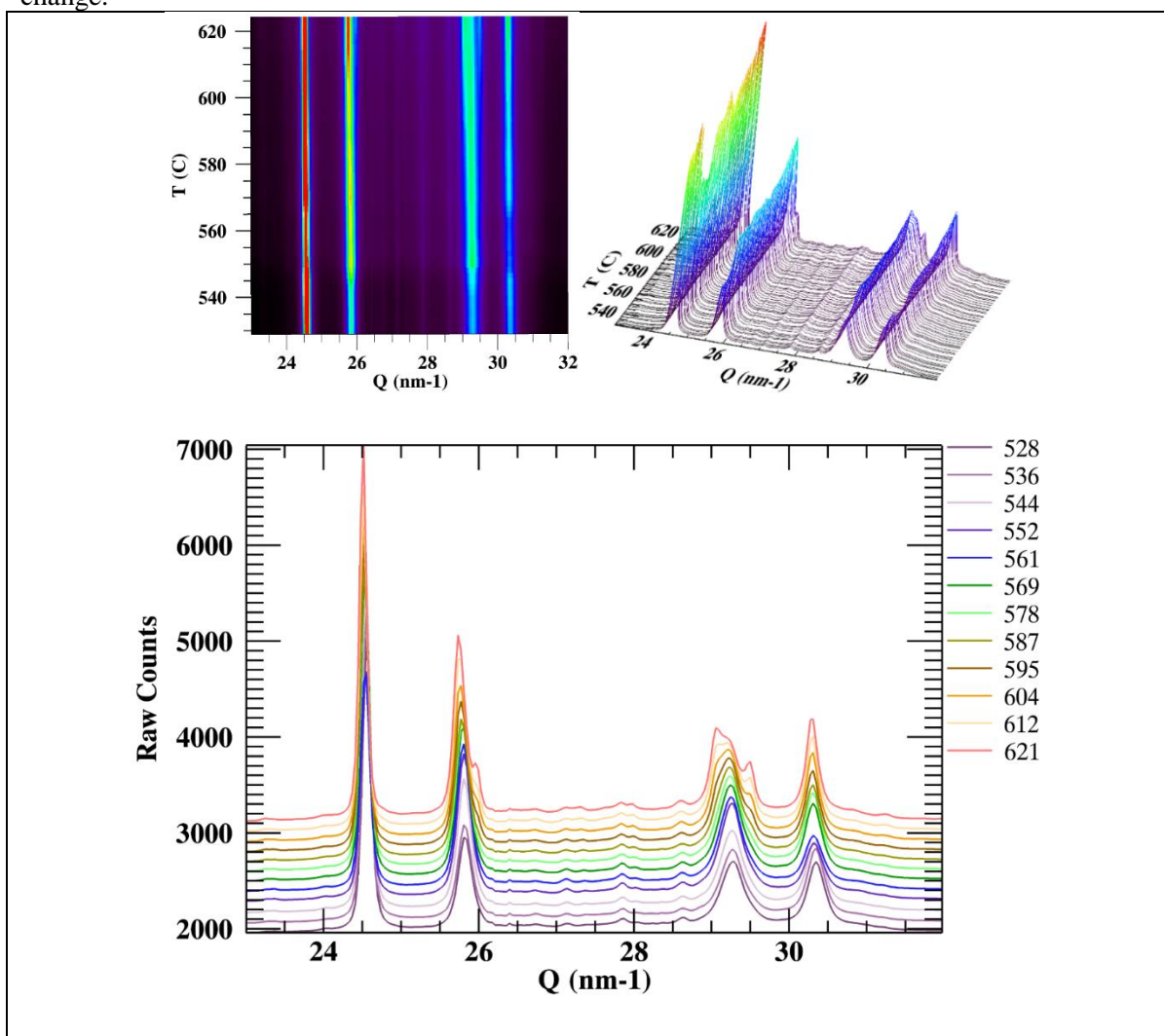
Figure S5. *In-situ*, variable-temperature PXRD patterns of quasicrystalline sample loaded as $Ca_{12.8(5)}Au_{52.6(1)}Al_{25.2(8)}$ (= $Ca_{1.00(4)}Au_{4.108(8)}Al_{1.97(6)}$, e/a = 1.70) from 530–610 ºC at a heating rate of 10 ºC/min.
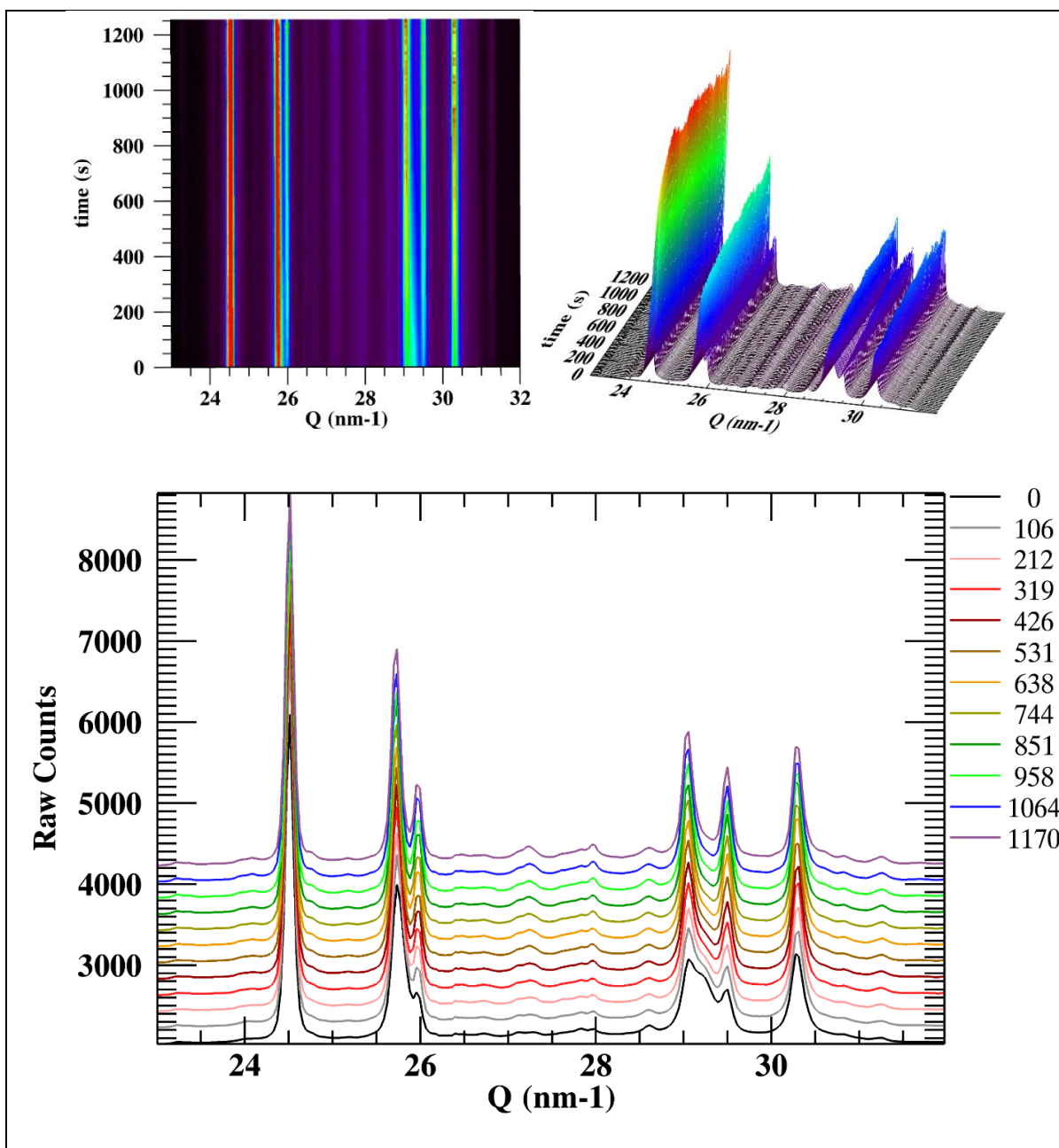
Figure S6. PXRD patterns of quasicrystalline sample loaded as $Ca_{12.8(5)}Au_{52.6(1)}Al_{25.2(8)}$ (= $Ca_{1.00(4)}Au_{4.108(8)}Al_{1.97(6),}$ $e/a = 1.70$) dwelling at 625 $^{\circ}$C for ~20 min.
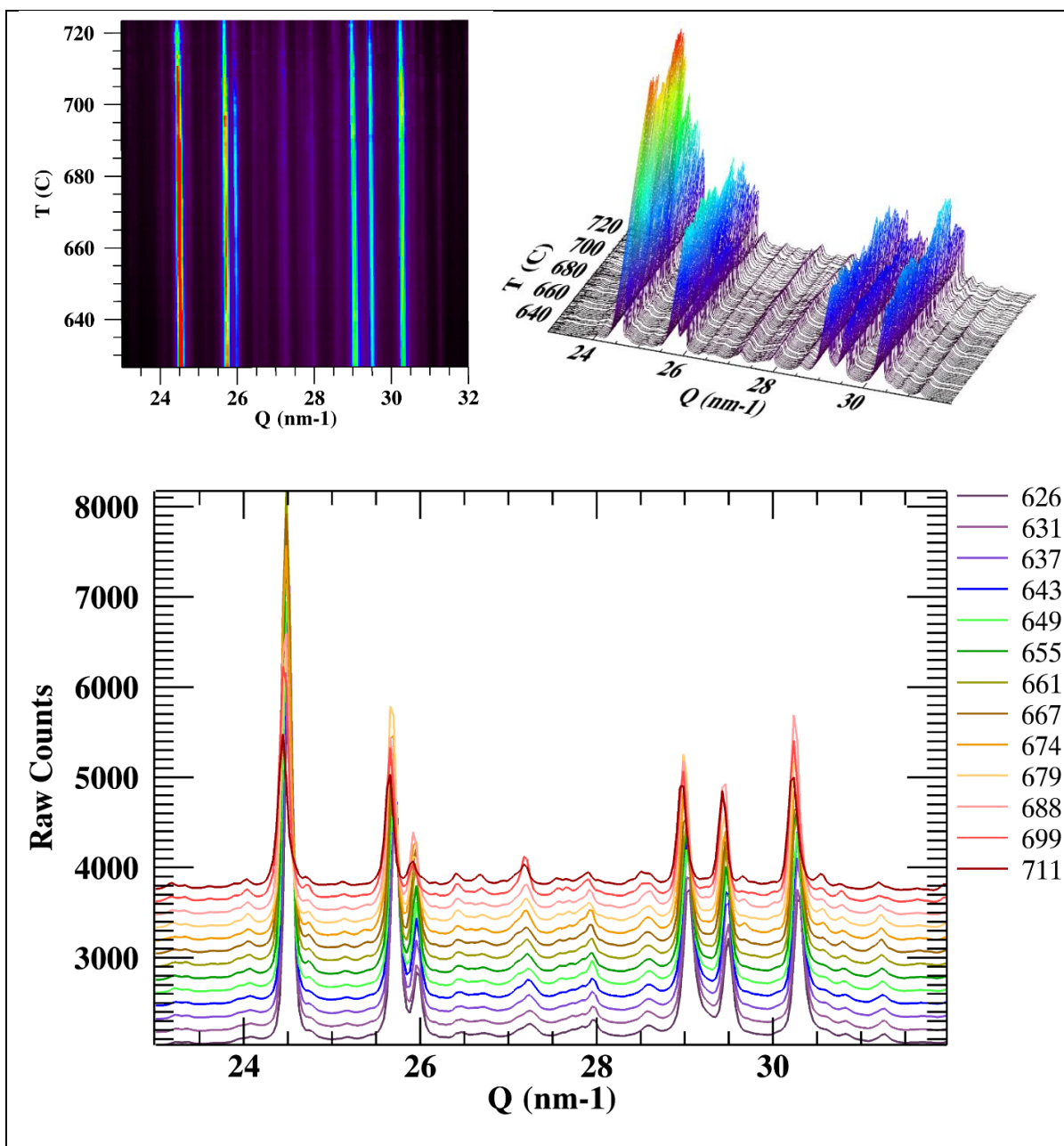
Figure S7. PXRD patterns of quasicrystalline sample loaded as $Ca_{12.8(5)}Au_{52.6(1)}Al_{25.2(8)}$ (= $Ca_{1.00(4)}Au_{4.108(8)}Al_{1.97(6)}$, $e/a = 1.70$) from 625–725 ºC at a heating rate of 10 ºC/min.
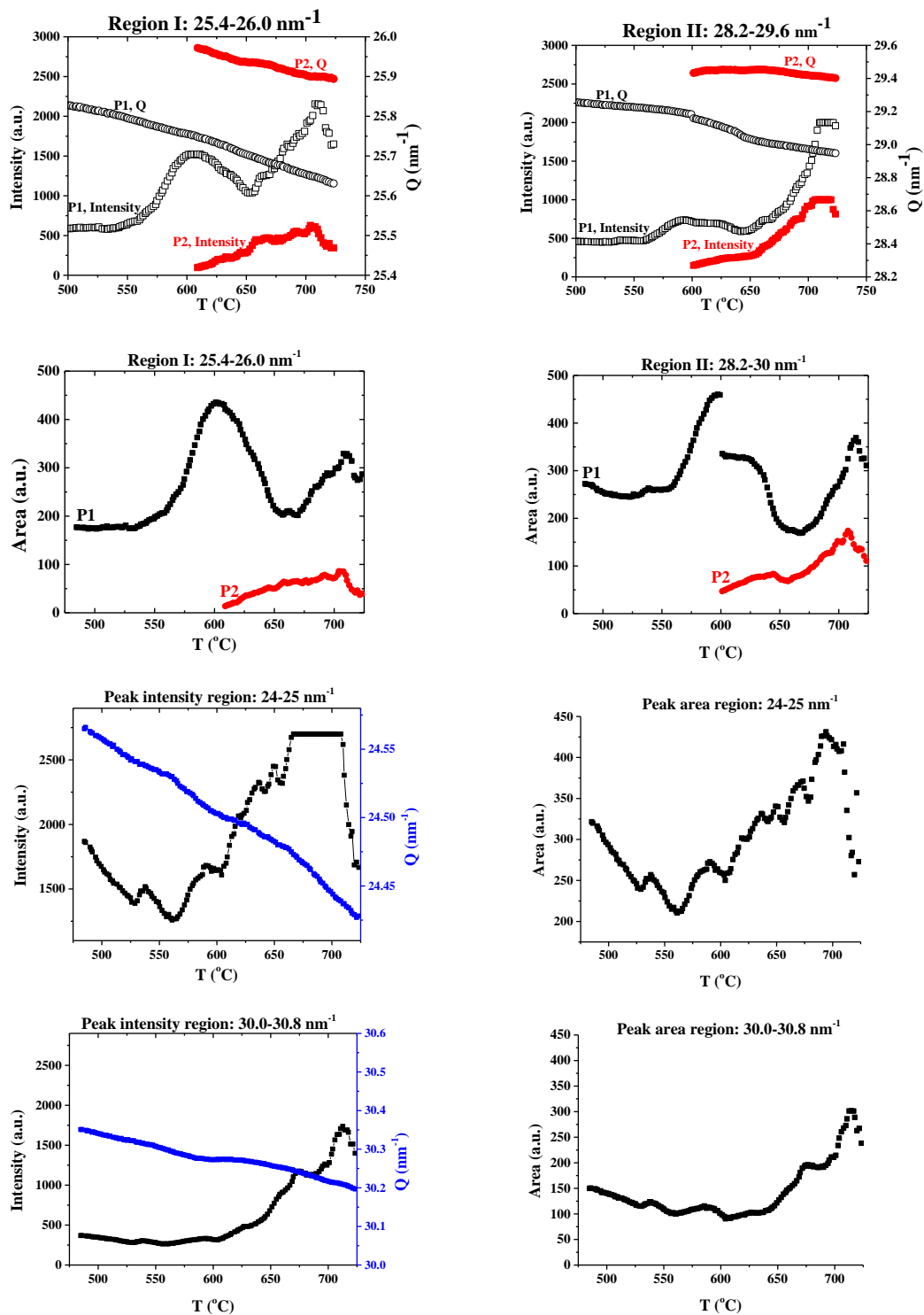
Figure S8. Peak fitting in the regions that split during i-QC–to–2/1 CA transformation according to in-situ, variable temperature PXRD. The area is calculated as a product of the peak intensity (height) and full-width at half-maximum. For the area in region II at ~600 °C, P1 is broadening before splitting and therefore the FWHM cannot be not evaluated very clearly. Additionally for comparison, the intensity and area of the peaks that did not undergo splitting are also included in the two bottom rows.
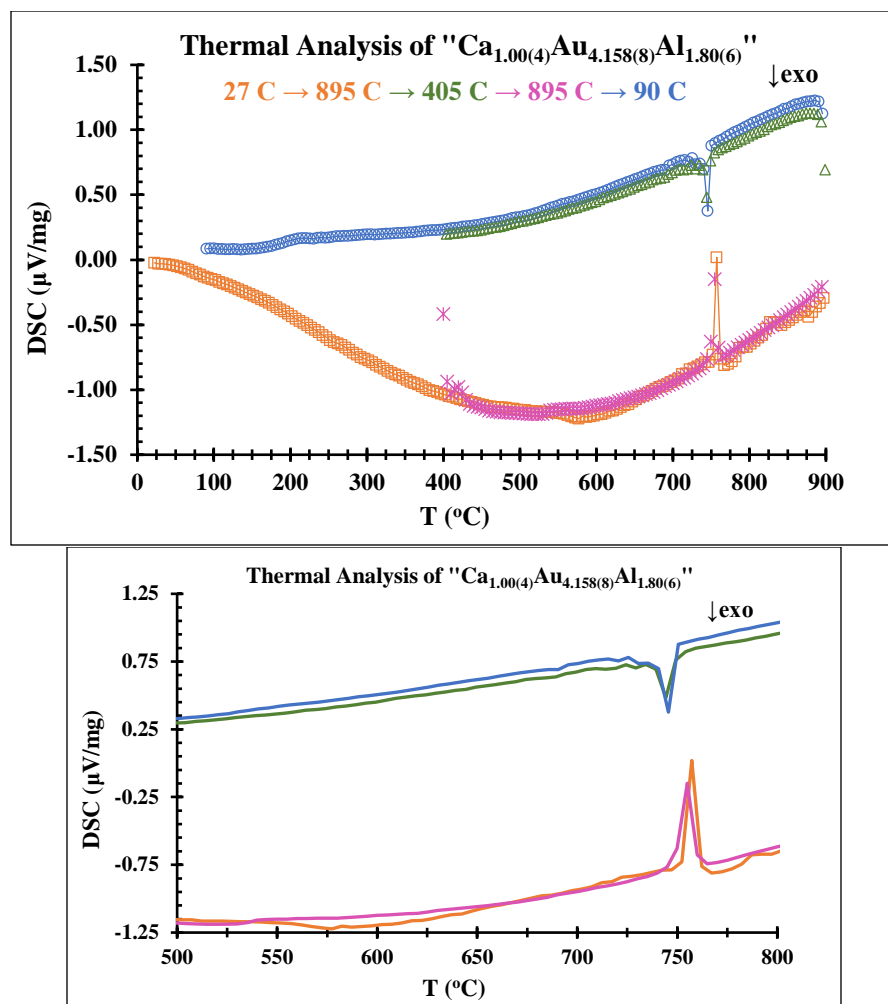
Figure S9. Thermal analysis of the quasicrystalline sample loaded as $Ca_{1.00(4)}Au_{4.158(8)}Al_{1.80(6)}$ ($x =$ 0.32(6), e/a = 1.66).
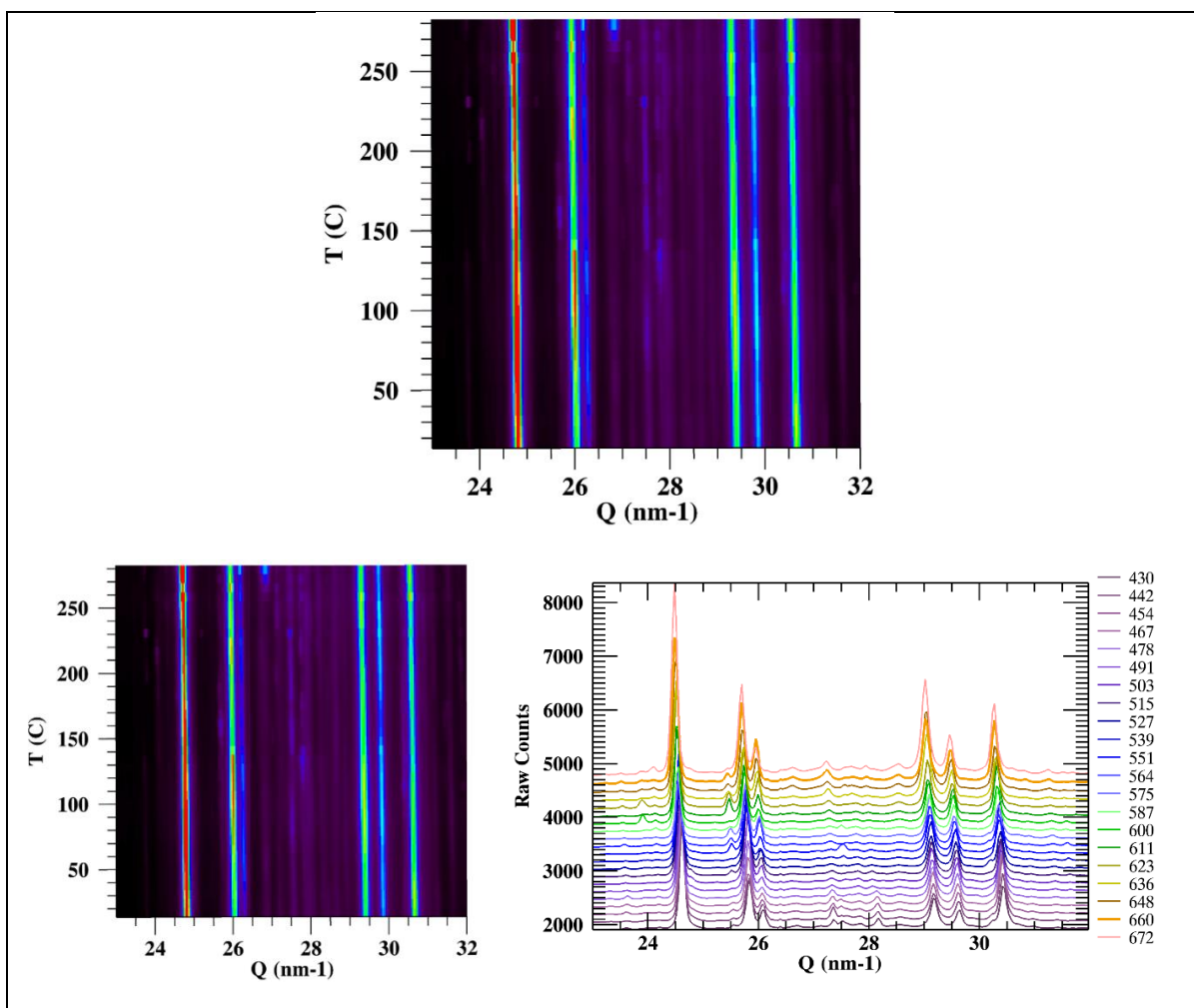
Figure S10. PXRD pattern of the 2/1 CA loaded as $Ca_{13.1(5)}Au_{55.0(1)}Al_{23.5(7)}$ ($= Ca_{1.00(4)}Au_{4.187(8)}Al_{1.79(6)}$, e/a = 1.66) from ~30–300 ºC (top) and from ~440–670 ºC (bottom) at 10 ºC/min showing no transformation from the 2/1 CA to the i-QC.
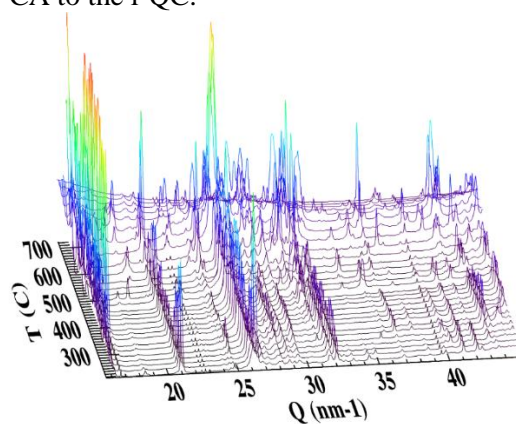
Figure S11. PXRD pattern of the 2/1 CA loaded as $Ca_{13.1(5)}Au_{55.0(1)}Al_{23.5(7)}$ ($= Ca_{1.00(4)}Au_{4.187(8)}Al_{1.79(6)}$, e/a = 1.66) upon cooling from 725 ºC–200 ºC at 100 ºC/min and showing no phase transformation from the 2/1 CA to the i-QC.

Table S7. Survey of CAs and their *e/a* using peaks up to 20% of the *I*$_{max}$ and a *d*-spacing < 3.0 Å

Compound (classification)	N	Peak (2θ) increasing intensity	Q (nm⁻¹) increasing intensity	d- spacing	(h k l)	mult.	VEC (*e/a*)	\<VEC\>
CaAu$_{4.39}$Al$_{1.61}$ 2/1 CA Tsai	728	35.416	24.810	2.5325	(5 0 8)	12×	1.208	1.814
		37.226	26.034	2.4134	(3 5 8)	24×	1.396	
		44.171	30.669	2.0487	(6 0 10)	12×	2.281	
		42.258	29.403	2.1369	(5 6 8)	24×	2.010	
		42.962	29.870	2.1036	(2 5 10)	24×	2.108	
"Ca$_{24}$Au$_{88}$Al$_{64}$" "1/1 CA Tsai"	176	35.289	24.724	2.5413	(3 0 5)	12×	1.180	1.812
		37.380	26.138	2.4038	(2 3 5)	24×	1.393	
		44.031	30.576	2.0549	(4 0 6)	12×	2.231	
		41.289	28.758	2.1848	(1 3 6)	24×	1.856	
		43.133	29.983	2.0956	(3 4 5)	24×	2.104	
CaAu$_3$Al 1/0 CA	40	35.680	24.989	2.5143	(0 2 3)	12×	1.227	1.873
		37.075	25.933	2.4227	(2 1 3)	24×	1.371	
		41.016	28.576	2.1987	(2 2 3)	24×	1.835	
		41.016	28.576	2.1987	(1 0 4)	12×	1.835	
		45.832	31.761	1.9783	(2 1 4)	24×	2.519	
		44.667	30.996	2.0271	(0 2 4)	12×	2.342	
Ca$_3$Au$_{12.07}$Ga$_{6.93}$ 1/1 CA Tsai	176	35.435	24.823	2.5312	(3 0 5)	12×	1.180	1.765
		37.534	26.242	2.3943	(2 3 5)	24×	1.394	
		44.216	30.698	2.0468	(4 0 6)	12×	2.231	
		41.461	28.873	2.1762	(1 3 6)	24×	1.856	
		43.313	30.102	2.0873	(3 4 5)	24×	2.104	
Mg$_{27}$Al$_{10.7(2)}$Zn$_{47.3(2)}$ 2/1 CA Bergman	680	38.664	27.002	2.3269	(3 5 8)	24×	1.494	2.803 1.849*
		36.779	25.733	2.4417	(5 0 8)	12×	1.293	
		44.644	30.980	2.0281	(2 5 10)	24×	2.256	
		43.910	30.497	2.0603	(5 6 8)	24×	2.152	
		64.978	43.813	1.4341	(5 8 13)	24×	6.382	
		39.073	27.277	2.3035	(0 0 10)	6×	1.540	
Sc$_{11.18(9)}$Mg$_{2.5(1)}$Zn$_{73.6(2)}$ 2/1 CA Tsai	698	39.784	27.753	2.2640	(3 5 8)	24×	1.455	1.869
		37.840	26.448	2.3757	(5 0 8)	12×	1.260	
		45.197	31.344	2.0046	(5 6 8)	24×	2.097	
		45.955	31.842	1.9733	(2 5 10)	24×	2.198	
		47.259	32.694	1.9218	(6 0 10)	12×	2.379	
		40.205	28.035	2.2412	(0 0 10)	6×	1.500	
(Yb/Ca)$_{13}$Cd$_{76}$ 2/1 CA Tsai	712	35.028	24.547	2.5597	(3 5 8)	24×	1.427	1.832
		39.738	27.723	2.2664	(5 6 8)	24×	2.055	
		33.331	23.392	2.6860	(5 0 8)	12×	1.235	
		41.527	28.917	2.1728	(6 0 10)	12×	2.333	
		40.396	28.163	2.2310	(2 5 10)	24×	2.155	
		35.395	24.796	2.5340	(0 0 10)	6×	1.471	

* This average is for if the VECs for *d*-spacing < 1.5 Å is not included.

Table S8. Survey of some reported i-QCs and their condensed compositions

Nominal i-QC Composition	A	B	Condensed Composition
$Ca_{13}Au_{56.79(6)}Al_{21.20}$[*]	Ca	Au + Al	$Ca(Au_{0.73}Al_{0.27})_{6.0}$
$Ca_{15.2}Au_{50.3}Ga_{34.5}$ [1]	Ca	Au + Ga	$Ca(Au_{0.59}Ga_{0.41})_{5.58}$
$Yb_{15}Au_{51}Al_{34}$ [2]	Yb	Au + Al	$Yb(Au_{0.60}Al_{0.47})_{5.67}$
$YbCd_{5.7}$ [3]	Yb	Cd	$YbCd_{5.7}$
$Sc_{16}Cu_{46}Al_{38}$ [4]	Sc	Cu + Al	$Sc(Cu_{0.55}Al_{0.45})_{5.25}$
$Fe_{15}Cu_{20}Al_{65}$ [5]	Fe	Cu + Al	$Fe(Cu_{0.24}Al_{0.76})_{5.67}$
$Sc_{16}Pd_{30}Al_{54}$ [6]	Sc	Pd + Al	$Sc(Pd_{0.36}Al_{0.64})_{5.25}$
$Yb_{14.5}Zn_{76.2}Mg_{9.3}$ [7]	Yb	Zn + Mg	$Yb(Zn_{0.89}Mg_{0.11})_{5.90}$
$Gd_{16}Ag_{42}In_{42}$ [8]	Gd	Ag + In	$Gd(Ag_{0.5}In_{0.5})_{5.25}$
$Cd_{65}Mg_{20}RE_{15}$ (RE =Y, Nd, Eu, Gd, Tb, Dy, Ho, Er, Tm, Yb, and Lu) [9]	RE	Cd + Mg	$RE(Cd_{0.76}Mg_{0.24})_{5.67}$

[*]Discussed in main text

[1] Lin, Q.; Corbett, J. D. *Inorganic Chemistry* **2008**, *47*, 7651.

[2] Ishimasa, T.; Tanaka, Y.; Kashimoto, S. *Philosophical Magazine* **2011**, *91*, 4218.

[3] Takakura, H.; Gomez, C. P.; Yamamoto, A.; De Boissieu, M.; Tsai, A. P. *Nat Mater* **2007**, *6*, 58.

[4] Honma, T.; Ishimasa, T. *Philosophical Magazine* **2007**, *87*, 2721.

[5] Tsai, A.-P.; Inoue, A.; Masumoto, T. *Japanese Journal of Applied Physics* **1987**, *26*, L1505.

[6] So, Y.-G.; So, T.; Yoshikawa, F.; Saruhashi, K.; Edagawa, R.; Tamura *Materials Transactions* **2011**, *52*, 2011.

[7] Mitani, T.; Ishimasa, T. *Philosophical Magazine* **2006**, *86*, 361.

[8] Wang, P.; Stadnik, Z. M.; Przewoźnik, J. *Journal of Alloys and Compounds* **2011**, *509*, 3435.

[9] Guo, J.; Abe, E.; Tsai, A.-P. *Japanese Journal of Applied Physics* **2000**, *39*, L770.

Table S9. Hypothetical 1/1 CA $Ca_{24}Au_{88}Al_{64}$ from the space group *I*23, lattice parameter a = 14.8181 Å, and with Al4 shifted to be a single central tetrahedron as derived from the $Ca_3Au_{12.07}Ga_{6.93}$ 1/1 CA

Atom	Wyck.	Site Sym.	x	y	z	Tsai-type shell
Al4	8*c*	.3.	0.43900	0.43900	0.43900	(I) "Tetrahedron"
Al2	24*f*	1	0	0.91600	0.24800	(II) Dodecahedron
Au4	8*c*	.3.	0.14970	0.14970	0.14970	
Au5	8*c*	.3.	0.85030	0.85030	0.85030	
Ca1	2*a*	23.	1/2	1/2	1/2	(III) Icosahedron
Al3	12*d*	2..	0.40920	0	0	(IV) Icosidodecahedron
Au2	24*f*	1	0.10330	0.19900	0.34040	(IV) Icosidodecahedron + (V) 80-vertex cluster
Au3	24*f*	1	0.89670	0.80100	0.65960	
Al5	8*c*	.3.	3/4	3/4	3/4	(V) 80-vertex cluster
Au1	24*f*	1	0	0.64370	0.59650	
Al1	12*e*	2..	0.79950	1/2	0	(V) 80-vertex cluster + (VI) Icosahedron
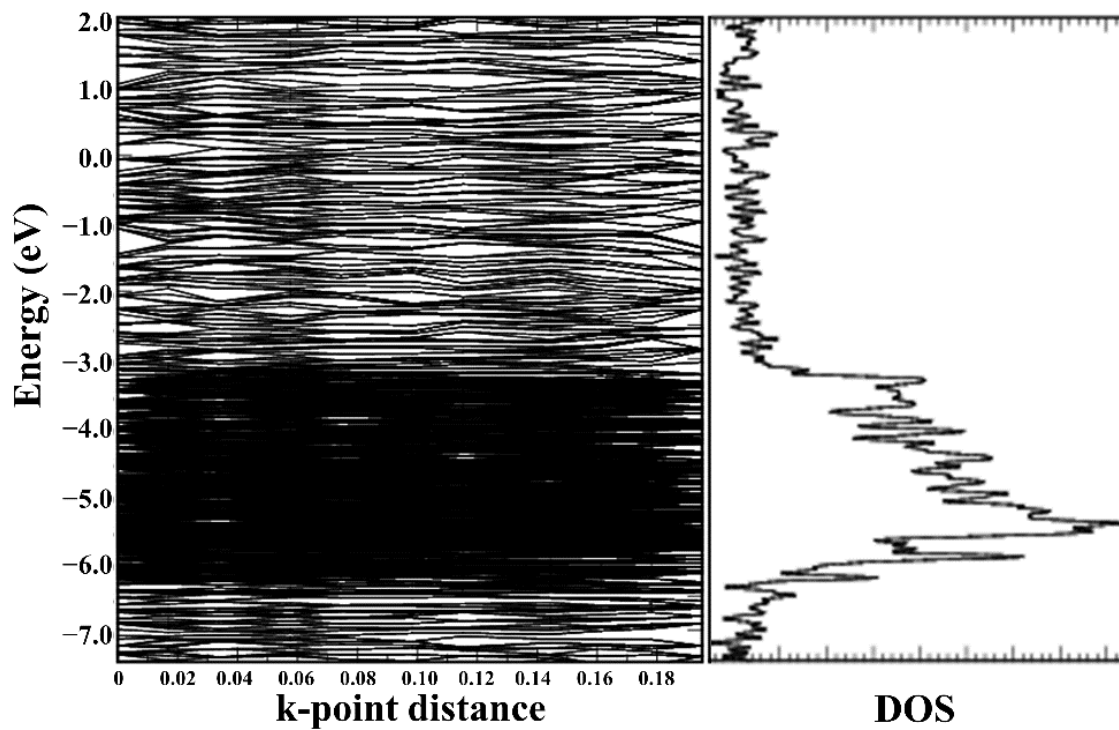
Figure S12. Electronic band structure and density of states (DOS) of the hypothetical 1/1 CA "$Ca_{24}Au_{88}Al_{64}$".

APPENDIX D

CHAPTER 6 SUPPORTING INFORMATION

AAuAl (A = Ca, Sc, and Ti): Peierls Distortion, Atomic Coloring, and Structural Competition

Contents

Table S1–S4. Selected crystallographic, atomic coordinates, and displacement parameters of ScAuAl in the Fe_2P substructure (S1 & S3) and Mg_2Ga superstructure (S2 & S4) as selected from the molar loading ratios 1Sc: 2Au: 5Al and 1Sc: 1Au: 1Al, respectively.

Figure S1. ScAuAl atomic coordination spheres in the asymmetric unit of the Fe_2P substructure.

Table S5. ScAuAl (Fe_2P) structural coloring models and numbers of selected interatomic distances for atomic site preference analysis.

Table S6–S7. ScAuAl (Fe_2P) and competing structural models total calculated energies, numbers of interatomic interactions at various distances, and formation energies.

Table S8–S9. CaAuAl (TiNiSi-type) and competing structural models total calculated energies, numbers of interatomic interactions at various distances, and formation energies.

Table S10–S11. TiAuAl (Ni_2In-type) and competing structural models total calculated energies, numbers of interatomic interactions at various distances, and formation energies.

Table S12. ScAuAl (Fe_2P) structural parameters before and after VASP optimization as used for subsequent electronic structural calculations and plots.

Table S13. Wigner Seitz radii for Ca, Sc, Ti, Au, and Al atoms as used for subsequent LMTO calculations and plotting of DOS and –COHP curves for pairwise interactions < 3.5 Å.

Figure S2. ScAuAl DOS and COHP curves in competing structures in the $CaIn_2$-type derivatives: NdPtSb, LiGaGe, and ScAuSi. The main text includes electronic structures of ScAuAl in the TiNiSi and Ni_2In structures, which are the most competitive to the experimental model.

Figure S3. CaAuAl DOS and COHP curves for the experimental (TiNiSi-type) and competing structures Fe_2P, Ni_2In, NdPtSb, LiGaGe, and ScAuSi.

Figure S4. TiAuAl DOS and COHP curves for the experimental (Ni_2In-type) and competing structures Fe_2P, TiNiSi, NdPtSb, LiGaGe, and ScAuSi.

Table S1. ScAuAl selected refined crystallographic data and structural parameters from loading 1Sc: 2Au: 5Al

instrument	Bruker CCD APEX II								
radiation; λ (Å)/ temp.(K)	Mo Kα; 0.71073/298								
θ range data collection	3.3°–31.4°			3.3°–29.7°			3.3°–31.1°		
absorp. coeff. μ (mm⁻¹)/ correction	71.83/ empirical			70.51/ empirical			70.49/ empirical		
meas./ indpnt./ obs. [I > 2σ(I)]/ para.	3879/ 226/ 213/ 15			655/ 184/ 167/ 15			1831/ 223/ 211/ 15		
R[F² > 2σ(F²)]/ wR(F²)/ Rint/ GOF	0.016/ 0.040/ 0.032/ 1.21			0.045/ 0.110/ 0.047/ 1.14			0.022/ 0.049/ 0.050/ 1.11		
space group/ Pearson symbol	$P\bar{6}2m$ / hP9								
Δρmax, Δρmin (e Å⁻³)	1.25, −2.00			4.36, −3.23			1.70, −3.00		
dimensions (Å)	a = 7.2067(6) c = 3.6217(3)			a = 7.219(4) c = 3.610(2)			a = 7.197(5) c = 3.633(2)		
volume (Å³)/ Z	162.90(2)/ 3			162.9(2)/ 3			163.0(2)/ 3		
index ranges	−10 ≤ h, k ≤ 10; −5 ≤ l ≤ 5			−9 ≤ h ≤ 10; −7 ≤ k ≤ 6; −3 ≤ l ≤ 5			−10 ≤ h ≤ 9; −10 ≤ k ≤ 10; −5 ≤ l ≤ 5		
absolute structure parameter	0.02(3)			0.04(7)			0.00(4)		
Au1 (1a, $\bar{6}2m$) x, y, z, U_iso	0, 0, 0		0.0110(2)	0, 0, 0		0.0173(6)	0, 0, 0		0.0054(3)
Au2 (2d, $\bar{6}$..) x, y, z, U_iso	1/3, 2/3, 1/2		0.0198(2)	1/3, 2/3, 1/2		0.0248(6)	2/3, 1/3, 1/2		0.0139(3)
Al (3f, m2m) x, y, z, U_iso	0.2642(5), 0, 1/2		0.0088(6)	0.267(1), 0, 1/2		0.011(1)	0.7371(7), 0, 1/2		0.0053(9)
Sc (3g, m2m) x, y, z, U_iso	0.5979(3), 0, 0		0.0157(5)	0.599(1), 0, 0		0.022(1)	0.4023(5), 0, 0		0.0096(7)
1a–1a (along c), 1a–3f, 1a–3g (Å)	3.6217(3)	2.627(1)	2.898(1)	3.610(2)	2.638(5)	2.893(9)	3.633(2)	2.623(2)	2.895(3)
2d–2d (along c), 2d–3f, 2d–3g (Å)	3.6217(3)	2.687(4)	2.8469(6)	3.610(2)	2.680(8)	2.859(5)	3.633(2)	2.689(5)	2.848(1)
doubled c with disordered sites	$P\bar{6}2c$/ hP18								
meas./ indpnt./ obs. [I > 2σ(I)]/	7249/ 383/ 229			8726/ 851/ 405			3473/ 377/ 249		
R[F² > 2σ(F²)]/ wR(F²)/ Rint/ GOF	0.015/ 0.039/ 0.035/ 1.05			0.035/ 0.099/ 0.113/ 0.97			0.023/ 0.068/ 0.052/ 1.19		
Δρmax, Δρmin (e Å⁻³)	1.13, −0.96			2.08, −3.85			1.46, −1.81		
dimensions (Å)	a = 7.2074(6); c = 7.2443(6)			a = 7.226(3); c = 7.242(4)			a = 7.196(5); c = 7.266(5)		
volume (Å³)/ Z/ param.	325.90(6)/ 6/ 23			327.5(3)/ 6/ 23			325.9(5)/ 6/ 23		
index ranges	−10 ≤ h, k ≤ 10; −5 ≤ l ≤ 5			−13 ≤ h, k, l ≤ 13			−10 ≤ h, k, l ≤ 10		
absolute structure parameter	0.00(3)			0.01(4)			0.00(4)		
Au1(2b), x, y, z, U_iso		0, 0, 1/4	0.0092(2)		0, 0, 1/4	0.0098(2)		0, 0, 1/4	0.0053(3)
Au2(4f), occ., x, y, z, U_iso	0.54(2)	1/3, 2/3, 0.0195(9)	0.0100(5)	0.55(2)	1/3, 2/3, 0.019(1)	0.0101(4)	0.55(2)	1/3, 2/3, 0.019(1)	0.0050(8)
Au3(4f), occ., x, y, z, U_iso	0.42(2)	2/3, 1/3, 0.0214(9)	0.0100(5)	0.45(2)	2/3, 1/3, 0.0204(1)	0.0101(4)	0.45(2)	2/3, 1/3, 0.0217(9)	0.0050(8)
Al/Au(6g), occ. x, y, z, U_iso	0.984/0.16(3)	0.2645(5), 0, 0	0.012(1)	0.981/0.019(4)	0.2649(6), 0, 0	0.010(1)	0.998/0.002(5)	0.2628(8), 0, 0	0.005(2)
Sc(6h), x, y, z, U_iso		0.4019(7), 0.4024(7), 1/4	0.0137(4)		0.401(1), 0.402(1), 1/4	0.0131(5)		0.4040(7), 0.4009(7), 1/4	0.0087(7)
2b–2b (c-axis), 2b–6g, 2b–6h	3.6221(3)	2.629(1)	2.899(6)	3.621(2)	2.635(3)	2.903(8)	3.633(3)	2.622(2)	2.896(6)
4f–4f (c-axis), 4f–6g, 4f–6h	3.312(9), 3.905(9)	2.689(2)	2.753(5), 2.942(6)	3.34(1), 3.90(1)	2.694(5)	2.764(7), 2.842(8)	3.318(9), 3.92(1)	2.693(6)	2.273(5), 2.928(6)

Table S2. ScAuAl selected refined crystallographic data and structural parameters from loading 1Sc: 1Au: 1Al

instrument	Bruker CCD APEX II					
radiation; λ (Å)/ temp.(K)	Mo Kα; 0.71073/298					
θ range data collection	3.3º–29.0º		3.3º–29.0º		3.3º–29.2º	
absorp. coeff. μ (mm^{-1})/ correction	34.96/ empirical		34.90/ empirical		35.08/ empirical	
meas./ indpnt./ obs. [I > 2σ(I)]/ para.	4550/ 307/ 291/ 19		2725/ 303/ 301/ 19		5164/ 316/ 296/ 19	
R[F^2 > 2σ(F^2)]/ wR(F^2)/ R$_{int}$/ GOF	0.018/ 0.036/ 0.035/ 1.15		0.016/ 0.038/ 0.033/ 1.13		0.022/ 0.054/ 0.061/ 1.10	
space group/ Pearson symbol	$P\bar{6}2c$/ hP18					
$\Delta\rho_{max}$, $\Delta\rho_{min}$ (e Å^{-3})	1.35, −1.33		1.52, −1.72		2.26, −2.00	
dimensions (Å)	a = 7.2362(10) c = 7.2448(10)		a = 7.234(3) c = 7.263(3)		a = 7.2224(2) c = 7.2487(3)	
volume (Å^3)/ Z	328.53(10)/ 3		329.2(3)/ 3		327.46(2)/ 3	
index ranges	−9 ≤ h, k, l ≤ 9		−9 ≤ h, k, l ≤ 9		−10 ≤ h, k, l ≤ 9	
absolute structure parameter	0.03(3)		0.03(3)		0.07(4)	
Au1 (2b, $\bar{6}$..) x, y, z, U$_{iso}$	0, 0, 1/4	0.0077(2)	0, 0, 1/4	0.0052(2)	0, 0, 1/4	0.0068(3)
Au2 (4f, 3..) x, y, z, U$_{iso}$	1/3, 2/3, 0.02100(6)	0.0079(2)	1/3, 2/3, 0.02139(6)	0.0058(2)	1/3, 2/3, 0.02013	0.0082(3)
Al (6g, .2.) x, y, z, U$_{iso}$	0.2628(6), 0, 0	0.0080(7)	0.2616(5), 0, 0	0.0064(7)	0.2623(7), 0, 0	0.0042(9)
Sc (6h, m..) x, y, z, U$_{iso}$	0.4096(4), 0.3947(4), 1/4	0.0075(5)	0.4101(3), 0.3950(4), 1/4	0.0060(4)	0.4092(5), 0.395(5), 1/4	0.0047(6)
2b–2b (along c), 2b–6g, 2b–6h (Å)	3.6224(5)	2.626(2) | 2.912(3)	3.632(2)	2.623(3) | 2.914(3)	3.6244(1)	2.622(2) | 2.907(4)
4f–4f (along c), 4f–6g, 4f–6h (Å)	3.3181(8), 3.9267(8)	2.708(2) | 2.831(2), 2.887(2)	3.321(2), 3.942(2)	2.713(4) | 2.832(2), 2.891(2)	3.3325(8), 3.9162(8)	2.705(2) | 2.826(4), 2.886(3)

Table S3. Fractional atomic coordinates and displacement parameters of ScAuAl in the Fe$_2$P substructure as selected from 1Sc:2Au:5Al.

|	atom	*wyck*	*sym*	*x*	*y*	*z*	U_{iso}	U_{11}	U_{22}	U_{33}	U_{12}	U_{13}	U_{23}
ScAuAl	Au1	1*a*	$\bar{6}2m$	0	0	0	0.0110 (2)	0.0102 (2)	0.0102 (2)	0.0126 (3)	0.0051 (1)	0.000	0.000
	Au2	2*d*	$\bar{6}..$	1/3	2/3	1/2	0.0198 (2)	0.0094 (2)	0.0094 (2)	0.0406 (3)	0.00472 (9)	0.000	0.000
	Al	3*f*	*m2m*	0.2642 (5)	0	1/2	0.0088 (6)	0.008 (10)	0.007 (2)	0.011 (1)	0.0037 (7)	0.000	0.000
	Sc	3*g*	*m2m*	0.5979 (3)	0	0	0.0157 (5)	0.0166 (8)	0.022 (1)	0.0105 (8)	0.0108 (6)	0.000	0.000
ScAuAl	Au1	1*a*	$\bar{6}2m$	0	0	0	0.0173 (6)	0.0181 (9)	0.0181 (9)	0.016 (1)	0.0090 (4)	0.000	0.000
	Au2	2*d*	$\bar{6}..$	1/3	2/3	1/2	0.0248 (6)	0.0172 (8)	0.0172 (8)	0.040 (1)	0.0086 (4)	0.000	0.000
	Al	3*f*	*m2m*	0.267 (1)	0	1/2	0.011 (1)	0.017 (4)	0.004 (5)	0.009 (4)	0.002 (2)	0.000	0.000
	Sc	3*g*	*m2m*	0.599 (1)	0	0	0.022 (1)	0.026 (3)	0.029 (5)	0.013 (3)	0.015 (2)	0.000	0.000
ScAuAl	Au1	1*a*	$\bar{6}2m$	0	0	0	0.0054 (3)	0.0062 (3)	0.0062 (3)	0.0039 (4)	0.0031 (2)	0.000	0.000
	Au2	2*d*	$\bar{6}..$	2/3	1/3	1/2	0.0139 (3)	0.0051 (3)	0.0051 (3)	0.0315 (5)	0.0026 (2)	0.000	0.000
	Al	3*f*	*m2m*	0.7371 (7)	0	1/2	0.0053 (9)	0.006 (2)	0.004 (2)	0.005 (2)	0.002 (1)	0.000	0.000
	Sc	3*g*	*m2m*	0.4023 (5)	0	0	0.0096 (7)	0.013 (1)	0.014 (2)	0.002 (1)	0.0072 (8)	0.000	0.000

Table S4. Fractional atomic coordinates and displacement parameters of ScAuAl in the Mg$_2$Ga superstructure as selected from 1Sc:1Au:1Al

	atom	wyck	sym	x	y	z	U_{iso}	U_{11}	U_{22}	U_{33}	U_{12}	U_{13}	U_{23}
ScAuAl	Au1	2b	$\bar{6}$..	0	0	1/4	0.0077 (2)	0.0062 (2)	0.0062 (2)	0.0106 (4)	0.0031 (1)	0.000	0.000
	Au2	4f	3..	1/3	2/3	0.02100 (6)	0.0079 (2)	0.0058 (2)	0.0058 (2)	0.0121 (3)	0.00291 (10)	0.000	0.000
	Al	6g	.2.	0.2628 (6)	0	0	0.0080 (7)	0.008 (1)	0.005 (2)	0.010 (2)	0.0025 (10)	−.0005 (7)	−.0001 (1)
	Sc	6h	m..	0.4096 (4)	0	1/4	0.0075 (5)	0.008 (1)	0.006 (2)	0.009 (1)	0.004 (1)	0.000	0.000
ScAuAl	Au1	2b	$\bar{6}$..	0	0	1/4	0.0052 (2)	0.0035 (2)	0.0035 (2)	0.0088 (3)	0.0017 (1)	0.000	0.000
	Au2	4f	3..	1/3	2/3	0.02139 (6)	0.0058 (2)	0.0032 (2)	0.0032 (2)	0.0109 (3)	0.0016 (1)	0.000	0.000
	Al	6g	.2.	0.2628 (6)	0	0	0.0064 (7)	0.005 (1)	0.003 (2)	0.011 (2)	0.0014 (9)	−.0008 (6)	−.002 (1)
	Sc	6h	m..	0.4096 (4)	0	1/4	0.0060 (4)	0.0049 (10)	0.0035 (10)	0.0083 (10)	0.0010 (10)	0.000	0.000
ScAuAl	Au1	2b	$\bar{6}$..	0	0	1/4	0.0068 (3)	0.0047 (3)	0.0047 (3)	0.0110 (4)	0.0023 (2)	0.000	0.000
	Au2	4f	3..	1/3	2/3	0.02013 (8)	0.0082 (3)	0.0043 (3)	0.0043 (3)	0.0159 (4)	0.0022 (1)	0.000	0.000
	Al	6g	.2.	0.2628 (6)	0	0	0.0042 (9)	0.002 (2)	0.004 (2)	0.007 (2)	0.002 (1)	−.0007 (9)	−.002 (2)
	Sc	6h	m..	0.4096 (4)	0	1/4	0.0047 (6)	0.003 (1)	−.001 (1)	0.009 (1)	−.003 (1)	0.000	0.000
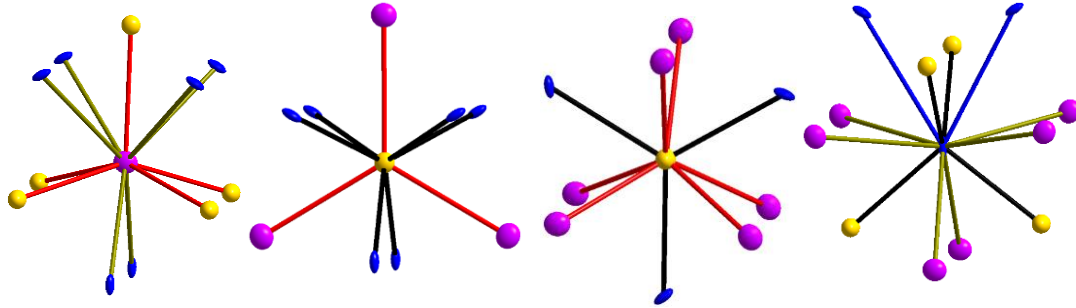
Figure S1. Coordination spheres of atoms in the asymmetric unit cell of the Fe$_2$P substructure: {[Au1(Au2)$_2$Al$_6$]@Sc}, {(Sc$_3$Al$_6$)@Au1}, {(Sc$_6$Al$_3$)@Au2} and {(Sc$_6$(Au1)$_2$(Au2)$_2$}. Sc atoms are represented in dark pink, Au atoms are in dark yellow, and Al atoms are in blue.

Table S5. ScAuAl (Fe$_2$P substructure) coloring models and frequencies of atomic interactions

distance (Å)	Experimental	α	β	γ	δ	ε
2.638(5)	Au–Al (×6)	Au–Al (×6)	Sc–Au (×6)	Sc–Au (×6)	Sc–Al (×6)	Sc–Al (×6)
2.681(1)	Au–Al (×6)	Au–Al (×6)	Sc–Au (×6)	Sc–Au (×6)	Sc–Al (×6)	Sc–Al (×6)
2.848(5)	Sc–Au (×12)	Sc–Al (×12)	Au–Al (×12)	Sc–Al (×12)	Au–Al (×12)	Sc–Au (×12)
2.893(5)	Sc–Au (×3)	Sc–Al (×3)	Au–Al (×3)	Sc–Al (×3)	Au–Al (×3)	Sc–Au (×3)
3.005(6)	Sc–Al (×6)	Sc–Au (×6)	Sc–Al (×6)	Au–Al (×6)	Sc–Au (×6)	Au–Al (×6)
3.125(3)	Sc–Al (×12)	Sc–Au (×12)	Sc–Al (×12)	Au–Al (×12)	Sc–Au (×12)	Au–Al (×12)
3.331(2)	Al–Al (×3)	Au–Au (×3)	Sc–Sc (×3)	Au–Au (×3)	Sc–Sc (×3)	Al–Al (×3)
ΔE (eV/f.u.)	0	+0.347	+0.960	+1.480	+1.759	+2.112

Table S6. ScAuAl competing structures with calculated total energies and numbers of selected interatomic distances

	Fe$_2$P (Expt.)	Co$_2$Si	NdPtSb	LiGaGe	Ni$_2$In	ScAuSi	Cu$_2$Sb
eV/f.u.	−15.478	−15.447	−15.401	−15.399	−15.397	−15.338	−14.674
ΔE$_{rel.}$	0.000	+0.031	+0.077	+0.079	+0.081	+0.140	+0.804
space group	P$\bar{6}$2m	Pnma	P6$_3$mc	P6$_3$mc	P6$_3$/mmc	P$\bar{6}$m2	P4/nmm
lattice para.							
a	7.287	6.674	4.459	4.459	4.467	4.427	4.242
b		4.378					
c	3.625	7.636	6.419	6.428	6.389	6.623	6.654
Å^3/f.u.	55.563	55.779	55.257	55.333	55.191	56.213	59.867
Sc–Au	2.848 (4×)	2.749 (1×)	3.176 (3×)	2.835 (3×)	3.143 (6×)	2.841 (3×)	
	2.893 (1×)	2.764 (2×)	3.329 (3×)	3.231 (3×)		3.107 (3×)	
		2.877 (1×)					
		2.893 (2×)					
Sc–Al	3.005 (2×)	2.571 (2×)	3.132 (3×)	2.850 (3×)	3.143 (6×)	2.797 (3×)	3.486 (4×)
	3.125 (4×)	2.612 (1×)	3.377 (3×)	3.212 (3×)		3.162 (3×)	
		2.633 (2×)					
		3.472 (1×)					
Sc–Sc		3.145 (1×)		3.423 (1×)		3.501 (0.5×)	
		3.216 (1×)					
Au–Al	2.638* (2×)	2.307 (2×)	2.596 (3×)	2.576 (3×)	2.451 (3×)	2.494 (3×)	2.725 (4×)
	2.681 (2×)	2.346 (1×)		2.752* (1×)			
		2.353* (1×)					
Al–Al	3.331 (1×)					2.762 (0.5×)	
Au–Au		2.660(×1)				2.936 (0.5×)	3.217 (2×)

*Interlayer distance crossing c-axis if the structure were represented as "layers".

Table S7. ScAuAl competing structures and calculated formation energies

Model	$\Delta E_{reaction}$ (eV/f.u.)	$\Delta E_{relative}$ (eV/f.u.)
Experimental (Fe$_2$P-type)	−2.308(1)	0.000
TiNiSi	−2.277(1)	+0.031
NdPtSb	−2.231(5)	+0.077
LiGaGe	−2.229(1)	+0.079
Ni$_2$In	−2.227(1)	+0.081
ScAuSi	−2.169(1)	+0.140
Cu$_2$Sb-type	−1.504(2)	+0.804

Table S8. CaAuAl competing structures with calculated total energies and numbers of selected interatomic distances

	Fe$_2$P	Co$_2$Si (Expt.)	NdPtSb	LiGaGe	Ni$_2$In	ScAuSi	Cu$_2$Sb
eV/f.u.	−10.976	−11.114	−10.900	−10.897	−10.897	−10.902	−10.606
$\Delta E_{rel.}$	+0.138	0.000	+0.213	+0.217	+0.216	+0.212	+0.508
space group	$P\bar{6}2m$	$Pnma$	$P6_3mc$	$P6_3mc$	$P6_3/mmc$	$P\bar{6}m2$	$P4/nmm$
lattice para.							
a	7.255	7.337	4.563	4.564	4.548	4.536	4.579
b		4.552					
c	4.310	7.824	7.526	7.513	7.597	7.703	6.896
Å^3/f.u.	65.485	65.319	67.836	67.752	68.043	68.642	72.314
Ca–Au	2.848 (×4)	3.061 (×1)	3.176 (×3)	2.835 (×3)	3.143 (×6)	2.841 (×3)	
	2.893 (×1)	3.101 (×2)	3.329 (×3)	3.231 (×3)		3.107 (×3)	
		3.209 (×2)					
Ca–Al	3.005 (×2)	3.18 (×1)	3.132 (×3)	2.850 (×3)	3.143 (×6)	2.797 (×3)	3.486 (×4)
	3.125 (×4)	3.209 (×2)	3.377 (×3)	3.212 (×3)		3.162 (×3)	
		3.416 (×2)					
Ca–Ca				3.423 (×1)		3.401 (×0.5)	
Au–Al	2.638* (×3)	2.666 (×1)	2.596 (×3)	2.576 (×3)	2.596 (×3)	2.596 (×3)	2.596 (×4)
	2.681 (×2)	2.671 (×1)		2.752* (×1)			
		2.687 (×2)					
Al–Al	3.331 (×1)	3.362 (×1)				2.762 (×0.5)	
Au–Au						2.936 (×0.5)	3.217 (×2)

* Interlayer distances crossing the c-axis if structure were represented in "layers".

Table S9. CaAuAl competing structures and calculated formation energies

Model	$\Delta E_{reaction}$ (eV/f.u.)	$\Delta E_{relative}$ (eV/f.u.)
CaAuAl (Co$_2$Si-type)	−2.144(3)	0.000
Fe$_2$P-type	−2.007(3)	+0.138
TiNiSi	−2.140(3)	+0.004
NdPtSb type	−1.932(3)	+0.213
LiGaGe type	−1.927(3)	+0.217
Ni$_2$In	−1.928(5)	+0.216
ScAuSi	−1.932(3)	+0.212
Cu$_2$Sb-type	−1.636(3)	+0.508

Table S10. TiAuAl competing structures with calculated total energies and numbers of selected interatomic distances

	Fe$_2$P	Co$_2$Si	NdPtSb	LiGaGe	Ni$_2$In (Expt.)	ScAuSi	Cu$_2$Sb
eV/f.u.	−16.174	−16.096	−16.311	−16.306	−16.331	−16.210	−15.562
Δ$E_{rel.}$	+0.137	+0.234	+0.020	+0.024	0.000	+0.121	+0.769
space group	$P\bar{6}2m$	$Pnma$	$P6_3mc$	$P6_3mc$	$P6_3/mmc$	$P\bar{6}m2$	$P4/nmm$
lattice para.							
a	6.694	6.516	4.365	4.363	4.461	4.395	3.988
b		4.001					
c	3.977	7.747	6.150	6.161	5.740	6.025	6.671
Å^3/f.u.	51.435	50.494	50.740	50.788	49.452	50.392	53.060
Ti–Au	2.848 (×4)	2.749 (×1)	3.176 (×3)	2.835 (×3)	2.932 (×6)	2.841 (×3)	
	2.893 (×1)	2.764 (×2)	3.329 (×6)	3.231 (×3)		3.107 (×3)	
		2.877 (×1)					
		2.893 (×2)					
Ti–Al	3.005 (×2)	2.571 (×2)	3.132 (×3)	2.850 (×3)	2.932 (×6)	2.797 (×3)	3.486 (×4)
	3.125 (×4)	2.612 (×1)	3.377 (×3)	3.212 (×3)		3.162 (×3)	
		2.633 (×2)					
		3.472 (×1)					
Ti–Ti		3.145 (×1)		3.423 (×1)	2.915 (×2)	3.401 (×0.5)	
		3.216 (×1)					
Au–Al	2.638* (×2)	2.307 (×2)	2.596 (×3)	2.576 (×3)	2.545 (×3)	2.494 (×3)	2.725 (×4)
	2.681 (×2)	2.346 (×1)		2.752* (×1)			
		2.353* (×1)					
Al–Al	3.331 (×1)					2.762 (×0.5)	
Au–Au		2.660 (×1)				2.936 (×0.5)	3.217 (×2)

* Interlayer distances crossing the *c*-axis if structure were represented in "layers".

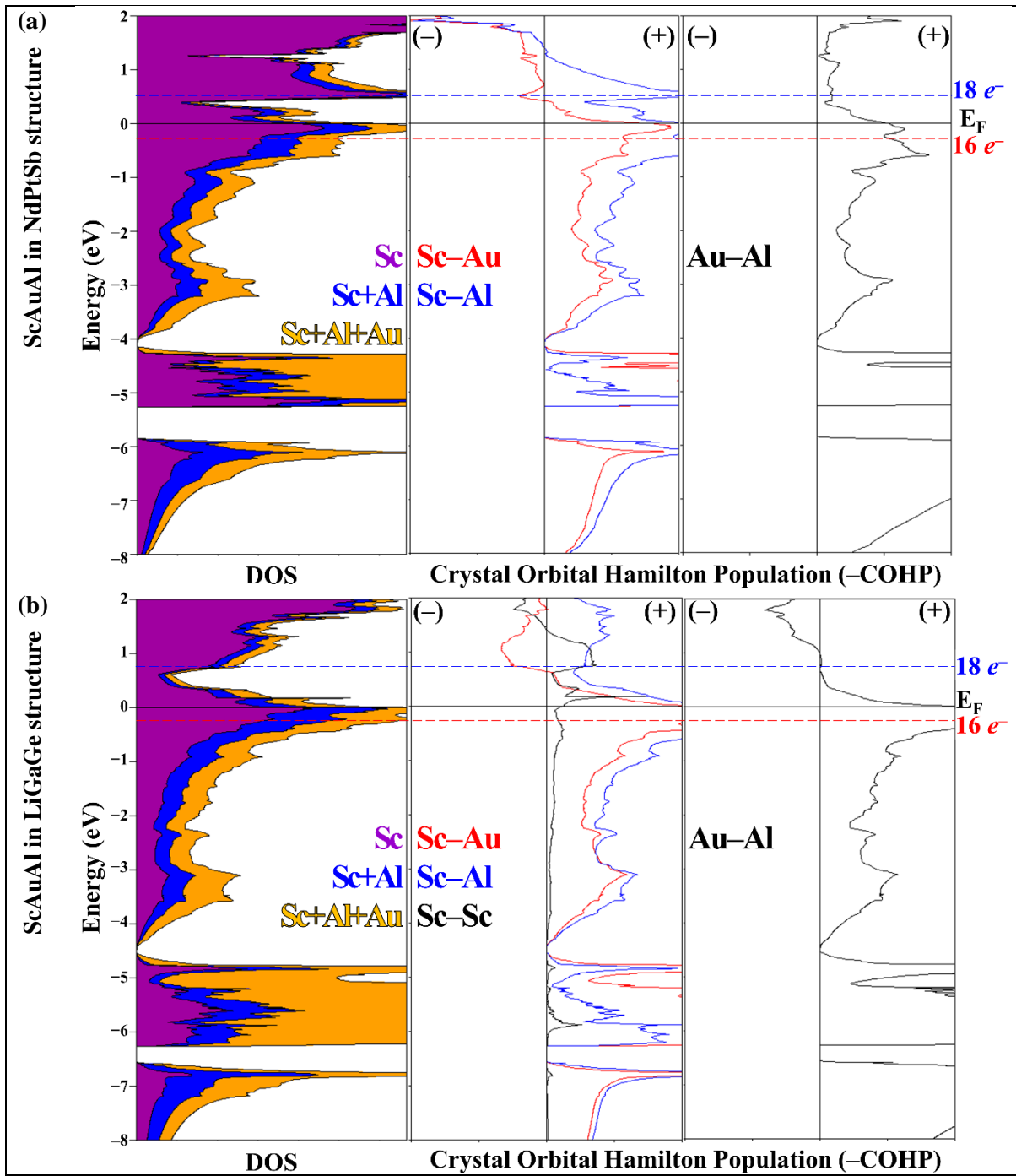**Table S11. TiAuAl competing structures and calculated formation energies**

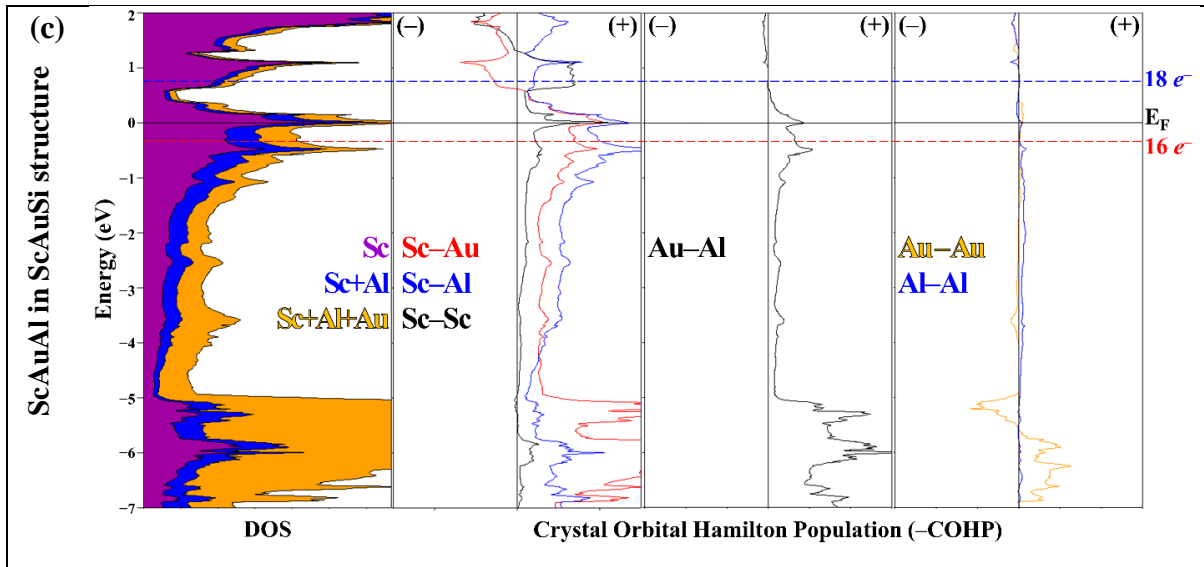| Model	Δ$E_{reaction}$ (eV/f.u.)	Δ$E_{relative}$ (eV/f.u.)
TiAuAl (Ni$_2$In-type)	−1.522(2)	0.000
Fe$_2$P	−1.365(2)	+0.137
TiNiSi	−1.288(2)	+0.234
NdPtSb	−1.502(2)	+0.020
LiGaGe	−1.498(2)	+0.024
Ni$_2$In	−1.523(5)	−0.001
ScAuSi	−1.401(2)	+0.121
Cu$_2$Sb	−0.753(2)	+0.769

Table S12. ScAuAl VASP optimization for electronic calculations

Parameter	Experimental input	Optimization output
a (Å)	7.219	7.2868
b (Å)	7.219	7.2868
c (Å)	3.610	3.6250
V (Å^3)	162.93	166.69
Sc (*x, y, z*)	0.401, 0, 1/2	0.3992, 0, 1/2
Au1 (*x, y, z*)	0, 0, 1/2	0, 0, 1/2
Au2 (*x, y, z*)	2/3, 1/3, 0	2/3, 1/3, 0
Al (*x, y, z*)	0.734, 0, 0	0.73636, 0, 0
Sc–Au1 (3*g*–1*a*) (Å)	2.893	2.909
Sc–Au2 (3*g*–2*d*) (Å)	2.849	2.872
Sc–Al (3*g*–3*f*) (Å)	3.005	3.138 and 3.053
Au1–Al (1*a*–3*f*) (Å)	2.638	2.641
Au2–Al (2*d*–3*f*) (Å)	2.681	2.719
Al–Al (3*f*–3*f*) (Å)	3.331	3.327
E_{tot} (eV/f.u.)	−15.465	−15.478

Table S13. Wigner-Seitz radii for LMTO calculations

Model	$R_{w.s.}$ (Å)		
Fe$_2$P	Sc: 3.317	Ca: 3.287	Ti: 3.311
	Au1: 2.980	Au1: 2.963	Au1: 2.981
	Au2: 3.064	Au2: 3.047	Au2: 3.071
	Al: 2.926	Al: 2.902	Al: 2.927
TiNiSi	Sc: 3.166	Ca: 3.759	Ti: 3.167
	Au: 2.592	Au: 2.942	Au: 2.593
	Al: 2.424	Al: 2.894	Al: 2.423
NdPtSb	Sc: 4.023	Ca: 4.023	Ti: 3.646
	Au: 2.856	Au: 2.856	Au: 2.650
	Al: 2.790	Al: 2.790	Al: 2.496
LiGaGe	Sc: 3.431	Ca: 3.431	Ti: 3.366
	Au: 2.928	Au: 2.928	Au: 2.872
	Al: 2.850	Al: 2.850	Al: 2.786
			E: 1.733
Ni$_2$In	Sc: 4.000	Ca: 4.000	Ti: 3.699
	Au: 2.650	Au: 2.650	Au: 2.512
	Al: 2.536	Al: 2.503	Al: 2.311
ScAuSi	Sc1: 3.482	Ca1: 3.482	Ti1: 3.482
	Sc2: 3.486	Ca2: 3.476	Ti2: 3.476
	Au: 2.812	Au1: 2.812	Au1: 2.812
	Al: 2.708	Al: 2.708	Al: 2.708

(a) ScAuAl in NdPtSb structure

(b) ScAuAl in LiGaGe structure

Energy (eV)

DOS

Crystal Orbital Hamilton Population (–COHP)

Sc Sc–Au
Sc+Al Sc–Al
Sc+Al+Au

Au–Al
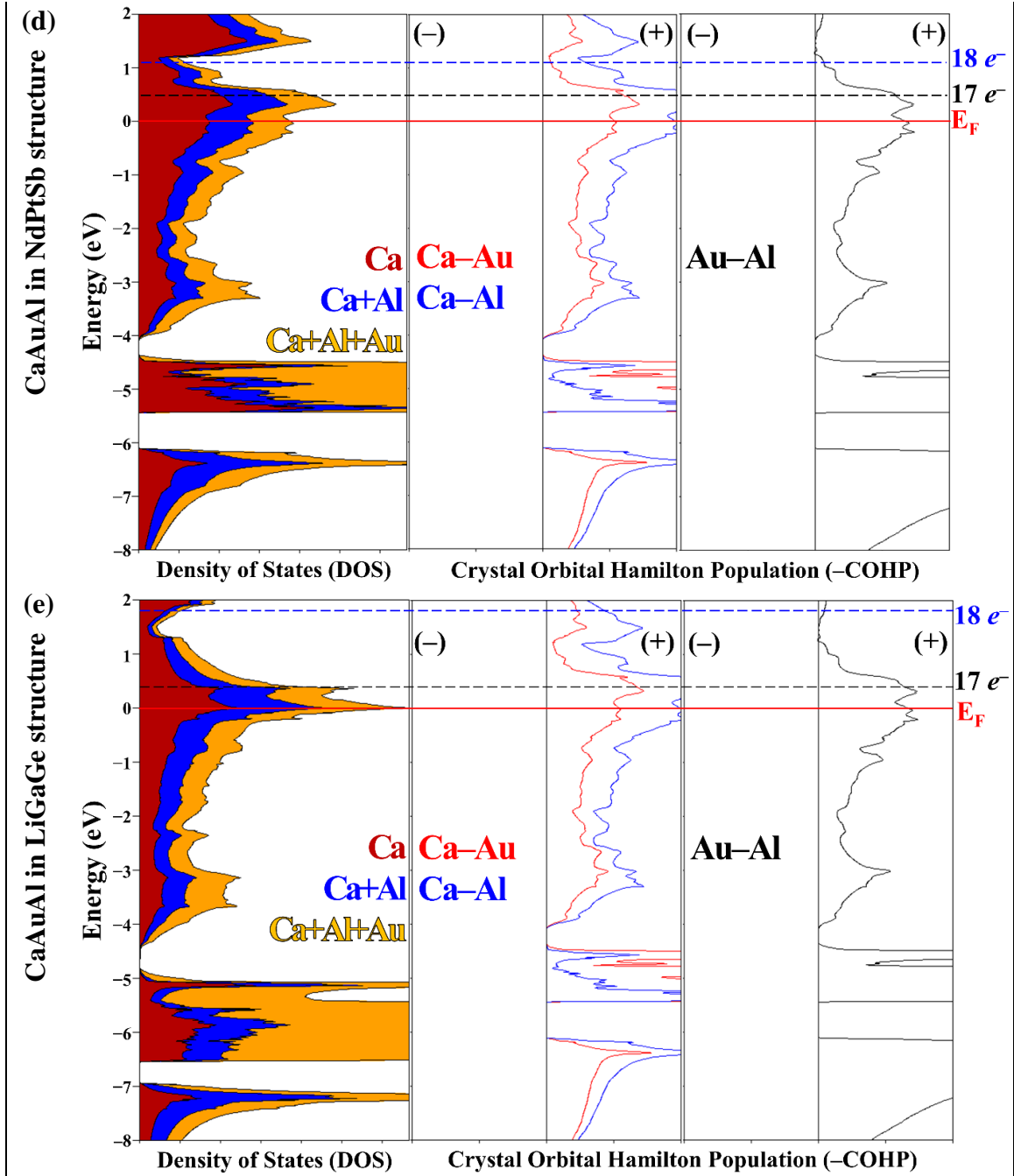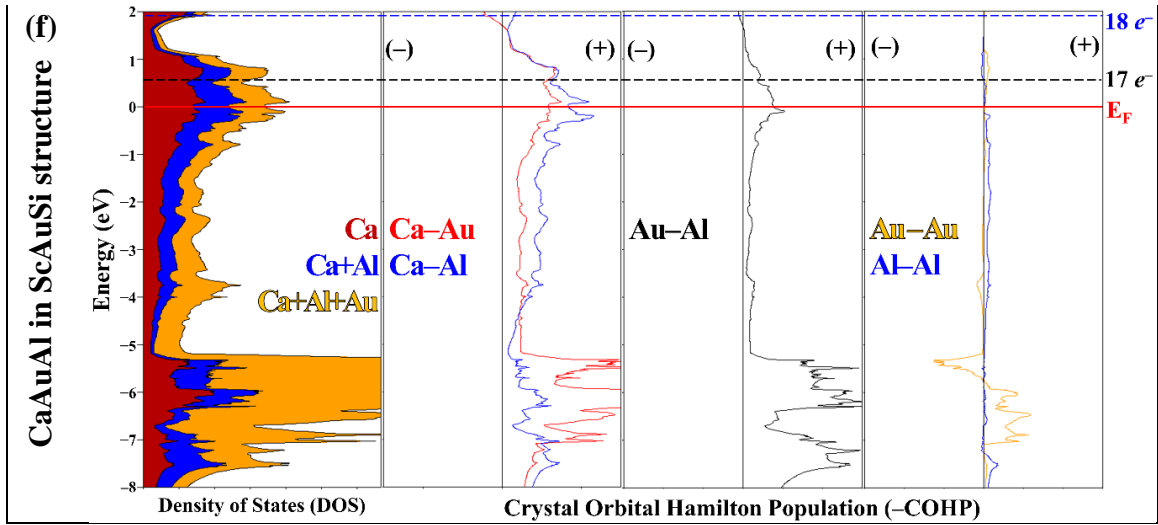
Sc Sc–Au
Sc+Al Sc–Al
Sc+Al+Au Sc–Sc

Au–Al

18 e⁻
E_F
16 e⁻

Figure S2. ScAuAl electronic structures in competing structures (a) NdPtSb (b) LiGaGe, and (c) ScAuSi, for all COHP interactions < 3.5 Å and (–) & (+) indicate antibonding and bonding, respectively.

(d) CaAuAl in NdPtSb structure

Energy (eV)

(−)   (+)   (−)   (+)

18 e⁻
17 e⁻
E_F

Ca   Ca–Au
Ca+Al   Ca–Al
Ca+Al+Au

Au–Al

Density of States (DOS)   **Crystal Orbital Hamilton Population (−COHP)**

(e) CaAuAl in LiGaGe structure

Energy (eV)

(−)   (+)   (−)   (+)

18 e⁻
17 e⁻
E_F

Ca   Ca–Au
Ca+Al   Ca–Al
Ca+Al+Au

Au–Al

Density of States (DOS)   **Crystal Orbital Hamilton Population (−COHP)**
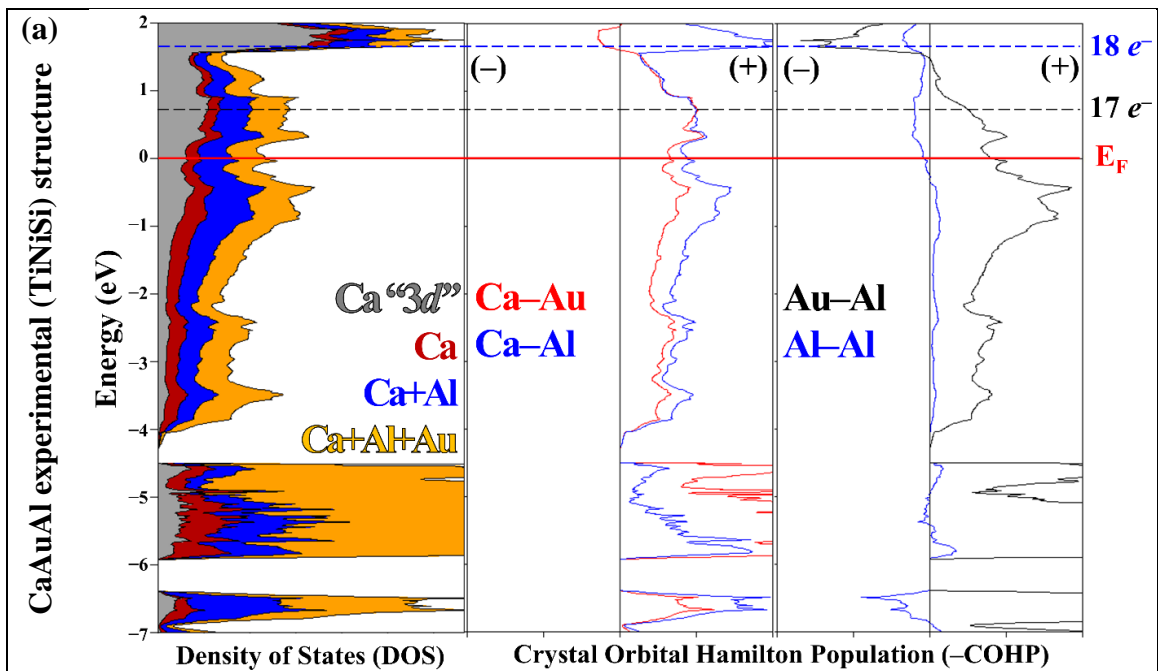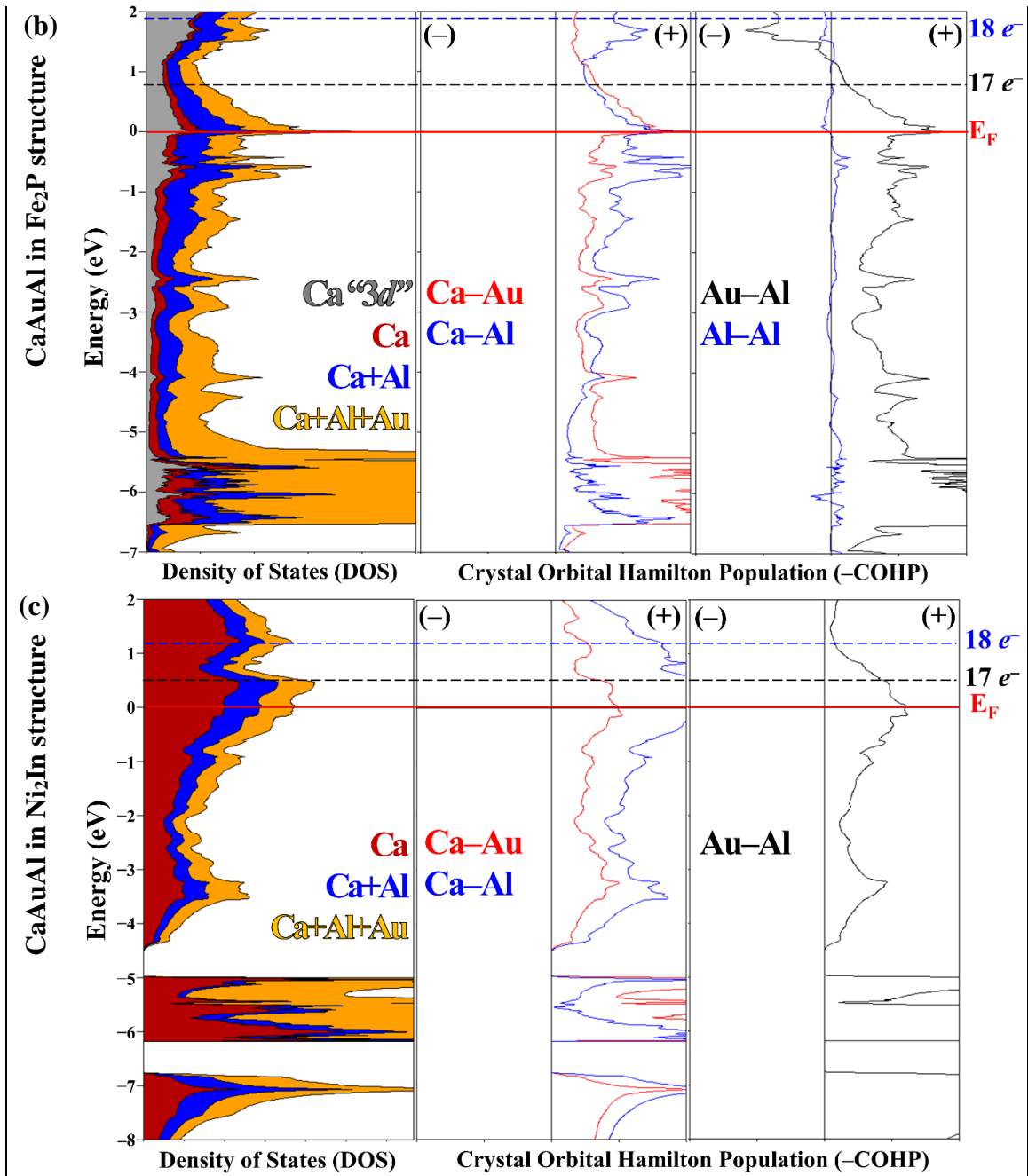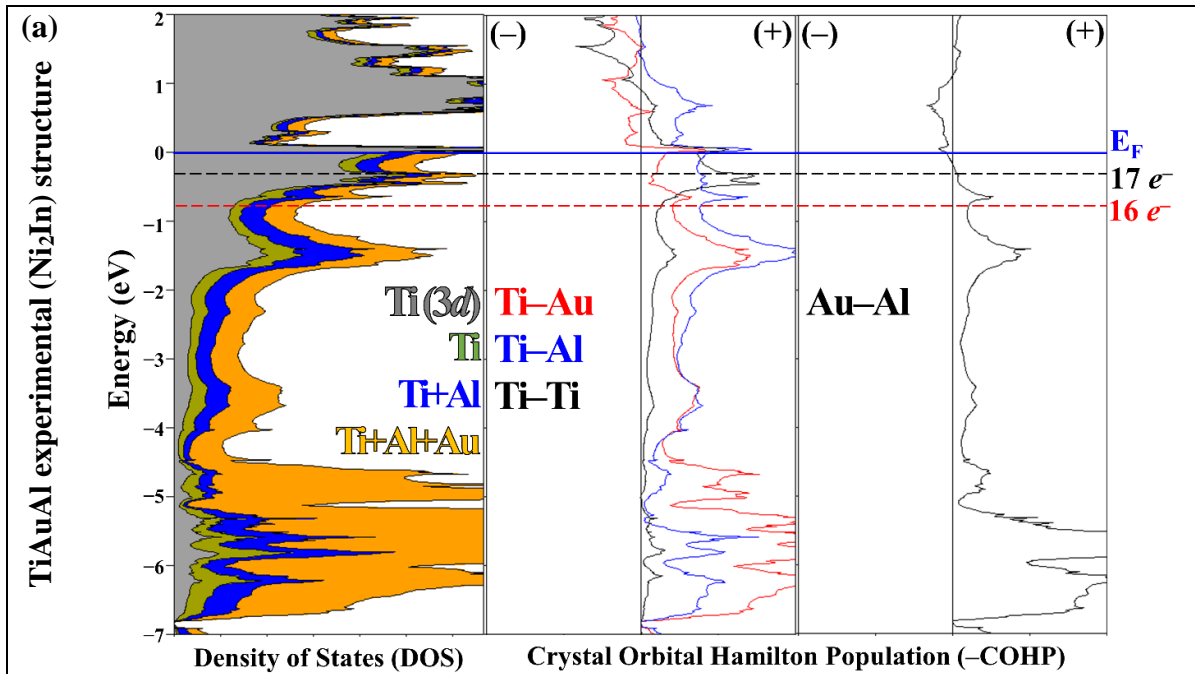
Figure S3. CaAuAl electronic structures (a) and in competing structures (b) Fe$_2$P (c) Ni$_2$In, (d) NdPtSb, (e) LiGaGe, and (f) ScAuSi, for all COHP interactions < 3.5 Å and (−) & (+) indicate antibonding and bonding, respectively.
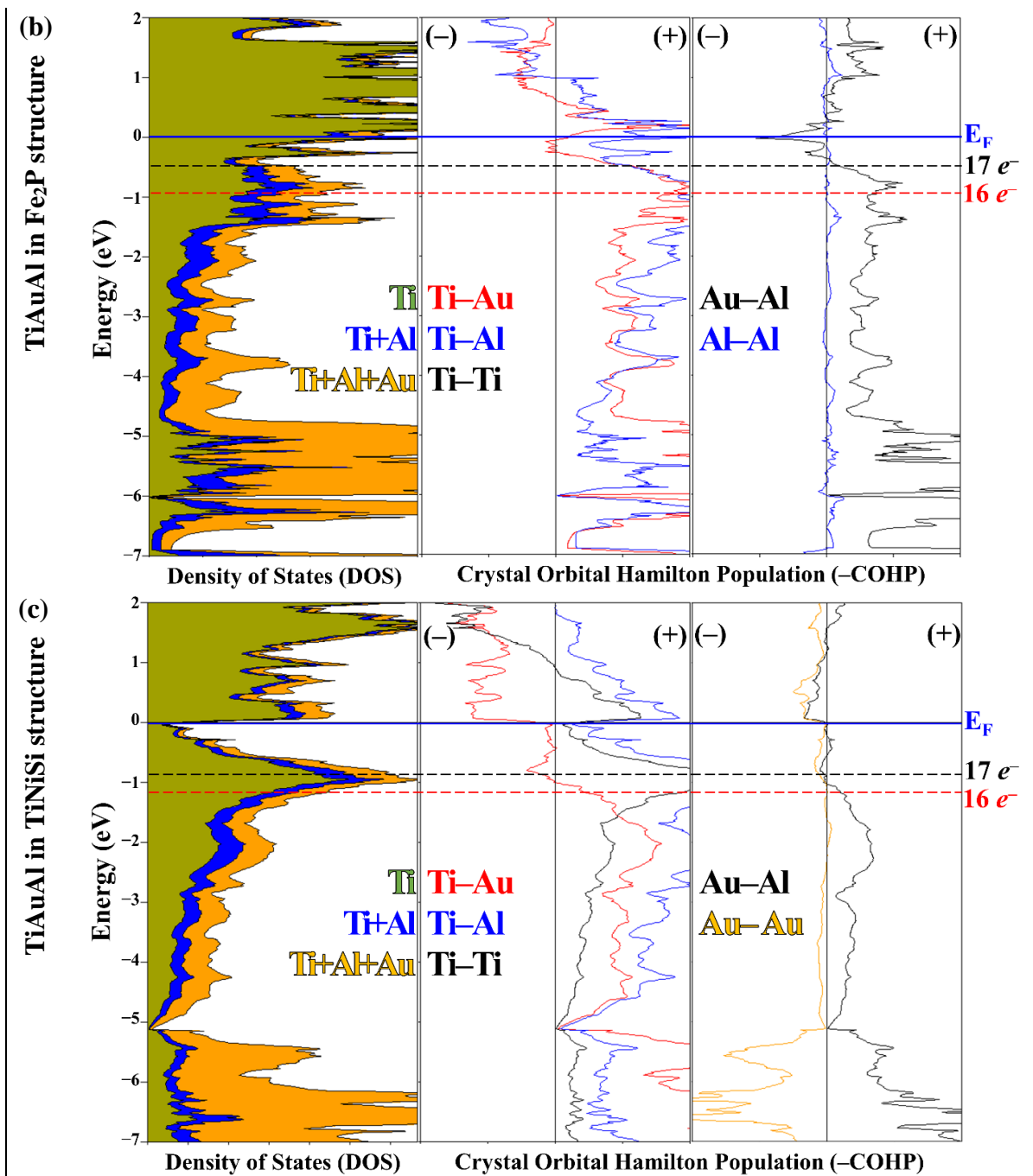
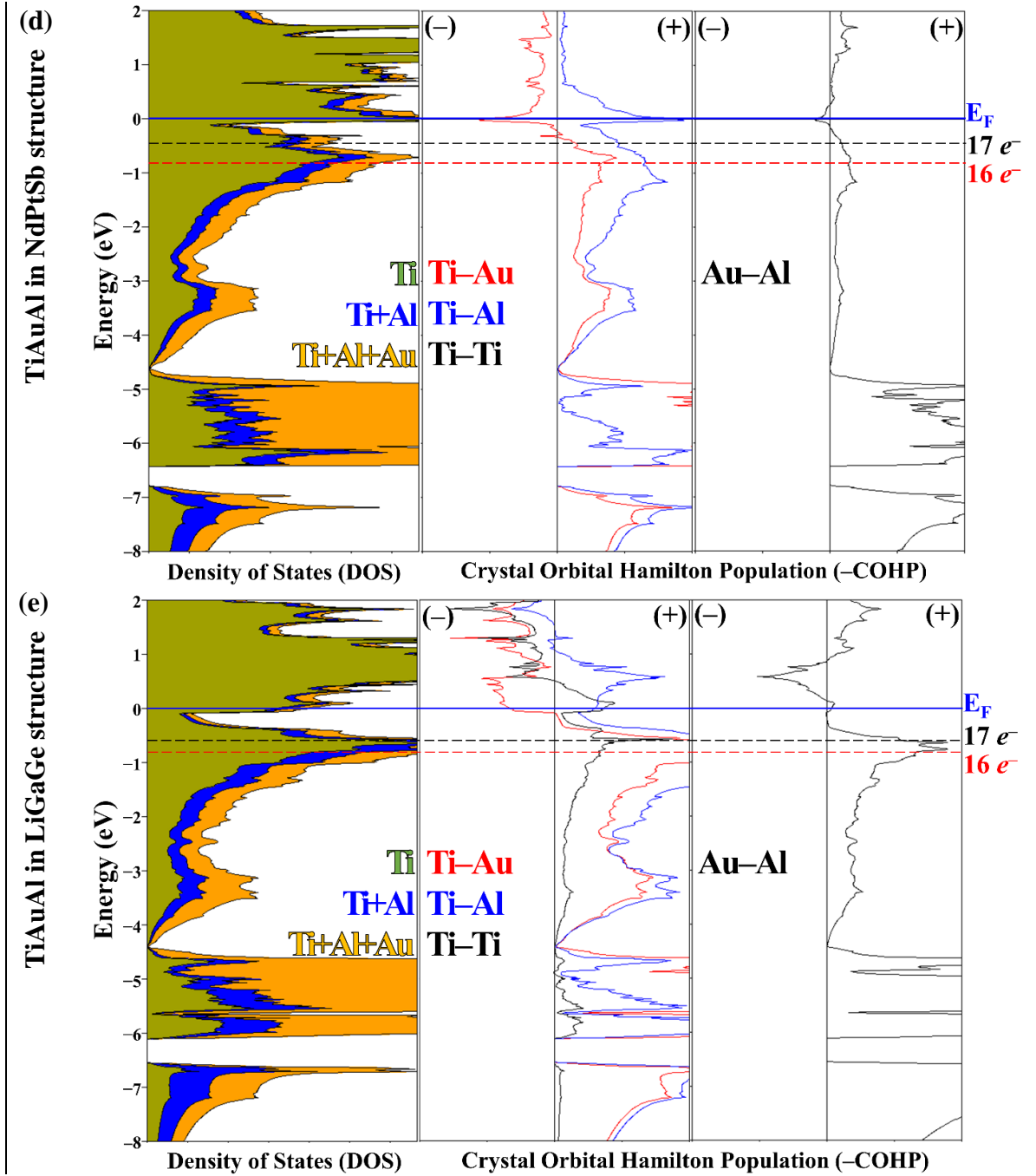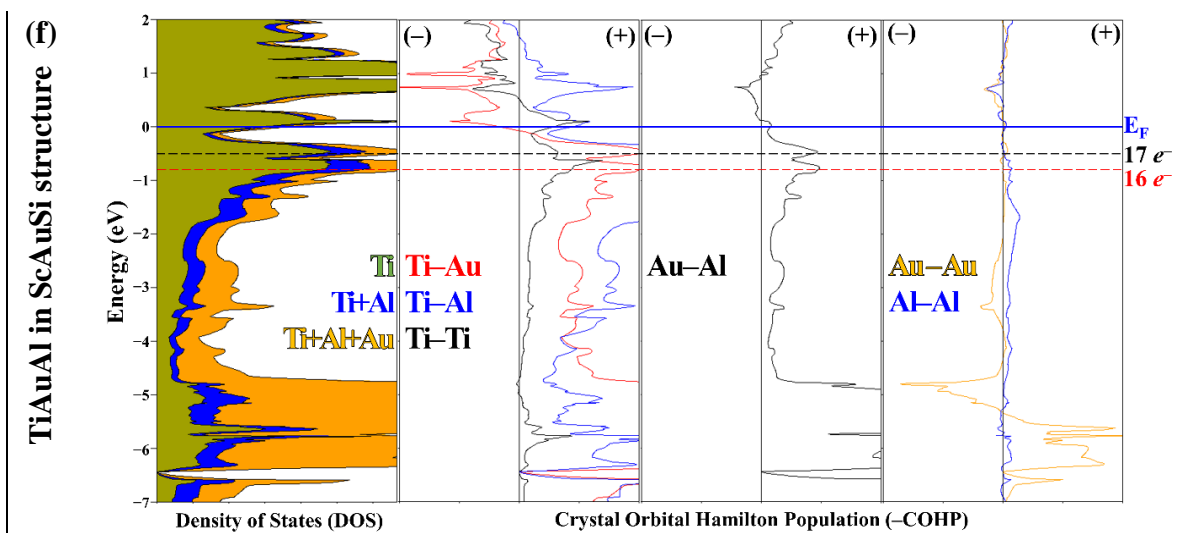**(b)** TiAuAl in Fe₂P structure

Density of States (DOS)

Crystal Orbital Hamilton Population (–COHP)

Ti   Ti–Au
Ti+Al   Ti–Al
Ti+Al+Au   Ti–Ti

Au–Al
Al–Al

(c) TiAuAl in TiNiSi structure

Density of States (DOS)

Crystal Orbital Hamilton Population (–COHP)

Ti   Ti–Au
Ti+Al   Ti–Al
Ti+Al+Au   Ti–Ti

Au–Al
Au–Au

(d) TiAuAl in NdPtSb structure

Energy (eV)

E_F

17 e^-

16 e^-

Ti   Ti–Au
Ti+Al   Ti–Al
Ti+Al+Au   Ti–Ti

Au–Al

Density of States (DOS)   **Crystal Orbital Hamilton Population (–COHP)**

(e) TiAuAl in LiGaGe structure

Energy (eV)

E_F

17 e^-

16 e^-

Ti   Ti–Au
Ti+Al   Ti–Al
Ti+Al+Au   Ti–Ti

Au–Al

Density of States (DOS)   **Crystal Orbital Hamilton Population (–COHP)**

Figure S4. TiAuAl electronic structures (a) and competing structures (b) Fe$_2$P (c) TiNiSi, (d) NdPtSb, (e) LiGaGe, and (f) ScAuSi, for all COHP interactions < 3.5 Å and (−) & (+) indicate antibonding and bonding, respectively.